

https://dspace.org/

Properties of R-HPDC Al-Zn-Mg-Cu aluminium alloys

Curle, Ulyate Andries

2015-06-01
http://hdl.handle.net/10539/18507

Downloaded from a DSpace repository. https://dspace.org/

PROPERTIES OF R-HPDC Al-Zn-Mg-Cu ALUMINIUM ALLOYS

Ulyate Andries Curle

A thesis submitted to the Faculty of Engineering and the Built Environment, University of the Witwatersrand, in the fulfilment of the requirements for the degree of Doctor of Philosophy.

Johannesburg, 1 June 2015

Declaration

I, Ulyate Andries Curle, declare that this thesis is my own work, except where otherwise acknowledged. It is being submitted for the degree of Doctor of Philosophy in Engineering at the University of the Witwatersrand, Johannesburg. It has not been submitted previously at this, or any other university for any degree or examination.

_____ _____

Signature Date

Summary

Five different Al-Zn-Mg-Cu alloys were produced by rheo-high pressure die casting (R-HPDC) of which the as-cast microstructures were characterised with scanning electron microscopy (SEM) and energy dispersive X-ray spectroscopy (EDX). The primary aluminium grains and eutectic phases were observed with SEM backscattered electrons (BSE). The overall compositions of the eutectics were measured with EDX and were found to be relatively similar, regardless of the alloy composition. Two further Al-Zn-Mg-Cu alloys were produced with the same compositions as the eutectics in the R-HPDC alloys. These eutectic alloys were also characterised with SEM and EDX. One of the R-HPDC alloys was also cooled in vacuum and characterised with SEM and EDX.

The as-cast alloys were characterised with differential scanning calorimetry (DSC) and X-ray diffraction (XRD). DSC results showed that all the as-cast alloys had different melting points depending on the phases present in the solidified alloy. XRD showed that the as-cast alloy eutectics had one of two crystal structures for the second component besides the (Al) phase, which were hexagonal or cubic, or a combination of both depending on the overall composition and cooling rate.

Modelling of non-equilibrium alloy solidification was also done using Thermo-Calc with the most recent aluminium database. It was found that the calculated and measured results compared favourably.

The remaining phases in all the alloys, after homogenisation and artificial ageing, were characterised with SEM and EDX to assess the influence of impurity elements. It was found that Fe and Mn react with Cu, and Si with Mg.

Experiments were also conducted to assess the effect of composition on the hardness and yield strength of all the alloys after homogenisation and artificial ageing. A precipitate composition for the T6 condition, from literature, was used for the calculations. It was found that there were reasonable straight line relationships if the impurity elements were neglected. On the other hand, there were near perfect linear fits when the influence of impurity elements was taken into account.

The optimum Al-Zn-Mg-Cu alloying ratio for a dilute aluminium alloy is the composition of the precipitate modelled. The ratios were $Al_{7.4}Zn_{45.4}Mg_{38.6}Cu_{8.6}$ for the T6 condition and $Al_{15}Zn_{39}Mg_{33}Cu_{13}$ for the T73 condition.

Acknowledgements

I would like to acknowledge the following contributions:

- Prof. Lesley Cornish, my supervisor at the University of the Witwatersrand for review of my work and a professional relationship.
- Dr. Sagren Govender, my co-supervisor and Research Group Leader in the Advanced Casting Technologies group of Light Metals at the CSIR for personal support through a difficult time during this work.
- Dr. Willie du Preez, the past Competency Area Manager of Light Metals in the Materials Science and Manufacturing unit at the CSIR.
- People without whom this work would be impossible: Danie Wilkins, Marius Grobler, David Ntuli, Linda Mahlatji and Dr. Sabine Verryn.
- Dr. Hein Möller and Pierre Rossouw, at the CSIR for being sound boards, sometimes not so voluntarily.
- Funding by the South African Department of Science and Technology (DST) through the Light Metals Development Network (LMDN) of the Advanced Metals Initiative (AMI).
- My family and family in-law for support.
- My beautiful and creative wife, Vanessa, my amazing and inquisitive son, Nathan, and our angel, Genevieve, for continual inspiration in achieving my life goals.
- To the Higher Power that led me $\sqrt[n]{2\alpha\ \Phi\Delta}$

Table of contents

1. INTRODUCTION 1

2. LITERATURE SURVEY 7

2.1. R-HPDC 7

2.2. The Al-Zn-Mg-(Cu) alloy system 8

2.3. Al-Zn-Mg-Cu as-cast microstructures 12

2.4. Eutectic compositions 18

2.5. XRD analyses 18

2.6. DSC analyses 21

2.7. Homogenisation heat treatment 23

2.8. Solution heat treatment 24

2.9. Quenching 24

2.10. Artificial ageing heat treatments 25

2.11. Material properties modelling as a function of composition 27

3. EXPERIMENTAL PROCEDURE 28

3.1. Alloying 28

3.2. Bulk alloy compositions 29

3.3. R-HPDC 29

3.3.1. CSIR rheo-processing 30

3.3.2. Modified CSIR rheo-processing 30

3.4. Casting geometries 33

3.4.1. Taper rods 33

3.4.2. Plate 33

3.5. Heat treatments 34

3.5.1. Homogenisation 34

3.5.2. Solution heat treatment 35

3.5.3. Quenching 35

3.5.4. T6 artificial ageing 36

3.5.5. T73 artificial ageing 36

3.6. Wrought Al-Zn-Mg-Cu aluminium alloy 36

3.7. Sample preparation 36

3.7.1. OES 36

3.7.2. SEM and EDX 37
3.7.3. XRD 38
3.7.4. DSC 38
3.7.5. Hardness 38
3.7.6. Grain size 39
3.8. Experimental techniques 39
3.8.1. OES 39
3.8.2. SEM 39
3.8.3. EDX 39
3.8.4. Thermodynamic modelling 39
3.8.5. XRD 40
3.8.6. DSC 40
3.8.7. Hardness 40
3.8.8. Grain size measurement 40

4. RESULTS 42
4.1. Visual examination of castings 42
4.2. Alloying element macro-segregation 42
4.3. Sample alloy compositions 44
4.4. SEM observations of as-cast microstructures 45
4.5. EDX analyses of as-cast eutectic structures 51
4.6. Vacuum cooling 53
4.7. Eutectic alloys 55
4.7.1. Eutectic alloy A 55
4.7.2. Eutectic alloy B 57
4.7.3. Eutectic alloy C 60
4.8. Thermo-Calc predictions for as-cast alloys 61
4.8.1. Equilibrium phase predictions 61
4.8.2. Non-equilibrium phase predictions 64
4.9. DSC of as-cast alloys 68
4.10. XRD of as-cast alloys 75
4.11. SEM observations of T6 microstructures 81
4.12. EDX analyses of T6 condition alloys 87
4.13. T73 microstructure observation and analysis 91

4.14. Grain size measurements **91**
4.14.1. As-cast grain sizes 91
4.14.2. T6 grain sizes 91
4.15. Hardness measurements **92**
4.15.1. T6 hardness 92
4.15.2. T7 hardness 92
4.16. T6 tensile property data **93**
4.16.1. T6 heat treatment 93
4.16.2. T6 tensile properties 94

5. DISCUSSION 95
5.1. Microstructure observations in the as-cast condition **95**
5.2. As-cast properties **96**
5.2.1. Phases present in as-cast alloys 96
5.2.2. Thermal behaviour 97
5.3. Solidification mechanism **99**
5.3.1. Solidification reactions 99
5.3.2. Effect of solidification cooling rate 99
5.3.3. Effect of alloy composition 100
5.3.4. Eutectic alloys 100
5.3.5. Al-Mg-Zn and Al-Mg-Cu system similarities 102
5.4. Microstructure observations in the T6 condition **103**
5.4.1. General observations 103
5.4.2. T6 impurity phases 104
5.5. T6 mechanical properties-grain size relationships **105**
5.5.1. Influence of grain size on T6 hardness 105
5.5.2. Influence of grain size on T6 yield strength 106

6. MECHANICAL PROPERTIES MODELLING 108
6.1. Mechanical properties-composition model considerations **108**
6.2. T6 mechanical properties-composition model **108**
6.2.1. Weight fraction to atomic fraction conversion 108
6.2.2. T6 Precipitate composition 109
6.2.3. T6 precipitate volume fraction calculations 109

6.2.4. T6 hardness-composition relationship 110
6.2.5. T6 yield strength-composition relationship 111
6.3. Improved T6 mechanical properties-composition model 112
6.3.1. Improved model considerations 112
6.3.2. Improved precipitate volume fraction calculations 112
6.3.3. Improved T6 hardness-composition relationship 114
6.3.4. Improved T6 yield strength-composition relationship 115
6.4. T6 hardness-composition model applied to wrought alloys 115
6.5. T6 yield strength-composition model applied to AA7075 T6 117
6.6. T73 mechanical property-composition model 119
6.6.1. T73 Precipitate composition 119
6.6.2. T73 hardness-composition relationship 120
6.6.3. Improved T73 hardness-composition relationship 121
6.6.4. A T73 hardness-composition model exception 123
6.6.5. Improved T73 model applied to a wrought alloy 125
6.7. Interpretation of mechanical properties-composition model 126
6.7.1. General comments 126
6.7.2. T6 and T73 precipitate compositions 127
6.7.3. T6 hardness-composition relationship 128
6.7.4. T6 yield strength-composition relationship 129
6.7.5. T73 hardness-composition relationship 130

7. CONCLUSIONS 131

REFERENCES 135

APPENDIX A 140

List of Figures

Figure 1.1. Graphical summary of aluminium alloy systems [2]. 1

Figure 2.1. Time sequence of thixotropic behaviour of a semi-solid metal billet, where a semi-solid metal slug was placed upright and subsequently deformed, showing the flow behavior on applying shear forces [24]. 7

Figure 2.2. Schematic thermal diagram of rheo- and thixo-processing, adapted from [24]. 8

Figure 2.3. Projection of the liquidus surface for the Al-Zn-Mg system [37] with shaded area for compositions in Table 2.1. 11

Figure 2.4. Eutectic phases found in as-cast Alloy A in Table 2.1 [26]. 13

Figure 2.5. Eutectic phases found in as-cast Alloy B in Table 2.1 [27]. 13

Figure 2.6. Eutectic phases found in as-cast Alloy D in Table 2.1 [28]. 14

Figure 2.7. Eutectic phases found in as-cast Alloy E in Table 2.1 [29]. 14

Figure 2.8. Eutectic phases found in as-cast Alloy G in Table 2.1 [31]. 15

Figure 2.9. Eutectic phases found in as-cast Alloy H in Table 2.1 [32]. 15

Figure 2.10. Eutectic phases found in as-cast Alloy I in Table 2.1 [33]. 16

Figure 2.11. Eutectic phases found in as-cast Alloy J in Table 2.1 [34]. 16

Figure 2.12. Eutectic phases found in as-cast Alloy K in Table 2.1 [35]. 17

Figure 2.13. Eutectic phases found in as-cast Alloy L in Table 2.1 [36]. 17

Figure 2.14. XRD patterns of as-cast Alloys B and C in Table 2.1 [27]. 19

Figure 2.15. XRD patterns of as-cast Alloy D in Table 2.1 [28]. 19

Figure 2.16. XRD patterns of as-cast Alloy E in Table 2.1 [29]. 20

Figure 2.17. XRD patterns of as-cast Alloy J in Table 2.1 [34]. 20

Figure 2.18. DSC curve of as-cast Alloy D in Table 2.1 [28]. 21

Figure 2.19. DSC curve of as-cast Alloy F in Table 2.1 [30]. 21

Figure 2.20. DSC curve of as-cast Alloy G in Table 2.1 [31]. 22

Figure 2.21. DSC curve of as-cast Alloy J in Table 2.1 [34]. 22

Figure 2.22. DSC curve of as-cast Alloy K in Table 2.1 [35]. 23

Figure 2.23. Tensile strength as a function of heat treatment condition [2]. 25

Figure 2.24. Iso-yield strength map for AA7075 indicating the experimental relationship between time, temperature and strength upon artificial ageing [1] and the red dot marks the artificial ageing heat treatment in this study. 26

Figure 3.1. Reduced pressure test device used for vacuum cooling. 29

Figure 3.2. R-HPDC cell with dosing furnace, CSIR-RCS device and HPDC machine. 31

Figure 3.3. Alloy 7A as an example of the taper rod casting with runner and biscuit. 33

Figure 3.4. Plate casting with runner and biscuit of Alloy 7E. 34

Figure 3.5. Heat treatment rack with taper rod and plate samples. 35
Figure 3.6. Quench tank with water. 35
Figure 3.7. Sectioned taper rod sample with OES and hardness samples. 37
Figure 4.1. Example of the surface of the taper rod castings. 42
Figure 4.2. Surface appearance of the plate. 42
Figure 4.3. SEM-BSE image of macro-segregation in the casting. 43
Figure 4.4. OES and hardness measurement areas. Yellow shaded area indicates the radius of the OES measurement area on the deformed side of the sample. The hardness measurement area was between the yellow and red radii around the sample; on the polished adjacent side of the sample. 43
Figure 4.5. SEM-BSE images of the matrix and eutectic in as-cast Alloy 7A: a) low magnification, and b) high magnification. 46
Figure 4.6. SEM-BSE images of the matrix and eutectic in as-cast Alloy 7B: a) low magnification, and b) high magnification. 47
Figure 4.7. SEM-BSE images of the matrix and eutectic in as-cast Alloy 7C: a) low magnification, and b) high magnification, also indicating shrinkage porosity. 48
Figure 4.8. SEM-BSE images of the matrix and eutectic in as-cast Alloy 7D: a) low magnification, and b) high magnification, also indicating eutectic colonies impinging. 49
Figure 4.9. SEM-BSE images of the matrix and eutectic in as-cast Alloy 7E: a) low magnification, and b) high magnification. 50
Figure 4.10. EDX results for as-cast Alloy 7A: a) SEM-BSE image, and b) qualitative analysis. 51
Figure 4.11. EDX results for as-cast Alloy 7B: a) SEM-BSE image, and b) qualitative analysis. 51
Figure 4.12. EDX results for as-cast Alloy 7C: a) SEM-BSE image, and b) qualitative analysis. 51
Figure 4.13. EDX results for as-cast Alloy 7D: a) SEM-BSE image, and b) qualitative analysis. 52
Figure 4.14. EDX results for as-cast Alloy 7E: a) SEM-BSE image, and b) qualitative analysis. 52
Figure 4.15. SEM-BSE image of Alloy 7D-V showing the eutectic at high magnification. 54
Figure 4.16. EDX results for the eutectic of Alloy 7D-V: a) SEM-BSE image, and b) qualitative analysis. 54

Figure 4.17. SEM-BSE image of the Al-rich (dark grey) and Al-Zn-Mg-Cu containing (light grey) eutectic microstructure of Alloy E-A. The rectangle indicates a colony boundry. 55
Figure 4.18. EDX results for eutectic Alloy E-A: a) SEM-BSE image, b) qualitative analysis of the Al-Zn-Mg-Cu containing phase (Point 1), and c) of the Al-rich phase (Point 2). 56
Figure 4.19. Binary threshold colour image of Alloy E-A. 56
Figure 4.20. SEM-BSE image of the Al-rich (dark grey) and Al-Zn-Mg-Cu containing (light grey) eutectic microstructure of Alloy E-B. 58
Figure 4.21. EDX results for eutectic Alloy E-B: a) SEM-BSE image, qualitative analysis of b) Al-Zn-Mg-Cu containing phase (Area 1), and c) the Al-rich phase (Area 2). 58
Figure 4.22. Binary threshold colour image of Alloy E-B. 59
Figure 4.23. SEM-BSE image of the Al-rich (dark grey) and Al-Zn-Mg-Cu containing (light grey) eutectic microstructure and the Al-Cu phase (mid grey) of Alloy E-C. 60
Figure 4.24. EDX results for eutectic Alloy E-C: a) SEM-BSE image, qualitative analysis of b) light grey Al-Zn-Mg-Cu containing phase (Area 1), c) dark grey Al-rich phase (Area 2), and d) medium grey Al-Cu containing phase (Area 3). 61
Figure 4.25. Thermo-Calc equilibrium phase proportion-temperature plot for Alloy 7A. 62
Figure 4.26. Thermo-Calc equilibrium phase proportion-temperature plot for Alloy 7B. 62
Figure 4.27. Thermo-Calc equilibrium phase proportion-temperature plot for Alloy 7C. 63
Figure 4.28. Thermo-Calc equilibrium phase proportion-temperature plot for Alloy 7D. 63
Figure 4.29. Thermo-Calc equilibrium phase proportion-temperature plot for Alloy 7E. 64
Figure 4.30. Thermo-Calc Scheil solidification calculation for Alloy 7A. 65
Figure 4.31. Thermo-Calc Scheil solidification calculation for Alloy 7B. 66
Figure 4.32. Thermo-Calc Scheil solidification calculation for Alloy 7C. 66
Figure 4.33. Thermo-Calc Scheil solidification calculation for Alloy 7D. 67
Figure 4.34. Thermo-Calc Scheil solidification calculation for Alloy 7E. 67
Figure 4.35. DSC heating curve of Alloy 7A. 69
Figure 4.36. DSC heating curve of Alloy 7B. 69
Figure 4.37. DSC heating curve of Alloy 7C. 69
Figure 4.38. DSC heating curve of Alloy 7D. 70
Figure 4.39. DSC heating curve of Alloy 7E. 70
Figure 4.40. DSC heating curve of Alloy 7D-V. 71
Figure 4.41. DSC heating curve of Alloy E-A. 71

Figure 4.42. DSC heating curve of Alloy E-B. 72
Figure 4.43. DSC heating curve of Alloy E-C. 72
Figure 4.44. DSC cooling curve of Alloy E-A. 73
Figure 4.45. DSC cooling curve of Alloy E-B. 74
Figure 4.46. DSC cooling curve of Alloy E-C. 74
Figure 4.47. XRD pattern for as-cast Alloy 7A. 75
Figure 4.48. XRD pattern for as-cast Alloy 7B. 76
Figure 4.49. XRD pattern for as-cast Alloy 7C. 76
Figure 4.50. XRD pattern for as-cast Alloy 7D. 77
Figure 4.51. XRD pattern for as-cast Alloy 7E. 77
Figure 4.52. XRD pattern for as-cast Alloy 7D-V. 78
Figure 4.53. XRD pattern for as-cast Alloy E-A. 78
Figure 4.54. XRD pattern for as-cast Alloy E-B. 79
Figure 4.55. XRD pattern for as-cast Alloy E-C. 79
Figure 4.56. SEM-BSE images of intermetallic phases in Alloy 7A in the T6 condition: a) low magnification, and b) high magnification. 82
Figure 4.57. SEM-BSE images of porosity and intermetallic phases in Alloy 7B in the T6 condition: a) low magnification, and b) high magnification. 83
Figure 4.58. SEM-BSE images of intermetallic phases in Alloy 7C in the T6 condition: a) low magnification, and b) high magnification. 84
Figure 4.59. SEM-BSE images of intermetallic phases in Alloy 7D in the T6 condition: a) low magnification, and b) high magnification. 85
Figure 4.60. SEM-BSE images of intermetallic phases in Alloy 7E in the T6 condition: a) low magnification, and b) high magnification. 86
Figure 4.61. EDX results for Alloy 7A in the T6 condition: a) SEM-BSE image, and b) qualitative analysis of Al-Mn-Cu dispersoid. 87
Figure 4.62. EDX results for Alloy 7C in the T6 condition: a) SEM-BSE image of needle shape, b) qualitative analysis for Al7FeCu2 needle shape (7C-y), c) SEM-BSE image of spherical shape, d) qualitative analysis for spherical shaped Mg2Si (7C-x), e) SEM-BSE image of a large eutectic phase, and f) qualitative analysis of the large Al-Zn-Mg-Cu eutectic phase (7C-z). 88
Figure 4.63. EDX results for Alloy 7D in the T6 condition: a) SEM-BSE image, and b) qualitative analysis of the Al-Mn-Cu intermetallic. 89
Figure 4.64. EDX results for Alloy 7E in the T6 condition: a) SEM-BSE image of needle shape, b) qualitative analysis for needle shape Al7FeCu2 (7E-x), c) SEM-BSE image of chunky shape, and d) qualitative analysis for chunky shape Al2MgCu (7E-y). 90

Figure 5.1. Comparison of eutectic melting peak heights between Alloys 7A to 7E. 98
Figure 5.2. Hardness of Alloys 7A to 7E, in the T6 condition, as a function of the inverse square root of the grain size. 106
Figure 5.3. Yield strength of Alloys 7A to 7E, in the T6 condition, as a function of the inverse squar root of the grain size. 107
Figure 6.1. Effect of precipitate volume fraction on T6 hardness, excluding impurity reactions. 110
Figure 6.2. Effect of precipitate volume fraction on T6 yield strength, excluding impurity reactions. 112
Figure 6.3. Effect of precipitate volume fraction on T6 hardness, including impurity element reactions. 115
Figure 6.4. Effect of precipitate volume fraction on T6 yield strength, including impurity element reactions. 116
Figure 6.5. Effect of precipitate volume fraction on T6 hardness, applied to wrought alloy literature data [53-56] (including impurity reactions). 117
Figure 6.6. Applying the composition model to the typical yield strength of the nominal composition of AA7075 in the T6 condition, including impurity reactions. 119
Figure 6.7. Effect of precipitate volume fraction on T73 yield strength, excluding impurity reactions. 121
Figure 6.8. Effect of precipitate volume fraction on T6 hardness, including impurity element reactions. 123
Figure 6.9. SEM-BSE image of AlFeMn intermetallic needles in Alloy 7D in the T73 condition. 124
Figure 6.10. SEM-BSE image of AlFeMn intermetallic compounds in Alloy 7A in the T73 condition. 124
Figure 6.11. SEM-BSE image of AlFeMn intermetallic compounds in Alloy 7B in the T73 condition. 125
Figure 6.12. Applying the composition model to the hardness of wrought alloys 7040 in the T73 condition, including impurity reactions. 126
Figure 6.13. Hardess of Alloys 7A to 7E in the T6 condition, as a function of the square root of the grain size and precipitate volume fraction. 128
Figure 6.14. Yield strength of Alloys 7A to 7E, in the T6 condition, as a function of the grain size and precipitate volume fraction. 129

Figure A.1. Full range XRD pattern for as-cast Alloy 7A. 140
Figure A.2. Full range XRD pattern for as-cast Alloy 7B. 141
Figure A.3. Full range XRD pattern for as-cast Alloy 7C. 142

Figure A.4. Full range XRD pattern for as-cast Alloy 7D. 143
Figure A.5. Full range XRD pattern for as-cast Alloy 7E. 144
Figure A.6. Full range XRD pattern for as-cast Alloy 7D-V. 145
Figure A.7. Full range XRD pattern for eutectic Alloy E-A. 146
Figure A.8. Full range XRD pattern for eutectic Alloy E-B. 147
Figure A.9. Full range XRD pattern for eutectic Alloy E-C. 148

List of Tables

Table 2.1. Alloy compositions and solidification rates of Al-Zn-Mg-Cu aluminium alloys [26-36]. 9

Table 2.2. Crystallographic properties of Al-Mg-Zn system [37] and Al-Mg-Cu system [38] phases. 11

Table 2.3. Overall compositions of the different eutectic structures for alloys in Table 2.1 [28,29,31,33-36]. 18

Table 2.4. Melting points and structures of the secondary phases of some of the the alloys in Table 2.1 [27-31,34,35]. 23

Table 2.5. Heat treatment procedure excerpt from AMS 2770J for Al-Zn-Mg-Cu aluminium alloys of different designations [43]. 26

Table 3.1. Bulk alloy compositions of the five alloys, as received. 29

Table 4.1. Experimental alloy compostions as measured with the OES. 44

Table 4.2. EDX results of the overall compositions of the eutectics in the different alloys. 52

Table 4.3. Corrected overall compositions of the eutectics of different R-HPDC processed alloys. 53

Table 4.4. Corrected eutectic composition of the vacuum cooled alloy. 54

Table 4.5. Corrected EDX compositions of the Al-rich and Al-Zn-Mg-Cu phases in eutectic Alloy E-A. 57

Table 4.6. Adjusted EDX compositions of the Al-rich and Al-Zn-Mg-Cu phases in eutectic Alloy E-B. 59

Table 4.7. Equilibrium solidification onset and end temperatures of Alloys 7A to 7E. 64

Table 4.8. Summary of Thermo-Calc solidification onset and end temperatures, eutectic percentages and the sum of major alloying elements. 68

Table 4.10. Summary of melting thermal events of Alloys E-A, E-B and E-C. 73

Table 4.11. Summary of solidification onset and peak temperatures of Alloys EA to E-C. 74

Table 4.9. Measured lattice parameters for phases in Alloys 7A to 7E, 7D-V, E-A and E-B. 80

Table 4.12. EDX analyses of intermetallic phases identified in the alloys in the T6 condition. 90

Table 4.13. Grain size measurements in the as-cast condition for Alloys 7A to 7E. 91

Table 4.14. Grain size measurements in the T6 conditions for Alloys 7A to 7E. 92

Table 4.15. Micro-Vickers hardness measurements (at 500g load) for alloys in the T6 condition. 92
Table 4.16. Micro-Vickers hardness measurements (at 500g load) for alloys in the T6 condition. 93
Table 4.17. Homogenisation/solution and artificial ageing heat treatments of Alloys 7A to 7E. 93
Table 4.18. Uni-axial tensile properties of Alloys 7A to 7E in the T6 condition, as reported by the CSIR. 94
Table 5.1. Weight percentages of phases found in each alloy. 96
Table 5.2. Lattice parameters (pm) of the phases identified with XRD in the as-cast alloys. Lattice parameters for Al, □ and □ from reference [37]. 97
Table 5.3. Summary of melting onset and end temperatures of Alloys 7A to 7E and 7D-V. 98
Table 5.4. Bulk compositions and Zn:Cu ratio of R-HPDC alloys. 100
Table 5.5. Corrected EDX values of eutectic alloy lamellae. 102
Table 5.6. Compositions of Al-Zn-Mg-Cu lamellae in Alloys E-C and H [32]. 102
Table 6.1. Atomic fractions of T6 precipitate by Sha et al. [52]. The Zn fraction is purple highlighted, the Mg fraction is blue highlighted and the Cu fraction is orange highlighted. 109
Table 6.2. Precipitate volume fraction calculations excluding impurity reactions. Purple blocks indicate Zn-limited, the blue block indicates Mg-limited and orange blocks indicate Cu-limited alloys. 111
Table 6.3. Precipitate volume fractions as a function of the element found in the precipitate, controled by the limiting element. Purple indicates a Zn limit, blue a Mg limit and orange a Cu limit. 114
Table 6.4. Composition and hardness data from literature [53-56] and calculated precipitate volume fractions, including impurity reactions. Purple blocks indicate Zn-limited, blue blocks indicate Mg-limited and the orange block indicates Cu-limited alloys. 116
Table 6.5. Composition specifications of AA7075 and the typical yield strength [57]. 118
Table 6.6. Precipitate volume fractions as a function of the element found in the precipitate, controled by the limiting element for the nominal comopostion of AA7075, including impurity element reactions. 118
Table 6.7. Atomic fractions of T73 precipitate by Marlaud et al. [4] where the Zn fraction is purple highlighted, the Mg fraction is blue highlighted and the Cu fraction is orange highlighted. 119

Table 6.8. Precipitate volume fraction calculations excluding impurity reactions. Orange blocks indicate Cu-limited alloys. 120
Table 6.9. Precipitate volume fractions as a function of the element found in the precipitate, including impurity reactions, where orange blocks denote a Cu limited composition. 122
Table 6.10. Precipitate volume fractions as a function of the element found in the precipitate, including impurity reactions. Orange block denote a Cu limited composition. 125

1. Introduction

Aluminium alloys are attractive because of their low density compared to steel. Heat treatable high strength aluminium alloys are valuable structural materials. The absolute strengths of some of these alloys are in the range of low alloy steels [1]. Aerospace and automotive products rely heavily on fossil fuels, which are becoming increasingly expensive [1]. Replacement of steel components with aluminium components, for the same level of performance is very attractive, especially for direct energy conservation and efficiency by weight saving [1].

Figure 1.1 is a summary of the different aluminium alloy systems [2], and Figure 1.1 is laid out by alloy families increasing in strength. Properties presented for each alloy family will be shortly discussed in order of strength, for the reader to appreciate the significance of this study.

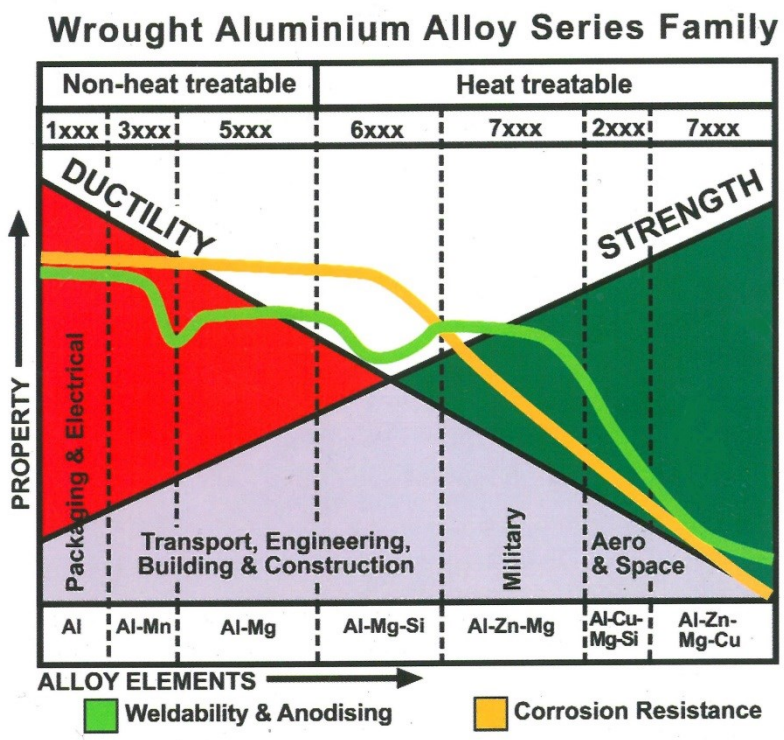


Figure 1.1. Graphical summary of aluminium alloy systems [2].

Commercially pure aluminium (Al), the 1xxx series, has the lowest strength but is very ductile. This family of alloys has high corrosion resistance due to the absence of alloying elements that interfere with the formation of the protective oxide layer that imparts corrosion resistance. The anodising properties are also very good for the same reason, which these properties make the 1xxx series Al alloys attractive for

packaging. The 1xxx series alloys are also good electrical conductors due to their purity [1].

The 3xxx series of aluminium alloys with manganese (Mn) as the major alloying element are non-heat treatable, but have about 20% more strength than the 1xxx series alloys. These alloys have moderate strength but have good workability, and are used for a wide variety of applications including cooking utensils, heat exchangers, general construction and architecture. The 1xxx series alloys also have good corrosion resistance [1].

The 5xxx series aluminium alloys are alloyed mainly with magnesium (Mg). This alloy series is also work-hardenable with a moderate strength, but higher strengths can be achieved than with 3xxx series alloys. The 5xxx series alloys have good corrosion resistance and are good for marine applications, and they are also used from beverage cans to crane parts [1].

The alloy families described above, 1xxx, 3xxx and 5xxx, are non-heat treatable alloys. The next alloy families, 6xxx, 2xxx and 7xxx, are all heat treatable or precipitation-hardenable alloys, meaning that their properties can be influenced by thermal treatments [1].

The 6xxx series alloys are mainly alloyed with magnesium (Mg) and silicon (Si) and are the most dilute of the heat treatable wrought alloys. The alloys have good corrosion resistance, formability, weldability, machinability, with moderate strength. Precipitation is improved with the addition of copper (Cu). Applications for these alloys are mostly structural [1].

The 2xxx series alloys are mainly alloyed with Cu. Alloys in this family can achieve strengths comparable to, or sometimes exceeding, low carbon steels by precipitation hardening. Precipitation can be enhanced with the addition of Mg. These alloys have limited weldability due to presence of Cu (>0.4 wt%) which has a larger shrinkage factor than the matrix (Al) upon solidification. Applications include automobile and aerospace parts which require good strength up 150 °C [1].

The 7xxx series alloys are the most highly alloyed series and are alloyed with zinc (Zn) and Mg. The addition of Cu to this family of alloys results in the highest strength aluminium alloys, in the peak-aged condition (T6). An example of a work-horse 7xxx series alloy is AA7075 with typical yield strength, ultimate tensile strength and ductility of 500 MPa, 570 MPa and 11 % respectively, in the peak-aged (T6)

condition. Unfortunately, Cu also reduces the stress corrosion resistance (exposure to a corrosive environment under stress (SCC)). These alloys are therefore used in the over-aged condition (T7) to improve corrosion resistance at the expense of some strength. Some high strength Al-Zn-Mg-Cu alloys have been developed to strike a balance between strength and resistance to SCC [1]. Weldability of these alloys is also poor, due to the difference of shrinkage coefficient between the alloying elements and the matrix upon solidification. Applications are mainly for highly stressed parts in the aerospace industry [1].

New Al-Zn-Mg-Cu wrought aluminium alloys are still being developed by international companies for improved properties [3,4], although a large number of Al-Zn-Mg-Cu alloys are already registered with the Aluminum Association. It is not clear what the optimum Al-Zn-Mg-Cu ratio is, but it probably depends on the application. Major alloying elements include: Zn between 4.5 - 8.2 wt%, Mg between 2.0 – 3.0 wt% and Cu between 1.0 - 2.5 wt% [1].

Al-Zn-Mg-Cu alloys are conventionally produced by the cost intensive wrought manufacturing route [1]. The process includes: melting, alloying, ingot casting, ingot homogenisation to reduce or eliminate segregation of alloying elements, annealing to soften the ingot, hot and/or cold working, solution heat treatment to take the alloying elements into solid solution in the matrix, quenching to keep the alloying elements in solid solution and natural and/or artificial ageing to control material properties by precipitation from the solid solution state. The wrought process produces thick section material in semi-finished shapes such as billet, bar or plate. Thin section sheet is a product produced from plate. Thick semi-finished products are then cut, pre-formed (by extrusion or forging) and machined to the final shape for smaller components, producing large volumes of scrap; 60-80 wt% is not uncommon [1].

The Council for Scientific and Industrial Research (CSIR) in South Africa developed and patented [5] the CSIR Rheocasting System (CSIR-RCS), which is a device that conditions (rheo-processes) liquid metal to a mixture of liquid and solid before final casting by high pressure die casting (HPDC). This manufacturing technology is called rheo-high pressure die casting (R-HPDC). A major focus at the CSIR is commercialising patented technologies. The overall aim of this research is to contribute towards commercialisation of the CSIR R-HPDC Technology. The CSIR R-HPDC technology can process any aluminium alloy, including high purity

aluminium [6], unmodified Al-Si binary eutectic [7], casting aluminium alloys [8,9], wrought aluminium alloys [10], aluminium metal matrix composites [11] and casting magnesium alloys [12]. A comprehensive overview can be found by Curle et al. [13].

The R-HPDC process competes with the wrought process by its ability to produce Al-Zn-Mg-Cu alloy components in near-net shape, thus avoiding the large volumes of scrap [14], thus avoiding the large volumes of scrap. R-HPDC processing consists of melting, alloying, controlled partial solidification during rheo-processing, complete solidification during HPDC, homogenisation of the casting, quenching, and natural and/or artificial ageing.

The similarities between the R-HPDC and wrought processes include the following: melting, alloying, casting. The appropriate metal melt must first be prepared by melting and cleaned by degasing and de-drossing. Thereafter, alloying is done if the metal melt was pure aluminium or alloy adjustment if the melt was prepared with some percentage of recycled scrap [1]. The liquid alloy is then cast into an ingot, for the wrought process, or a component in the case of R-HPDC. It could be expected, were it not for the controlled partial solidification of the R-HPDC process mentioned in the previous paragraph, after these processing steps, that these as-cast microstructures would have similarities.

One objective of this research is to investigate and explain the solidification properties of different R-HPDC processed Al-Zn-Mg-Cu aluminium alloy compositions in comparison with properties of wrought alloys of the same family from the published literature.

The next similarity between the R-HPDC and wrought processes is homogenisation. Homogenisation of the ingot in the wrought process is performed to eliminate microsegregation of alloying elements that distributed to grain boundaries during the non-equilibrium solidification process [1]. Homogenisation for the rheo-cast components also has to be performed because of the microsegregation of the liquid phase that takes place during R-HPDC.

After homogenisation, comes quenching for the R-HPDC process; wrought alloy ingots are normally not quenched because of their large size; quench cracks can form and the quench rates are highly variable between the surface and the centre of the ingot [1]. On the other hand with R-HPDC, the components are small and a more standard quench rate can be obtained.

A difference between the two processes, R-HPDC and wrought, is that R-HPDC misses the hot or cold deformation step after annealing (to soften the alloy to facilitate the production of semi-finished wrought products [1]) because the R-HPDC formed component is already in a near-net shape after casting.

The alloying elements for heat treatable aluminium alloys, e.g. Al-Zn-Mg-Cu alloys, have to be supersaturated in the FCC solid solution, therefore a solution heat treatment is before being wrought [1]. A state of supersaturation is also reached for heat treatable aluminium alloys that were processed be R-HPDC. Material in the R-HPDC process does not go through a softening step and the solution heat treatment step can therefore also be counted as a continuation from the homogenisation step, providing the homogenisation step takes place at the solution heat treatment temperature. Quenching is then done after the solution heat treatment [1].

Lastly, a similarity between the R-HPDC and wrought processes is that the heat treatable alloy has to be artificially aged. For the wrought and R-HPDC these temperatures and times are similar [1].

The R-HPDC process is a more economical option in comparison to the wrought process, to produce near-net shape components, because expensive capital cost forming equipment for basic shape forming is eliminated and scrap associated per component can be reduced to around 10-20 wt%.

Alloying is a challenge, not only for the wrought process, but also for semi-solid metal (SSM) processing. The SSM processing (thixo- and rheo-processing) of typical wrought aluminium alloys achieves close to typical wrought alloy strengths, but with very low ductility [15]. Attention has been given to alloy adjustment of typical 7xxx series wrought aluminium alloy compositions, mainly with the aim of alleviating the processing problems, e.g. castability [16]. Little attention has been given to alloy development for improved material properties in the semi-solid processing knowledge domain [17-23].

The novel R-HPDC manufacturing technology [14] has the potential to be extremely cost competitive in producing high strength aluminium alloy components if the processed alloys are better understood. It is therefore important to explain phase evolution for R-HPDC processed alloys, as well as modelling material properties to enable alloy development for improvement.

The primary objective of this research is to model the T6 and T73 mechanical properties of R-HPDC processed alloys on a semi-theoretical base as a function of

alloy composition and testing the applicability of the model to wrought processed alloys.

The last objective is to propose an overall optimum Al:Zn:Mg:Cu ratio for Al-Zn-Mg-Cu aluminium alloys, for alloy development.

2. Literature survey

2.1. R-HPDC

Semi-solid material has thixotropic properties, implying that the material will flow if a shear stress is applied, but will retain its shape if left undisturbed. Figure 2.1 is an example of an alloy that displays thixotropic behaviour whereby the material flows when a shear force is applied [24].

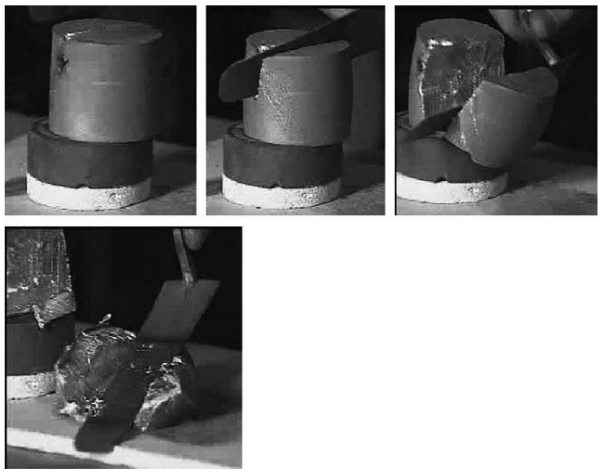


Figure 2.1. Time sequence of thixotropic behaviour of a semi-solid metal billet, where a semi-solid metal slug was placed upright and subsequently deformed, showing the flow behavior on applying shear forces [24].

Semi-solid metal processing is a technique whereby metal is processed in the two-phase state, liquid plus solid. This can be achieved by the two ways shown schematically in Figure 2.2. Firstly, the alloy can be cast into a basic shape of a bar, with a globular microstructure, and cooled to room temperature. This material is then feedstock material for thixo-processing [24]. The alloy is then heated again to the liquid + solid phase field, as shown by the red line in Figure 2.2. The thixo-processed material is then formed. On the other hand, rheo-processing is where the alloy is cooled directly to the liquid + solid phase field and then formed [24]. The thermal process is depicted schematically by the green line in Figure 2.2. The rheo-processing route results in a considerable energy saving. The SSM alloy can then be shaped by forging for high solid fractions or casting for low solid fractions [13].

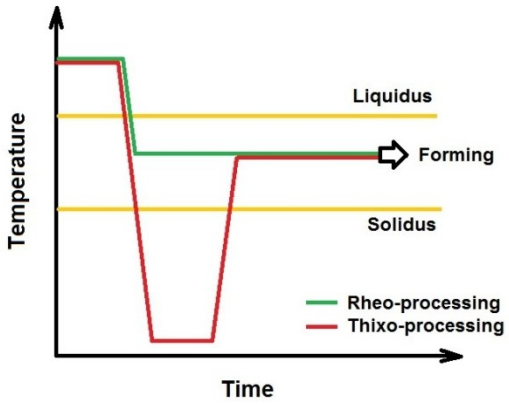


Figure 2.2. Schematic thermal diagram of rheo- and thixo-processing, adapted from [24].

Advantages of SSM processing are normally compared to the casting process because casting alloys are usually used for research. However, the advantages should be compared to the wrought process for wrought alloys such as the Al-Zn-Mg-Cu aluminium alloy system. Especially, R-HPDC [14] has the advantage that components can be cast directly to near-net shape, without the difficulties associated with this traditionally difficult to cast alloy system, i.e. hot tearing and shrinkage porosity. Shrinkage porosity and hot tearing can be eliminated with the aid of intensification pressure during HPDC.

2.2. The Al-Zn-Mg-(Cu) alloy system

Rheo-high pressure die casting of Al-Zn-Mg-Cu aluminium alloys might lead to unique microstructures and as-cast properties compared to microstructures and properties of similar alloys produced with ingot casting during the wrought process.

The objective of alloying Al with Zn, Mg and Cu is to improve mechanical properties relative to the unalloyed metal. New phases could appear during non-equilibrium solidification as compositions become more complex.

Solidification has a composition-temperature-time relationship. Thermodynamically, the two solidification models followed at the different time extremes, to calculate the phases that should appear in an alloy, from the elemental composition are the Lever and Scheil models [25].

The Lever model is used for equilibrium conditions, implying infinitely low solidification rates, where there is enough time for diffusion of alloying elements to take place. Alloying elements diffuse into the matrix phase to form solid solution phases depending on the solid solubility limits [25].

The Scheil model is used for non-equilibrium conditions, implying infinitely high solidification rates. In this case, there is not enough time for diffusion of alloying elements to occur into the matrix phase. It results in a situation where the last liquid to solidify is enriched with alloying elements [25].

The Back-Diffusion model is followed for rates in between. In this case, there is some time available for diffusion of alloying elements to occur into the matrix phase, but not to the same extent as with equilibrium conditions. Ingot casting is probably more related to the Back-Diffusion model, while HPDC probably follows the Scheil model; each model has its own phase predictions [25].

Solidification rates are governed by the chosen manufacturing process, as shown in Table 2.1. Normally, manufacturing of wrought aluminium alloy products is accomplished by ingot metallurgy. Table 2.1 also shows the compositions of a number of different Al-Zn-Mg-Cu aluminium alloys [26-36]; the alloy labels are used for differentiation in subsequent tables and figures in this section.

Table 2.1. Alloy compositions and solidification rates of Al-Zn-Mg-Cu aluminium alloys [26-36].

		Zn	Mg	Cu		
Alloy	Designation		wt%		Cooling rate	Reference
A	AA7050	6.56	2.37	2.60	0.45 °C/min	[26]
B	AA7055	8.00	1.80	2.60	~ 15 °C/min	[27]
C	AA7055	8.00	2.00	2.30	~ 15 °C/min	[27]
D	AA7085	7.81	1.62	1.81	Ingot	[28]
E	AA7050	6.31	2.33	1.70	SC 200 mm	[29]
F	AA7010	6.32	2.40	2.32	SC 200 mm	[30]
G	7B04	6.13	2.65	1.61	DC SC 120 mm	[31]
H	AA7050	6.24	2.26	2.32	DC 100 mm	[32]
I	AA7278	6.70	2.60	2.00	R-HPDC	[33]
J	7A55	7.86	2.09	2.06	SC 400 mm	[34]
K	not specified	8.10	2.05	2.30	Ingot	[35]
L	AA7050	6.10	2.30	2.20	DC 120 mm	[36]

7B04: Equivalent to AA7075 7A55: Equivalent to AA7055

SC: Semi-continuous cast DC SC: Direct chill Semi-continuous cast

DC: Direct Chill R-HPDC: Rheo-high pressure die casting

Equilibrium phases and reactions can be predicted thermodynamically with the aid of equilibrium phase diagrams. Figure 2.3 shows the Al-Zn-Mg projected liquidus surface [37]. The area in which all the alloy compositions in Table 2.1 fall is demarcated by the blue shaded area, near the Al corner of the diagram. An approximation can be assumed by adding the Cu contents of the alloys in Table 2.1 to their respective Zn fraction. Since all the alloys fall between the two red lines, the solidification paths would reach the monovariant line between $\mathbf{e_1}$ and $\mathbf{U_1}$. Equation 2.1 is the eutectic reaction equation for $\mathbf{e_1}$:

$$L \leftrightarrow (Al) + \tau \qquad 2.1$$

where *L* is the liquid phase, (Al) is face centred cubic (FCC) aluminium solid solution and τ is the $Mg_{32}(Zn,Al)_{48}$ cubic structure phase.

Equation 2.2 is the quasi-peritectic invariant reaction equation for $\mathbf{U_1}$:

$$L + \tau \leftrightarrow (Al) + \eta \qquad 2.2$$

where *L*, (Al), and τ have the same meanings as before; η is the $MgZn_2$ hexagonal structure phase. The phases that can coexist upon final solidification after reaction $\mathbf{U_1}$ are $\tau_1 + (Al) + \eta$.

In the Al-Mg-Cu system [38], there are two phases which have isotypic crystal structures to those of Equation 2.2. The one similar to τ_1 is the cubic structure T phase with the formula $Mg_{32}(Cu,Al)_{48}$. The other one, similar to η, is the hexagonal structure λ_3 phase with the formula $Mg(Cu,Al)_2$.

Table 2.2 shows the crystallographic properties of the relevant phases in the Al-Mg-Zn and Al-Mg-Cu systems respectively.

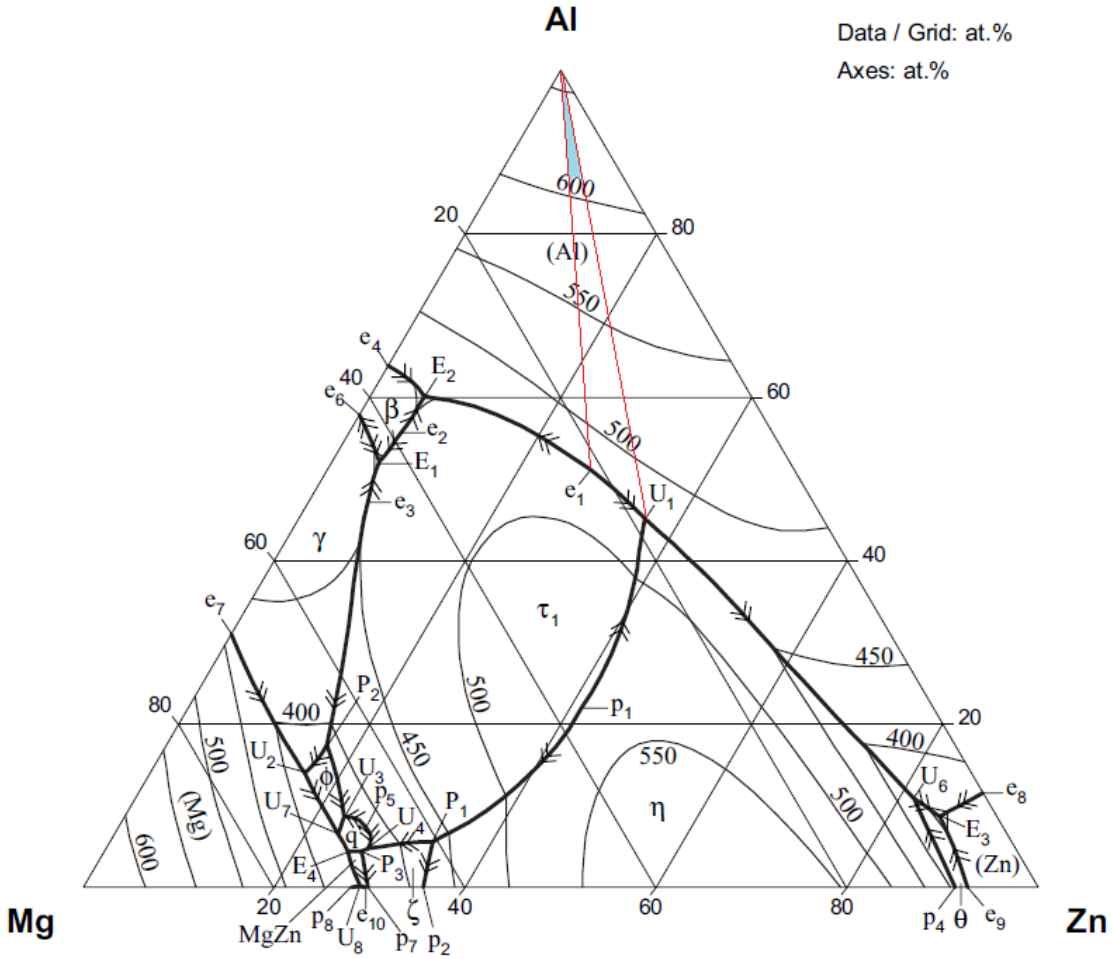


Figure 2.3. Projection of the liquidus surface for the Al-Zn-Mg system [37] with shaded area for compositions in Table 2.1.

Table 2.2. Crystallographic properties of Al-Mg-Zn system [37] and Al-Mg-Cu system [38] phases.

Al-Mg-Zn system

Phase	Formula	Crystal system	Space group	Prototype
τ_1	$Mg_{32}(Al,Zn)_{48}$	Cubic	Im-3	$Mg_{32}(Al,Zn)_{48}$
η	$MgZn_2$	Hexagonal	P63/mmc	$MgZn_2$

Al-Mg-Cu system

Phase	Formula	Crystal system	Space group	Prototype
T	$Mg_{32}(Cu,Al)_{48}$	Cubic	Im-3	$Mg_{32}(Al,Zn)_{48}$
λ_3	$Mg(Cu,Al)_2$	Hexagonal	P63/mmc	$MgZn_2$

2.3. Al-Zn-Mg-Cu as-cast microstructures

The majority of work in wrought Al-Zn-Mg-Cu aluminium alloy literature determined phase evolution during solidification and homogenisation [26-32,34-36]. Heat treatable alloys are mostly used in the artificially aged condition, subsequent to homogenisation and solution heat treatment, to ensure that all the precipitate strengthening elements are dissolved. Insoluble phases at the homogenisation and solution heat treatment temperatures reduce the ductility of the alloy, do not contribute to the strength and reduce the corrosion resistance.

A large ingot has a relatively slow cooling rate, allowing time for back diffusion of alloying elements during solidification. The result is that a number of equilibrium phases can appear.

Figures 2.4 to 2.13 show the Al-Zn-Mg-Cu eutectic structures and phases found in a number of the wrought alloys, i.e. η ($MgZn_2$), T ($Al_2Mg_3Zn_3$), S (Al_2MgCu) and θ (Al_2Cu) [26-32,34-36], whereas Figure 2.10 that shows a R-HPDC alloy [33].

In R-HPDC, the solidification rate is extremely fast [39] because of the relatively small size of the casting, as well as the thermal gradients and heat transfer between the liquid alloy and the dies. This forces non-equilibrium solidification reactions. The result is that, seemingly at the lower magnification, a binary eutectic structure forms (Figure 2.10) which consists of all the major alloying elements, i.e. σ ($Mg(Al,Cu,Zn)_2$) [33], together with solid solution Al as the other phase. The morphology of this eutectic structure was lamellar. It was proposed that the composition of the phase containing Al, Zn, Mg and Cu is based on the η phase with Al and Cu substituting for Zn [40].

Figures 2.4 to 2.13 also show the morphology of the lamellar eutectics. Some eutectics were accompanied by impurity element intermetallic phases. They were an Al-Cu-Fe-Cr-Mn-Si containing intermetallic phase (labelled 2) and an Al-Mg-Cu-Fe-Mn intermetallic phase (labelled 3) in Figure 2.8. The phase labelled 1,2 and 3 in Figure 2.9 was the Al-Zn-Mg-Cu phase in the eutectic. Figure 2.10 shows a low magnification image of the eutectic in Alloy I. In Figure 2.11, the intermetallic phases labelled A and B were both Al_7FeCu_2; the regions labelled C, D and E were Al-Zn-Mg-Cu eutectics. In Figure 2.12, the intermetallic phase was Al_7FeCu_2 (labelled A); the phases labelled B and C were Al-Zn-Mg-Cu eutectics. Both phases labelled 1 and 2 in Figure 2.13 were Al-Zn-Mg-Cu eutectics.

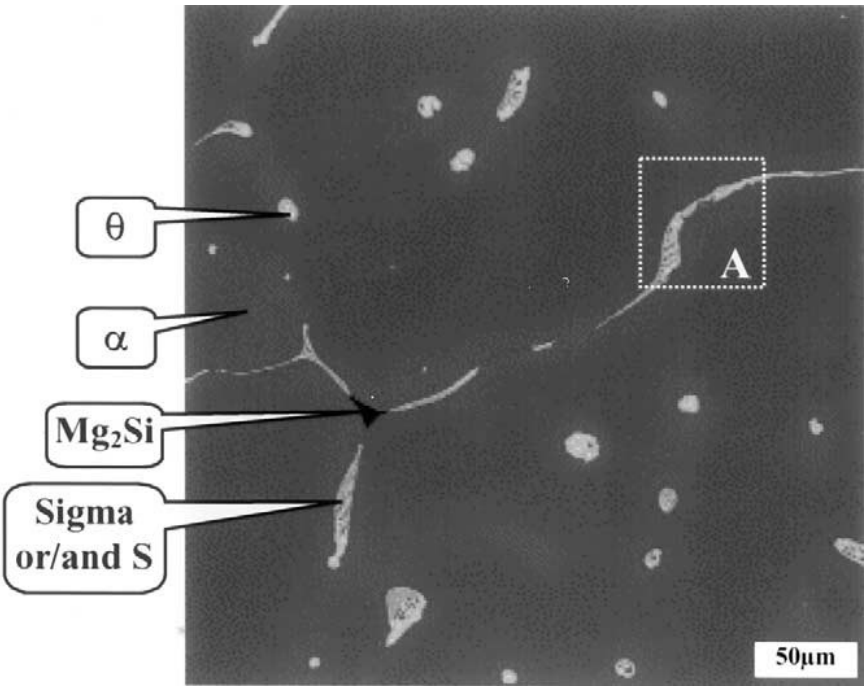


Figure 2.4. Eutectic phases found in as-cast Alloy A in Table 2.1 [26].

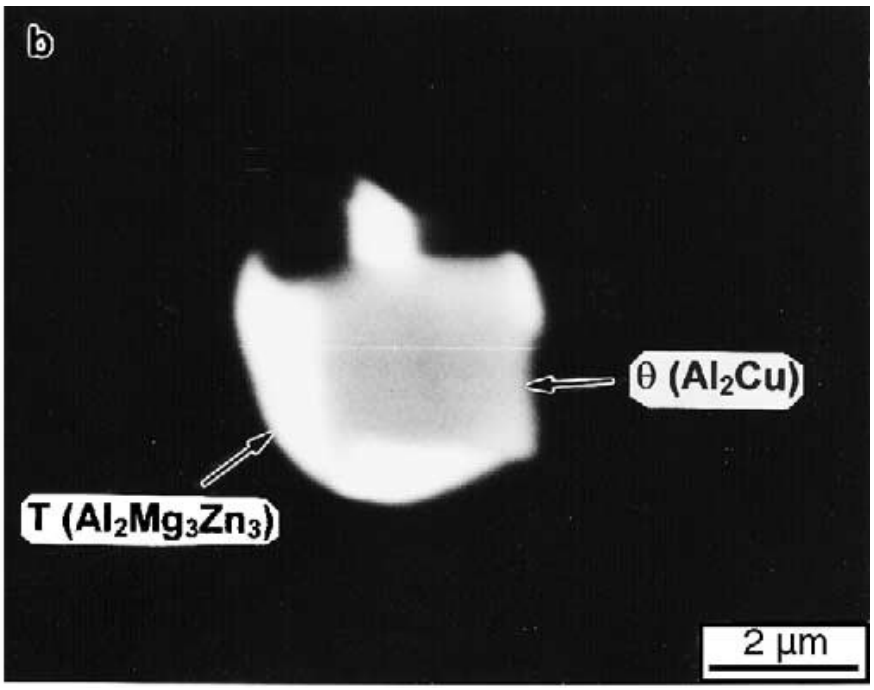


Figure 2.5. Eutectic phases found in as-cast Alloy B in Table 2.1 [27].

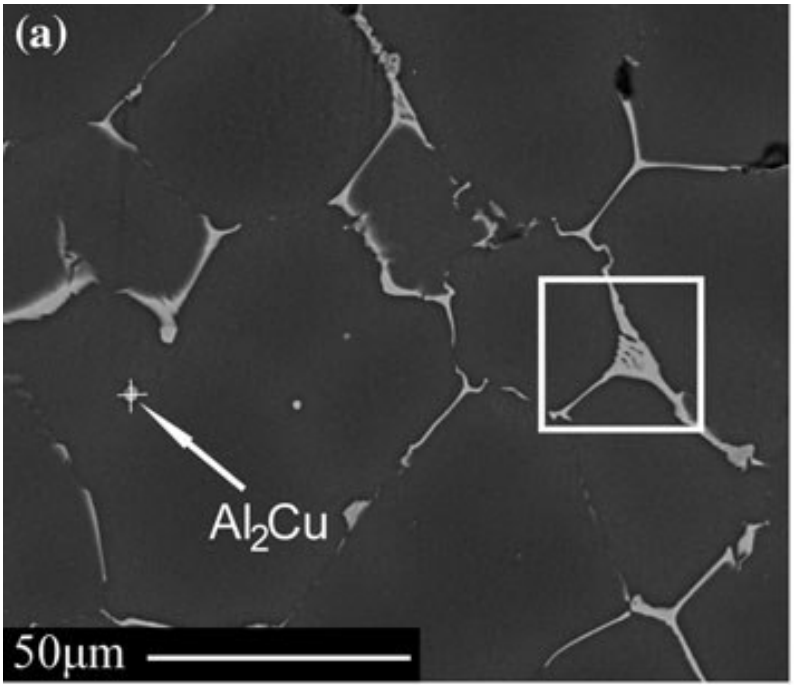


Figure 2.6. Eutectic phases found in as-cast Alloy D in Table 2.1 [28].

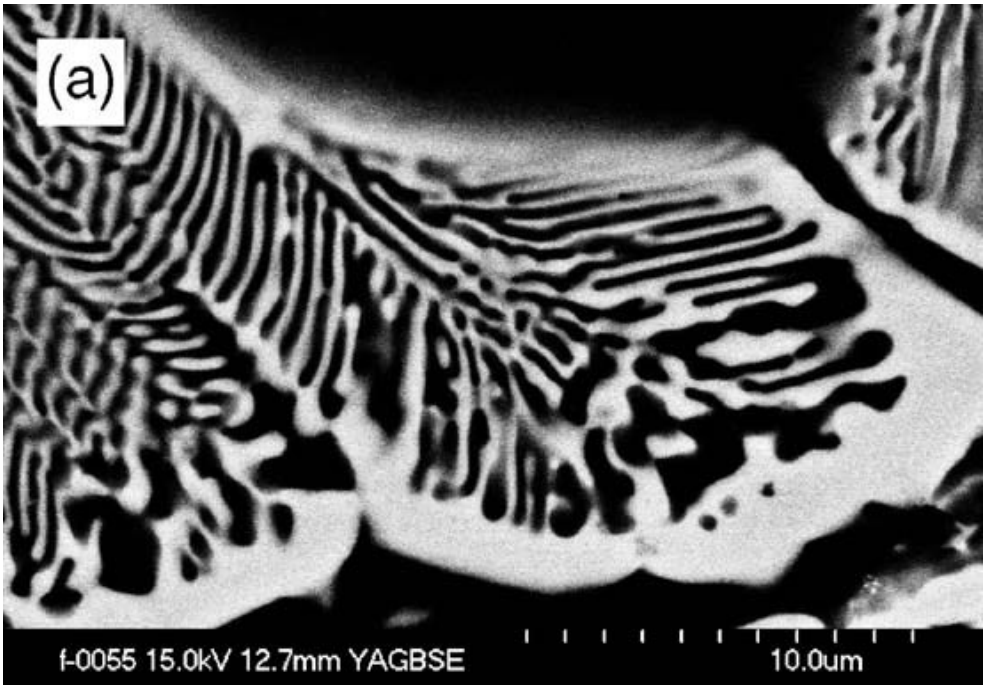


Figure 2.7. Eutectic phases found in as-cast Alloy E in Table 2.1 [29].

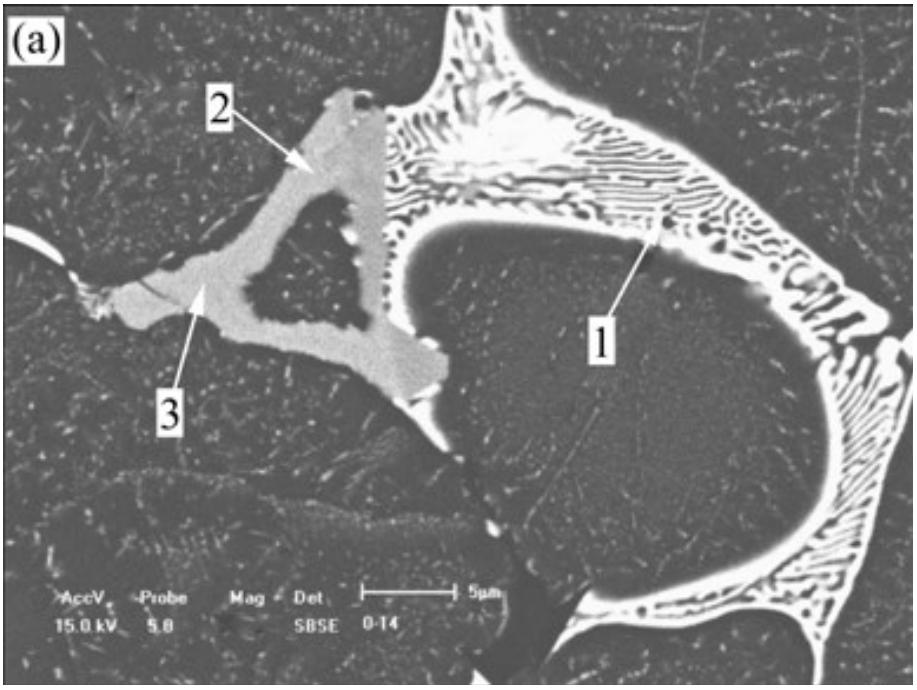


Figure 2.8. Eutectic phases found in as-cast Alloy G in Table 2.1 [31].

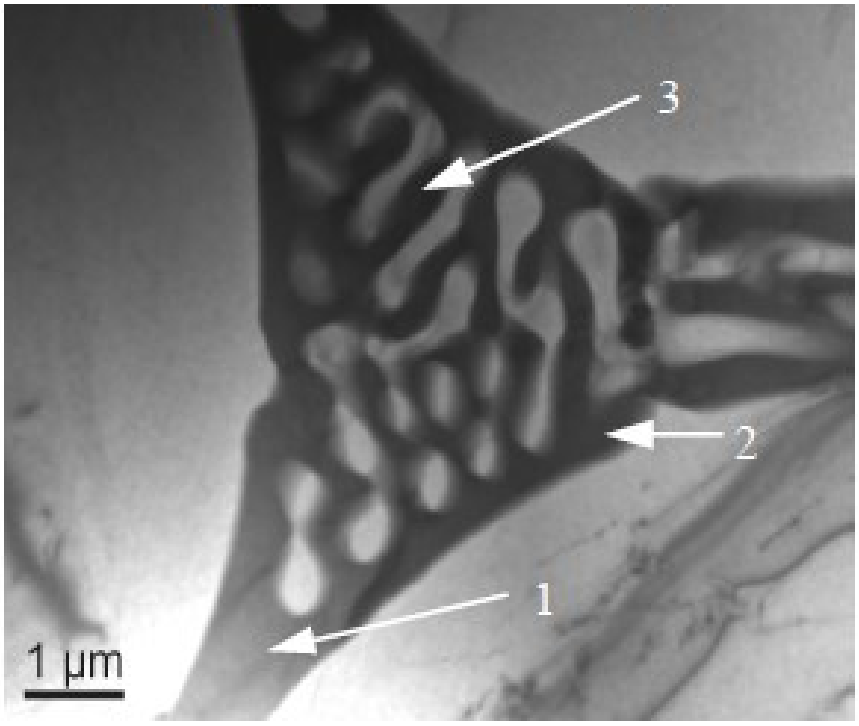


Figure 2.9. Eutectic phases found in as-cast Alloy H in Table 2.1 [32].

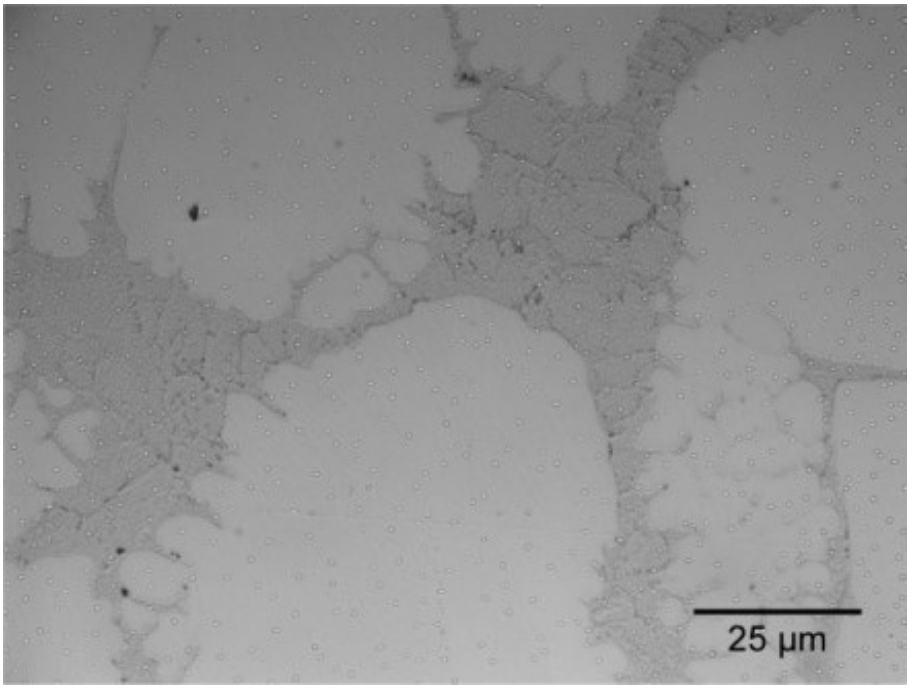


Figure 2.10. Eutectic phases found in as-cast Alloy I in Table 2.1 [33].

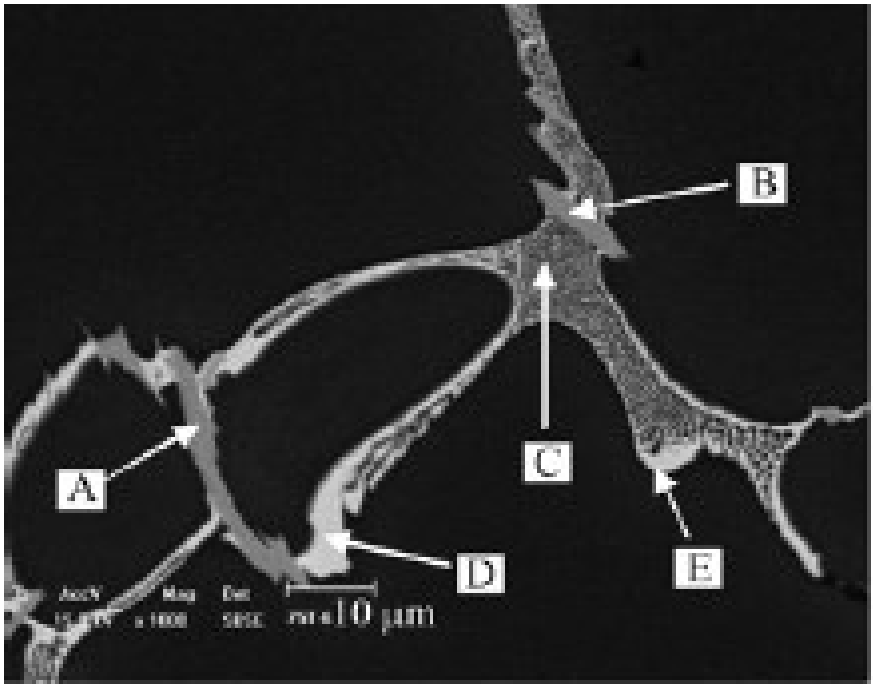


Figure 2.11. Eutectic phases found in as-cast Alloy J in Table 2.1 [34].

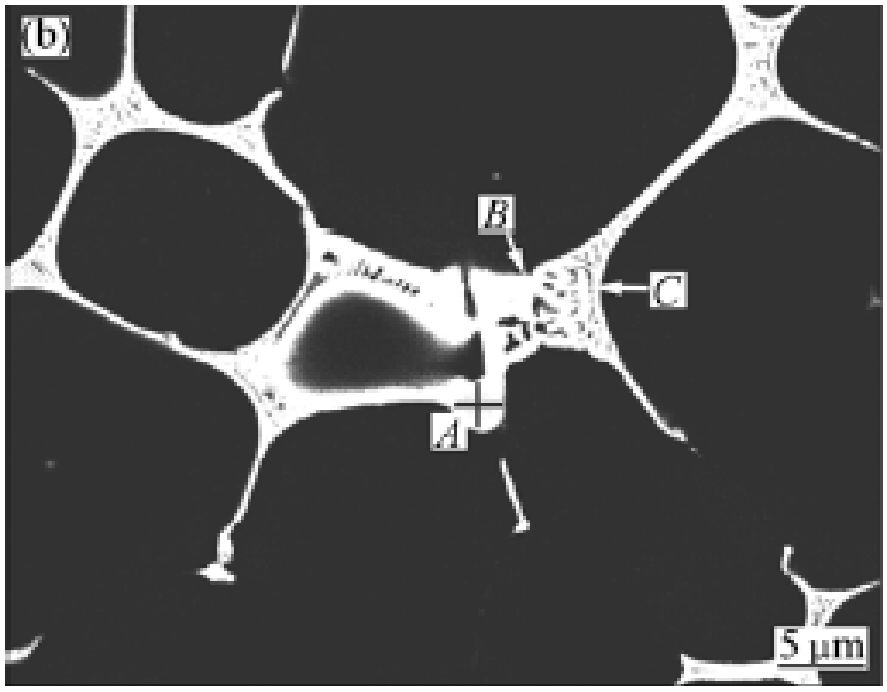


Figure 2.12. Eutectic phases found in as-cast Alloy K in Table 2.1 [35].

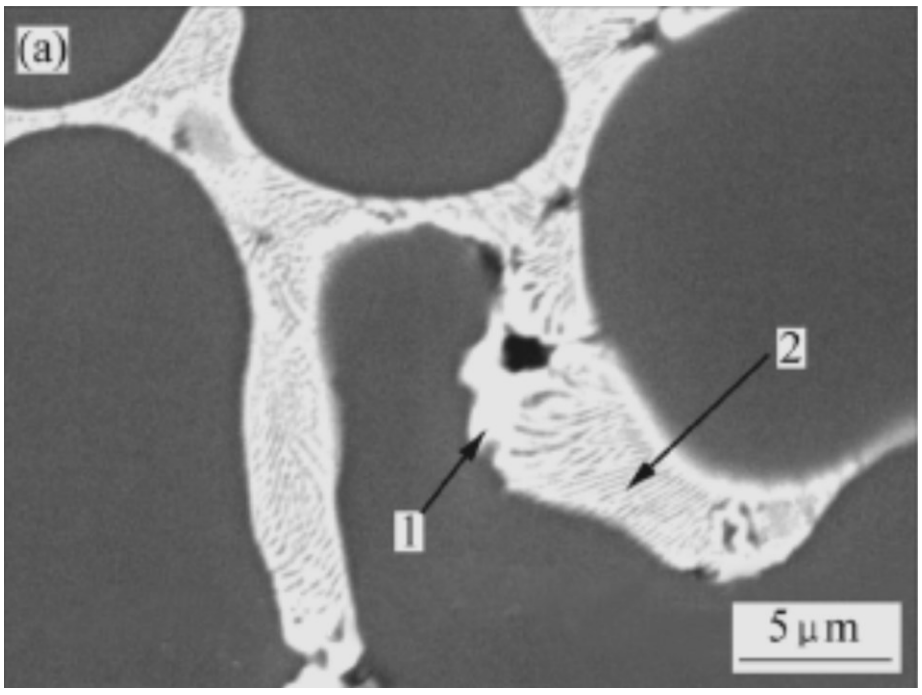


Figure 2.13. Eutectic phases found in as-cast Alloy L in Table 2.1 [36].

2.4. Eutectic compositions

Table 2.3 shows the overall eutectic compositions of the structures indicated in some of the alloys in Table 2.1, determined by EDX. It is clear that the eutectic structures consisted of Al, Zn, Mg and Cu in narrow ranges, indicating that there might be phase similarities regardless of the differing bulk alloy compositions in Table 2.1. It is unusual from an experimental viewpoint that the compositions in Table 2.3 were report to two decimal places instead of one.

Table 2.3. Overall compositions of the different eutectic structures for alloys in Table 2.1 [28,29,31,33-36].

	Al	Zn	Mg	Cu	Reference
Alloy	at.%				
D	39.08	18.98	26.98	14.96	[28]
E	51.47	16.42	19.35	12.76	[29]
G	47.77	19.95	21.65	10.63	[31]
I	58.00	16.00	18.00	8.00	[33]
J	58.47	15.21	17.65	8.67	[34]
K	62.43	13.00	16.55	8.02	[34]
L	62.65	16.34	13.97	7.04	[36]

2.5. XRD analyses

Figures 2.14 to 2.17 show the phases that were identified in the different Al-Zn-Mg-Cu as-cast alloys in Table 2.1 by X-ray diffraction (XRD) [27-29,34]. The large peaks were always the (Al) matrix, while the most common secondary crystal structure found was hexagonal $MgZn_2$. The S phase (Al_2MgCu) and T phase ($Al_2Mg_3Zn_3$) were sometimes reported, but are questionable because of the very small peaks, as for the S phase in the top curve of Figure 2.14. Iron-containing intermetallic phases were also identified in Figure 2.17, but overlapped with the η phase and if present, were a result of Fe impurities in the alloy.

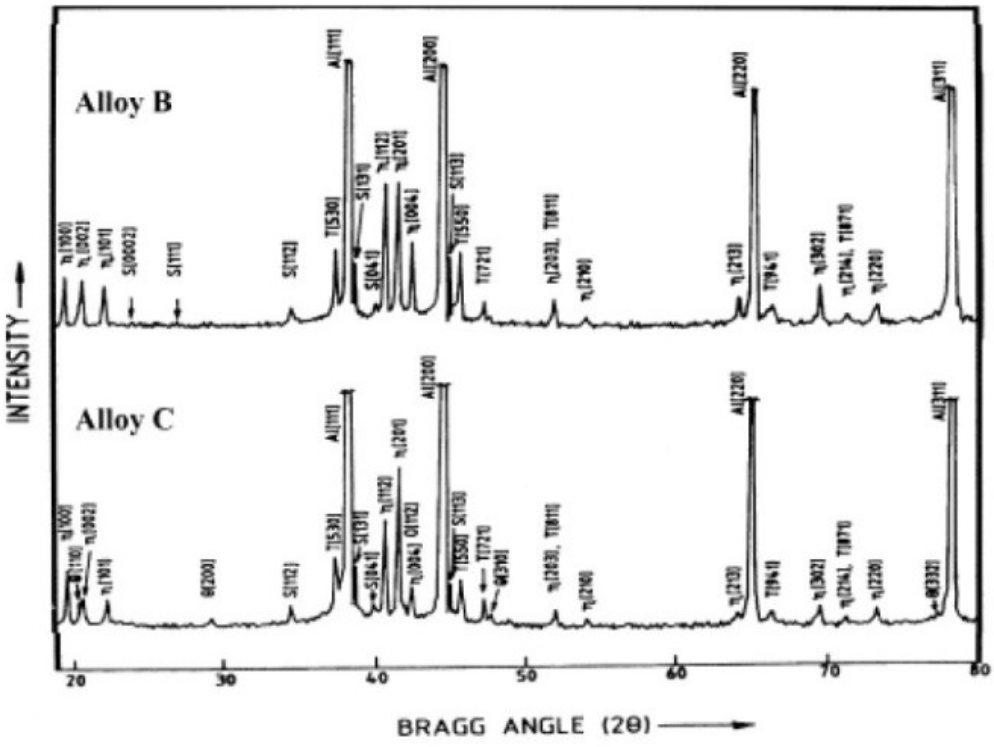


Figure 2.14. XRD patterns of as-cast Alloys B and C in Table 2.1 [27].

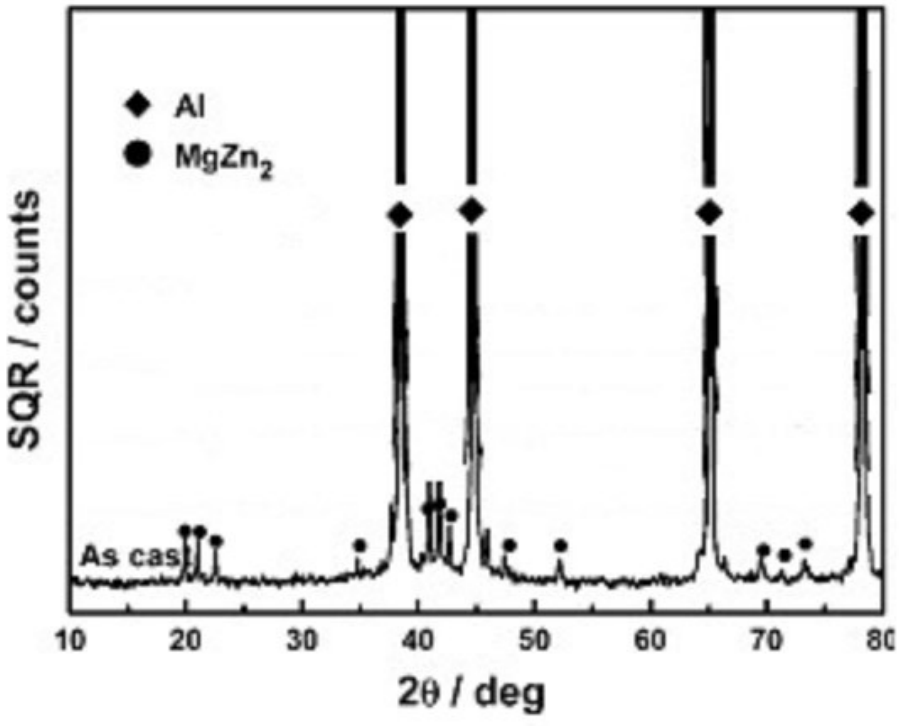


Figure 2.15. XRD patterns of as-cast Alloy D in Table 2.1 [28].

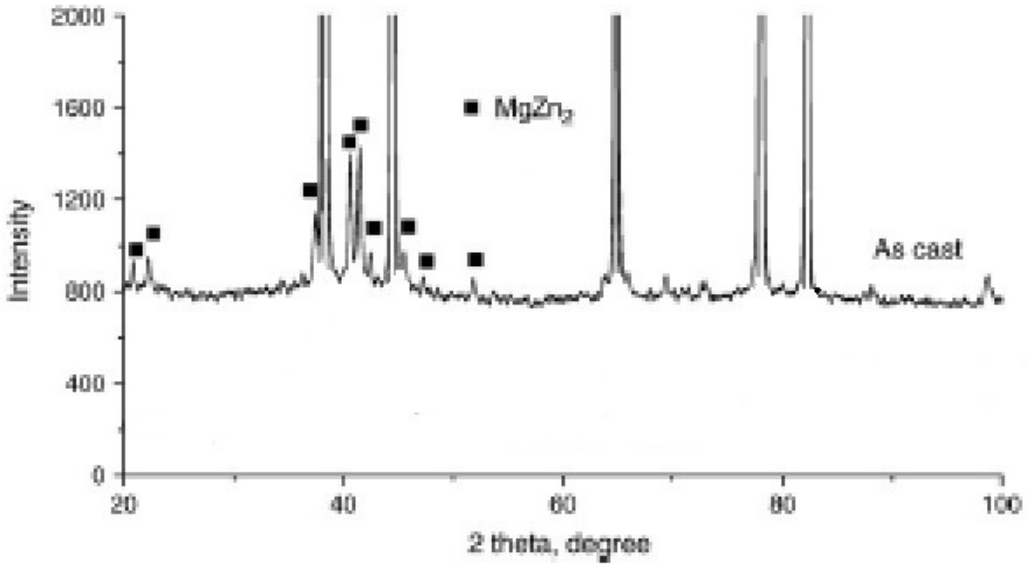


Figure 2.16. XRD patterns of as-cast Alloy E in Table 2.1 [29].

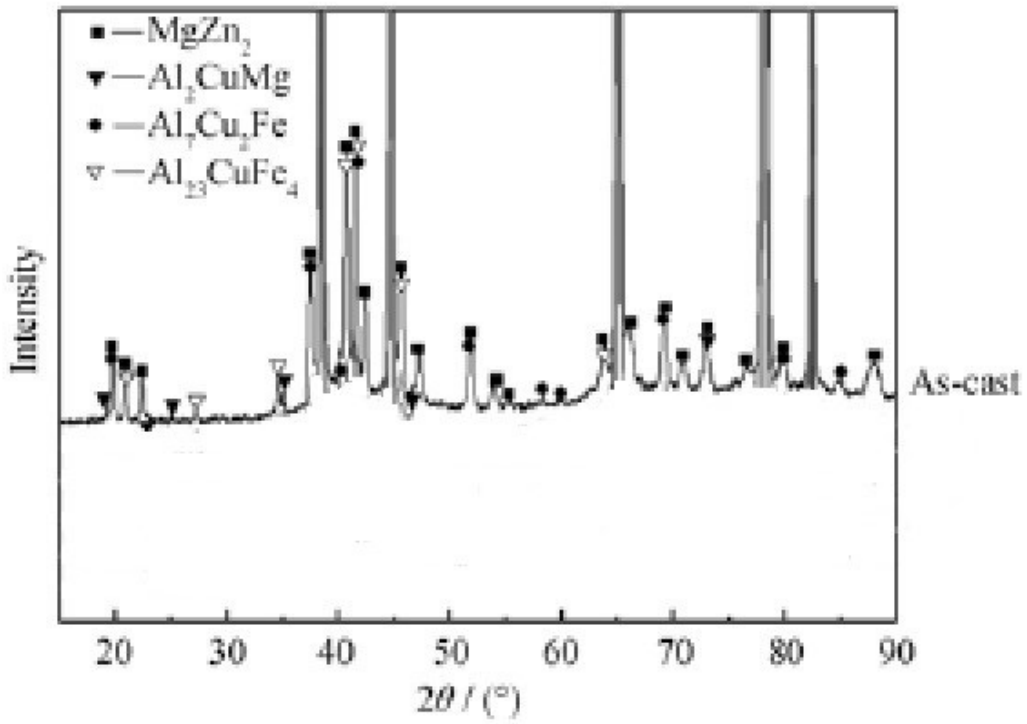


Figure 2.17. XRD patterns of as-cast Alloy J in Table 2.1 [34].

2.6. DSC analyses

Figures 2.18 to 2.22 show differential scanning calorimetry (DSC) curves for some of the alloys in Table 2.1 [28,30,31,34,35]. The curves show the onset of melting of the eutectic in Al-Zn-Mg-Cu alloys in the as-cast condition. In all cases, the peaks were sharp, indicating a reaction with the formation of liquid. The onsets are in a narrow range, even if the various alloy compositions differed more widely. It was not clear and no reason was given why the endothermic peak for Alloy F was in the opposite sense (exothermic) for heating of the alloy, Figure 2.19 [30].

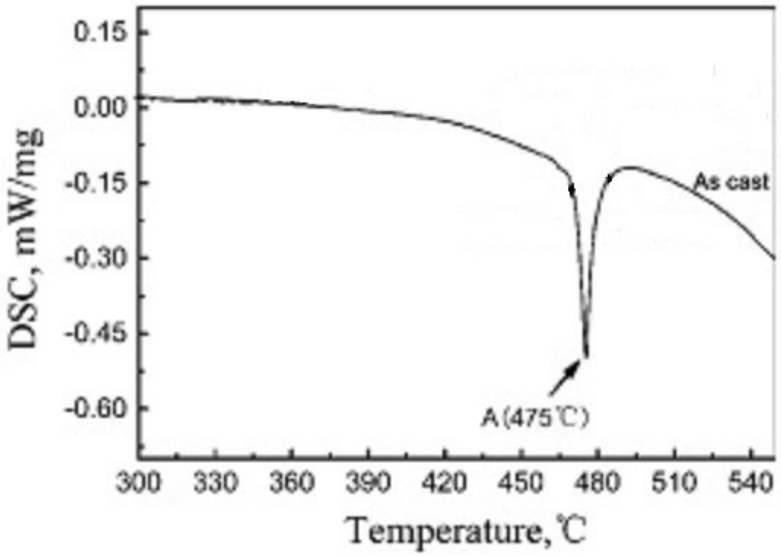


Figure 2.18. DSC curve of as-cast Alloy D in Table 2.1 [28].

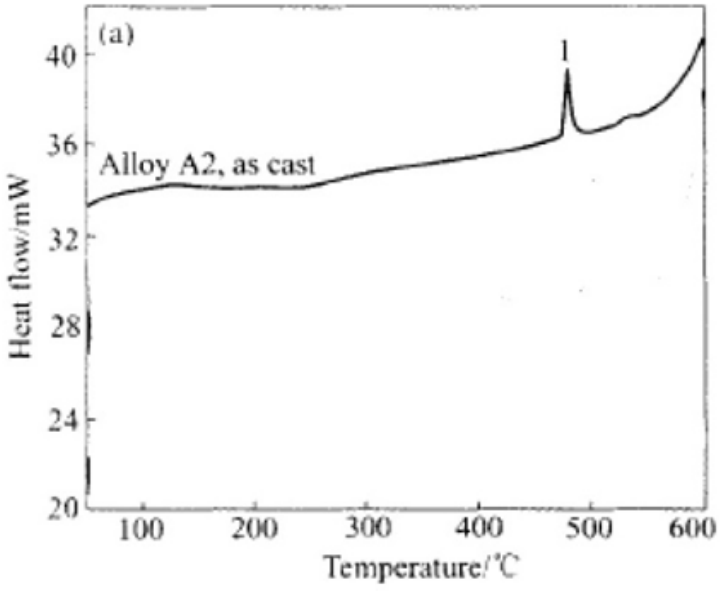


Figure 2.19. DSC curve of as-cast Alloy F in Table 2.1 [30].

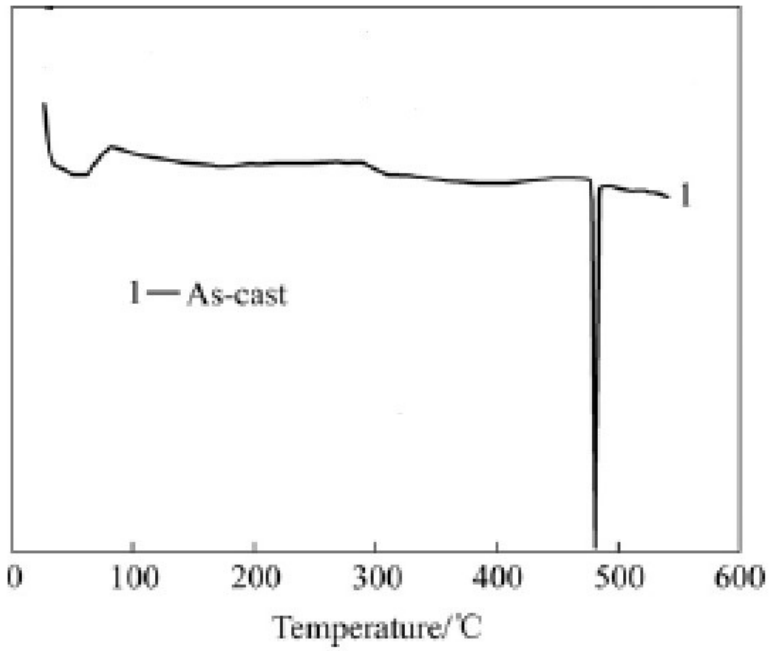


Figure 2.20. DSC curve of as-cast Alloy G in Table 2.1 [31].

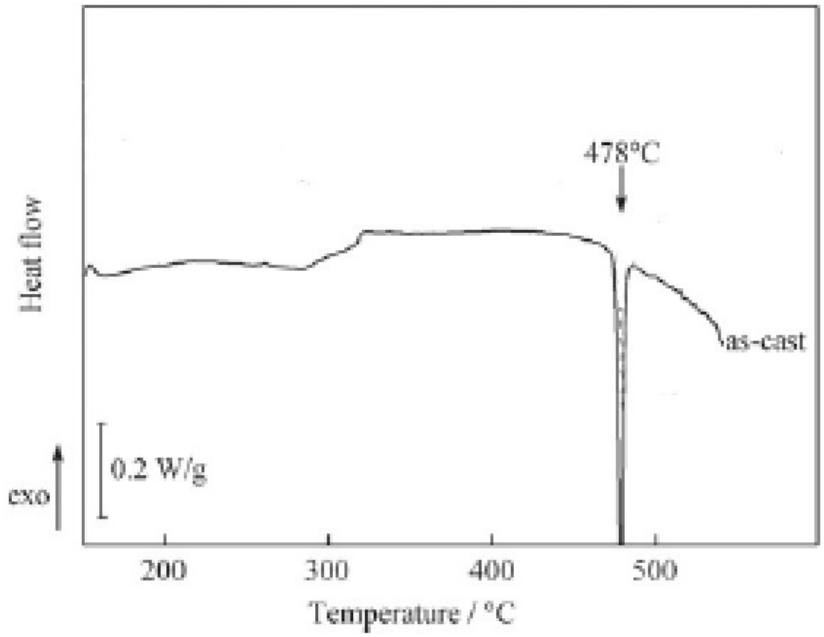


Figure 2.21. DSC curve of as-cast Alloy J in Table 2.1 [34].

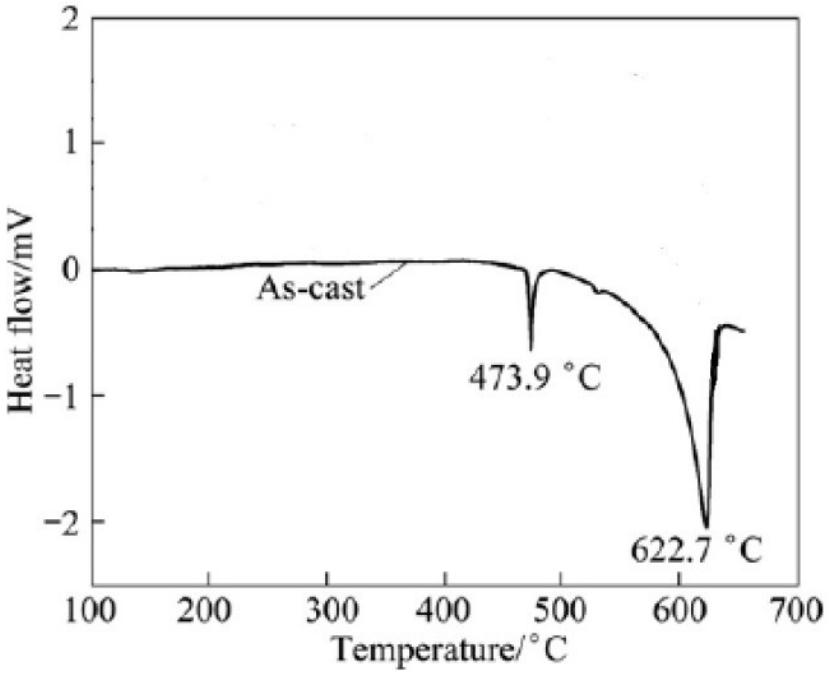


Figure 2.22. DSC curve of as-cast Alloy K in Table 2.1 [35].

Table 2.4 is a summary of the phases and melting points reported in Figures 2.1 to 2.22.

Table 2.4. Melting points and structures of the secondary phases of some of the the alloys in Table 2.1 [27-31,34,35].

Alloy	Melting peak (°C)	"Hexagonal phase"	"Cubic phase"	Reference
B	-	Yes	Yes	[27]
C	-	Yes	Yes	[27]
D	475	Yes	-	[28]
E	-	Yes	-	[29]
F	474	-	-	[30]
G	478	-	-	[31]
J	478	Yes	-	[34]
K	474	-	-	[35]

2.7. Homogenisation heat treatment

Homogenisation heat treatments are done on large cast ingots to dissolve the non-equilibrium phases that formed upon solidification during the casting process, that is, to take the alloying elements into solid solution in the primary Al-rich phase [1]. The preceding sections clearly showed the phases and thermal properties of such cast ingots.

Specific homogenisation heat treatments had been developed for specific Al-Zn-Mg-Cu aluminium alloys [1]. These programs include slow heating rates to take different types of furnaces into account and to minimise the temperature gradient in large sized ingot caused heat transfer considerations [1].

The maximum homogenisation temperature must be below the melting point of the alloy. A common maximum temperature is in the range of 460 °C to 470 °C. The DSC results in the Section 2.5 showed that melting of as-cast Al-Zn-Mg-Cu aluminium alloys start at around 476 °C.

Homogenisation times can vary as a consequence of the cooling rate that the alloy was subjected to during solidification. Industrial homogenisation times for ingots can be as long as 48 hours [41].

These alloys are then typically annealed to the O condition (fully soft) in preparation for the forming process. Precipitation of the alloying elements occurs during annealing [1].

2.8. Solution heat treatment

A solution heat treatment has to be performed after the forming process. It is necessary to dissolve the alloying elements into solid solution again. Typical temperatures used depend on the form that the material is in, e.g. extruded rod, extruded bar, rolled plate or sheet [1]. Al-Zn-Mg-Cu aluminium alloys (7xxx series alloys) are not cast and therefore no solution heat treatment specified. Solution heat treatment times also depend on the form the alloy is in. Rolled sheet requires a shorter solution heat treatment than large forgings. Thermal gradients are again a major consideration [1].

2.9. Quenching

Products have to be quenched after solution heat treatment to keep the alloying elements in solid solution at room temperature. Different quenching media can be used in order to acquire the highest practical cooling rate [1].

Thermal gradients again play a role. Quench cracks can form if the thermal gradient becomes too large. Distortion of the material is another problem, if the rate of cooling is not that same over thick and thin sections. Once quenched, the alloy is now ready for subsequent heat treatments [1].

2.10. Artificial ageing heat treatments

Precipitation is a diffusion related process by which compositions of the matrix and precipitates change with temperature and time [4]. The precipitation sequence, by which Al-Zn-Mg-Cu aluminium alloys obtain their strength, is given by Equation 2.3:

$$GP\ zones \rightarrow \eta' \rightarrow \eta \qquad 2.3$$

where GP zones are Gunier-Preston zones, η' are precipitates coherent with the matrix and η are equilibrium precipitates.

Although outside the scope of this study, it is worth mentioning that η' was the precipitate thought to be responsible for the maximum strength (T6) obtained by heat treatment of Al-Zn-Mg-Cu aluminium alloys and η for stress corrosion resistance (T73) [42]. Figure 2.23 shows the relationship of tensile strength as a function of heat treatment [2]. Maximum strength is reached in the T6 condition, while strength was the lowest in the T61 and T73 conditions. T73 is of great importance because of the increased stress corrosion resistance of Al-Zn-Mg-Cu aluminium alloys in this condition.

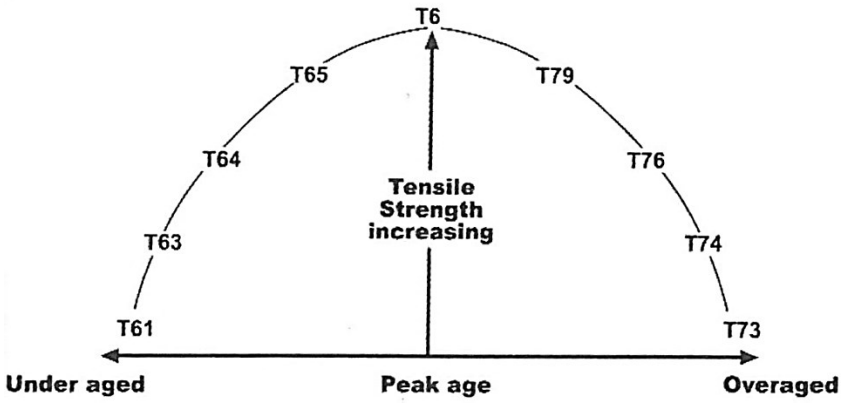


Figure 2.23. Tensile strength as a function of heat treatment condition [2].

Figure 2.24 is the iso-yield strength map for wrought AA7075 as a function of time and temperature [1]. The peak aged condition results in maximum strength. The time-temperature combinations for the shaded area labelled T6 are intended for saving time during industrial processing. The T73 condition can be achieved by a combination of times and temperatures indicated by the shaded area labelled T73 in Figure 2.24. Table 2.5 is an excerpt from AMS 2770J [43] which shows that the procedures to produce the T73 condition were different for different alloy

designations. Table 2.5 also shows that the Mandatory, Preferred and Alternative procedures differed.

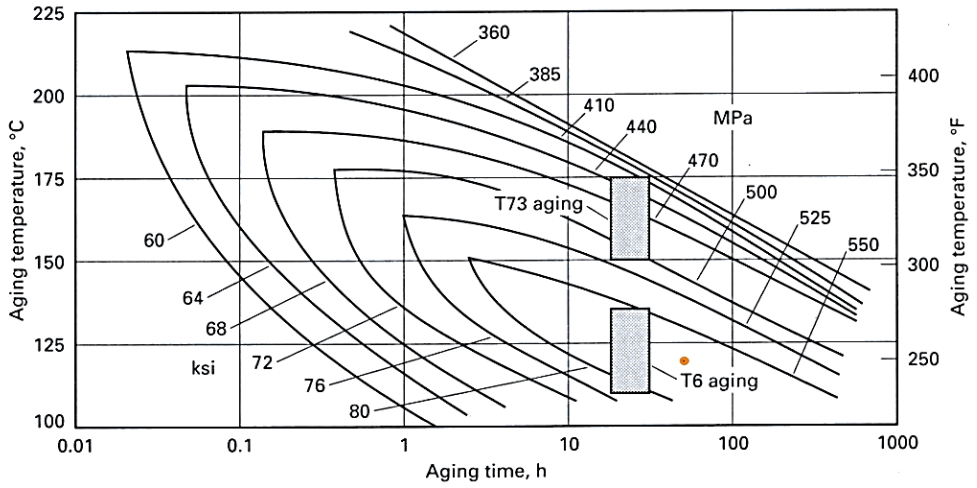


Figure 2.24. Iso-yield strength map for AA7075 indicating the experimental relationship between time, temperature and strength upon artificial ageing [1] and the red dot marks the artificial ageing heat treatment in this study.

Table 2.5. Heat treatment procedure excerpt from AMS 2770J for Al-Zn-Mg-Cu aluminium alloys of different designations [43].

Alloy	Form	Starting Temper (4)(5)	Final Temper (2)	Mand, Pref or Alt. (1)	1st Step Temp °F	1st Step Temp °C	1st Step Time (12) Hours	2nd Step (14) Temp °F	2nd Step (14) Temp °C	2nd Step (14) Time (12) Hours	Notes (4)
7049 7149	Extruded Bar and Shapes	W	T73	M	250	121	23-25	330	166	21-22	6,7,8
		W	T76	M	250	121	23-25	330	166	14-15	6,8
	Forgings	W	T73	M	250	121	23-25	330	166	13-14	6,8
7050	Rivets	AQ, W	T73	M	250	121	4 Min	355	179	8 Min	
	Plate, Extruded Bar, & Shapes	AQ, W	T73	M	250	121	6-8	350	177	11.5-12.5	6,8
	Plate	AQ, W	T76	M	250	121	6-8	350	177	6.5-7	6,8
	All Except Plate	AQ, W	T76	M	250	121	6-8	350	177	3.5-4.5	6,8
	All	AQ, W	T74(9)	M	250	121	6-8	350	177	6-8	6,8
7075	All	AQ, W	T6, T62	M	250	121	23-25				
	Sheet, Plate	AQ, W	T73	P	225	107	6-7	325	163	26-28	3,8
				A	250	121	4-5	350	177	8-10	3,8
			T76	P	225	107	6-7	325	163	16-18	8
				A	250	121	4-6	350	177	5-7	8
	Wire, Rolled Bar, Forgings	AQ, W	T73	P	225	107	6-7	350	177	8-10	8
				A	250	121	4-5	350	177	8-10	8
			T76	P	250	121	3-4	325	163	16-18	8
				A	225	107	6-7	325	163	16-18	8
	Extruded Bar & Shapes	AQ, W	T73	P	225	107	6-7	350	177	6-8	8
				A	250	121	4-5	350	177	6-8	8
			T76	P	250	121	3-4	320	160	19-21	8
				A	225	107	6-7	320	160	19-21	8
7178	All	AQ, W	T62	M	250	121	23-25				
	Sheet, Plate	AQ, W	T76	P	250	121	23-25	325	163	16-18	8
				A	250	121	4-6	325	163	16-18	8
	Extruded Bar & Shapes	AQ, W	T76	P	250	121	23-25	320	160	18-20	8
				A	250	121	4-6	320	160	18-20	8
7249	Forgings	W	T73	M	250	121	10-12	325	162	6.5-7.5	6,8
	Extrusions	W	T76	M	250	121	4-28	325	162	4-10	6,8
7475	Sheet	AQ, W	T61	M	250	121	3-5	315	157	3-3.25	8
		AQ, W	T761	M	250	121	3-5	325	163	10-12	8
	Plate	AQ, W	T6	M	250	121	23-25				
		AQ, W	T76	M	250	121	3-5	325	163	12-18	8
		AQ, W	T73	M	250	121	3-5	325	163	24-30	8

2.11. Material properties modelling as a function of composition

No publication, to the knowledge of the author, was available on the modelling of Al-Zn-Mg-Cu aluminium alloy mechanical properties as a function of composition for the peak-aged (T6) condition. The publication by Starink and Wang [44] was highly-cited and comprehensively modelled the influence of composition, precipitation during artificial ageing, and grain structure on the yield strength of Al-Zn-Mg-Cu aluminium alloys in specifically the over-aged (T7) condition. In this case for the composition modelling, it took into account the effect of iron as an impurity element in forming Al_7FeCu_2. Silicon as an impurity element, forming Mg_2Si, was neglected in the model because of its absence, or presence in limited amounts, in some commercial 7xxx series of aluminium alloys. The model predicts the yield strength of an alloy by a combination of the chemistry, ageing behaviour and the grain structure.

Unfortunately, hardness was not modelled by Starnik and Wang [44]. Hardness is a very convenient measure of material properties. It can indicate that changes in a material have reached some type of equilibrium by reaching a plateau with time for a given set of conditions. It is also reasonable to assume that the hardness is related to alloy composition for a given set of ageing conditions and microstructures, and that alloys can be directly compared.

The reason for the lack of material property modelling as a function of composition is undoubtedly the difficulty in obtaining a number of alloys with different composition ranges. The wrought process is a long and expensive route to produce alloys for research. Alloy material is in any case difficult to source, even for the choice not to custom produce alloys.

The aim with this section was to ascertain whether the hardness and yield strength of the Al-Zn-Mg-Cu aluminium alloys tested in this study were functions of the structure and chemical composition as presented by Equation 2.4:

$$Mechanical\ property \propto f(grain\ size, composition) \qquad 2.4$$

3. Experimental procedure

Alloyed castings were received from the CSIR in the as-cast state. Castings of four of the alloys were in the form of taper rods, while one alloy was in the form of a plate.

Sections 3.1 to 3.4 deal with the production of castings by the CSIR, with the CSIR R-HPDC process.

Section 3.5 deals with the heat treatments to which the alloys were subjected.

Section 3.6 deals with a commercial wrought alloy that was used for comparison and validation of the hardness-composition model.

Section 3.7 describes the experimental techniques used.

Section 3.8 describes sample preparation procedure in detail.

3.1. Alloying

Alloys were made by melting super purity aluminium (99.99 %Al) in a resistance furnace with a capacity of 25 kg. Addition of alloying elements started once the liquid aluminium (melting point: 660 °C) reached a temperature of 700 °C. The required weight of high purity Zn was first added with the required weight of high purity Cu. The alloy was then mechanically stirred for 20 minutes. The required weight of high purity Mg was then added. The alloy was then again stirred for 10 minutes. The liquid alloy was then de-gassed for 30 minutes with argon through a carbon lance after alloying, to remove any dissolved hydrogen and inclusions.

A reduced pressure test (RPT) was used to assess the quality of the melt. The RPT works by pouring the liquid metal into a cup and solidifying under vacuum to exaggerate growth of any dissolved gas in the solidifying alloy. The solidified metal billet was cut with a band saw and ground on a linisher, and the exposed surface was then inspected for porosity. High quality melts were known to have been achieved by observing no macro porosity in the vacuum solidified material. Figure 3.1 shows the RPT device, the cup and the billet that was solidified under vacuum.

The sample solidified under vacuum was also used for comparison to samples that were solidified under the high cooling rates of R-HPDC.

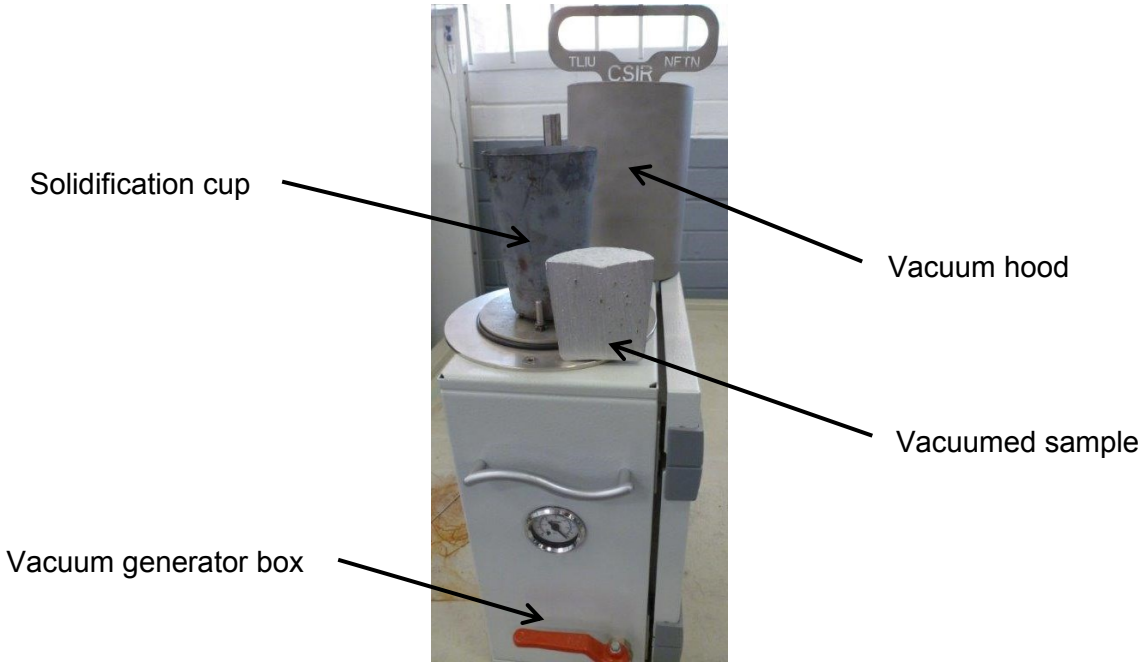


Figure 3.1. Reduced pressure test device used for vacuum cooling.

3.2. Bulk alloy compositions

A sample of each alloy was poured into a cup from the furnace to determine the bulk alloy compositions. Table 3.1 shows the alloy compositions that resulted from the alloying procedure.

Table 3.1. Bulk alloy compositions of the five alloys, as received.

	Zn	Mg	Cu	Si	Fe	Mn	Al
Alloy				wt%			
7A	7.78	2.13	0.91	-	0.02	0.35	88.81
7B	8.09	2.19	1.00	-	0.01	0.11	91.45
7C	9.73	3.94	2.05	0.12	0.09	-	87.17
7D	7.80	3.07	1.64	-	0.02	0.39	89.63
7E	6.70	2.55	2.00	-	0.06	-	90.00

3.3. R-HPDC

Rheo-processing was performed with the small scale CSIR Rheocasting System (CSIR-RCS) device. This device consisted of an induction coil which was integrated with a compressed air coil for forced air cooling [5].

3.3.1. CSIR rheo-processing

Figure 3.2 shows that R-HPDC cell. The ladle furnace is shown as well as the small scale CSIR-RCS device and the HPDC machine.

R-HPDC processing at the CSIR for alloys as was described by Curle et al. [13] and follows. The melt was prepared in the furnace and a sample was poured for chemical analysis with an optical emission spectrometer (OES) on site. The actual composition from the OES was then used as input to a thermodynamic database (ProCast) to calculate the theoretical thermal properties of the liquid alloy, including the liquidus temperature and the 0.3 solid fraction temperature ($T_{fs}^{0.3}$). The pouring temperature with a superheat of between 10 and 20 °C was calculated and the furnace temperature was set to stabilise and control at the calculated pouring temperature. Processing was ready to commence at this point.

The processing sequence started by ladling the liquid alloy into the processing cup and transferring to the CSIR-RCS. The cup was positioned in the processing coils where the cooling rate was controlled by the forced air cooling, while the contactless stirring action was controlled by the power input into the induction coil. Processing continued until the $T_{fs}^{0.3}$ temperature was reached, at which point the processing cup was ejected from the processing coil. The SSM material in the cup was then transferred to the HPDC machine and emptied into the shot sleeve and subsequently HPDC.

3.3.2. Modified CSIR rheo-processing

The process above was adapted due to the temperature measurement thermocouple inside the cup causing poor casting flow of the semi-sold metal. This effect was due to the liquid metal solidifying on the thermocouple and leaving a hole in the middle of the semi-solid billet after the thermocouple was extracted subsequent to rheo-processing.

The solid fraction is normally expressed as a function of temperature, but the solid fraction can also be expressed as a function of time. The temperature and the processing time are related by the cooling rate which is constant. The solid fraction curve is commonly given as a function of temperature which can be written as some function of temperature, as in Equation 3.1:

$$-\frac{df_s}{dT} = z(T) \quad 3.1$$

where df_s is the solid fraction differential, dT the temperature differential and $z(T)$ a function with temperature as the variable (this function is not linear). The negative sign indicates that the solid fraction increases as the temperature decreases.

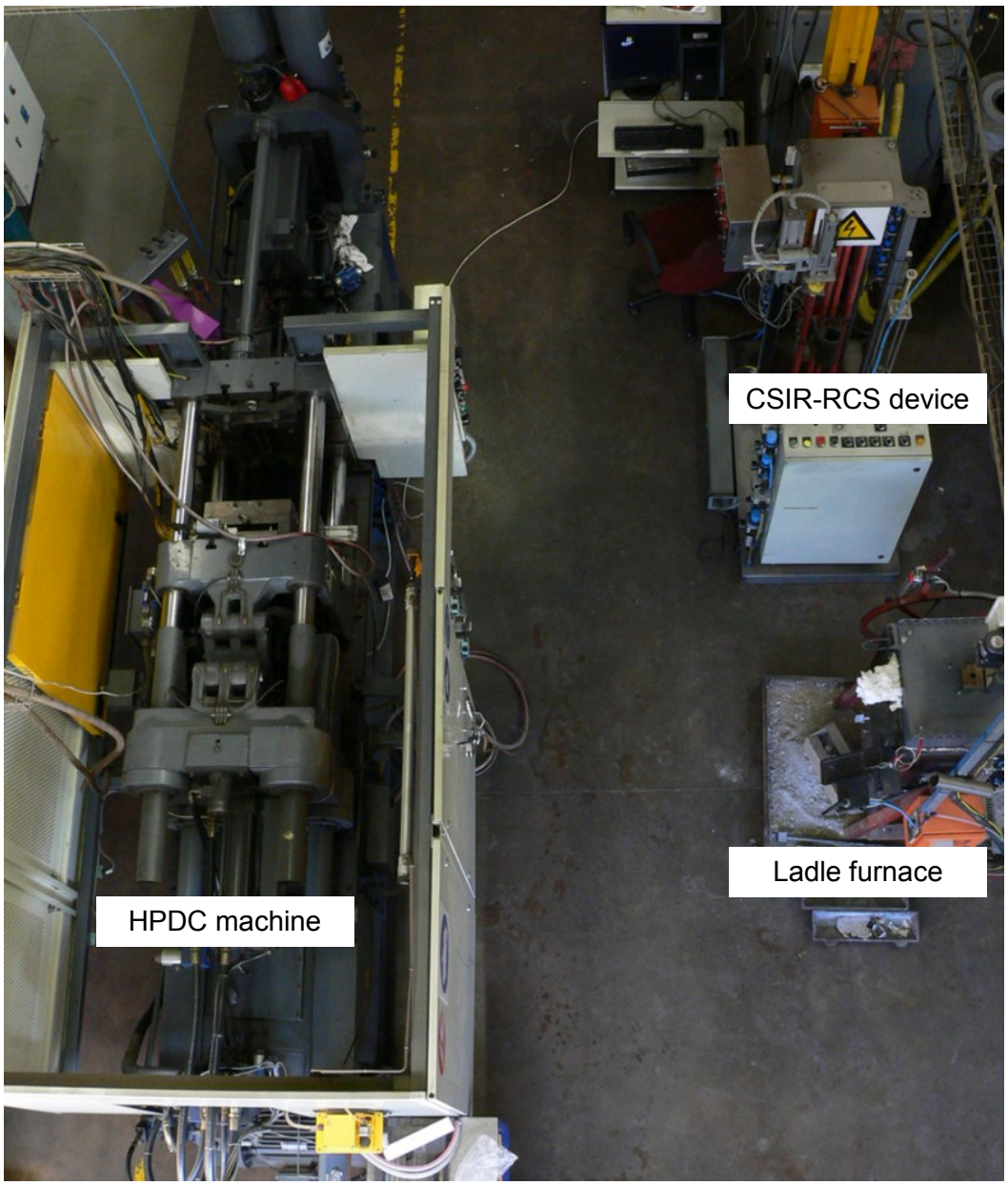


Figure 3.2. R-HPDC cell with dosing furnace, CSIR-RCS device and HPDC machine.

The terms can be separated by elementary differential calculus equations according to Equation 3.2:

$$df_s = -z(T)dT \quad 3.2$$

Integration of Equation 3.2 therefore results in Equation 3.3:

$$f_s - f_0 = Z(T_1) - Z(T_2) \quad 3.3$$

where $Z(T_x)$ is an integral function of $z(T)$, T_2 is the temperature at which the solid fraction is sought and T_1 is the initial solid fraction temperature. T_1 was taken as the as the calculated liquidus temperature (T_L) at which temperature the solid fraction is marginally larger than zero and solidification starts (T_L is a constant).

Substitution of the above values results in Equation 3.4:

$$f_s = Z(T_L) - Z(T_2) \quad 3.4$$

The cooling rate, for a cup of alloy processed, is a constant and can be expressed as Equation 3.5:

$$-\frac{dT}{dt} = k \quad 3.5$$

where the heat transfer constant, k, took into account the forced air temperature, pressure, flow, the cup material, cup wall thickness, heat generated during induction and the volume of alloy processed.

After integration and substitution Equation 3.5 can be written as Equation 3.6:

$$T_2 = T_L - kt_2 \quad 3.6$$

where t_2 is the processing time, $t_1=0$, k is the cooling rate constant and T_2 and T_L have the same meanings as above.

Equation 3.7 is the result of substituting T_2 in Equation 3.4 with T_2 in Equation 3.6:

$$f_s = Z(T_L) - Z(T_L - kt_2) \quad 3.7$$

This shows that the solid fraction can be taken as a function of the processing time. It was acknowledged that the cooling rate constant was a function of the alloy volume poured into the cup, while the rest of the heat transfer parameters remained constant. Processing therefore took place for 16 to 24 seconds depending on the liquid metal volume in the cup. Cups with less liquid metal were processed for shorter times, while fuller cups were processed for longer times; for the time range indicated above. The aim was to achieve a smooth billet consistency in the semi-solid state.

The cup was then ejected from the processing coil and manually transferred to the high pressure die casting (HPDC) machine. The cup was emptied into the shot sleeve of the LK DCC130 cold chamber shot controlled HPDC machine. Injection by the piston was manually initiated once the billet was in the shot sleeve. The piston then followed the specified distance-speed injection shot control program, filling the die cavity. The casting was taken out once the die opened. These castings were referred to as being in the “As-cast” condition.

3.4. Casting geometries

3.4.1. Taper rods

Alloys 7A to 7D were cast into the taper rods casting geometry. Figure 3.3 shows of the entire casting with taper rods, runner and biscuit.

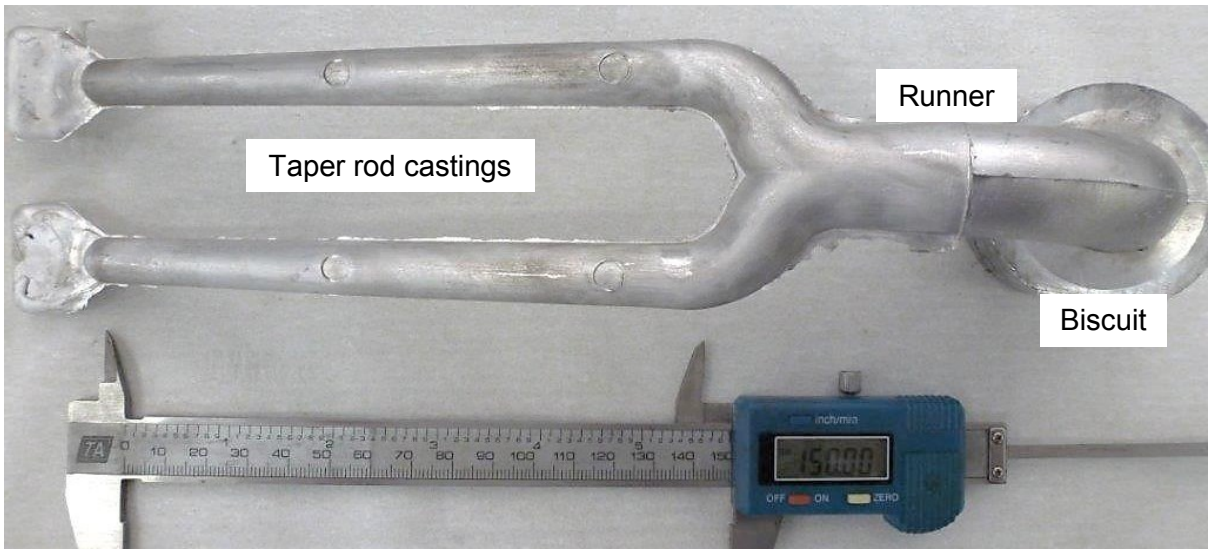


Figure 3.3. Alloy 7A as an example of the taper rod casting with runner and biscuit.

3.4.2. Plate

One alloy, Alloy 7E, was cast into the plate geometry. Figure 3.4 shows the entire casting with plate, runner and biscuit of Alloy E.

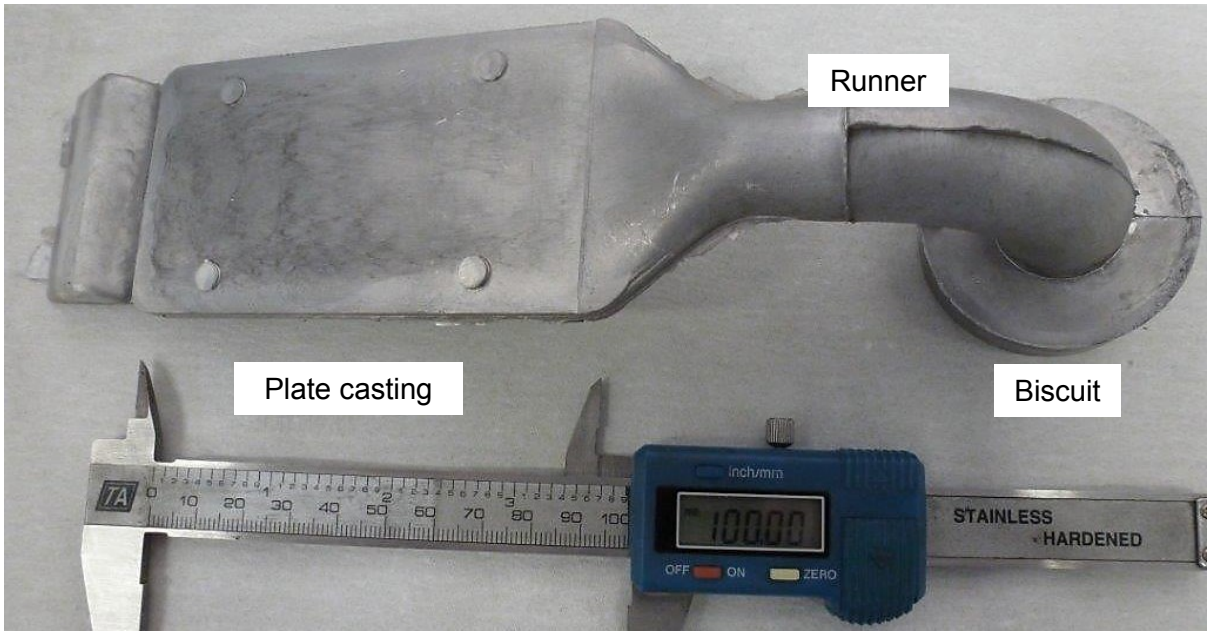


Figure 3.4. Plate casting with runner and biscuit of Alloy 7E.

3.5. Heat treatments

It was not an aim of the study to evaluate different heat treatment practises for the R-HPDC and wrought alloys tested. It will be shown that the chosen heat treatment resulted in mechanical properties similar to the conventional heat treatment of Al-Zn-Mg-Cu aluminium alloys to the T6 condition.

3.5.1. Homogenisation

A Carbonite HRF 7/22 circulating air furnace was used for homogenisation and solution heat treatment in a single-step heat treatment. The furnace was set to 470 °C and left to reach this temperature. The taper rod and plate samples were inserted into the furnace in a rack, once the furnace was at temperature. Figure 3.5 shows the samples in the rack. The temperature fell by ~10 °C before closing the furnace door. The procedure was acceptable since the furnace returned to temperature with only a 1 °C over-shoot. The temperature was controlled to ±0.5 °C. The time for homogenisation was chosen to be 170 hours in order to approach near-equilibrium conditions by allowing enough time for solute elements to dissolve completely.

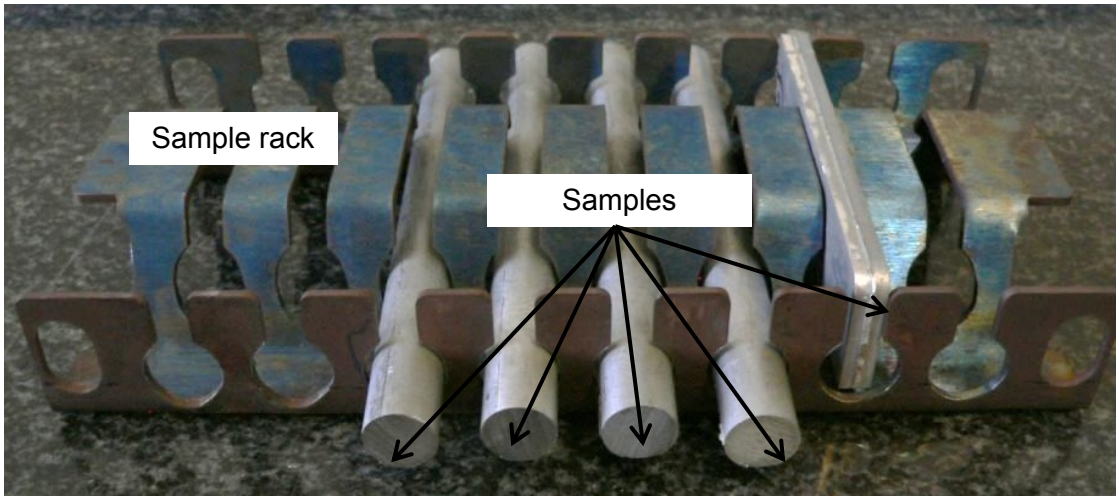


Figure 3.5. Heat treatment rack with taper rod and plate samples.

3.5.2. Solution heat treatment

The solution heat treatment was combined into a single step to coincide with homogenisation temperate.

3.5.3. Quenching

Figure 3.6 shows the heat treatment rack and 20 ℓ water quench container in which the solution heat treated samples were quenched in water at ambient temperature. The samples were moved around during quenching to avoid a steam blanket forming around the samples, which severely retards heat transfer to the water.

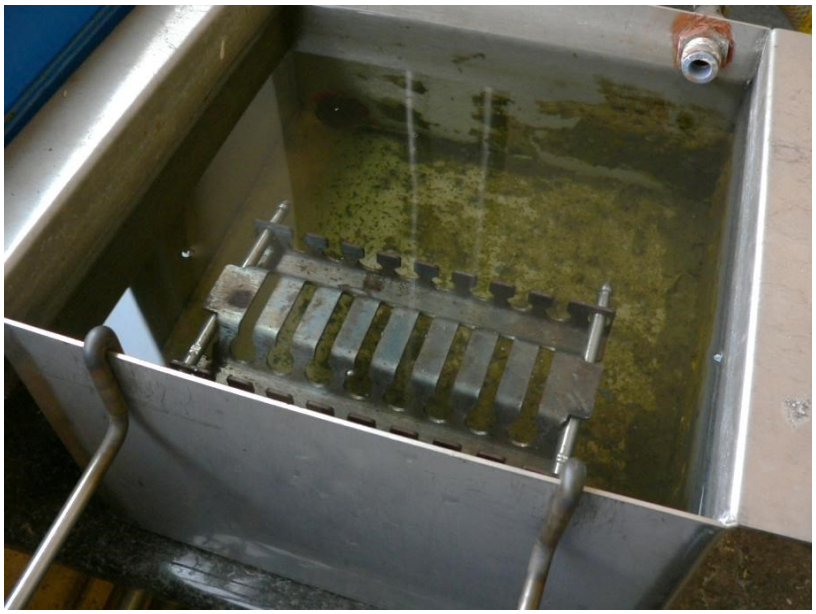


Figure 3.6. Quench tank with water.

3.5.4. T6 artificial ageing

Artificial ageing was performed in a second air circulating furnace, Carbonite HRF 7/22. The furnace temperature was set to reach 120 °C and left to stabilise pre-quenching. The rack with the samples was removed from the quench container and inserted into the artificial ageing furnace at temperature. The time for artificial ageing was chosen to be 50 hours. The chosen parameters, red point in Figure 2.24, fell in the middle of the plateau to ensure peak ageing. The temperature was again controlled to ±0.5 °C. This heat treatment condition was referred to as the T6 condition in the peak aged state. Time was not a restriction to this study as in industry.

3.5.5. T73 artificial ageing

The T73 heat treatment was performed in the same manner as the T6 heat treatment, except that the first step was at 120 °C for 3 hours and then the second step was 160 °C for 24 hours. This heat treatment was chosen to ensure full over-ageing and was the mandatory artificial ageing for aluminium alloy 7475, according to AMS 2770J [43].

3.6. Wrought Al-Zn-Mg-Cu aluminium alloy

A sample of wrought Al-Zn-Mg-Cu aluminium alloy (AA7040) plate was acquired through a local aerospace company. The sample was subjected to the same T6 heat treatment as the R-HPDC material. The only difference was that the solution heat treatment was for 1 hour, because the material was already homogenised.

This wrought material was used for comparison with R-HPDC material and validation of the T6 hardness-composition model developed later in the study.

3.7. Sample preparation

3.7.1. OES

A piece was cut from the left arm back-end of each alloy's taper rod, for optical emission spectroscopy (OES). These pieces were also placed in the furnace at 470 °C with the taper rod samples for homogenisation and were removed after 48 hours and quenched in a bucket of water. This heat treatment procedure softened the pieces for deformation with a 16 ton press. The reason for this procedure was

that the aperture of the OES was 15 mm, while the diameter of the back-end of the taper rod was only 12 mm. This procedure increased the diameter of the OES sample to at least 17 mm, which was sufficient for analysis. The samples were water ground on a polishing machine with only 800 grit SiC grinding paper at a set speed of 200 rpm.

Figure 3.7 shows the deformed sample from the back-end of the taper rod as well as the position of the hardness sample. The arrows indicate that the OES and hardness measurements were made on the adjacent sides of the cut. It was difficult to preserve the polished surface for hardness measurement after OES measurement due to the destructive nature of the OES measurement of the surface. Therefore were the adjacent sides of the cut used for the correlation between hardness as a function of composition.

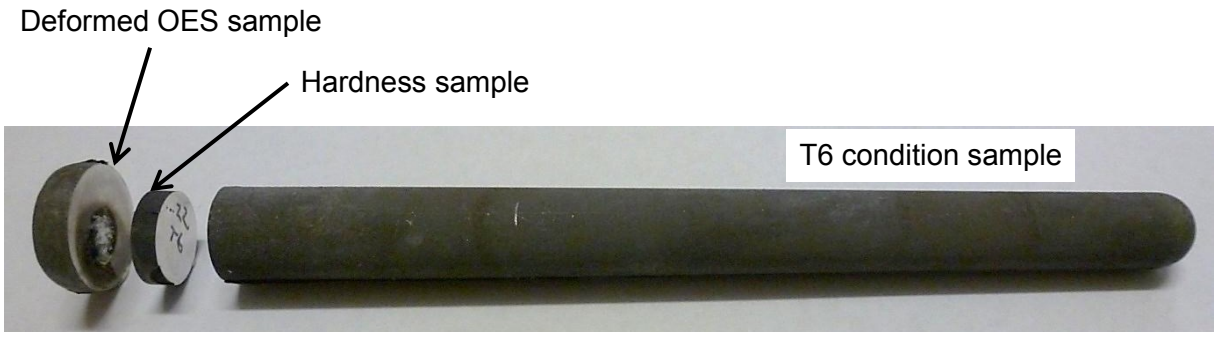


Figure 3.7. Sectioned taper rod sample with OES and hardness samples.

The plate sample was removed with a cut-off disk. Two millimetres of the plate sample was ground off. This sample was metallographically hand-prepared by water grinding with 80, 240, 600, 1200, 2400 and 4000 grit SiC grinding papers. The sample was then polished with 3 µm diamond solution, and finally polished with 50 nm colloidal SiO_2. All steps were performed at a speed of 200 rpm. The sample was left unetched. The sample was analysed with the OES only after the hardness measurements were done. The wrought sample was prepared in the same way as the plate sample.

3.7.2. SEM and EDX

A sample was taken from the right arm back-end of each alloy's taper rod, as well as the plate, in the as-cast condition, by cutting with an ATM Brillant 221 precision cut-off machine. The samples were metallographically prepared by hand on an ATM Safir 550 polishing machine. Samples were water ground with 1200, 2400 and

4000 grit SiC grinding papers and then polished with 3 µm diamond solution and finally polished with 50 nm colloidal silica (SiO_2). A grinding speed of 200 rpm was used for all steps. Samples were left unetched.

A sample was taken from the left arm back-end of each alloy's taper rod as well as the plate, in T6 condition, by cutting with a precision cut-off machine. The samples were metallographically prepared by hand, by water grinding on 1200, 2400 and 4000 grit SiC grinding papers. The samples were then polished with 3 µm diamond solution and finally polished with 50 nm colloidal SiO_2. All steps were performed at a speed of 200 rpm. Samples were left unetched.

Hand-preparation was preferred over mounting in Bakelite because a hot mounting process (160 °C for 10 min) would probably cause over-ageing of the T6 samples, aged at 120 °C.

3.7.3. XRD

The XRD samples were the same samples as the as-cast alloy samples mentioned in Section 3.7.2.

3.7.4. DSC

Cylindrical samples with a diameter of 5.5 mm were turned on a lathe from the back-end of each of the as-cast taper rods, including the plate. Disks were cut on the precision cut-off machine from these cylinders. The disks were then ground until they reached a weight of 32 mg for all alloys.

3.7.5. Hardness

Samples in the T6 condition were cut with the precision cut-off machine, again from the back-end of the heat treated taper rods. These cylinders were hand-prepared metallographically by water grinding with 1200, 2400 and 4000 grit SiC grinding papers. The samples were then polished with 3 µm diamond solution and finally polished with 50 nm colloidal SiO_2. All steps were performed at a speed of 200 rpm. Samples were left unetched.

Figure 3.7 also shows a section that was used for hardness measurements. The intention was to improve the correlation between the composition analysis and the hardness evaluation by using adjacent sides of the cut for each type of measurement. The polished side of the cut was preserved for hardness because the OES spark damages the surface.

3.7.6. Grain size

The as-cast and T6 sample, for optical light microscopy, were etched with 0.5 % HF, after all other measurements were completed.

3.8. Experimental techniques

3.8.1. OES

Optical emission spectroscopy (OES) was performed with a Scientific ARL Quantris OES, at the CSIR. The OES had a calibrated Al database.

3.8.2. SEM

The JEOL JSM-6510 scanning electron microscope (SEM), at the CSIR, was used to analyse the as-cast and T6 material. Acceleration voltages of 6 kV and 20 kV were used for observation, always in the backscattered energy (BSE) image mode.

3.8.3. EDX

A Thermo Scientific UltraDry detector was used for EDX measurements and the data were analysed with Thermo Fisher Scientific NSS 2.2 software. EDX measurements were done in BSE mode at a working distance of 10 mm and an acceleration voltage of 20 kV for large features, and 6 kV for very small features. The reason for the lower acceleration voltage used was to reduce the size of the interaction volume, to ensure that the signals were collected from only the regions of interest. The acquisition time was increased to allow for more counts. Area analysis was also chosen over point analysis for better representation of the area.

Oxygen and nitrogen were also included in the analyses to assess their contribution to the overall analysis. Contributions of these elements were excluded from the calculation of the compositions of phases to find the quantitative result.

3.8.4. Thermodynamic modelling

The Scheil module in Thermo-Calc Classic S with the TTAl8 aluminium database was used, at the University of the Witwatersrand, to calculate equilibrium phase diagrams and non-equilibrium solid fraction curves for each alloy using the appropriate OES Zn, Mg, Cu and Al (balance) measured compositions as alloying inputs.

3.8.5. XRD

The as-cast samples were outsourced for XRD to Xrd Analytical & Consulting; results were interpreted in collaboration with the author. XRD measurements were performed with a PANalytical Empyrean diffractometer with a PIXcel detector. The exposed measurement area was 5 mm in diameter. Fixed slits with Fe filtered Co-Kα radiation were used. Data were analysed with X'Pert Highscore Plus Version 3.05 software and the PAN-ICSD database. The weight percentages of phases were determined using a function in the software.

3.8.6. DSC

A NETZSCH STA 449F3 Jupiter was used for DSC. The thermal cycle of the experiment was started with argon purging, after which the sample followed a ramp rate of 20 °C/minute to 680 °C followed by a hold for 10 minutes and was cooled at the same rate as the heating rate. This fast ramp rate was chosen to exaggerate the appearance of non-equilibrium melting peaks. Data were analysed with NETZSCH Proteus Version 6.1.0 software. The melting onset temperatures were determined with the DCS software which used an extrapolation according to DIN and ISO standards, as quoted by the manufacturer. The accuracy of temperature measurement for this device was also quoted by the manufacturer as ±1.5 °C or 0.25 % (whichever is greater). Note that the error of ±1.5 °C is greater than the error at 476 °C which was ±1.19 °C.

3.8.7. Hardness

Vickers hardness testing was performed with a Future-Tech FM-700 microhardness tester. A load of 500 g was used. The hardness value of each alloy was calculated as the average of six measurements in the area correlating to the OES spark mark.

3.8.8. Grain size measurement

Optical light micrographs were captured at 100x magnification on a Leica DMI5000M microscope equipped with a Leica DFC295 digital camera and Image-Pro Plus Version 6.3.0.512 software.

Grain sizes were measured by the linear intercept method according to Equation 3.8:

$$d = \frac{l}{n} \qquad 3.8$$

where *d* was the grain diameter, *l* a known line length at the appropriate scale and *n* the number of grain boundary intersections with the line. Three random lines were used to calculate the average grain size.

4. Results

4.1. Visual examination of castings

All casting received were visually examined. The casting had bright surfaces, no cold shuts and showed complete filling. Figure 4.1 shows an example of the surface appearance of the taper rod castings while Figure 4.2 shows the plate casting.



Figure 4.1. Example of the surface of the taper rod castings.

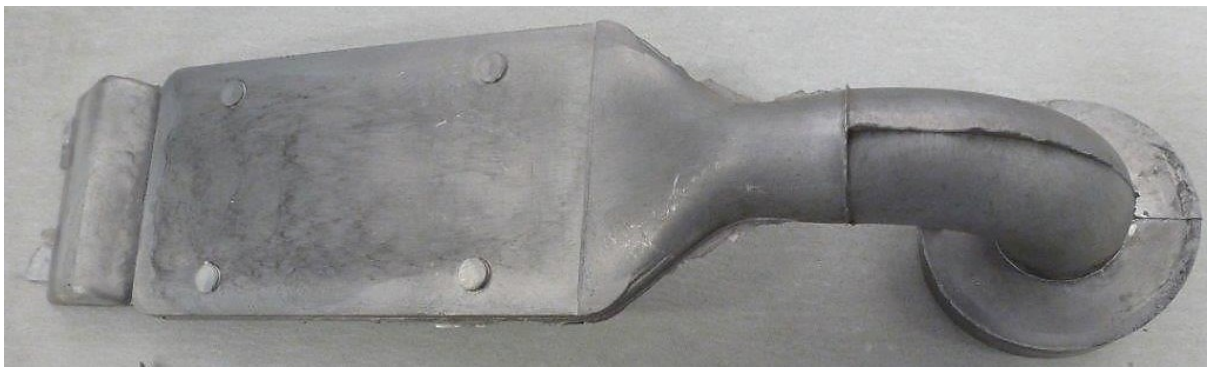


Figure 4.2. Surface appearance of the plate.

4.2. Alloying element macro-segregation

Figure 4.3 shows the microstructure of the taper rods from the middle of the rod to the surface at a low magnification. It is clear that there is some macro-segregation of alloying elements at the surface. The liquid that contained the alloying elements segregated to the surface during casting due to the flow of semi-sold material in the die cavity.

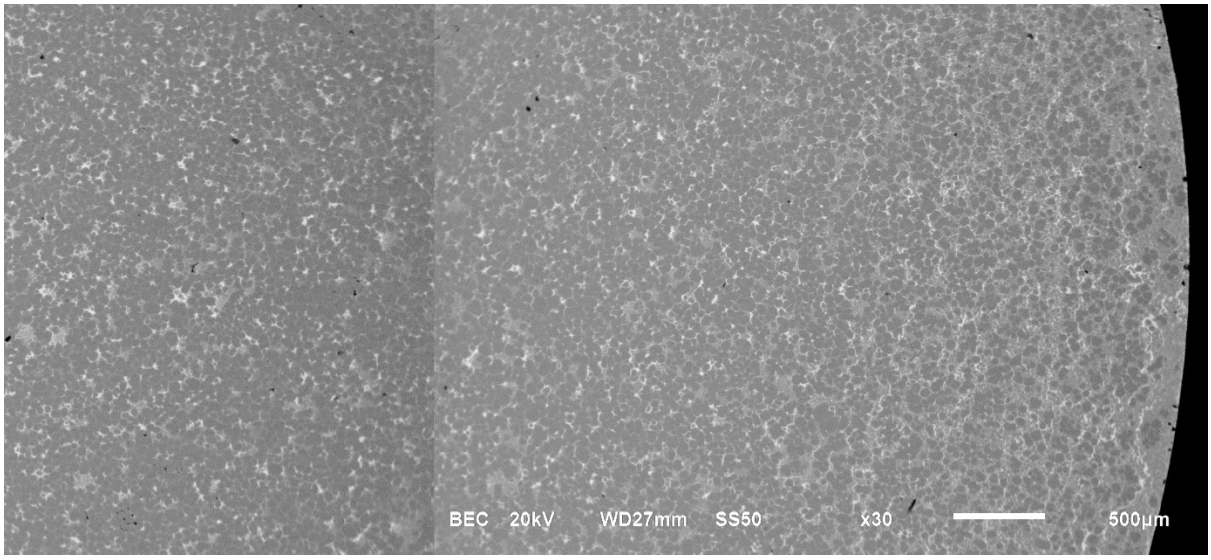


Figure 4.3. SEM-BSE image of macro-segregation in the casting.

Figure 4.4 shows a cross section of a taper rod. The yellow circle indicates the area from which the OES measurement was taken. The hardness measurements were made between the yellow boundary and red line. The aim of this procedure was to improve the correlation between hardness and composition measurements.

The effect of taper of the casting on the solidification rate was also eliminated by this technique, because sampling was always done in the yellow area and close to the centre.

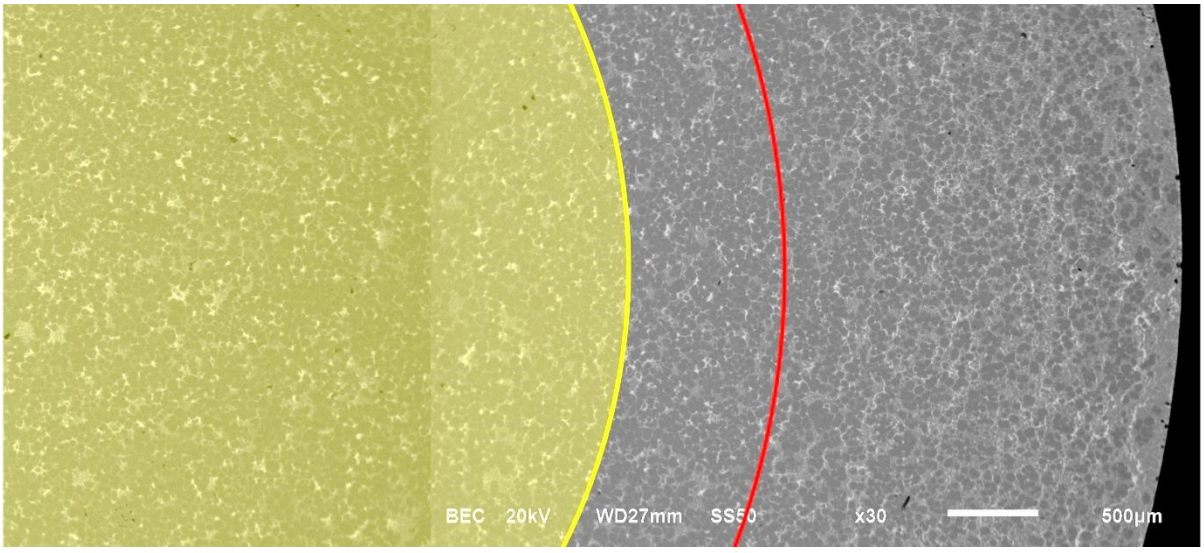


Figure 4.4. OES and hardness measurement areas. Yellow shaded area indicates the radius of the OES measurement area on the deformed side of the sample. The hardness measurement area was between the yellow and red radii around the sample; on the polished adjacent side of the sample.

4.3. Sample alloy compositions

The sample alloy compositions, used from this point in this study, as measured with OES in the yellow shaded area indicated Figure 4.4 are given in Table 4.1. The alloy compositions varied significantly. Alloy 7A and 7B were very similar in their Zn, Mg and Cu contents and they also had the lowest Cu content. Alloy 7C had the highest alloy content of all. Alloy 7D had intermediate Zn and Cu contents among the alloys. Alloy 7E had the lowest Zn content of all, with a relatively high Mg content and one of the highest Cu contents.

The impurity contents of all the alloys were very low, especially Si. Iron is one of the impurities that is picked up during processing, but still remained at low levels. Alloy 7D had the highest combined impurity contents of all.

Alloys 7A, 7B and 7D were received from the CSIR as manganese-containing alloys, with the intention that adding Mn would restrict grain growth during the homogenisation heat treatment.

Table 4.1. Experimental alloy compostions as measured with the OES.

	Zn	Mg	Cu	Si	Fe	Mn	Al
Alloy				wt%			
7A	6.91	1.82	0.76	-	0.02	0.33	90.18
7B	6.25	1.52	0.67	-	0.01	0.11	91.45
7C	8.38	2.62	1.63	0.13	0.07	-	87.17
7D	6.50	2.14	1.32	-	0.02	0.40	89.63
7E	5.86	2.46	1.63	-	0.05	-	90.00

4.4. SEM observations of as-cast microstructures

Figures 4.5 to 4.9 show the as-cast microstructures of all the alloys produced. Basically, two features were prominent in all the alloys, as indicated by the labels and arrows. The globular features, characteristic of SSM processing in general, were the primary (Al) phase (dilute aluminium solid solution) and were the “matrix”. The bright inter-globular features, between the primary (Al) phase, were the eutectic, containing most of the alloying elements. It was striking that the features between the alloys were so similar.

The eutectic coarseness increased as the level of alloying increased. Alloy 7A (Figures 4.5a and b) and Alloy 7B (Figures 4.6a and b) showed the least coarse eutectics, while Alloy 7C (Figures 4.7a and b) and Alloy 7D (Figures 4.8a and b) showed the coarsest eutectics. The distribution of the eutectic in Alloy 7E (Figures 4.9a and b) was somewhat different from the other alloys, with both fine distributions and very coarse regions of eutectic. The reason could be that the geometry of the plate influenced the segregation flow pattern more during casting. The primary (Al) phase was also more dendritic than the other alloys which could have been the result of slight difference in processing.

The eutectics mainly had a lamellar structure, resolved at the higher magnifications. The lamellar structures were very fine, although sometimes they were not resolved (and appeared grey). Noticeable shrinkage porosity was observed only in Alloy 7C, Figure 4.7b, at high magnification. One eutectic area, as shown in Figure 4.8b, marked by the rectangle, indicated a joint solidification front within the eutectic, where two eutectic colonies impinged.

The almost-white features within all the eutectics were a result of polishing, and were caused by the eutectic structure that smeared easily, giving the comet shapes.

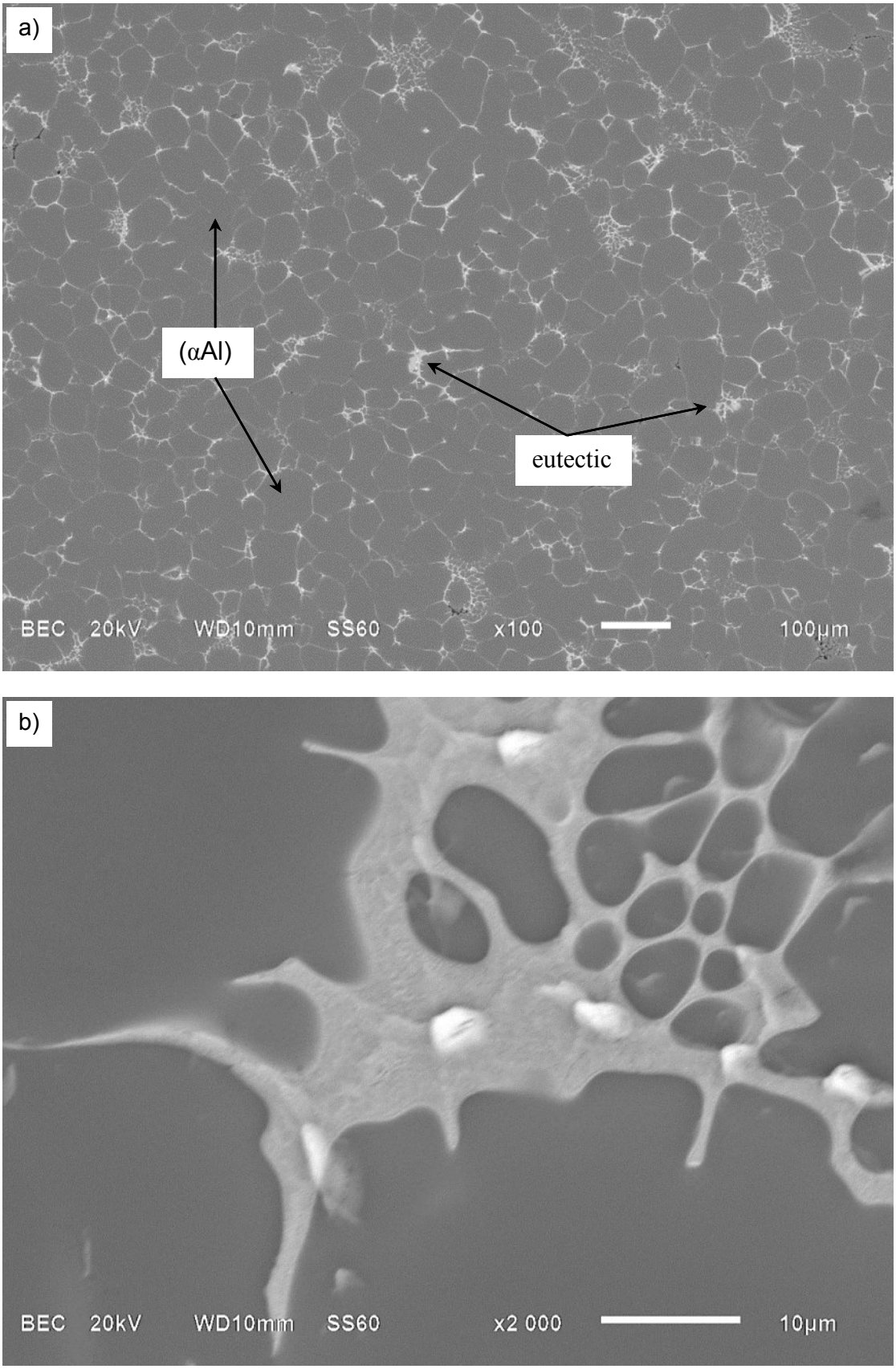


Figure 4.5. SEM-BSE images of the matrix and eutectic in as-cast Alloy 7A: a) low magnification, and b) high magnification.

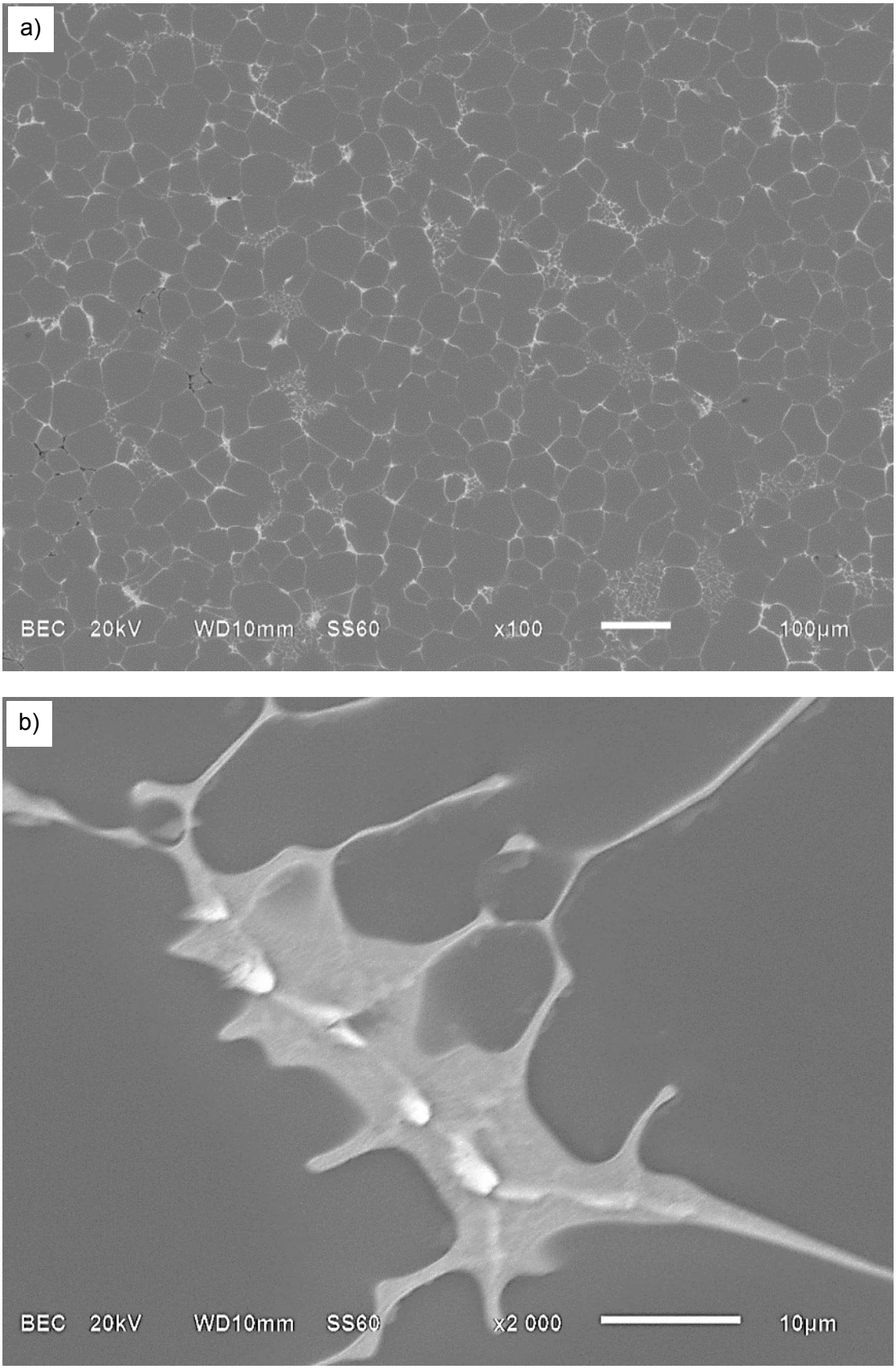


Figure 4.6. SEM-BSE images of the matrix and eutectic in as-cast Alloy 7B: a) low magnification, and b) high magnification.

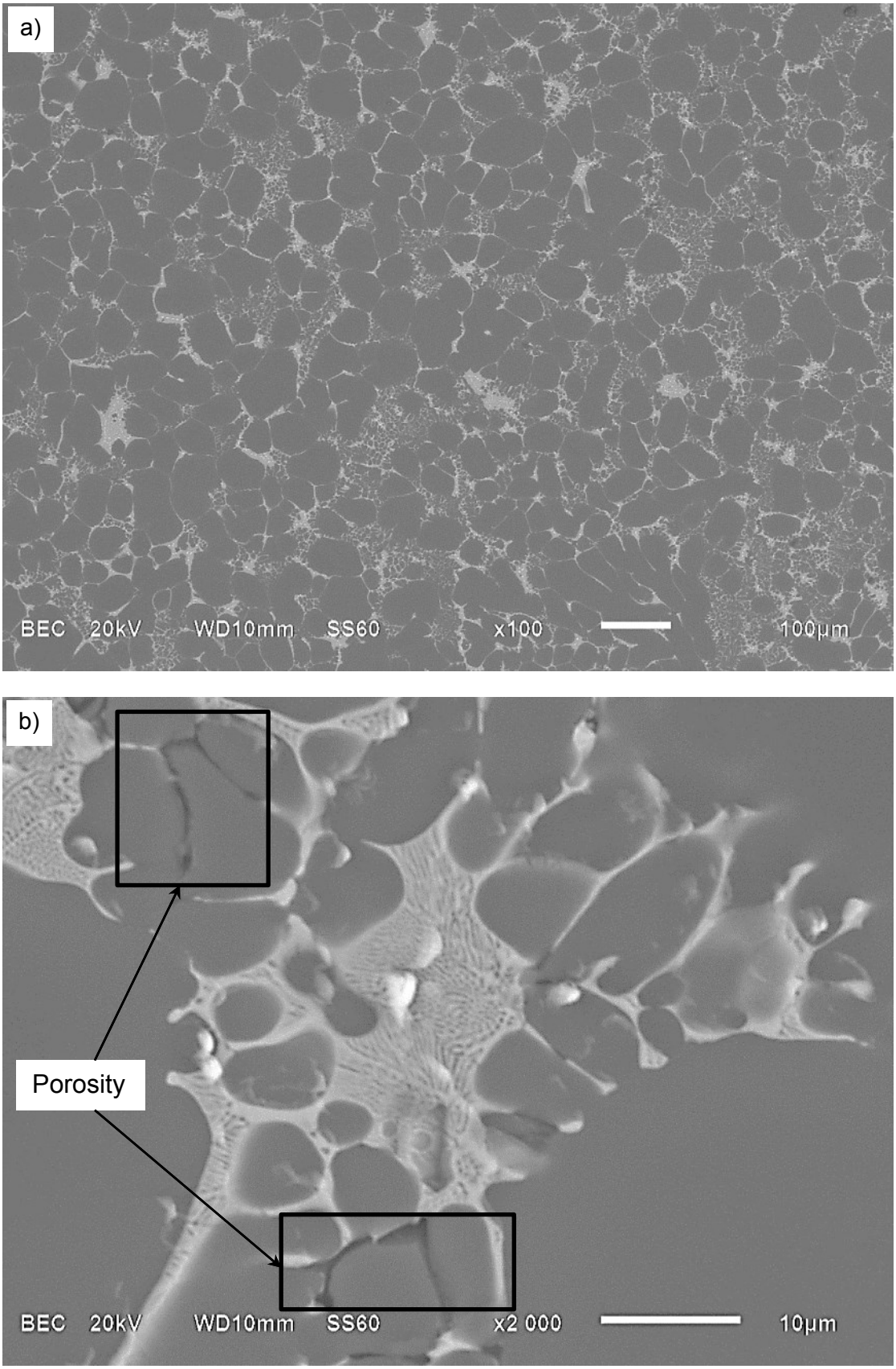


Figure 4.7. SEM-BSE images of the matrix and eutectic in as-cast Alloy 7C: a) low magnification, and b) high magnification, also indicating shrinkage porosity.

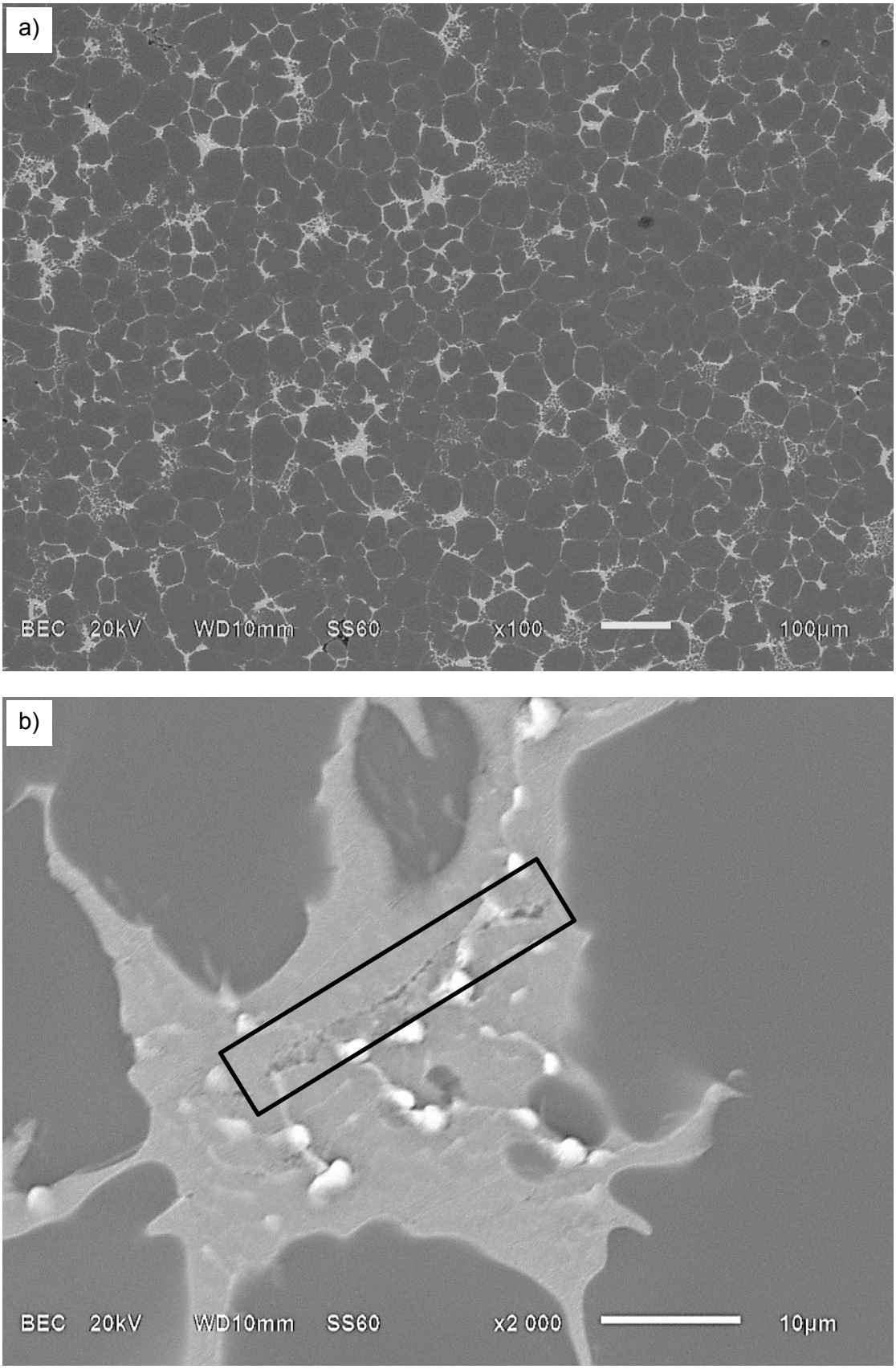


Figure 4.8. SEM-BSE images of the matrix and eutectic in as-cast Alloy 7D: a) low magnification, and b) high magnification, also indicating eutectic colonies impinging.

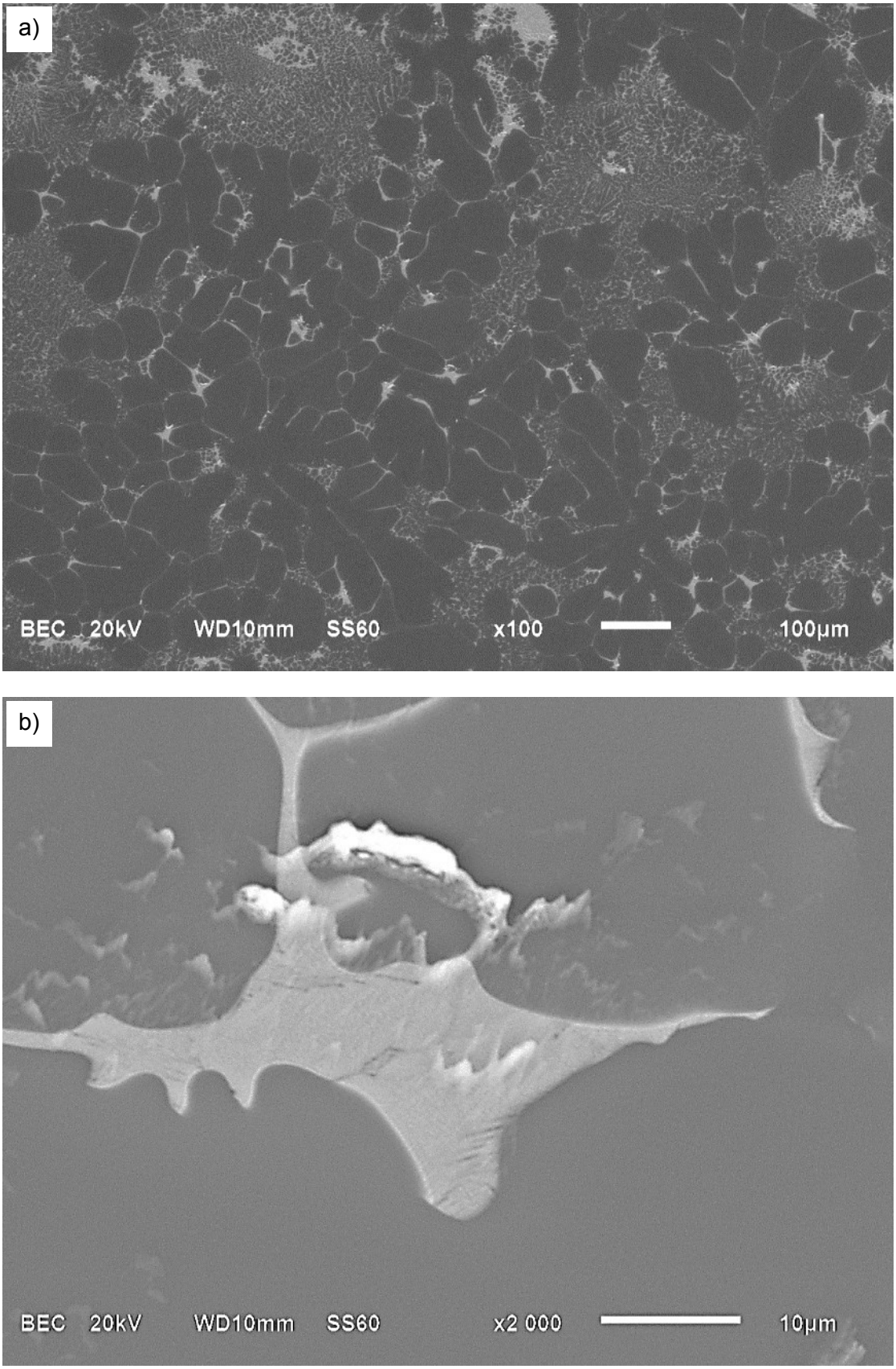


Figure 4.9. SEM-BSE images of the matrix and eutectic in as-cast Alloy 7E: a) low magnification, and b) high magnification.

4.5. EDX analyses of as-cast eutectic structures

Figures 4.10 to 4.14 show the EDX area composition results for the eutectics of each alloy. It was clear that all the alloys consisted of Al, Zn, Mg and Cu. Figure 4.12b shows a small Fe peak which was present due to the level of Fe in the alloy.

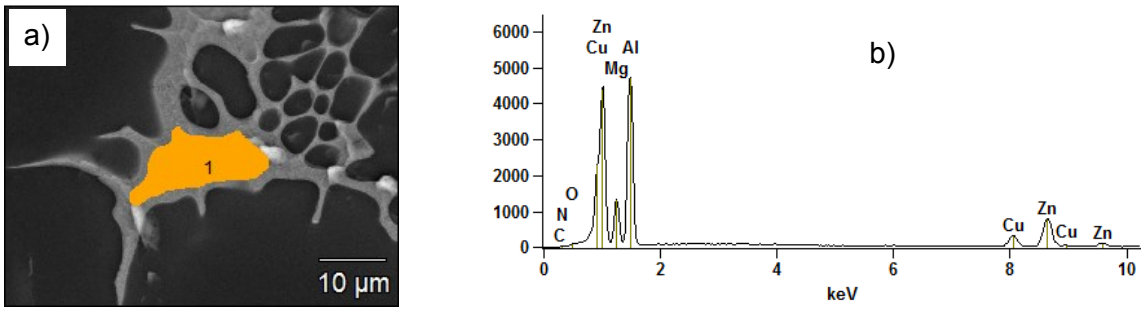


Figure 4.10. EDX results for as-cast Alloy 7A: a) SEM-BSE image, and b) qualitative analysis.

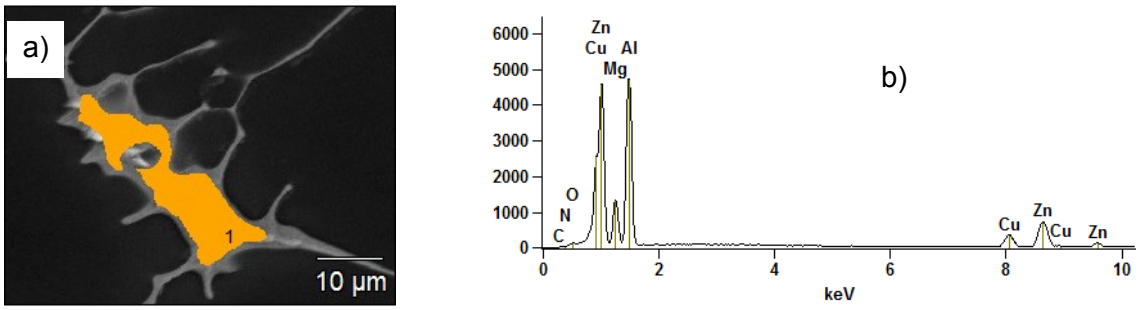


Figure 4.11. EDX results for as-cast Alloy 7B: a) SEM-BSE image, and b) qualitative analysis.

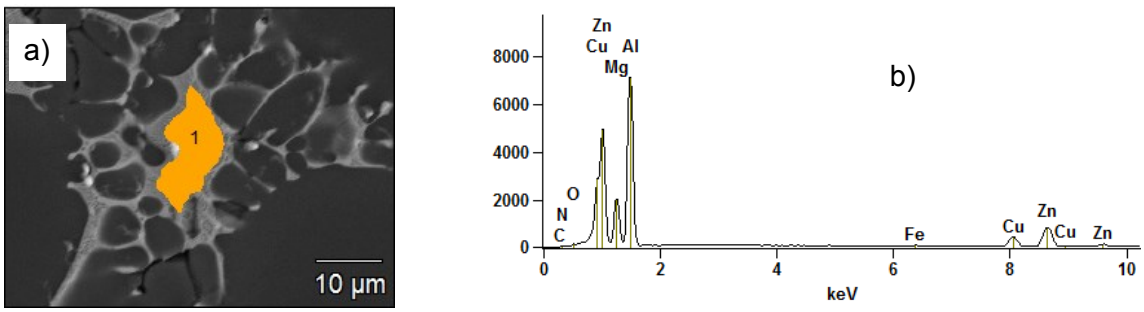


Figure 4.12. EDX results for as-cast Alloy 7C: a) SEM-BSE image, and b) qualitative analysis.

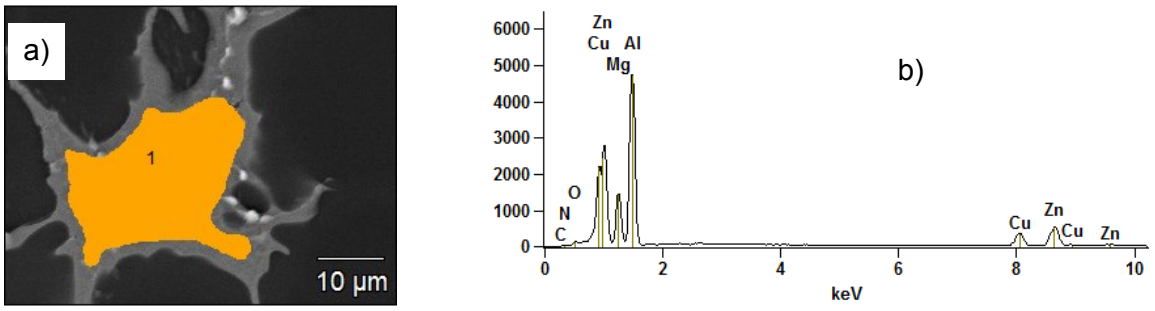


Figure 4.13. EDX results for as-cast Alloy 7D: a) SEM-BSE image, and b) qualitative analysis.

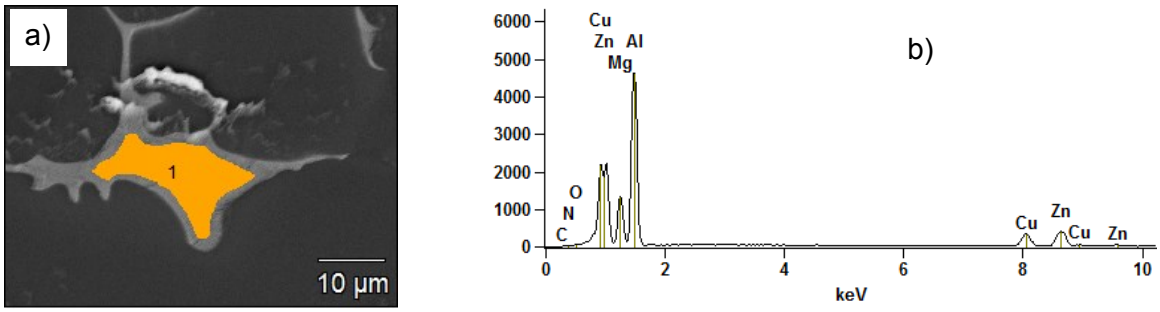


Figure 4.14. EDX results for as-cast Alloy 7E: a) SEM-BSE image, and b) qualitative analysis.

Table 4.2 shows the quantitative analysis for the eutectic of each alloy, as well as the percentage error for the measurement of each element, and indicates that the eutectic consisted of Al, Zn, Mg and Cu. Impurity elements, i.e. Fe and Si, were also found within the eutectic areas of the alloys that contained these elements in the overall composition. Manganese was an alloying element but it was not found in the eutectic area analyses of the Mn-containing alloys. The reason could be that it solidified within the matrix phase during processing.

Inclusion of N and O in the analysis made the contributions of each alloying element more accurate. Otherwise the contributions of N and O in the analysis were added to the selected elements that were analysed.

Table 4.2. EDX results of the overall compositions of the eutectics in the different alloys.

	N K	O K	Mg K	Al K	Cu K	Zn K	Fe K	Si K	Mn K
Alloy					at.%				
7A	3.4 ± 0.6	1.5 ± 0.2	14.0 ± 0.5	51.1 ± 0.3	7.1 ± 0.3	23.0 ± 0.4	-	-	-
7B	4.5 ± 0.6	2.6 ± 0.3	14.6 ± 0.5	49.6 ± 0.4	7.6 ± 0.3	21.2 ± 0.4	-	-	-
7C	3.1 ± 0.4	2.2 ± 0.2	16.0 ± 0.4	53.6 ± 0.3	6.5 ± 0.2	18.3 ± 0.3	0.3 ± 0.0	0.1 ± 0.1	-
7D	2.9 ± 0.6	2.4 ± 0.4	16.4 ± 0.5	53.7 ± 0.4	8.4 ± 0.3	16.2 ± 0.4	-	-	-
7E	3.6 ± 0.7	1.8 ± 0.3	16.1 ± 0.5	55.3 ± 0.4	8.4 ± 0.3	14.9 ± 0.4	0.3 ± 0.1	-	-

Element & Line at 20kV

The average compositions of the eutectic in each alloy were corrected using the results in Table 4.2 by removing the N and O contributions. The Al, Zn, Mg and Cu content of the eutectic was found by calculating the fraction of each element by Equation 4.1.

$$\frac{at.\%_i}{\sum_i at.\%_i} \times 100 \qquad 4.1$$

where i is Al, Zn, Mg and Cu.

Table 4.3 shows the eutectic compositions after this correction. The Cu content, of all the elements, was the lowest for each alloy. The amount of Zn decreased from the top of Table 4.3 to the bottom, to where the Zn content was even lower than that of Mg. It is clearly seen that Al was just over half of the eutectic composition. This agrees with the microstructures of the eutectics, that one of the two phases in the eutectic was Al-based, while the other contained the rest of the alloying elements.

Table 4.3. Corrected overall compositions of the eutectics of different R-HPDC processed alloys.

	Al	Zn	Mg	Cu
Alloy	at.%			
7A	53.7	24.1	14.7	7.4
7B	53.4	22.8	15.7	8.2
7C	56.8	19.4	16.9	6.9
7D	56.7	17.1	17.3	8.9
7E	58.5	15.7	17.0	8.8

4.6. Vacuum cooling

The reduced pressure test of Alloy 7D was taken as an example of the vacuum cooled alloy (Alloy 7D-V). Figure 4.15 clearly shows that the eutectic had the same appearance as the other eutectics, with the same lamellar features. The whitish features appear to be from smearing during polishing. The EDX area analysis is shown in Figure 4.16, indicating the presence of Al, Zn, Mg and Cu.

Table 4.4 shows the composition of the eutectic of the vacuum cooled sample of Alloy 7D. Comparing Alloys 7D and 7D-V, it can be seen that the eutectics had

essentially the same composition, which was anticipated since it was the same alloy, albeit processed differently.

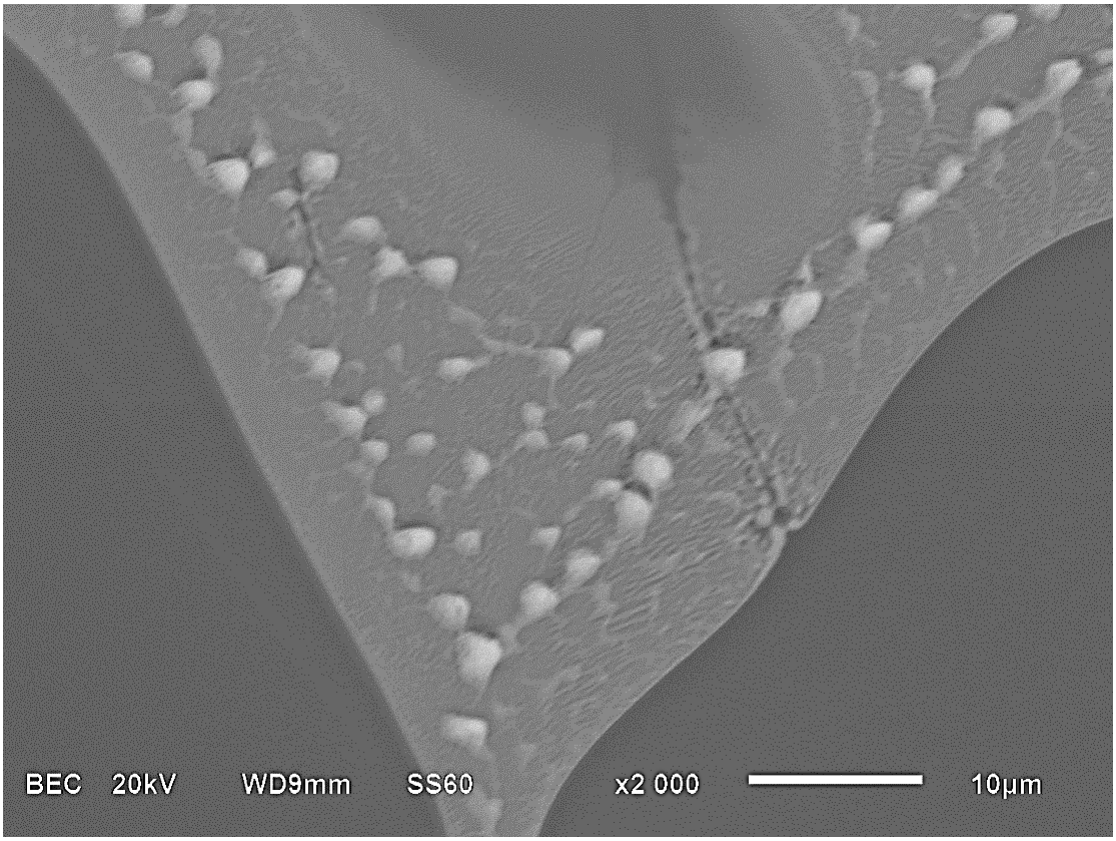


Figure 4.15. SEM-BSE image of Alloy 7D-V showing the eutectic at high magnification.

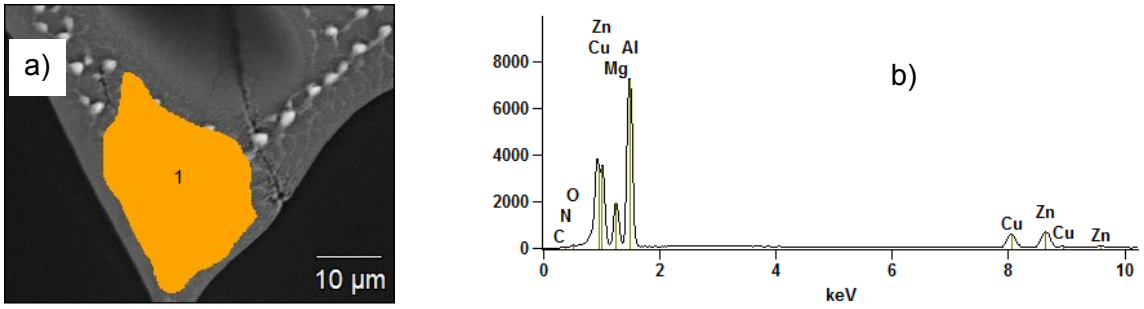


Figure 4.16. EDX results for the eutectic of Alloy 7D-V: a) SEM-BSE image, and b) qualitative analysis.

Table 4.4. Corrected eutectic composition of the vacuum cooled alloy.

	Al	Zn	Mg	Cu
Alloy	at.%			
7D-V	57.4	15.9	16.0	10.6
7D	56.7	17.1	17.3	8.9

4.7. Eutectic alloys

Two eutectic alloys (Alloys E-A and E-B) were produced with compositions according to the measured EDX results of the overall eutectic compositions in Alloy 7A and Alloy 7D, respectively. These alloys were produced by induction heating of the pure metals and subsequent cooling in air.

4.7.1. Eutectic alloy A

Figure 4.17 shows the eutectic microstructure of Alloy E-A. It clearly had a lamellar structure with two alternating phases. A eutectic colony boundary is visible on the left side of Figure 4.17, indicated by the rectangle.

Figure 4.18 shows the analysed region and the qualitative EDX results which showed that the dark grey phase was Al-rich, while the light grey phase comprised Al-Zn-Mg-Cu.

Figure 4.19 is a black and white image and was a binary colour threshold adjustment to calculate the area fraction of the light and dark grey phases in the microstructure.

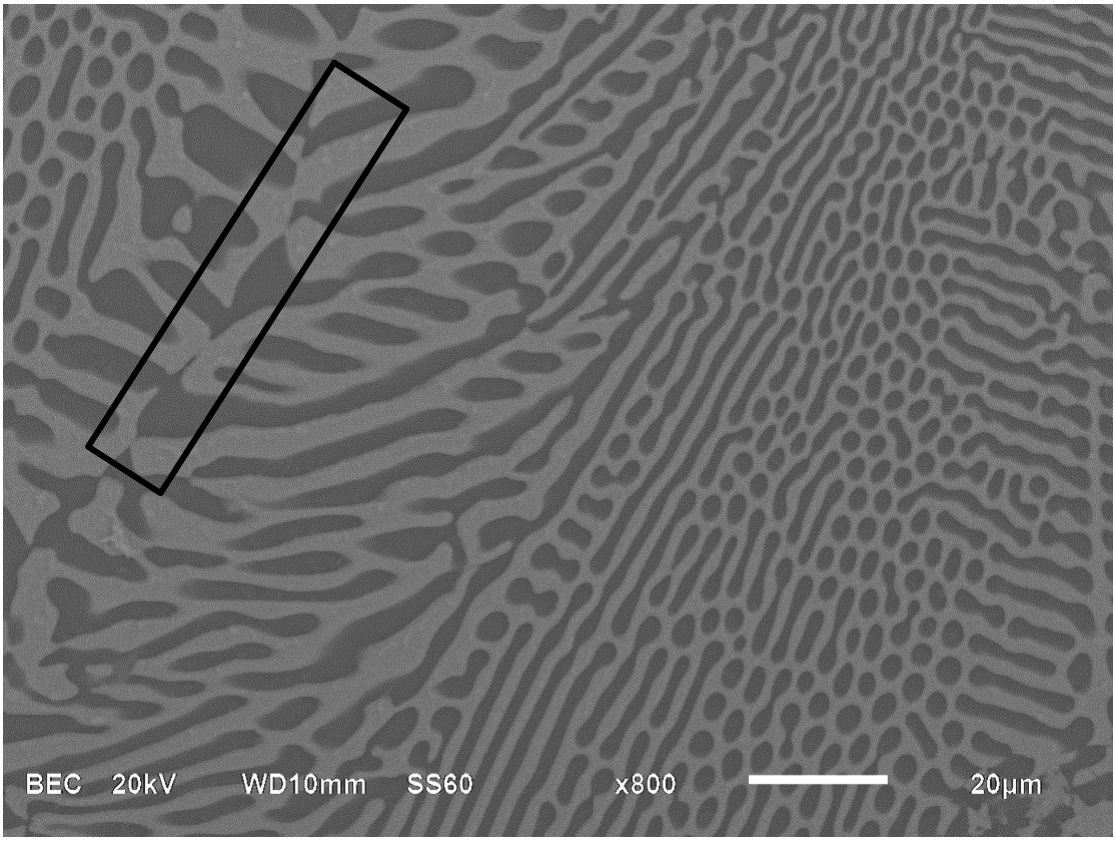


Figure 4.17. SEM-BSE image of the Al-rich (dark grey) and Al-Zn-Mg-Cu containing (light grey) eutectic microstructure of Alloy E-A. The rectangle indicates a colony boundry.

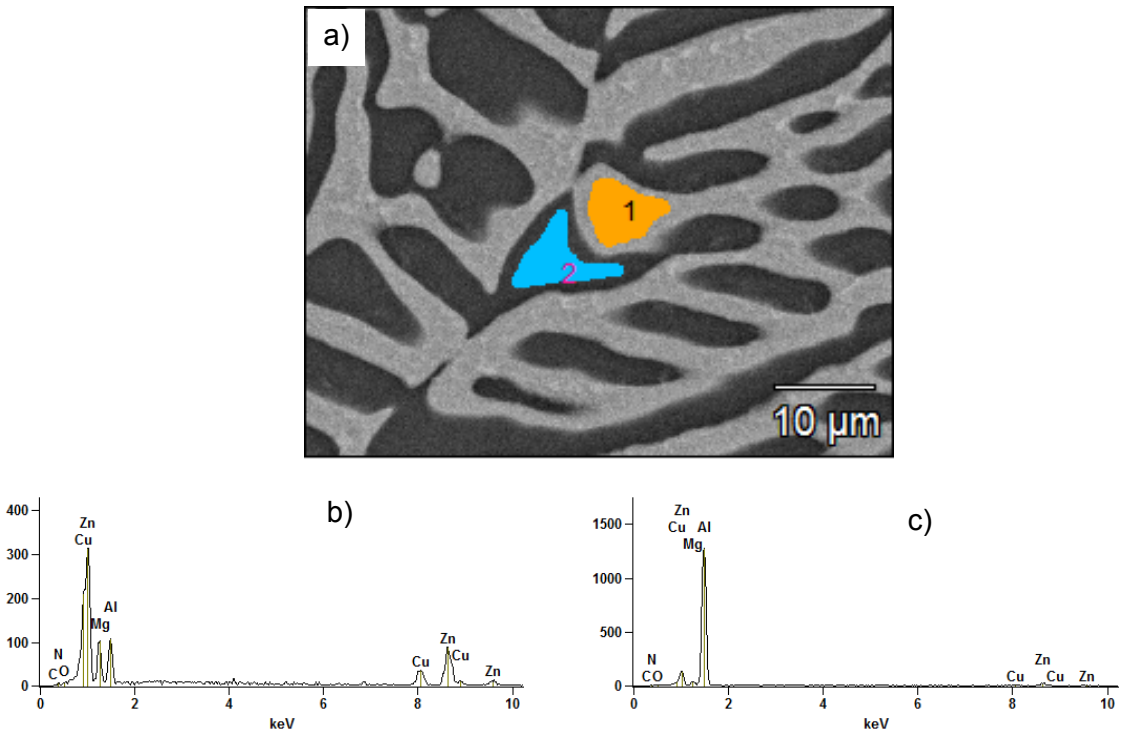


Figure 4.18. EDX results for eutectic Alloy E-A: a) SEM-BSE image, b) qualitative analysis of the Al-Zn-Mg-Cu containing phase (Point 1), and c) of the Al-rich phase (Point 2).

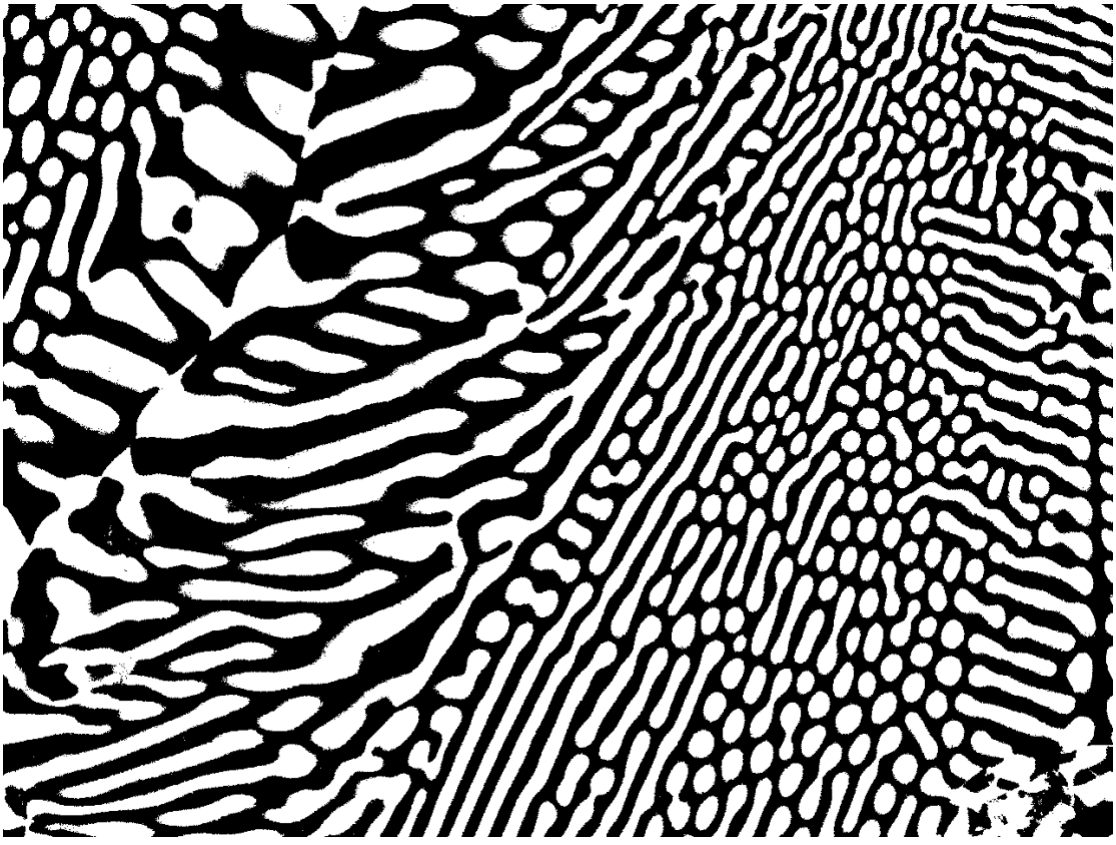


Figure 4.19. Binary threshold colour image of Alloy E-A.

Table 4.5 shows the corrected quantitative EDX phase compositions measured for two different lamellae in Alloy E-A (errors assumed the same as indicated in Table 4.2). The measured area of each phase is also indicated as a fraction. The molar composition balance of Alloy E-A was the same as the intended composition of the eutectic in Alloy 7A (Table 4.3).

Table 4.5. Corrected EDX compositions of the Al-rich and Al-Zn-Mg-Cu phases in eutectic Alloy E-A.

	Al	Zn	Mg	Cu	
	at.%				Area fraction
Al-Zn-Mg-Cu lamella	22.8	38.5	25.9	12.8	0.53
Al-rich lamella	89.2	7.7	2.2	0.9	0.47
Composition of Alloy E-A by molar balance	54.1	24.0	14.7	7.2	1.00
Overall eutectic composition of Alloy 7A	53.8	24.1	14.7	7.4	

4.7.2. Eutectic alloy B

Figure 4.20 shows the lamellar microstructure of Alloy E-B, the eutectic alloy of the eutectic of dilute Alloy 7D. Figure 4.21 shows the qualitative EDX analyses of the two phases found in the eutectic. The dark grey phase was Al-rich, while the light grey phase was composed of Al-Zn-Mg-Cu. The wavy appearance of the Al-Zn-Mg-Cu phase in Figure 4.21a was a polishing artefact and not another phase. Figure 4.22 shows the binary black and white threshold image of the area fractions of the two eutectic phases.

Table 4.6 shows the molar composition balance for Alloy E-B as calculated from the area fraction analysis of the two phases in combination with the EDX analyses of the two phases. It is clear from Table 4.6 that the calculated composition was very close, with marginal differences, to the targeted eutectic composition of Alloy 7D (Table 4.3).

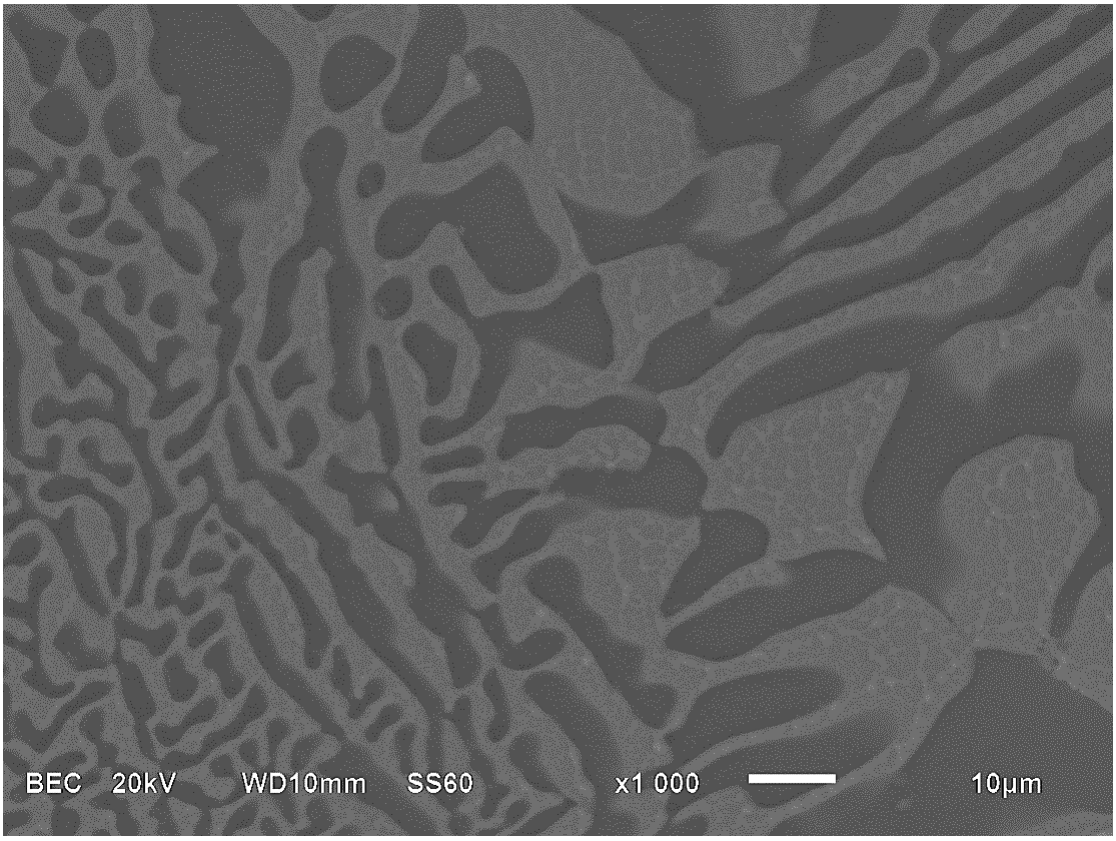


Figure 4.20. SEM-BSE image of the Al-rich (dark grey) and Al-Zn-Mg-Cu containing (light grey) eutectic microstructure of Alloy E-B.

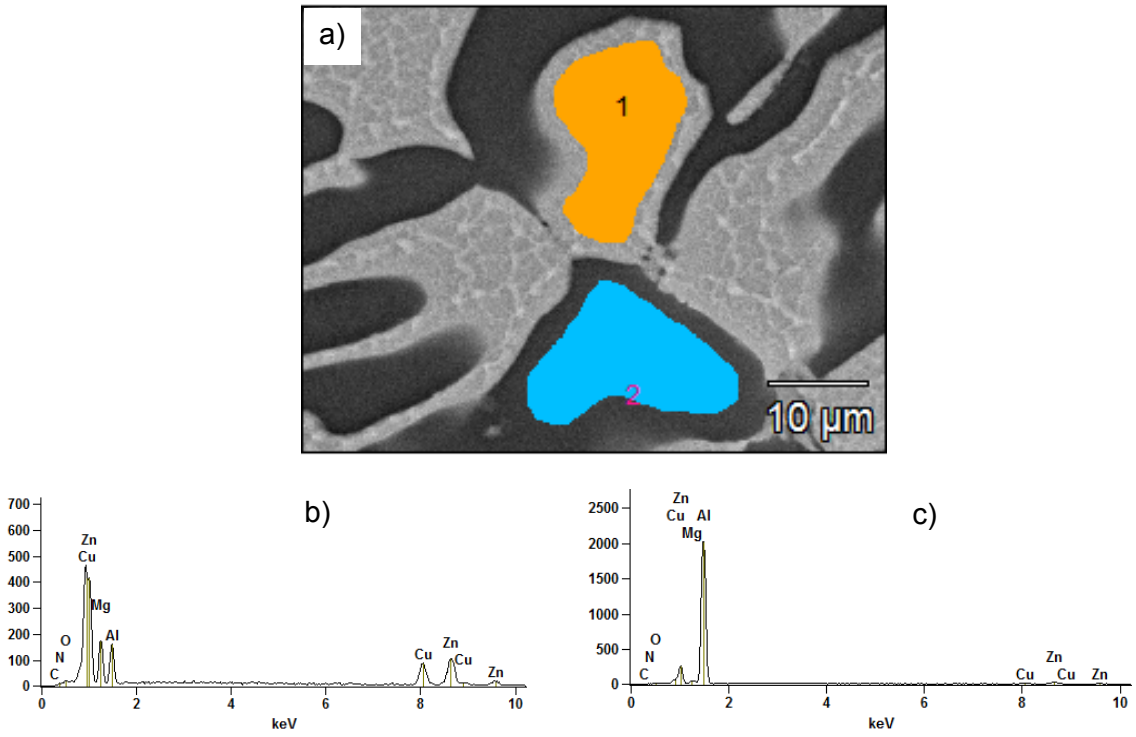


Figure 4.21. EDX results for eutectic Alloy E-B: a) SEM-BSE image, qualitative analysis of b) Al-Zn-Mg-Cu containing phase (Area 1), and c) the Al-rich phase (Area 2).

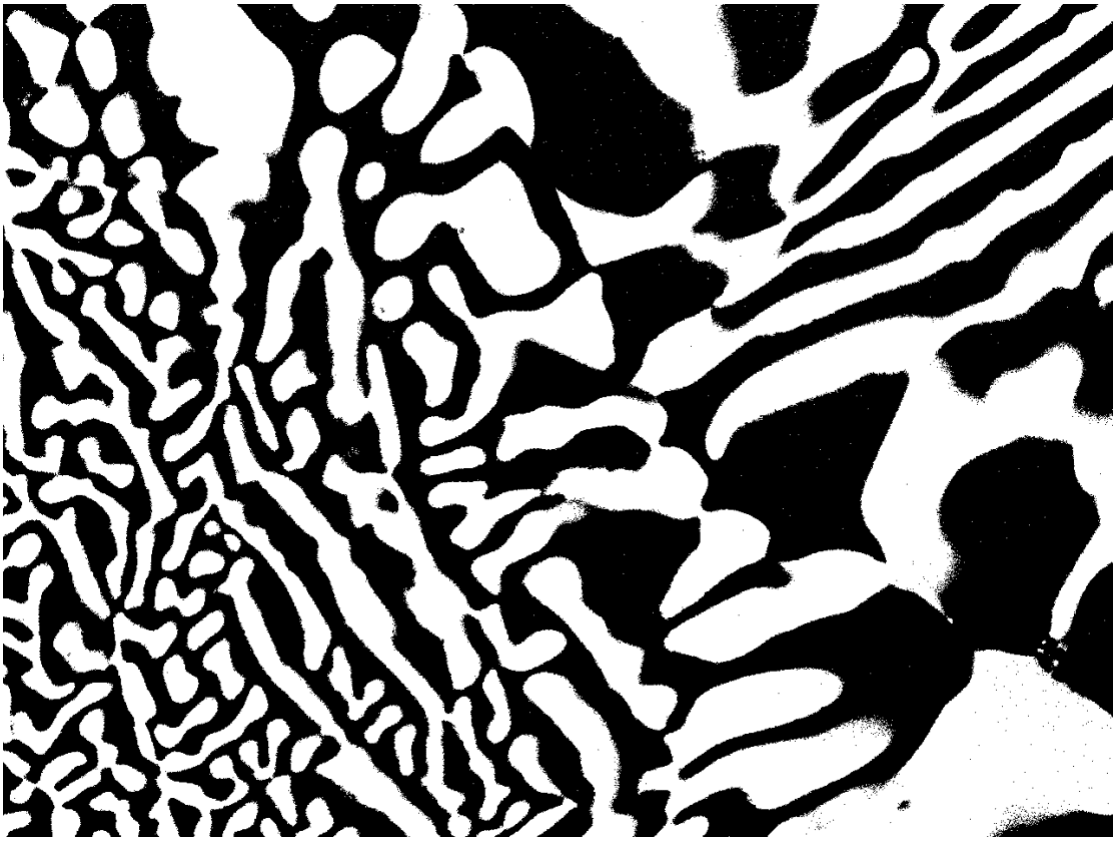


Figure 4.22. Binary threshold colour image of Alloy E-B.

Table 4.6. Adjusted EDX compositions of the Al-rich and Al-Zn-Mg-Cu phases in eutectic Alloy E-B.

	Al	Zn	Mg	Cu	
	at.%				Area fraction
Al-Zn-Mg-Cu lamella	23.4	29.9	28.5	18.2	0.487
Al-rich lamella	87.7	6.7	2.8	2.8	0.513
Composition of Alloy E-B by molar balance	56.4	18.0	15.3	10.3	1.000
Overall eutectic composition of Alloy 7D	56.7	17.1	17.3	8.9	

4.7.3. Eutectic alloy C

A third eutectic alloy (Alloy E-C) was produced, with an Al:Zn:Mg:Cu composition ratio of 5:1:1:1, in the same manner as Alloys E-A and E-B. The intention with this alloy was to compare the Al-Zn-Mg-Cu phase in the eutectic with the composition measured for the same phase of the eutectic in Alloy H (Section 2.3).

Figure 4.23 shows the microstructure of Alloy E-C. There were three phases visible in the microstructure, a lamellar eutectic consisting a light grey and a dark grey phase and a phase with a mid-grey contrast. Figure 4.24 shows the qualitative EDX analyses of the phases found in the rectangle in indicated in Figure 4.23. The dark grey phase was Al-rich, the light grey phase contained Al-Zn-Mg-Cu and the mid grey phase contained Al-Cu together with a very minor amount of Mg.

There was a fine eutectic structure as well as a coarse eutectic structure. The coarse parts in the microstructure were interpreted as a ternary eutectic. The Al-Cu phase seemed to be divorced from the other two phases in the structure.

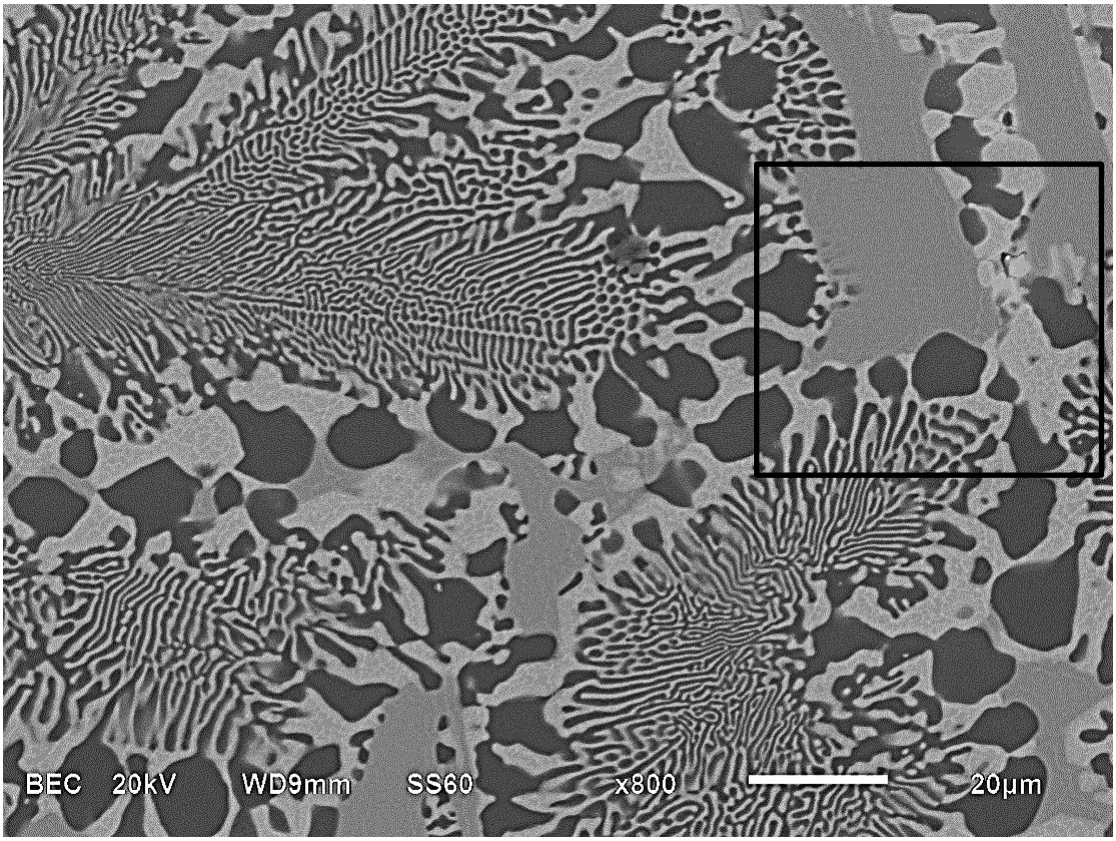


Figure 4.23. SEM-BSE image of the Al-rich (dark grey) and Al-Zn-Mg-Cu containing (light grey) eutectic microstructure and the Al-Cu phase (mid grey) of Alloy E-C.

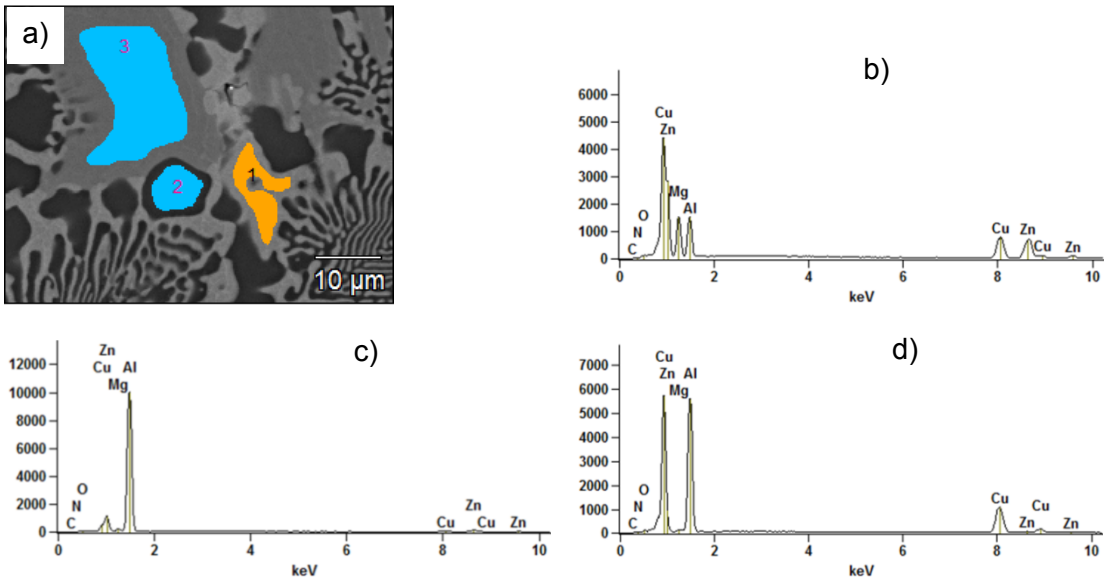


Figure 4.24. EDX results for eutectic Alloy E-C: a) SEM-BSE image, qualitative analysis of b) light grey Al-Zn-Mg-Cu containing phase (Area 1), c) dark grey Al-rich phase (Area 2), and d) medium grey Al-Cu containing phase (Area 3).

4.8. Thermo-Calc predictions for as-cast alloys

Thermo-Calc software with the most recent aluminium database (TTAL8) was a commercial thermodynamic package with which it was possible to calculate thermodynamic properties of the R-HPDC aluminium alloys.

4.8.1. Equilibrium phase predictions

Thermo-Calc was used to calculate the equilibrium phases in the alloys. Figures 4.25 and 4.29 show the phases that would be present in Alloys 7A and 7B upon cooling were the (Al) solid solution, $MgZn_2$ and the T(Al,Cu,Mg,Zn) phase. Figures 4.27 to 4.29 show the S phase (Al_2CuMg) present in Alloys 7 C to 7E, besides the same phases in Alloy 7A and 7B. The S phase could be expected in the alloys with a high Cu content. The $MgZn_2$ phase appears around 400 °C in all the alloys. Table 4.7 shows the onset and end of solidification of the different alloys.

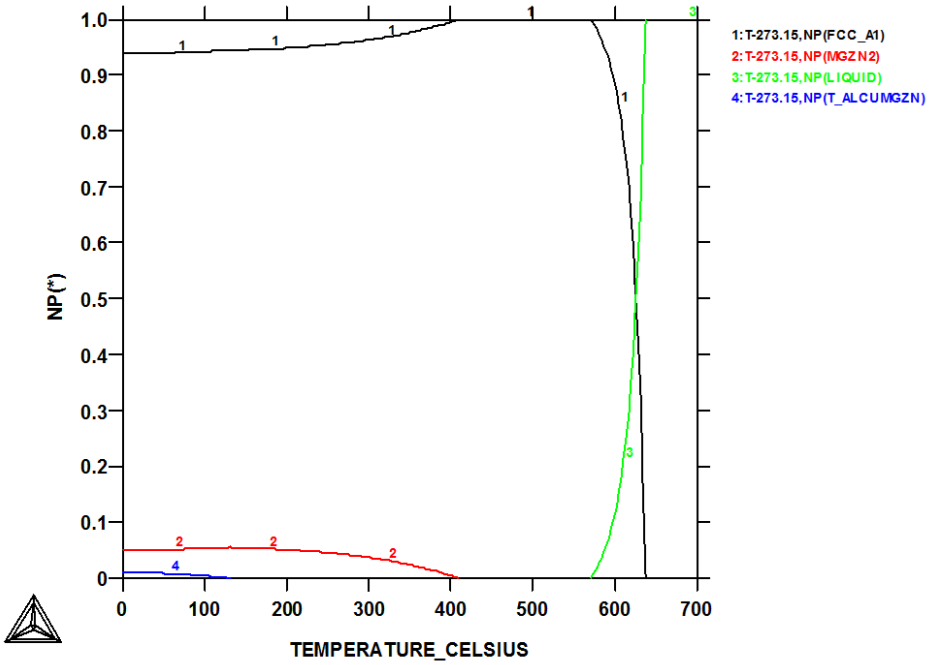


Figure 4.25. Thermo-Calc equilibrium phase proportion-temperature plot for Alloy 7A.

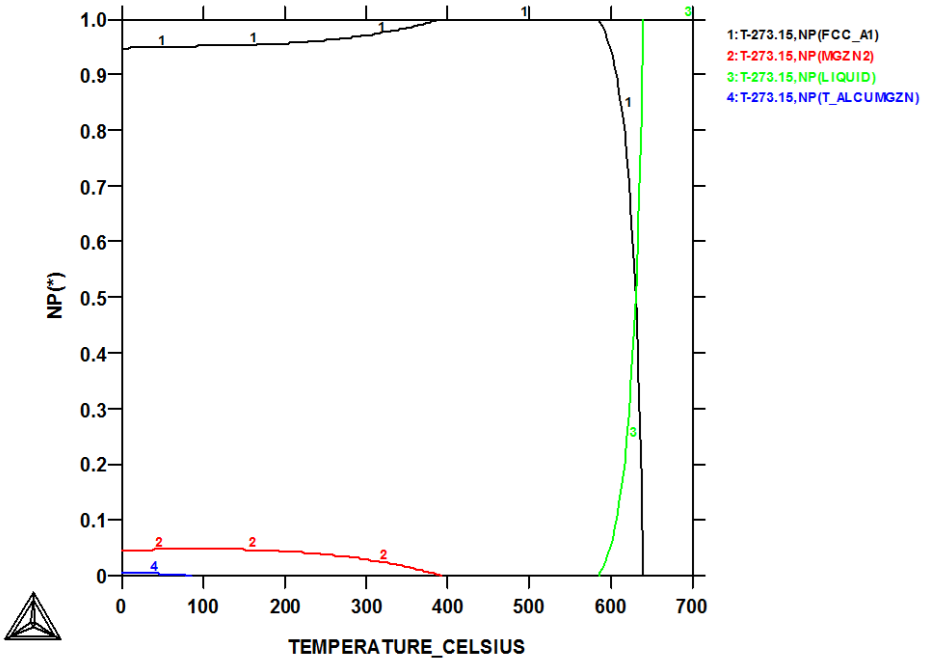


Figure 4.26. Thermo-Calc equilibrium phase proportion-temperature plot for Alloy 7B.

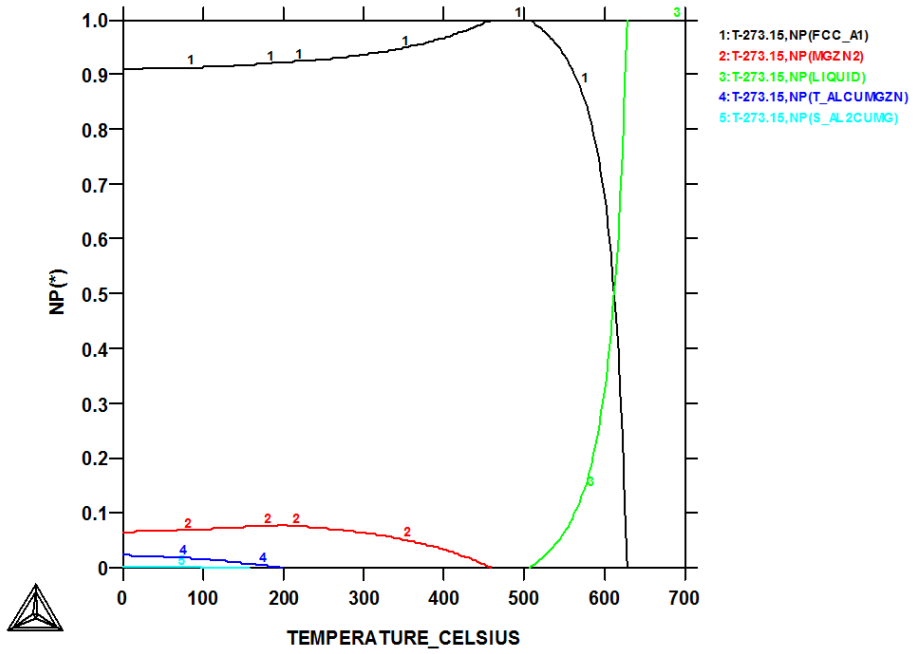


Figure 4.27. Thermo-Calc equilibrium phase proportion-temperature plot for Alloy 7C.

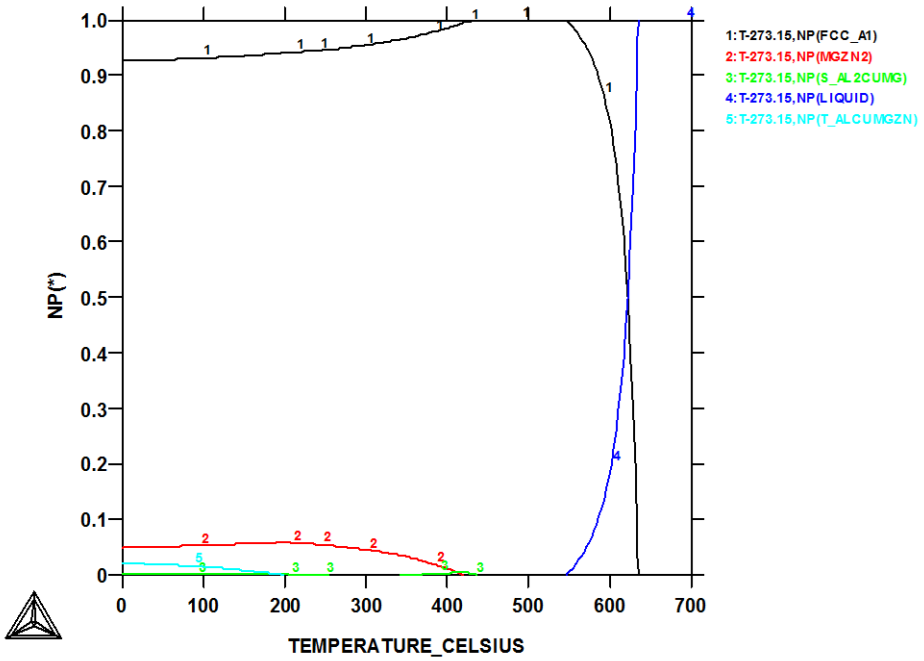


Figure 4.28. Thermo-Calc equilibrium phase proportion-temperature plot for Alloy 7D.

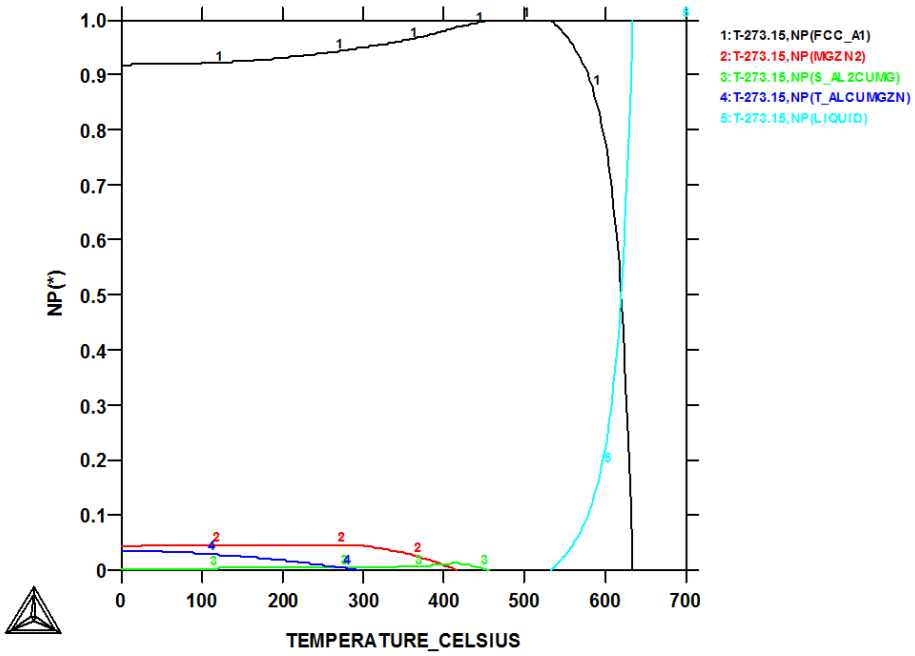


Figure 4.29. Thermo-Calc equilibrium phase proportion-temperature plot for Alloy 7E.

Table 4.7. Equilibrium solidification onset and end temperatures of Alloys 7A to 7E.

	Solidification	
	End	Onset
Alloy	°C	
7A	570	637
7B	585	636
7C	508	633
7D	545	633
7E	533	633

4.8.2. Non-equilibrium phase predictions

The temperature range between 450 °C and 500 °C, where the start of melting occurs, or in other words, the final solidification temperature, was of major interest for this study. The reason was that melting of the alloys had to be prevented during homogenisation.

Confidence in the Scheil calculations with this package and database was very high, due to the success stated by Thermo-Calc Software by validation of the calculated non-equilibrium properties with experimental data [45].

Figures 4.30 to 4.34 show the same calculated solidification temperatures and phases for the different alloys. The $MgZn_2$ and T(Al,Cu,Mg,Zn) phases appeared in all the calculations at the end of solidification. All alloys had relatively flat slopes near the onset of solidification, but very steep slopes near the end of solidification. The broken line in each case indicates equilibrium solidification.

It is interesting that the T(Al,Cu,Mg,Zn) phase appears before the $MgZn_2$ phase in Alloy 7A compared to the other alloys. The reason for this result was unclear but was experimentally verified later in Section 4.8.

Table 4.8 shows the non-equilibrium fraction that solidified last depended on the extent of alloying, i.e. higher alloying resulted in larger non-equilibrium phase fractions. Alloy 7B had the smallest fraction, while Alloy 7C had the largest. The amounts of eutectic calculated with Thermo-Calc are also shown in Table 4.8.

The final solidification temperatures of all the alloys were calculated to be the same at 476 °C. The solidification onset temperatures again varied according to the extent of alloying: increasing alloying resulted in decreasing of the solidification onset temperature.

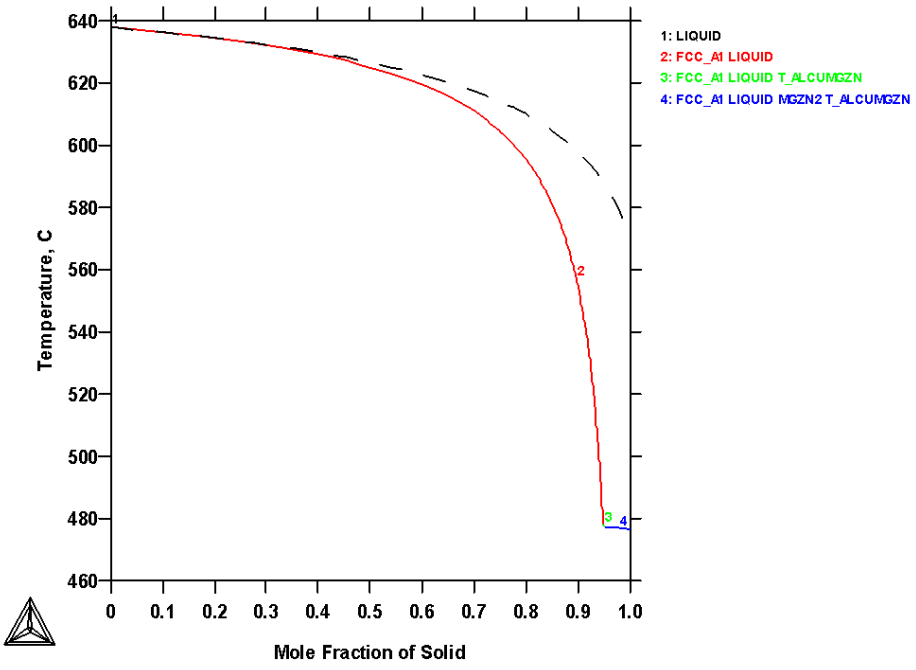


Figure 4.30. Thermo-Calc Scheil solidification calculation for Alloy 7A.

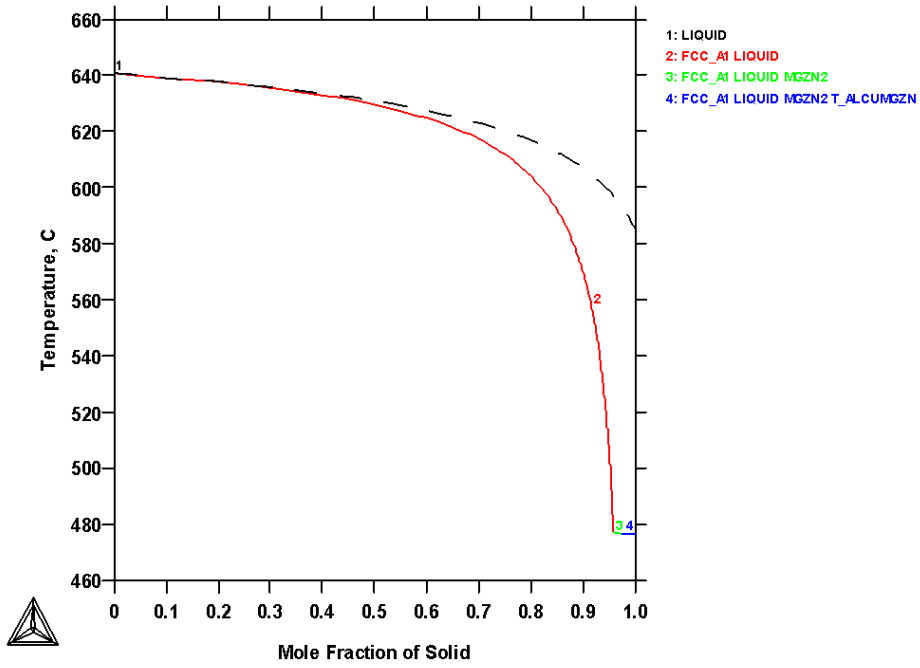


Figure 4.31. Thermo-Calc Scheil solidification calculation for Alloy 7B.

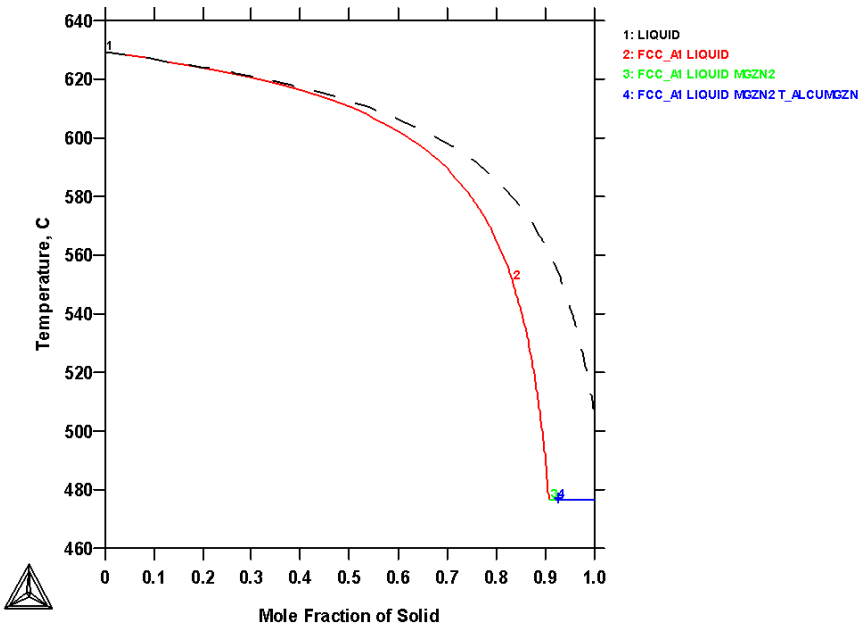


Figure 4.32. Thermo-Calc Scheil solidification calculation for Alloy 7C.

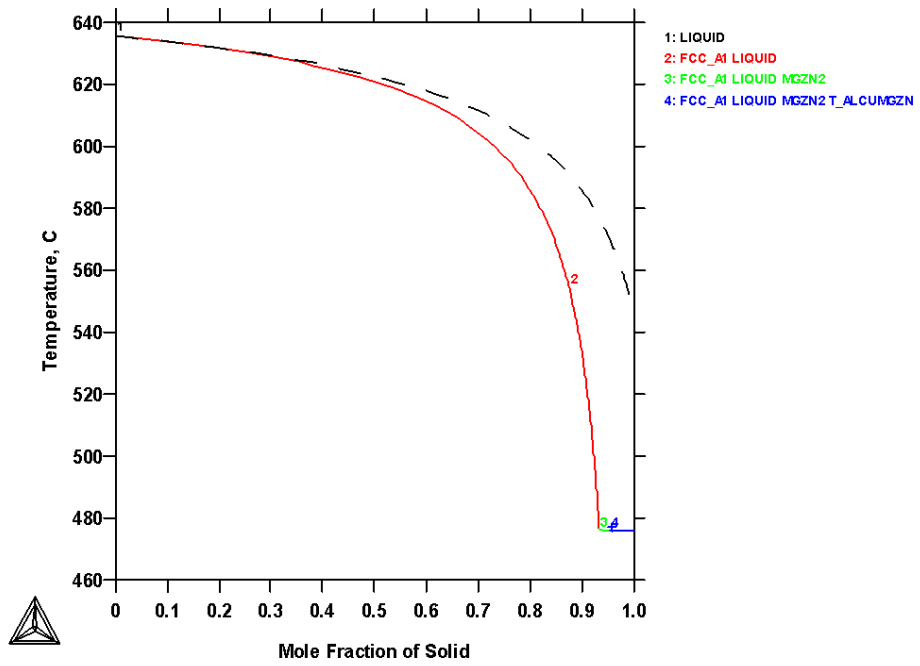


Figure 4.33. Thermo-Calc Scheil solidification calculation for Alloy 7D.

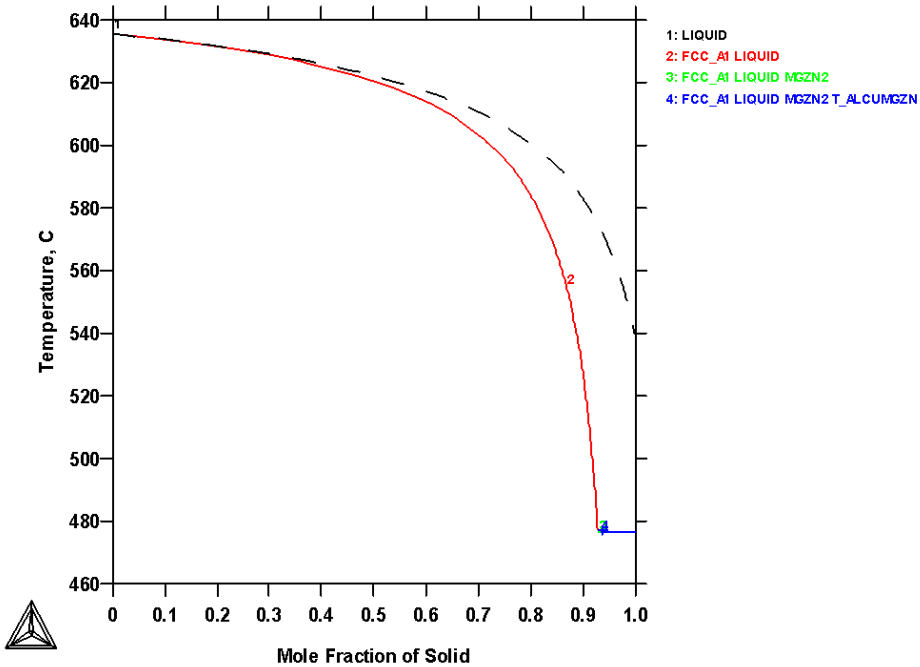


Figure 4.34. Thermo-Calc Scheil solidification calculation for Alloy 7E.

Table 4.8. Summary of Thermo-Calc solidification onset and end temperatures, eutectic percentages and the sum of major alloying elements.

	End	Onset	Eutectic	Zn + Mg + Cu
Alloy	°C		%	at.%
7A	476	639	4.90	5.42
7B	476	640	4.40	4.73
7C	476	629	9.20	7.48
7D	476	636	7.20	5.87
7E	476	637	7.20	6.09

4.9. DSC of as-cast alloys

The main reason for the DSC measurements of the as-cast alloys was to determine the melting temperatures. These measurements were necessary to choose temperatures for homogenisation that would prevent the material from melting during homogenisation, but that would enhance the dissolution of the solidified alloying elements.

The presentation of the DSC measurement curves here is to show the starts and ends of melting. Figures 4.44 to 4.48 show the results of the DSC heating experiments of the as-cast condition alloys. The general features of the curves shown were the eutectic melting peak at temperatures below 500 °C and the melting peak of the primary (Al) phase at higher temperatures. The DSC curves over the full melting range show the relative height of the eutectic reaction peaks to the total alloy.

The non-equilibrium Thermo-Calc results indicate that there should be no other reactions besides the two major peaks. However, there seems to be slight peaks between the eutectic melting peak and the primary phase peak, especially Alloy 7C. These peaks could be reactions involving the impurity or minor alloying elements.

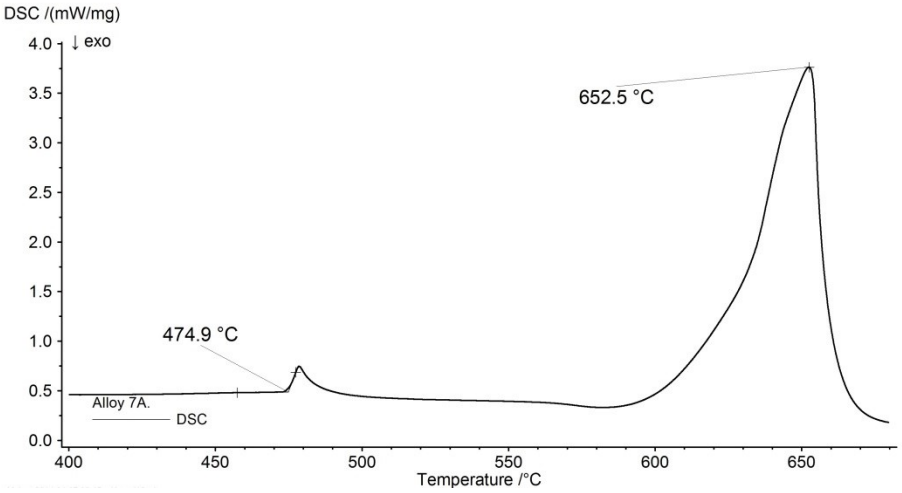


Figure 4.35. DSC heating curve of Alloy 7A.

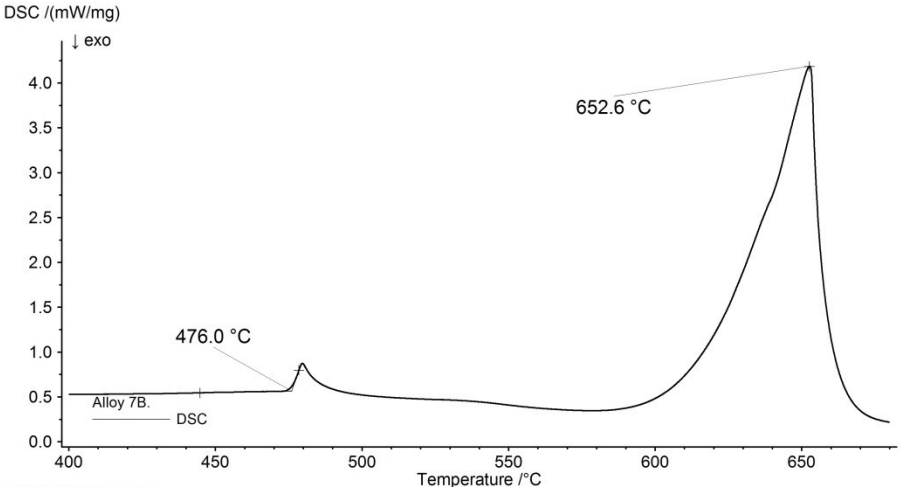


Figure 4.36. DSC heating curve of Alloy 7B.

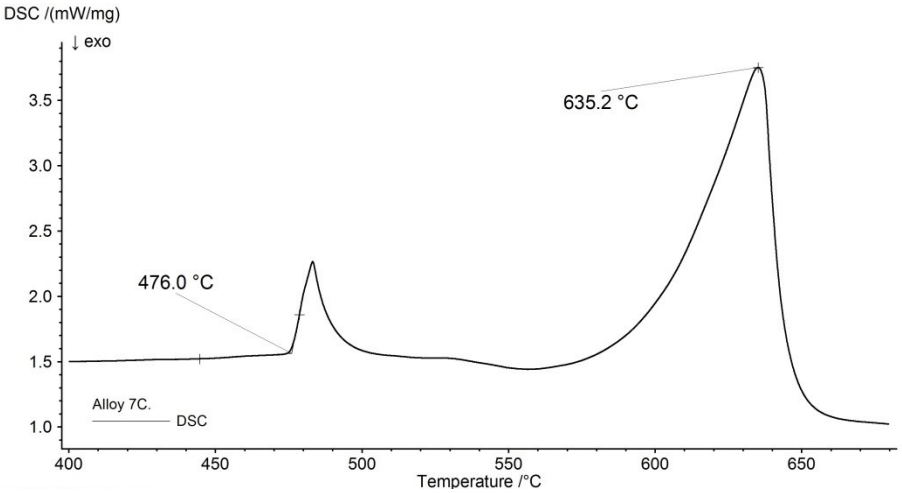


Figure 4.37. DSC heating curve of Alloy 7C.

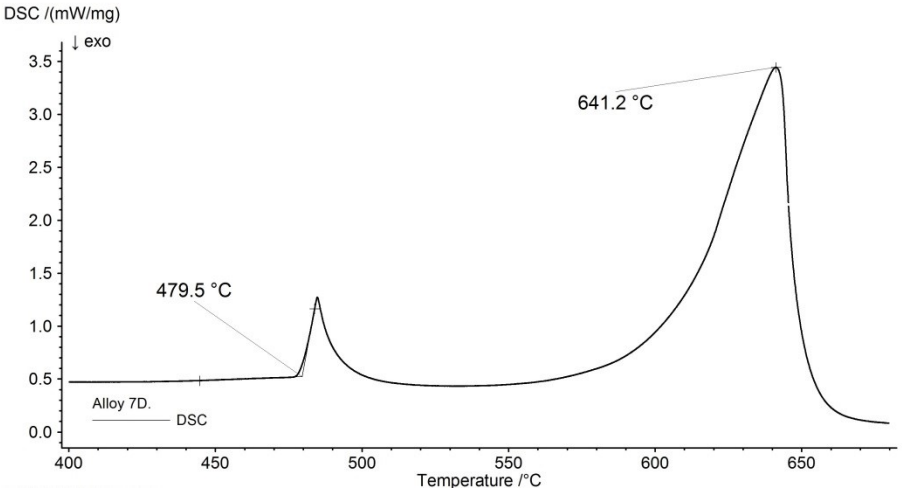


Figure 4.38. DSC heating curve of Alloy 7D.

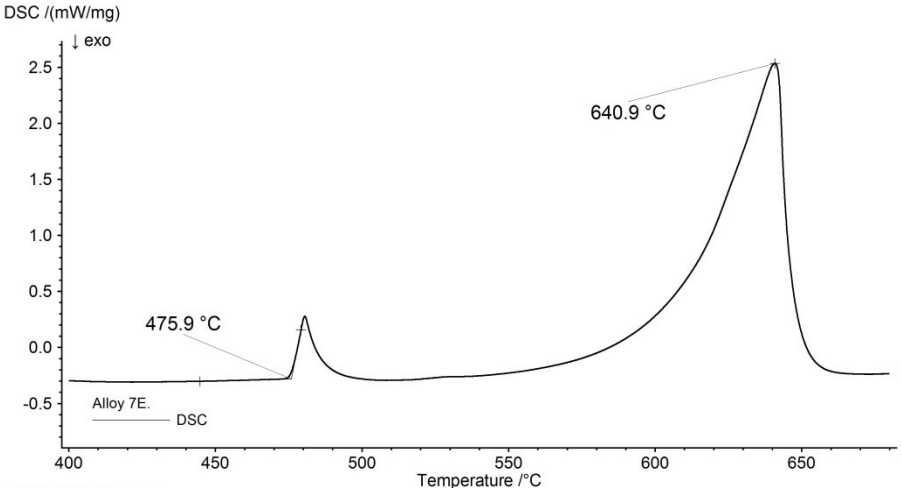


Figure 4.39. DSC heating curve of Alloy 7E.

Figure 4.49 shows the DSC curve of Alloy 7D-V. It would be expected that the features of the curve would be the same as that of Alloy 7D, but it is not the case. The onset of melting for Alloy 7D-V is at 475.9 °C, while that for Alloy 7D is higher at 479.5 °C. It clearly indicates that the difference in solidification rate of the alloy affects the thermal behaviour.

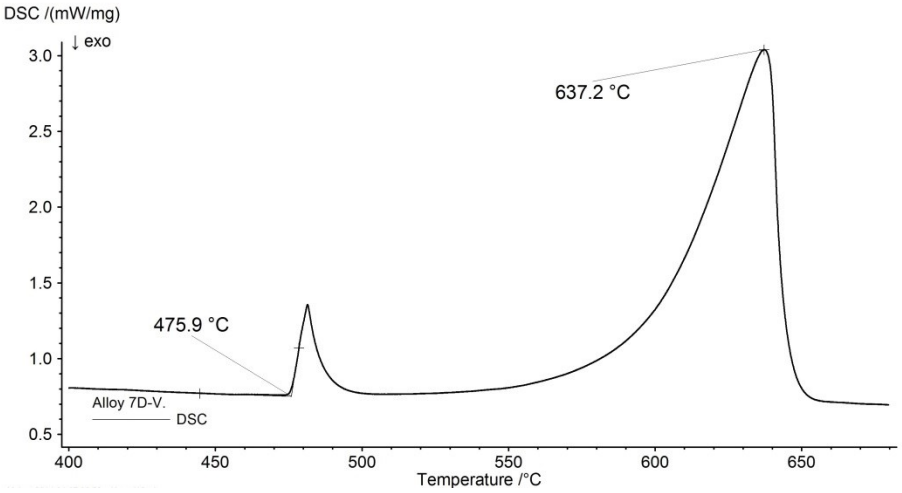


Figure 4.40. DSC heating curve of Alloy 7D-V.

Figures 4.50 to 4.52 show the DSC *heating* curves of Alloys E-A, E-B and E-C. The DSC curves look very similar with only one major peak. There could be a minor reaction in Alloy E-B as indicated by the small kink in the curve at around 465 °C.

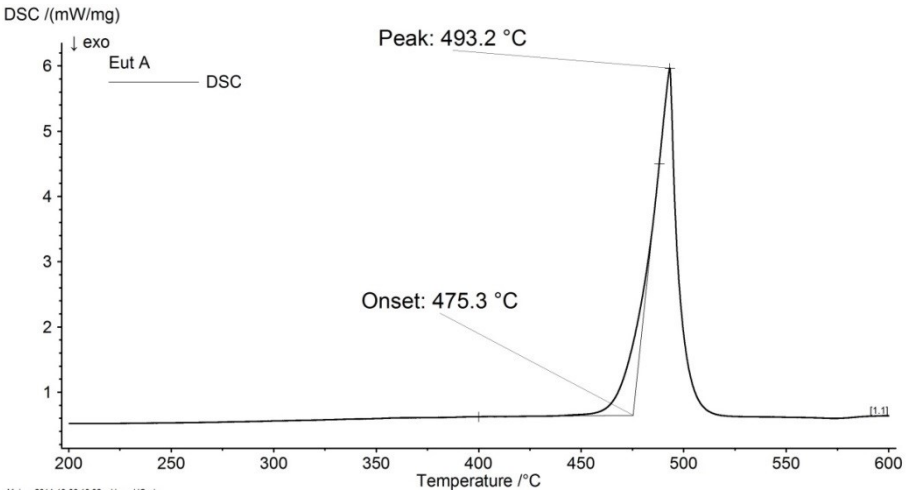


Figure 4.41. DSC heating curve of Alloy E-A.

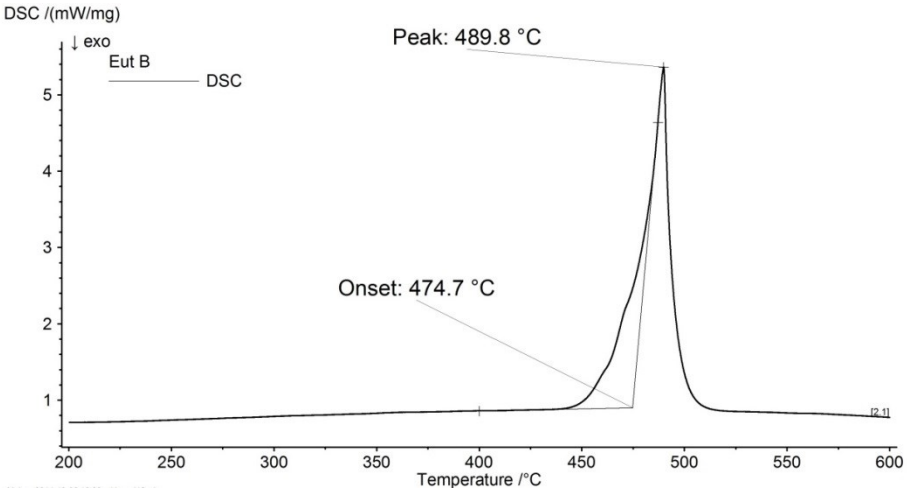


Figure 4.42. DSC heating curve of Alloy E-B.

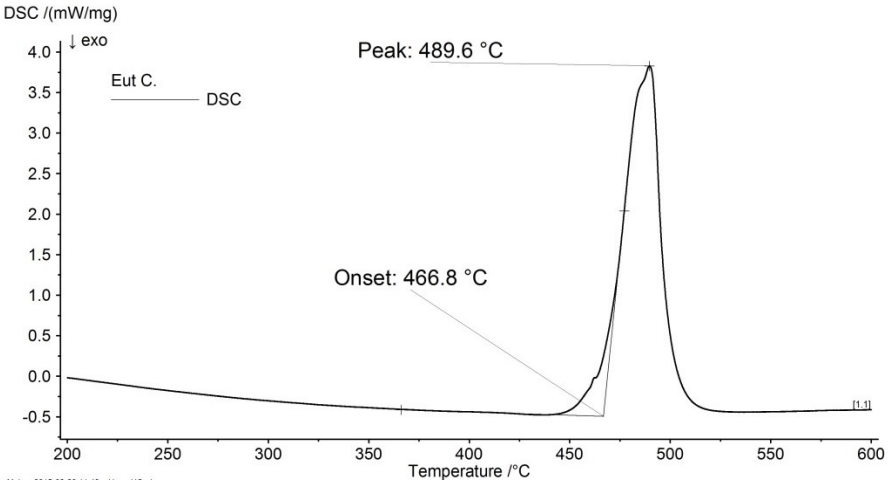


Figure 4.43. DSC heating curve of Alloy E-C.

Table 4.10 shows that the onset and peak temperatures for melting of Alloys E-A and E-B were the same. Alloy E-C had a lower onset temperature than Alloys E-A and E-B, which could indicate the onset of a different reaction or a different composition. The onset temperatures of the eutectic Alloys E-A and E-B were also the same as the melting temperatures for Alloys 7A, 7B, 7C and 7E.

Table 4.9. Summary of melting thermal events of Alloys E-A, E-B and E-C.

	Onset	Peak
Alloy	°C	
E-A	475	493
E-B	475	490
E-C	467	490

Figures 4.53 to 4.55 show the DSC *cooling* curves of Alloys E-A, E-B and E-C. There was a change in the solidification behaviour of the eutectic alloys as the Cu content increased and the Zn content decreased. Figure 4.53 shows a single peak on cooling of Alloy E-A. Figure 4.54, of Alloy E-B, shows a large peak after the onset of solidification, followed by a small second peak. Figure 4.55, of Alloy E-C, shows that the first peak after the onset becomes much smaller relative the second peak. The two peaks were indicative of two solidification reactions.

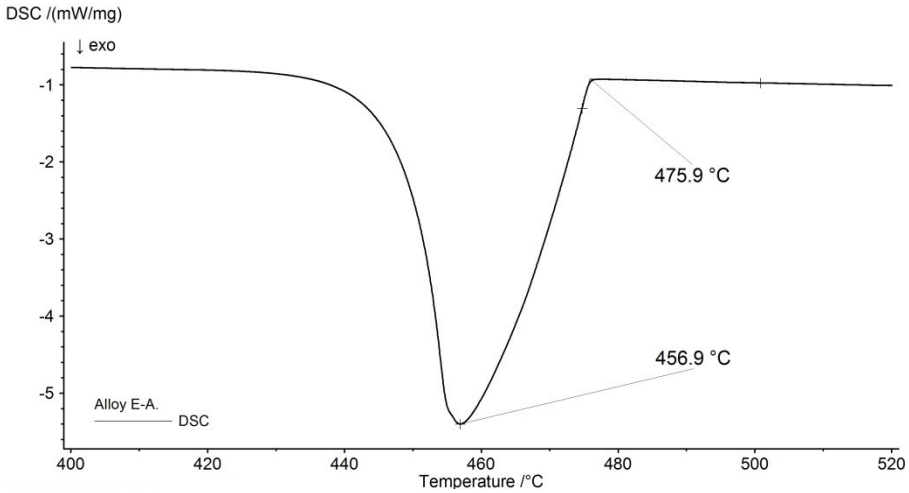


Figure 4.44. DSC cooling curve of Alloy E-A.

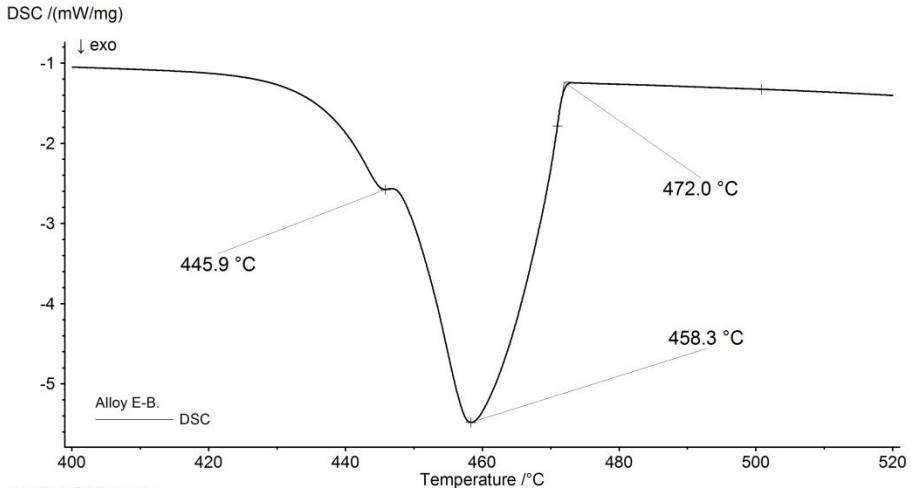


Figure 4.45. DSC cooling curve of Alloy E-B.

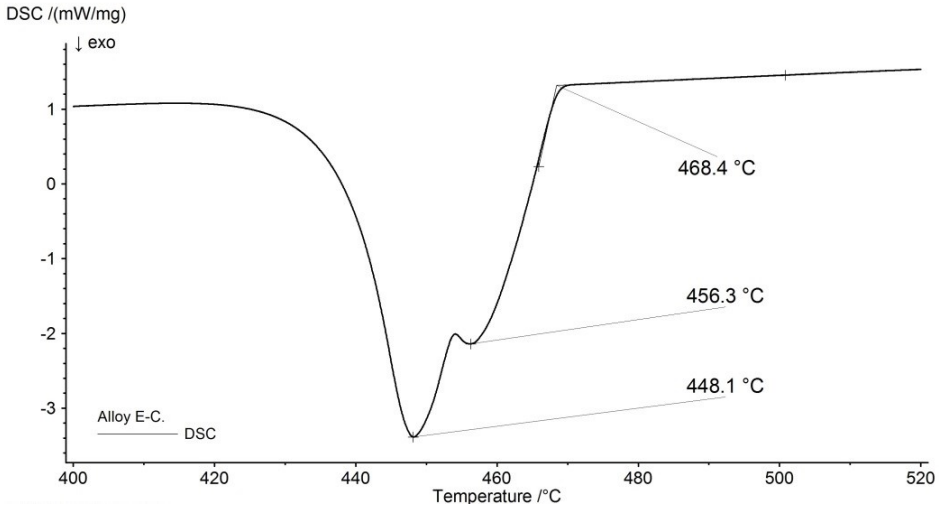


Figure 4.46. DSC cooling curve of Alloy E-C.

Table 4.11 shows that the onset of solidification temperature decreases from Alloy E-A to E-C and also shows that the temperatures of the first peaks coincide (within experimental error), as well as the temperatures of the second peaks.

Table 4.10. Summary of solidification onset and peak temperatures of Alloys EA to E-C.

	Onset	Peak 1	Peak 2
Alloy		°C	
E-A	475.9	456.9	-
E-B	472.0	458.3	445.9
E-C	468.4	456.3	448.1

4.10. XRD of as-cast alloys

Figures 4.35 to 4.39 show the XRD results of the as-cast alloys, as excerpts of the XRD curves between 2θ equal to 42° and 55°. This range was chosen because it clearly indicates the different crystal structures found in these alloys. The complete curves, from 22° to 105° of 2θ, are given in Appendix A. Peak matches for the phases in the Al-Zn-Mg-Cu system are also shown in each figure.

All the samples showed two major peaks at 2θ equal to 45° and 52°; these are the primary (Al) phase with a face centred cubic (FCC) crystal structure. This phase is the matrix and common to all the alloys in this investigation.

Figures 4.35 and 4.36 show that Alloys 7A and 7B had the same patterns, and hence the same crystal structures. The second phase identified by XRD was $MgZn_2$ which has a hexagonal crystal structure. Figure 4.38 for Alloy 7D shows that there was a third phase present which had a cubic crystal structure. The lattice parameters agreed with both the τ_1 phase in the Al-Zn-Mg [37] and the T phase in the Al-Cu-Mg [38] systems, showing that they were the same. Figures 4.37 and 4.39, for Alloys 7C and 7E, show that both of the above-mentioned phases, cubic and hexagonal, were present in the as-cast microstructures. Table 4.9 shows the results for the lattice parameters of the phases found in Alloys 7A to 7E and Alloys E-A and E-B.

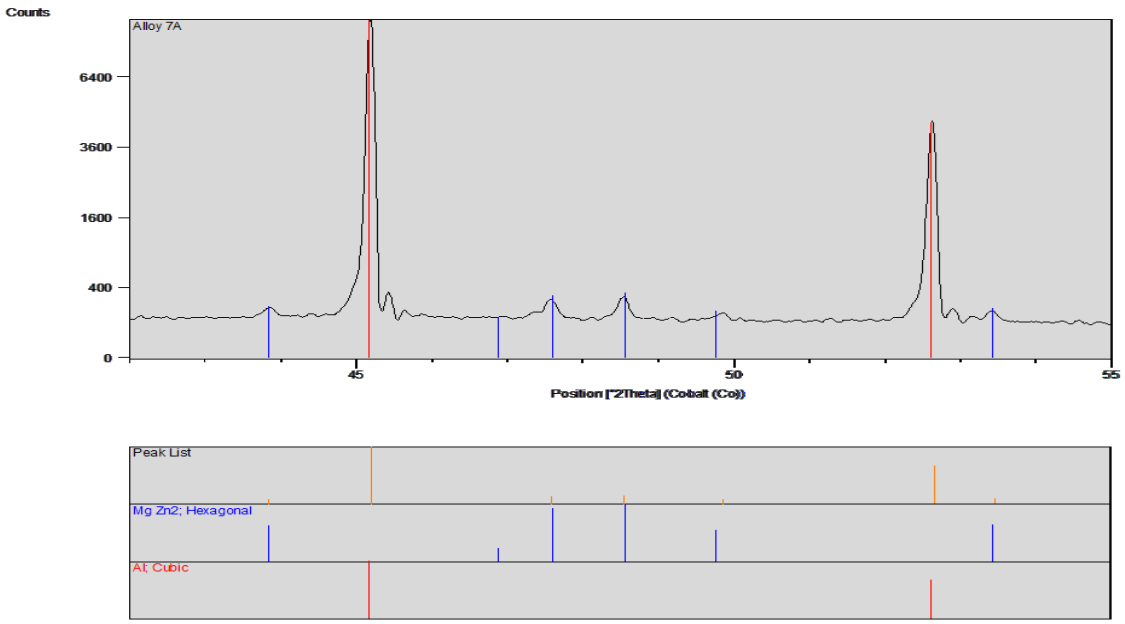


Figure 4.47. XRD pattern for as-cast Alloy 7A.

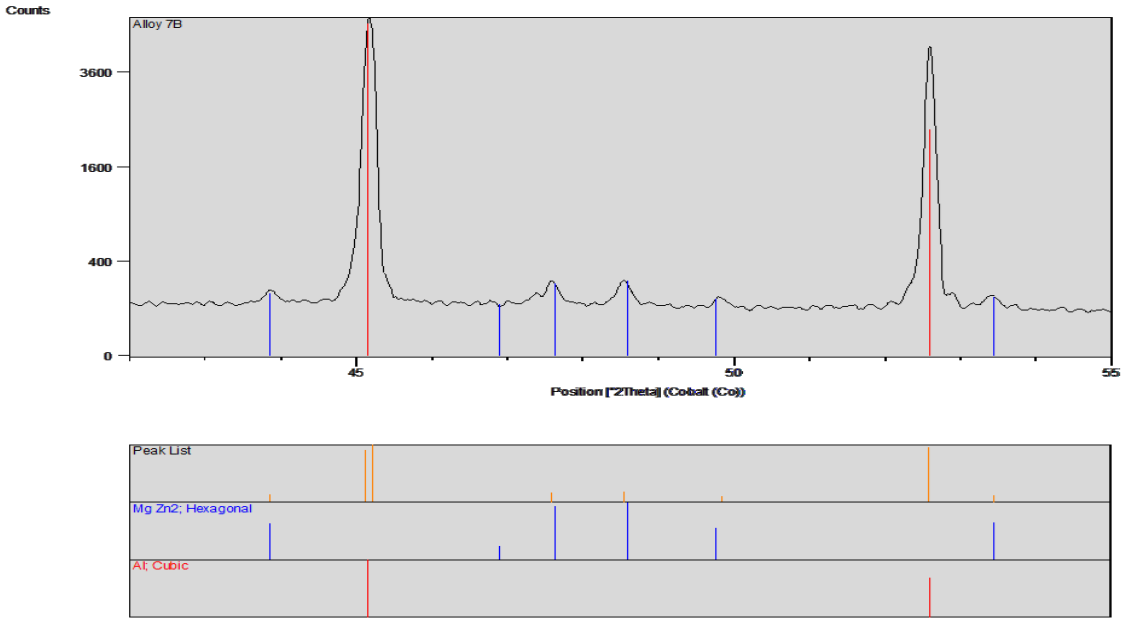


Figure 4.48. XRD pattern for as-cast Alloy 7B.

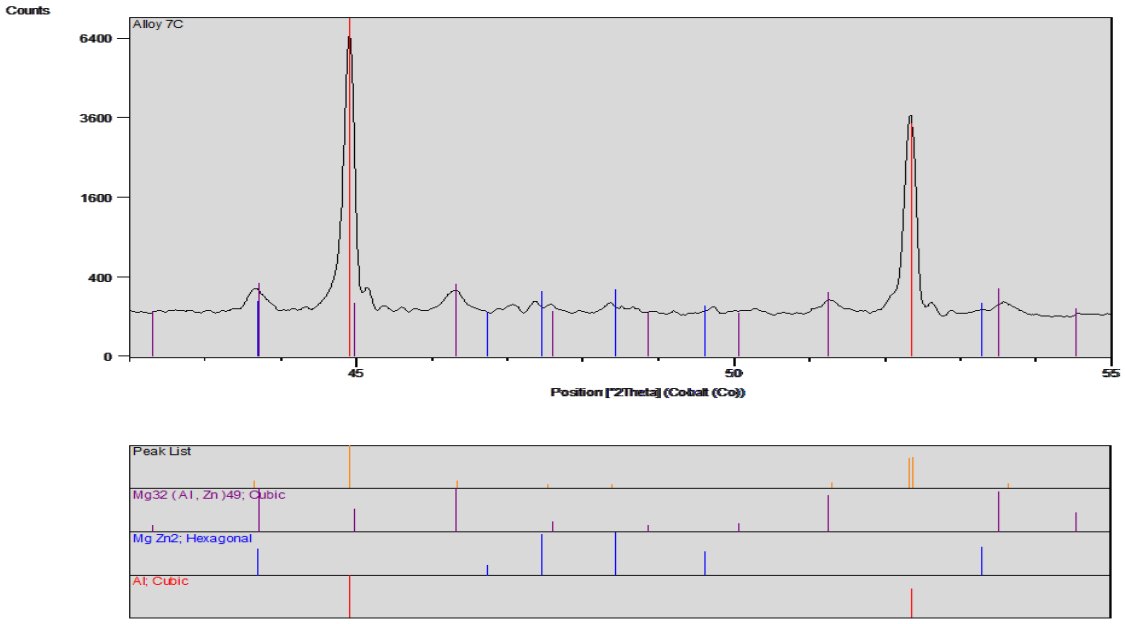


Figure 4.49. XRD pattern for as-cast Alloy 7C.

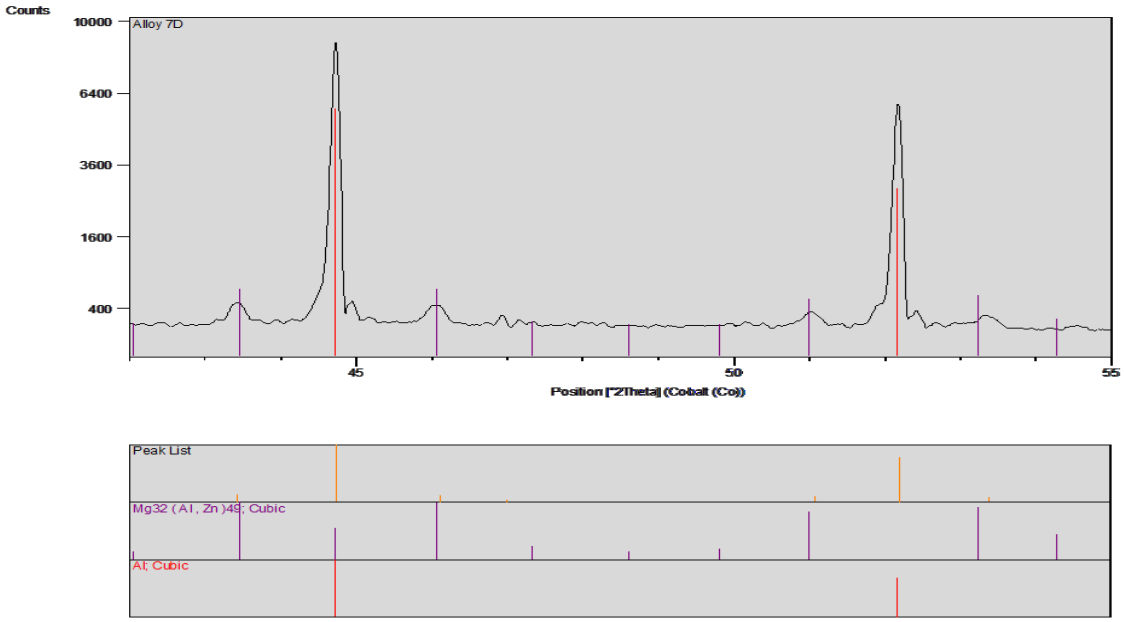


Figure 4.50. XRD pattern for as-cast Alloy 7D.

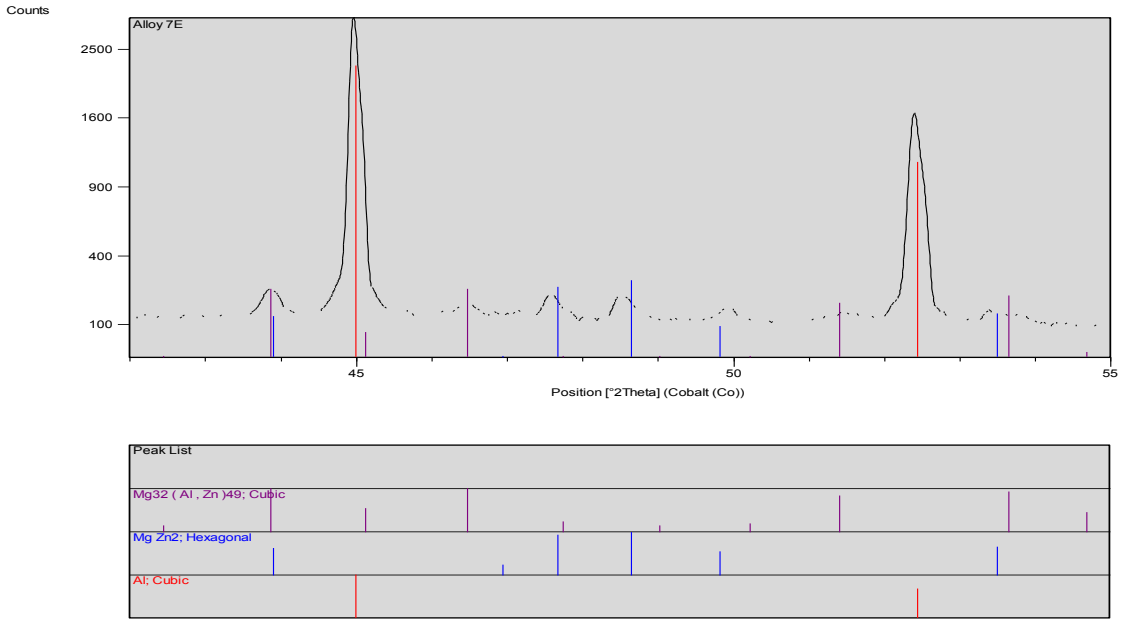


Figure 4.51. XRD pattern for as-cast Alloy 7E.

Figure 4.40 of Alloy 7D-V shows only a match for the $MgZn_2$ hexagonal phase and the (Al) cubic phase.

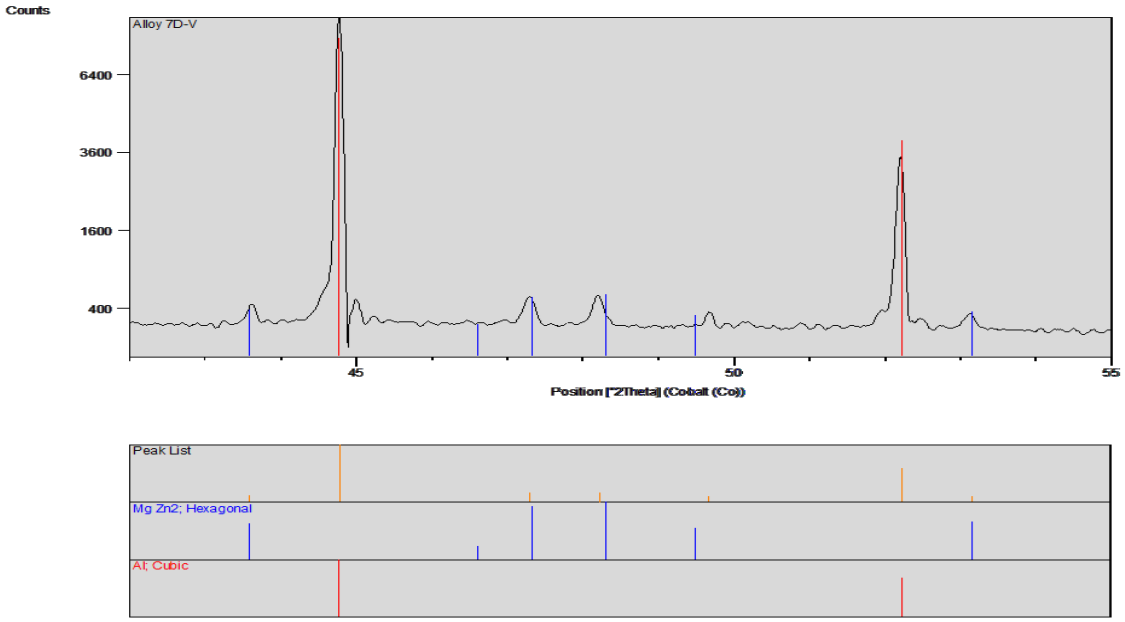


Figure 4.52. XRD pattern for as-cast Alloy 7D-V.

Figures 4.41 to 4.43 are the XRD results for Alloys E-A, E-B and E-C which clearly showed the $MgZn_2$ hexagonal crystal structure, together with the (Al) FCC crystal structure.

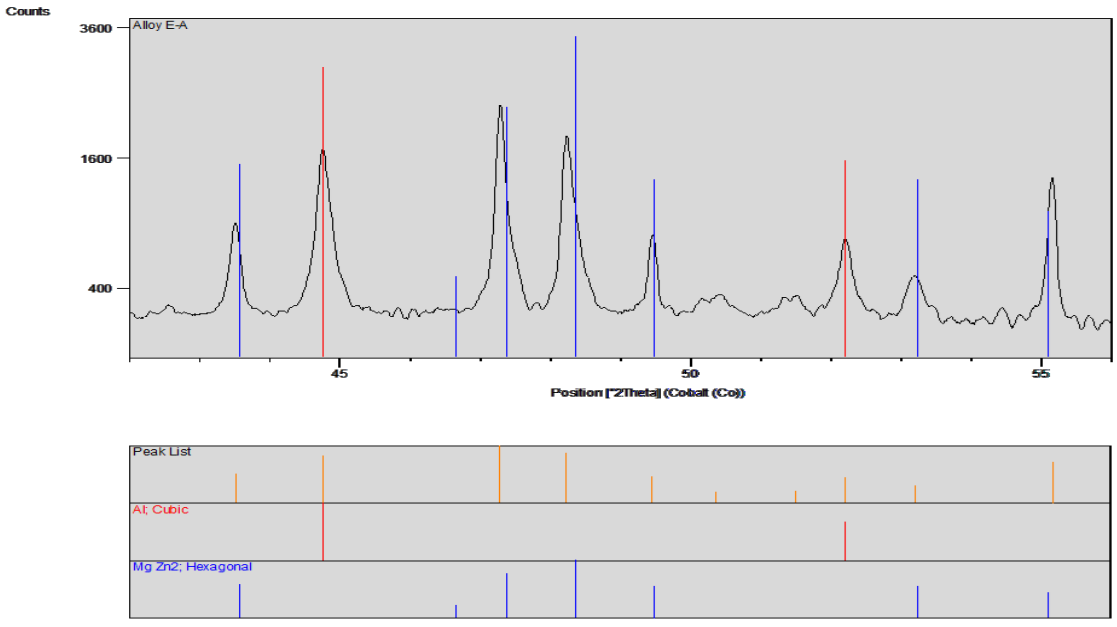


Figure 4.53. XRD pattern for as-cast Alloy E-A.

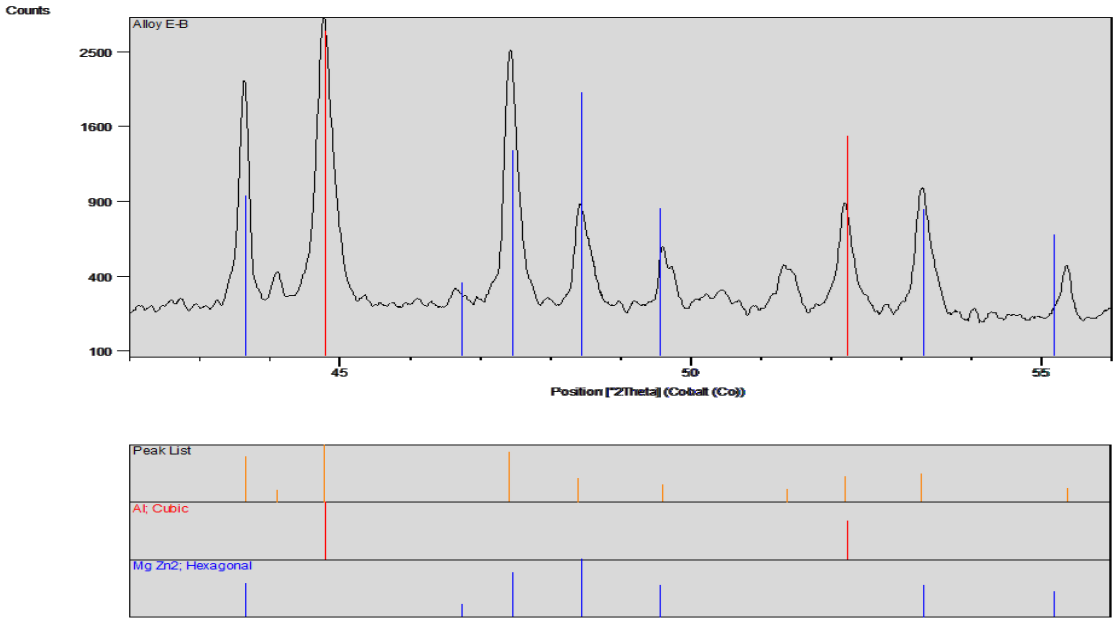


Figure 4.54. XRD pattern for as-cast Alloy E-B.

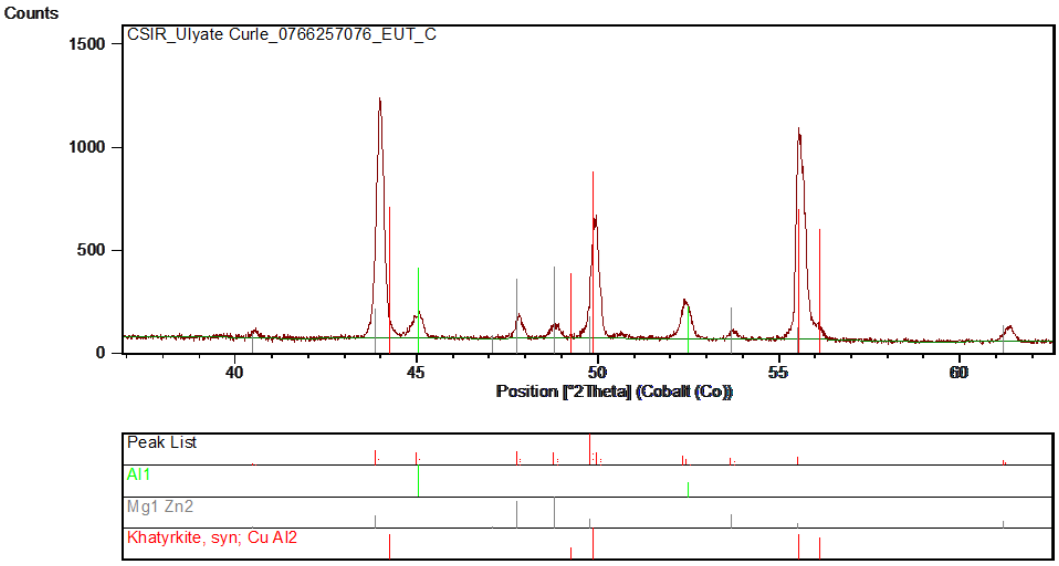


Figure 4.55. XRD pattern for as-cast Alloy E-C.

Table 4.11. Measured lattice parameters for phases in Alloys 7A to 7E, 7D-V, E-A and E-B.

Alloy	(αAl)	Cubic (*a*)	Hexagonal (*a*)	Hexagonal (*c*)
7A	405.16	-	522.27	853.30
7B	405.30	-	522.20	853.20
7C	405.40	1402.10	519.60	851.40
7D	404.94	1402.30	-	-
7E	405.43	1399.20	520.53	849.22
7D-V	405.54	-	521.97	849.52
E-A	404.70	-	520.20	851.10
E-B	404.90	-	518.70	849.10

4.11. SEM observations of T6 microstructures

Figures 4.56 to 4.60 show representative general appearances of the alloys in the T6 condition. These were taken at two different magnifications to show the general microstructures and the detailed microstructures. The microstructures at low magnification seem featureless because the micro-segregation had been eliminated by the homogenisation heat treatment. The micrographs at low magnification should be compared to the low magnification micrographs of the as-cast condition (Figures 4.5 to 4.9). Fine phases became apparent at high magnification.

Figure 4.56, of Alloy 7A, shows shrinkage porosity that spheroidised during the solution heat treatment and appeared as black spots. Two types of particles are visible in Figure 4.56b. These were larger needle-shaped particles and small spherical-shaped particles. The needle-shaped particles seemed to be an intermetallic phase on the grain boundaries, while the spherical particles seemed to be dispersoids within the grains.

Figure 4.57a, of Alloy 7B, shows that there were, again, a number of pores (dark spots) after homogenisation. These pores were shrinkage porosity that spheroidised. Figure 4.57b shows one bright particle that seemed to be the same as the dispersoids in Figure 4.40b.

Figure 4.58, of Alloy 7C, shows dark grey globules and bright features which were intermetallic phases that did not dissolve, even after the long time at the specific solution heat treatment temperature. The globules probably spheroidised during the solution heat treatment. Some particles also had two contrasts, but the brighter contrast was due to a polishing effect.

Figure 4.59a, of Alloy 7D, shows that there were no clearly distinguishable features visible at low magnification. In contrast, Figure 4.59b shows spherical dispersoids and a larger rounded intermetallic phase on the grain boundaries, at higher magnification.

Figure 4.60, of Alloy 7E, shows some bright chunky particles left in the alloy after solution heat treatment. In Figure 4.60b, at higher magnification, also needle shaped particles are seen. There were to be two different contrast intermetallic compounds, they were assumed to be the same intermetallic compound at different depths from the surface.

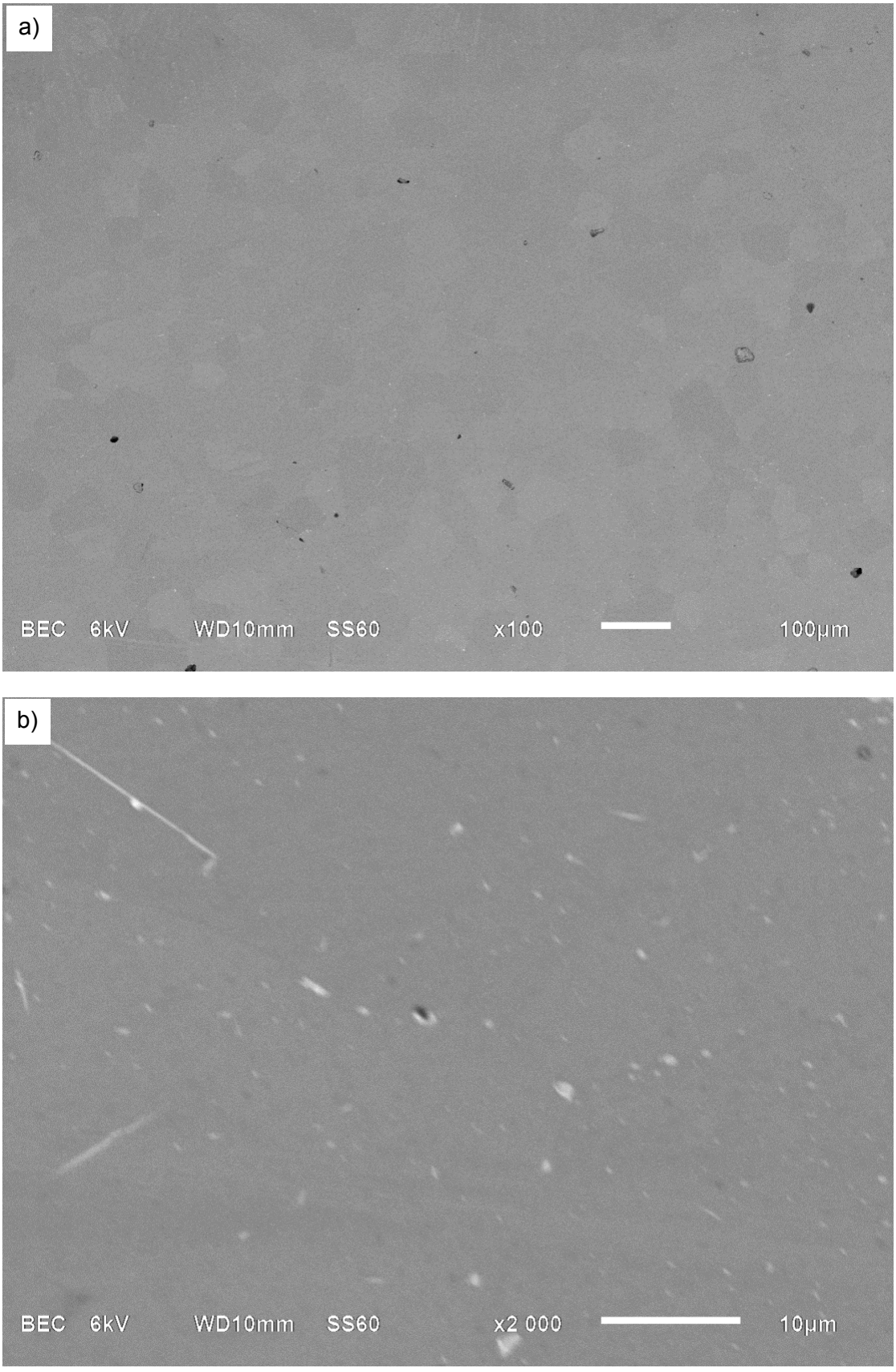


Figure 4.56. SEM-BSE images of intermetallic phases in Alloy 7A in the T6 condition: a) low magnification, and b) high magnification.

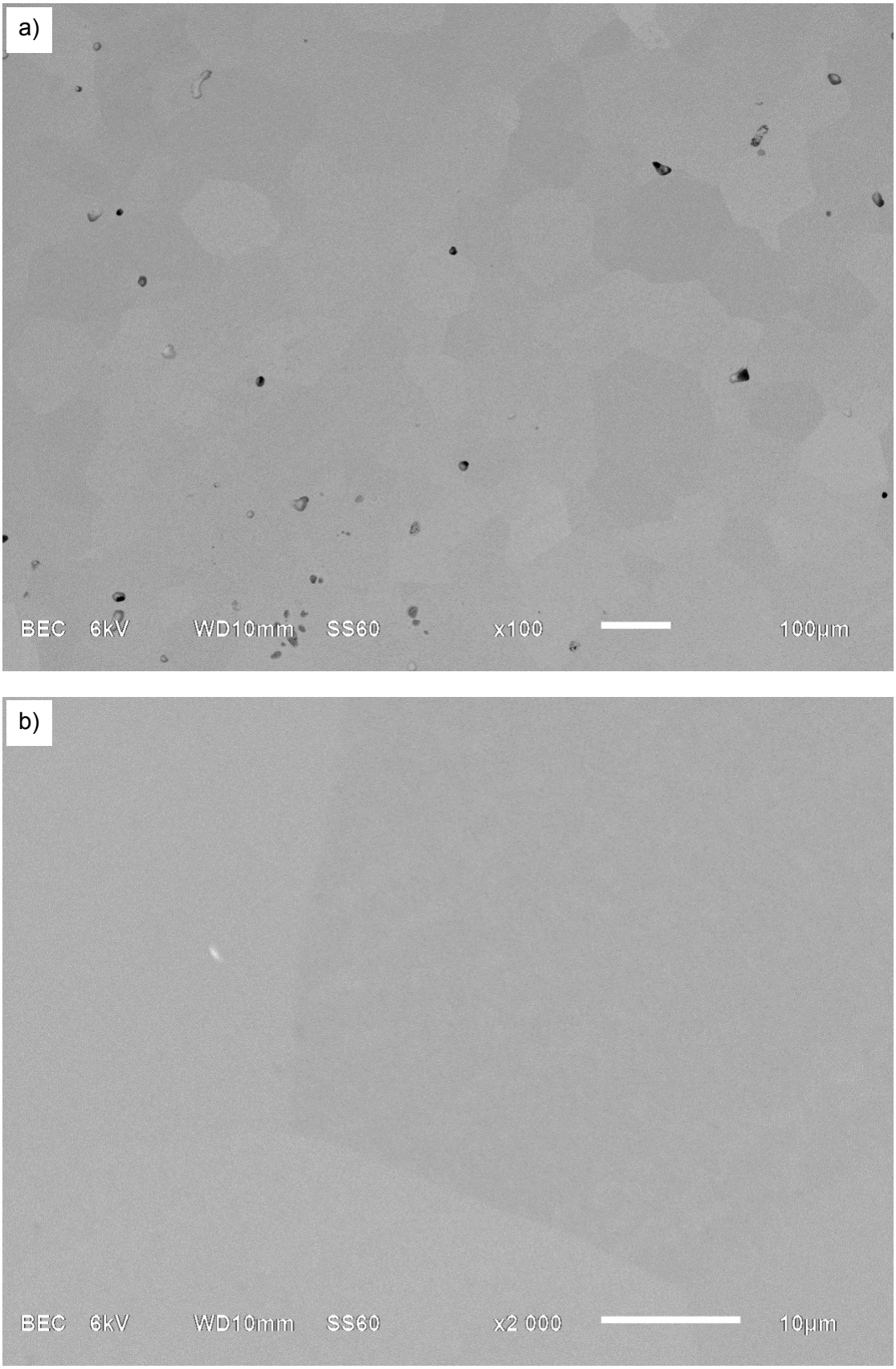


Figure 4.57. SEM-BSE images of porosity and intermetallic phases in Alloy 7B in the T6 condition: a) low magnification, and b) high magnification.

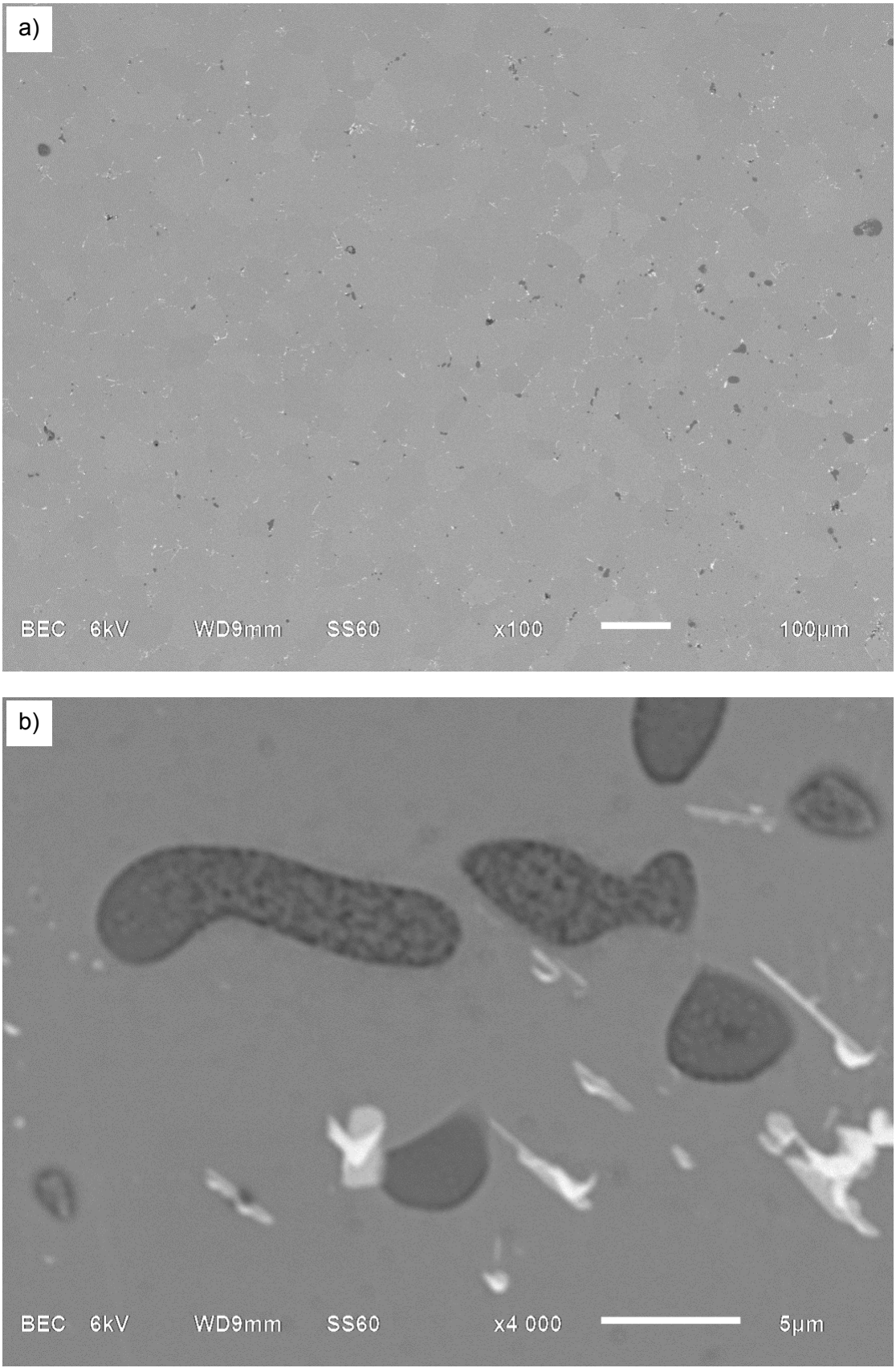


Figure 4.58. SEM-BSE images of intermetallic phases in Alloy 7C in the T6 condition: a) low magnification, and b) high magnification.

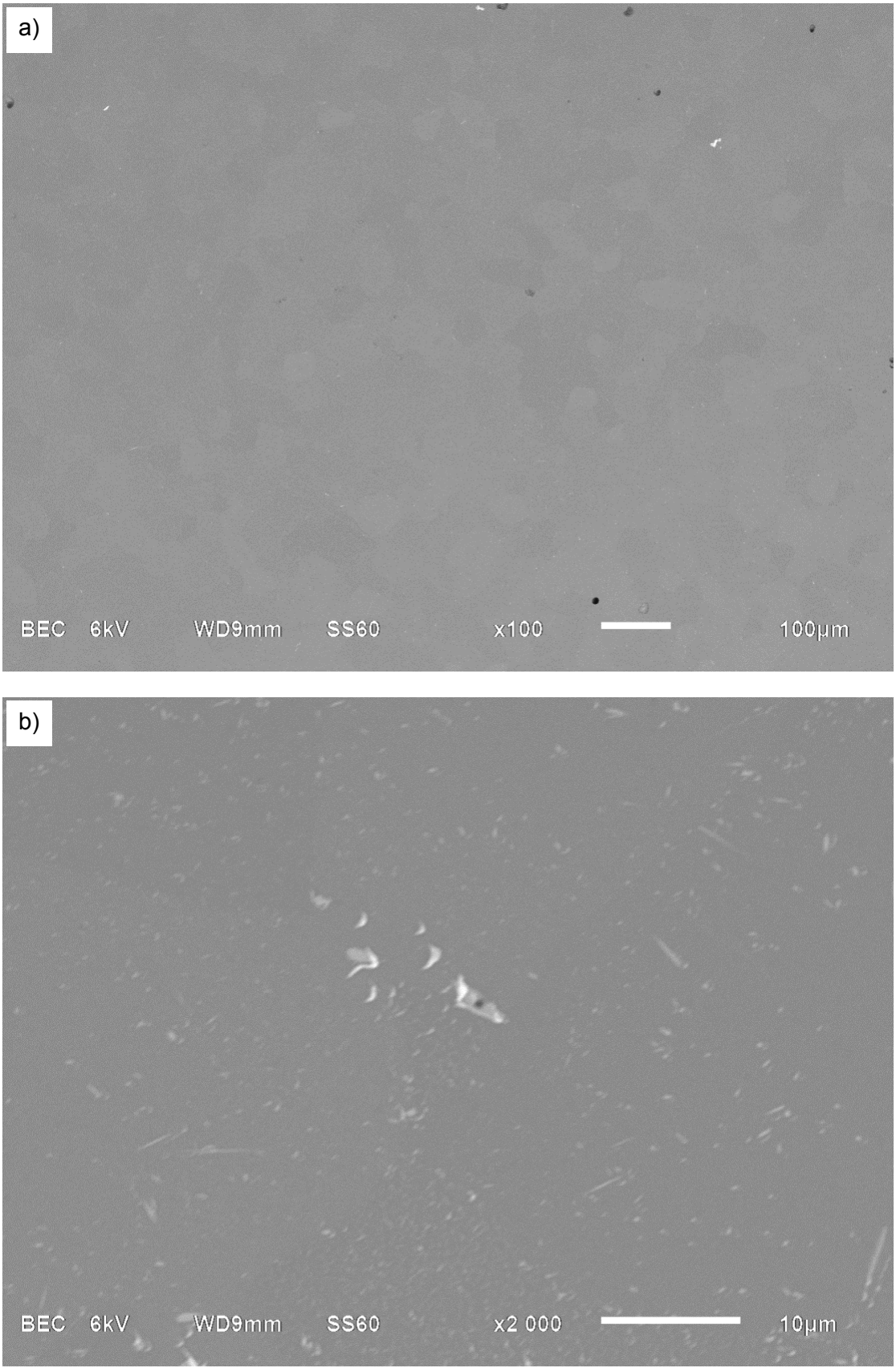


Figure 4.59. SEM-BSE images of intermetallic phases in Alloy 7D in the T6 condition: a) low magnification, and b) high magnification.

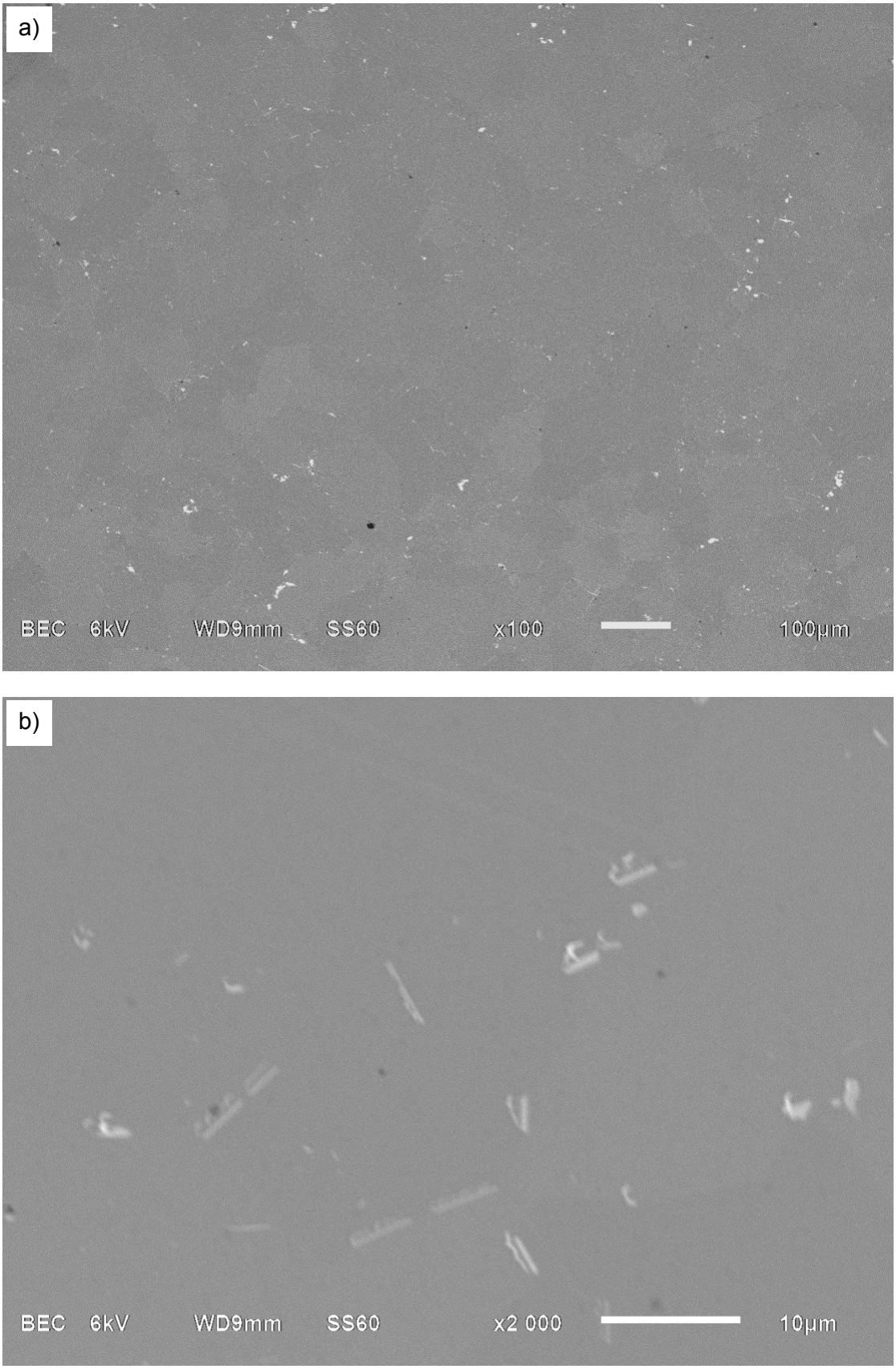


Figure 4.60. SEM-BSE images of intermetallic phases in Alloy 7E in the T6 condition: a) low magnification, and b) high magnification.

4.12. EDX analyses of T6 condition alloys

Figures 4.61 to 4.64 show the qualitative EDX composition analyses of the analysed points for the alloys in the T6 condition.

Figure 4.61 shows a point analysis of Alloy 7A. Alloy 7A was a Mn-containing alloy and it was expected that the Mn probably reacted with Cu in the alloy, to give Al-Cu-Mn intermetallic phases on grain boundaries and dispersoids within grains. The EDX analysis, in Figure 4.61b, clearly shows the presence of Mn and Cu in the intermetallic phase. The C peaks in all the analyses were from rinsing the sample with ethanol after polishing. The Al peak is probably larger due to the Al matrix background, as was the case for all the analyses.

Alloy 7B had the lowest Mn concentration, so it was expected that there would be much fewer secondary phases, as was seen in Figure 4.57b. These intermetallic compounds were not analysed but assumed to be the same Mn-containing compound as in Alloy 7A.

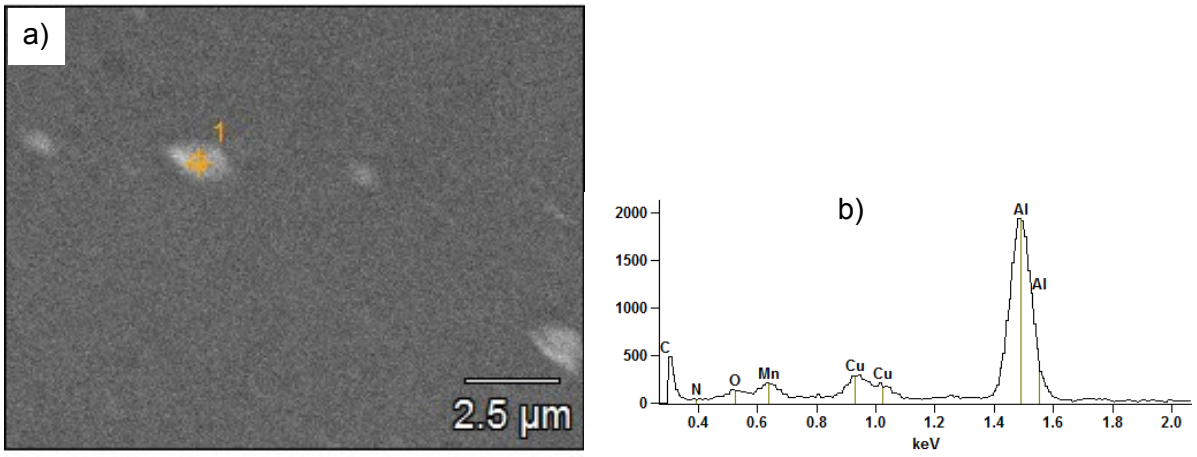


Figure 4.61. EDX results for Alloy 7A in the T6 condition: a) SEM-BSE image, and b) qualitative analysis of Al-Mn-Cu dispersoid.

Figure 4.62 shows the microstructure and qualitative analysis of intermetallic phases in Alloy 7C. This alloy was interesting because it did not contain any other impurity elements besides Fe and Si. The EDX analysis (Figure 4.62b) of the bright needle-like intermetallic phase in Figure 4.46a clearly shows, qualitatively, the presence of Fe and Cu. The EDX analysis (Figure 4.62d) of the dark intermetallic phase in Figure 4.62c shows the presence of Si and Mg. The EDX analysis of the dark intermetallic phase also shows a large O peak. From experience, this is due to some colloidal silica becoming lodged in the softer dark phase during polishing.

Figures 4.62e and 4.62f show that there were also still some undissolved Al-Zn-Mg-Cu eutectic left in Alloy 7C.

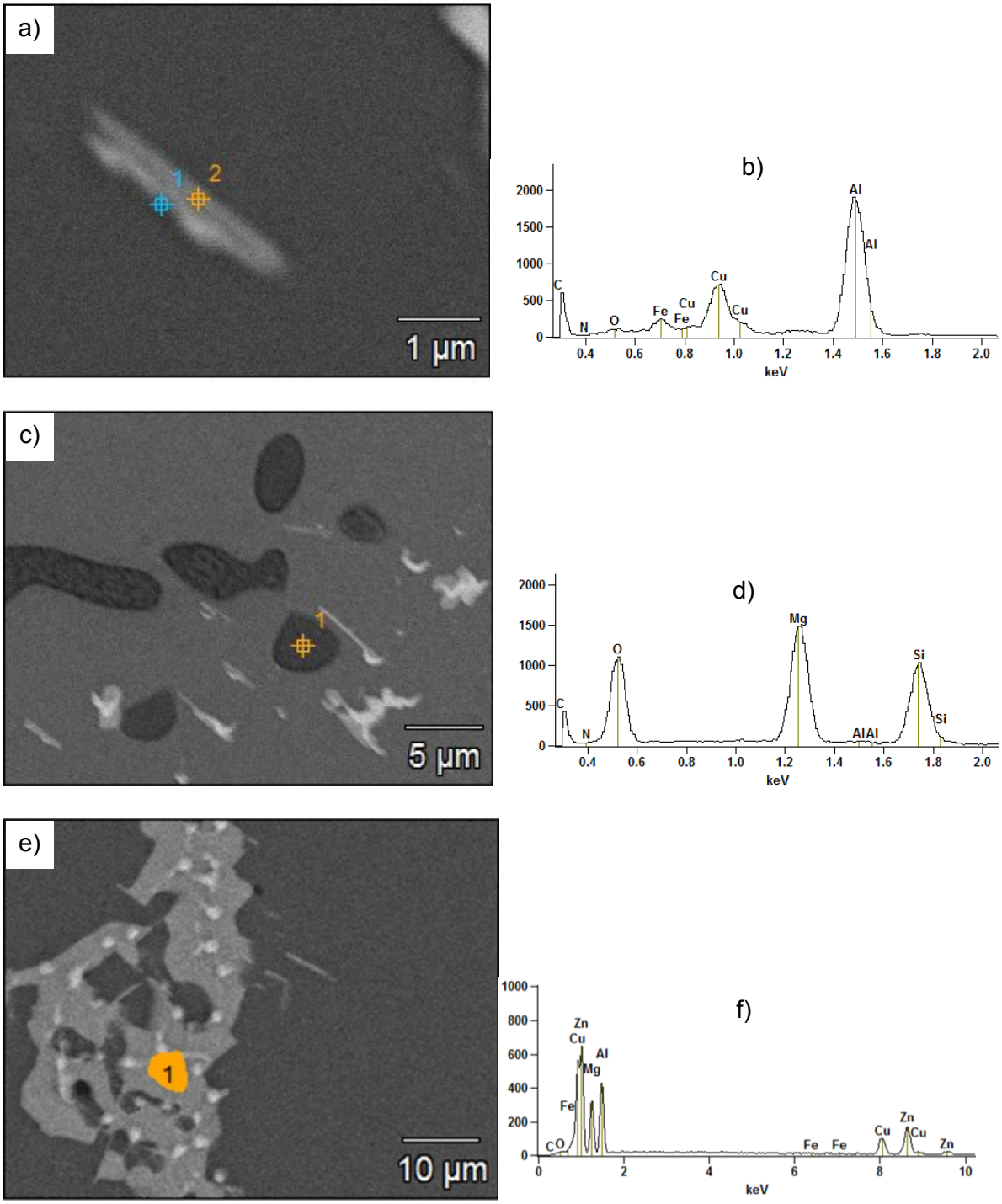


Figure 4.62. EDX results for Alloy 7C in the T6 condition: a) SEM-BSE image of needle shape, b) qualitative analysis for Al_7FeCu_2 needle shape (7C-y), c) SEM-BSE image of spherical shape, d) qualitative analysis for spherical shaped Mg_2Si (7C-x), e) SEM-BSE image of a large eutectic phase, and f) qualitative analysis of the large Al-Zn-Mg-Cu eutectic phase (7C-z).

Figure 4.63 shows the intermetallic phases and dispersoids of Alloy 7D. This alloy is again a Mn-containing alloy. The qualitative EDX analysis, in Figure 4.63, shows the intermetallic needle containing Mn and Cu.

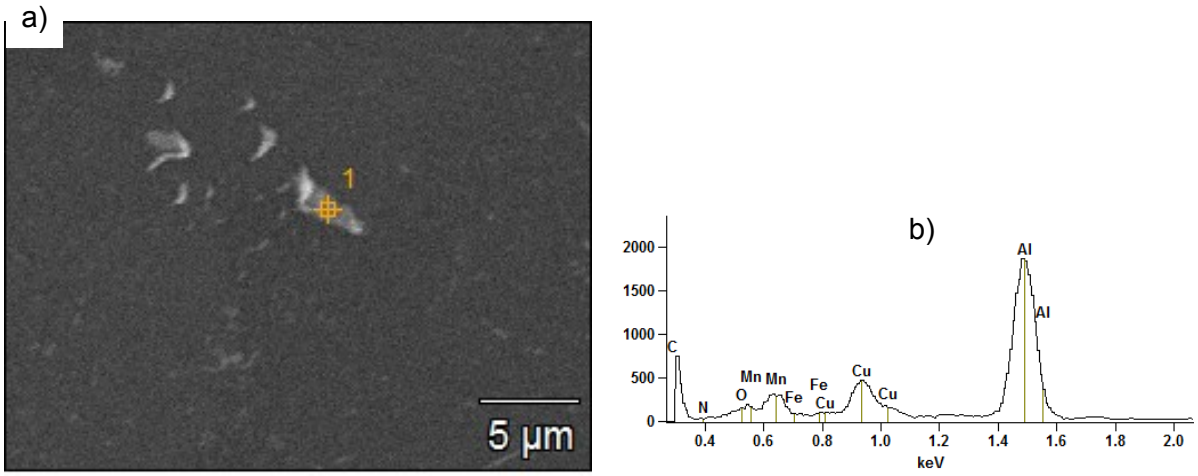


Figure 4.63. EDX results for Alloy 7D in the T6 condition: a) SEM-BSE image, and b) qualitative analysis of the Al-Mn-Cu intermetallic.

Figure 4.64 shows the qualitative intermetallic phases analyses of Alloy 7E. This alloy contained Fe which reacted with Cu. This Fe phase does not dissolve at the solution heat treatment temperature used and was therefore a remnant. It is interesting to note that this intermetallic phase had a needle shape. Another intermetallic phase in this alloy was an Al-Mg-Cu intermetallic phase, which was left after the long solution heat treatment. It probably did not dissolve due to super-saturation of the matrix in the vicinity of the inter-globular eutectic.

Table 4.12 shows the EDX measurements of the intermetallic phases found in the different alloys. The intermetallic phases in Alloys 7A, 7B and 7D contained Mn and Cu with a ratio of ~2:1. Two intermetallic phases were found in Alloy 7C, one contained Fe and Cu with a ratio of ~1:2, while the other contained Mg, Si and O with a ratio of ~1:1:1. Alloy 7E also had two intermetallic phases, one (7E-x) the same as in

Alloy 7C (7C-y) which contained Fe and Cu with a ratio of ~1:2. The other intermetallic phase (7E-y) contained Cu and Mg with a ratio of ~1:1.

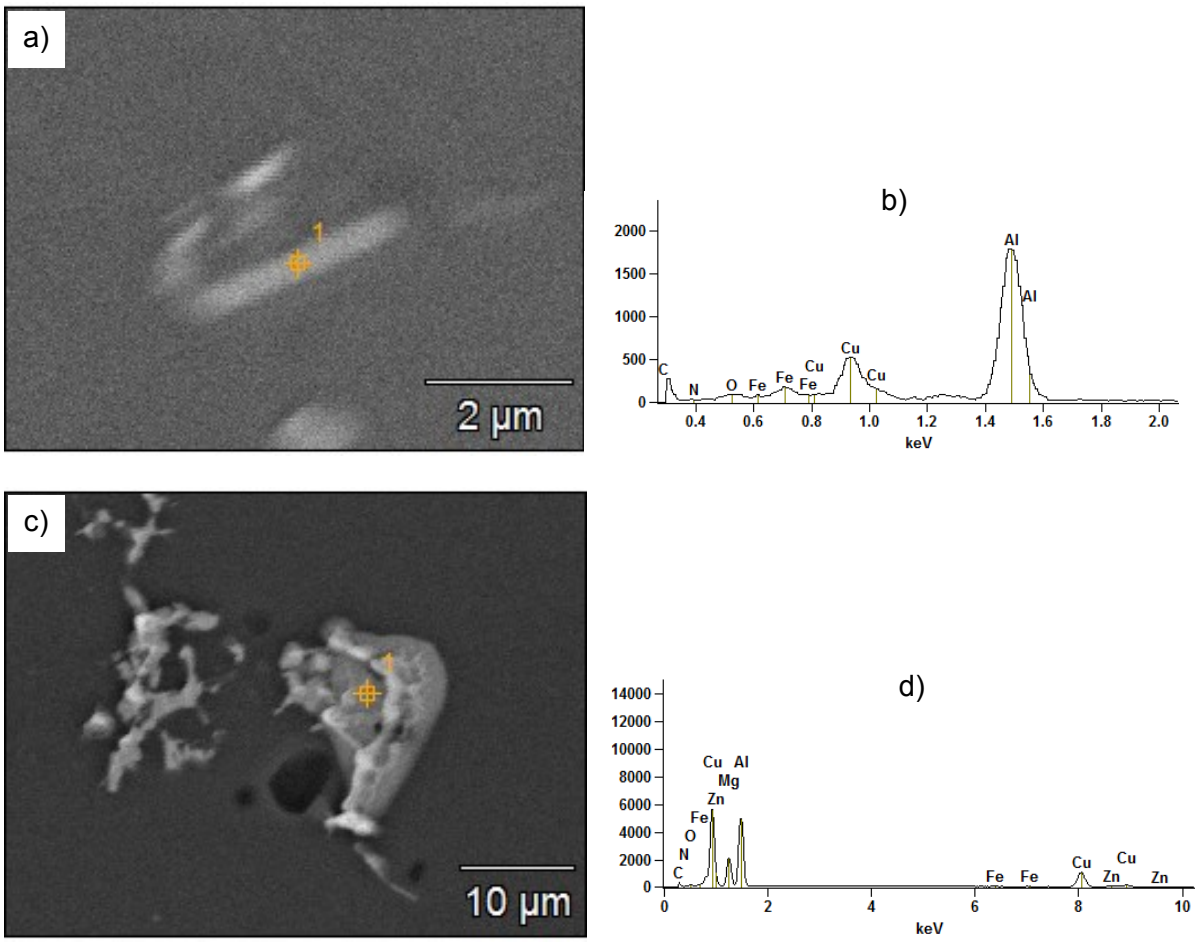


Figure 4.64. EDX results for Alloy 7E in the T6 condition: a) SEM-BSE image of needle shape, b) qualitative analysis for needle shape Al_7FeCu_2 (7E-x), c) SEM-BSE image of chunky shape, and d) qualitative analysis for chunky shape Al_2MgCu (7E-y).

Table 4.12. EDX analyses of intermetallic phases identified in the alloys in the T6 condition.

Alloy	Compound shape	O K	Al K	Cu K	Cu L	Fe L	Mn L	Si K	Mg K	Zn K
		at.%								
7A	spherical	2.3 ± 0.4	77.0 ± 0.7	-	7.7 ± 0.4	-	13.0 ± 0.9	-	-	-
7C-x	needle	29.9 ± 0.5	0.3 ± 0.2	-	-	-	-	36.3 ± 0.5	33.5 ± 0.4	-
7C-y	spherical	3.1 ± 0.3	69.0 ± 0.6	-	17.9 ± 0.3	10.1 ± 0.5	-	-	-	-
7C-z	chunky	2.6 ± 0.6	31.9 ± 0.8	12.7 ± 0.8	-	-	-	-	26.7 ±1 .5	25.8 ± 1.2
7D	irregular	-	64.0 ± 0.6	-	12.2 ± 0.4	2.6 ± 0.6	21.2 ± 0.6	-	-	-
7E-x	needle	3.3 ± 0.3	74.1 ± 0.7	-	14.6 ± 0.3	8.1 ± 0.5	-	-	-	-
7E-y	chunky	2.7 ± 0.2	51.1 ± 0.4	23.6 ± 0.4	-	-	-	-	21.0 ± 0.5	1.6 ± 0.3

Element & Line at 6 kV

4.13. T73 microstructure observation and analysis

The T73 condition alloys had precisely the same microstructure as the equivalent T6 sample. The artificial ageing temperatures were too low to result in a changed microstructure.

4.14. Grain size measurements

Grain sizes of the Alloys 7A to 7E in the as-cast and T6 conditions were measured by the linear intercept method according to Equation 3.8 in Section 3.8.8

4.14.1. As-cast grain sizes

Table 4.13 shows the measured grain sizes of Alloys 7A to 7E in the as-cast condition. Most of the grain sizes were very similar, although Alloy 7E had the largest grains. A fast cooling rate normally results in small grain sizes, thus indicating that Alloy 7E experienced a slower cooling rate. The main difference in cooling rate could come from a longer transfer time of the billet between rheo-processing and HPDC.

Table 4.13. Grain size measurements in the as-cast condition for Alloys 7A to 7E.

Alloy	µm
7A	47 ± 3
7B	48 ± 4
7C	54 ± 5
7D	48 ± 1
7E	68 ± 3

4.14.2. T6 grain sizes

Table 4.14 shows the grain sizes of Alloys 7A to 7E in the T6 condition, and reveals that the grain sizes in the T6 condition for Alloys 7A, 7C and 7D were very similar, while the grain sizes for Alloys 7B and 7E were similar.

The grain size errors for Alloys 7D and 7E were large compared to the other alloys. The difference could have been caused by irregular grain shapes.

Table 4.14. Grain size measurements in the T6 conditions for Alloys 7A to 7E.

Alloy	μm
7A	56 ± 1
7B	77 ± 5
7C	55 ± 4
7D	57 ± 8
7E	79 ± 8

4.15. Hardness measurements

4.15.1. T6 hardness

Table 4.15 shows the measured hardness of each alloy in the T6 condition, as the average of six hardness measurements per alloy. Alloy 7C had the highest average hardness. Alloys 7E and 7D followed: both had similar hardness. Alloys 7B and Alloy 7A had lower hardness: both were similar.

Table 4.15. Micro-Vickers hardness measurements (at 500g load) for alloys in the T6 condition.

Alloy	HV
7A	173 ± 3
7B	176 ± 5
7C	215 ± 1
7D	198 ± 3
7E	200 ± 2

4.15.2. T7 hardness

Table 4.16 shows the measured hardness of the T6 condition alloys, again as the average of six hardness measurements per alloy. Alloys 7C to 7E had similar hardness. Alloys 7A and 7B both had similar hardness but lower than the other three alloys. The overall hardnesses of the samples in the T7 heat treatment condition were lower than the samples in the T6 heat treatment condition.

Table 4.16. Micro-Vickers hardness measurements (at 500g load) for alloys in the T6 condition.

Alloy	HV
7A	152 ± 4
7B	153 ± 3
7C	189 ± 6
7D	191 ± 4
7E	191 ± 2

4.16. T6 tensile property data

4.16.1. T6 heat treatment

Table 4.17 shows the heat treatments, by the CSIR, that were used to prepare samples for tensile testing of the as-received Alloys 7A to 7E. Homogenisation is normally followed by a solution heat treatment, but in this case, these two steps were combined into a single step, as mentioned in Section 3.4.1.

Table 4.17 shows that the homogenisation time differed for the different alloys, which could be justified on the grounds that the extent of alloying differed, although the microstructures were similar. Alloys 7A and 7B were much lower alloyed than Alloys 7C, 7D and 7E which would require a shorter time to homogenise by diffusion, while longer times would be necessary for the higher alloyed material.

The artificial ageing step is normally performed for 24 hours, at which point a plateau is reached in the change of properties [1]. It was shown in Section 2.10 in Figure 2.24 that 24 hours and 50 hours of artificial ageing both fall on the iso-yield strength plateau. It was therefore assumed to be equivalent.

Table 4.17. Homogenisation/solution and artificial ageing heat treatments of Alloys 7A to 7E.

Alloy	Heat treatment
7A	470 °C/12h - Water quench - 120 °C/50h
7B	470 °C/12h - Water quench - 120 °C/50h
7C	470 °C/19h - Water quench - 120 °C/50h
7D	470 °C/24h - Water quench - 120 °C/24h
7E	465 °C/24h - Water quench - 120 °C/24h

4.16.2. T6 tensile properties

Table 4.18 gives the yield strength (YS), ductility (% elongation) and the ultimate tensile strength (UTS), and shows that Alloy 7C had the same values for the yield and tensile strengths. Alloy 7C failed in the elastic region of the tensile curve, the yield strength and ultimate tensile strength was therefore taken to be the same, only data for one sample was available (no errors indicated for the test).

Table 4.18. Uni-axial tensile properties of Alloys 7A to 7E in the T6 condition, as reported by the CSIR.

Alloy	YS (MPa)	UTS (MPa)	% Elongation
7A	447 ± 1	507 ± 2	11.7 ± 1.7
7B	454 ± 6	500 ± 2	9.7 ± 3.7
7C	563	563	0.3
7D	518 ± 6	552 ± 12	2.0 ± 0.6
7E	522 ± 6	534 ± 10	1.8 ± 0.4

5. Discussion

5.1. Microstructure observations in the as-cast condition

All the as-cast alloys had similar features. They all consisted of globular primary (αAl) grains with eutectics, enriched with alloying elements, in between. The exception was Alloy 7E, which had more dendritic (Al) grains. It is most likely that the alloy solidified differently from the other as-received alloys. It was indicated, by the CSIR, that Alloy 7E was produced with a higher pouring temperature. This would have resulted in less initial nucleation under the same processing conditions as Alloys 7A to 7D. The grain size, Table 4.13, and shape were largely a function of amount of nucleation and subsequent growth during turbulent flow during semi-solid processing [17-23]. Alloy 7E had the largest grain size. A fast cooling rate normally results in small grain sizes, thus indicating that Alloy 7E, cast into a plate, experienced a slower cooling rate. The main difference in cooling rate could come from a longer transfer time of the billet between rheo-processing and HPDC.

The eutectic regions were finely distributed, and coarser in the higher alloyed samples. The microstructures were so similar that it was difficult to visually distinguish between the alloys. Even at higher magnification, the eutectics of all the alloys again looked remarkably the same, and the inter-globular sizes of the eutectics were also very similar. The eutectics were lamellar and very fine, due to the high cooling rate, in the order of 10^3 Ks^{-1}, during the HPDC processing [39].

The vacuum-cooled sample (Alloy 7D-V) had the same features as its R-HPDC alloy equivalent. The differences were that the globular primary (Al) grains and the lamellar structure were coarser, and the inter-globular size of the eutectic was also larger.

The eutectic composition alloys, Alloys E-A and E-B, were similar to the dilute alloys, Alloys 7A and 7D. The primary (Al) phase was not present, as expected, indicating that the alloy compositions were correctly produced, as indicated by Tables 4.5 and 4.6 in Sections 4.7.1 and 4.7.2. It was clear that there were only two phases present in Alloys E-A and E-B, since the eutectic structures had the appearance of regular lamellar eutectics.

5.2. As-cast properties

One of the aims of this study was to determine the as-cast properties of R-HPDC Al-Zn-Mg-Cu aluminium alloys. A mechanism by which these properties could have arisen, is also proposed.

5.2.1. Phases present in as-cast alloys

The quantitative XRD analyses in Table 5.1 show that there were only two phases present besides the FCC (Al) solid solution phase. The two phase structures were a cubic phase and/or a hexagonal phase. Alloys 7A, 7B, 7D and 7D-V had only one of these structures present, but in Alloys 7C and 7E there was a mixture of these structures.

Table 5.1. Weight percentages of phases found in each alloy.

	Cubic phase	Hexagonal phase
Alloy	wt%	wt%
7A	-	2.73
7B	-	2.90
7C	6.00	1.24
7D	5.60	-
7E	2.50	2.78
7D-V	-	3.88

The lattice parameters of the phases detected by XRD in each alloy are given in Table 5.2. The lattice parameters of the similar phases in the Al-Mg-Zn system [37] are shown for comparison. The calculated lattice parameters of the phases present in the alloys were very close to the reported lattice parameters of the (Al) solid solution phase [37], cubic τ ($Mg_{32}(Al,Zn)_{48}$) phase [37] and hexagonal η ($MgZn_2$) phase [37].

The lattice parameters of the phases found in eutectic Alloys E-A and E-B are also shown in Table 5.2. Eutectic Alloys E-A and E-B both only had the (Al) solid solution FCC phase and hexagonal phases present. The lattice parameters of the phases of Alloys E-A and E-B also correlate well with the (Al) solid solution phase and the hexagonal η ($MgZn_2$) phase.

Table 5.2. Lattice parameters (pm) of the phases identified with XRD in the as-cast alloys. Lattice parameters for Al, τ and η from reference [37].

Alloy	(αAl)	Cubic (a)	Hexagonal (a)	Hexagonal (c)
7A	405.16	-	522.27	853.30
7B	405.30	-	522.20	853.20
7C	405.40	1402.10	519.60	851.40
7D	404.94	1402.30	-	-
7E	405.43	1399.20	520.53	849.22
7D-V	405.54	-	521.97	849.52
E-A	404.70	-	520.20	851.10
E-B	404.90	-	518.70	849.10
Al	404.96	-	-	-
τ	-	1413.00	-	-
η	-	-	522.00	856.70

The lattice parameters of the phases measured in the alloys were marginally different from the reported lattice parameters for the (Al), τ and η phases [37]. The difference must have resulted from compositions that differed from the reported phases. It would seem from the above that the hexagonal phase in Alloys 7A, 7B, 7C and 7E was the η phase, while the cubic phase in Alloys 7C, 7D and 7E was the τ phase.

5.2.2. Thermal behaviour

Inspecting the onset of melting temperatures measured with DSC presented in Table 5.3 reveal that the melting temperatures are the same for all the alloys except for Alloy 7D. The melting onset temperature for Alloys 7A, 7B, 7C and 7E was 476 °C while for Alloys 7D the melting onset was 480 °C. Figure 5.1 shows that the onsets of melting curves started with very steep deviation from the horizontal. A sudden peak is normally associated with a liquid-forming reaction, e.g. an eutectic reaction [46].

Table 5.3. Summary of melting onset and end temperatures of Alloys 7A to 7E and 7D-V.

	Melting (DSC)		Solidification (Thermo-Calc)	
	Onset	End	Onset	End
Alloy	°C		°C	
7A	475	653	639	476
7B	476	653	640	476
7C	476	635	629	476
7D	480	641	636	476
7E	476	641	637	476
7D-V	476	637	636	476

Figure 5.1 shows the relative peak heights of the different R-HPDC alloys (Alloys 7A to 7E). The peak heights increase as the level of alloying increases. Alloy 7D should have had a lower peak height than Alloy 7E which was higher alloyed. Alloy 7C should also have had the highest peak because it was alloyed the highest. The reason for these discrepancies probably arises from the specific volume of material from where the DSC sample was taken. It was demonstrated that the flow pattern during casting causes segregation on a macro level and differs between different castings [47]. It is not possible to take the same volume of material for DSC on which the OES was performed, in which case the problem would probably have been solved. Alloy 7C showed a slight change in slope which could be indicative of a second reaction taking place, since the τ and η phases were both present in the alloy.

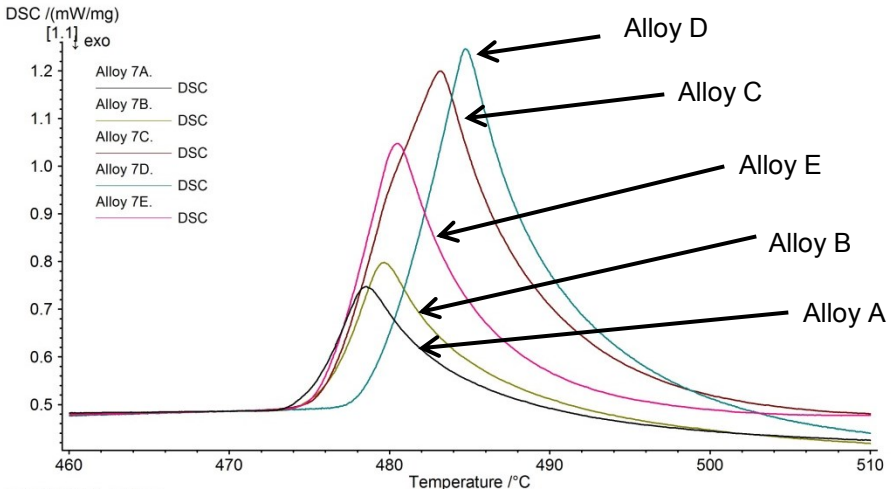


Figure 5.1. Comparison of eutectic melting peak heights between Alloys 7A to 7E.

5.3. Solidification mechanism

5.3.1. Solidification reactions

It appears from Section 5.2.1 and 5.2.2 that there was a strong correlation of the phase structures and thermal behaviours of the R-HPDC Al-Zn-Mg-Cu aluminium alloys with the phase structures and thermal behaviours of the equilibrium Al-Mg-Zn ternary system [37].

(The reactions in Section 2.2, Equations 2.1 and 2.2, are given again for reference. Equation 2.1 is the eutectic reaction at 480 °C:

$$L \leftrightarrow (Al) + \tau \qquad 2.1$$

where *L* is the liquid phase, (Al) is face centred cubic (FCC) aluminium solid solution and τ is the $Mg_{32}(Zn,Al)_{48}$ cubic structure phase.

Equation 2.2 is the quasi-peritectic reaction at 476 °C:

$$L + \tau \leftrightarrow (Al) + \eta \qquad 2.2$$

where *L*, *(Al)*, and τ have the same meanings as before; η is the $MgZn_2$ hexagonal structure phase.)

The phases that can coexist after solidification after the reaction of Equations 2.1 and 2.2 are $\tau + (\mathrm{Al}) + \eta$, depending the progress of the reaction in Equation 2.2.

5.3.2. Effect of solidification cooling rate

It seemed surprising that the τ phase was present only in Alloy 7D, while Alloy 7D-V had only the η phase, especially given that both had the same composition. Alloy 7D was produced with HPDC where the cooling rate was extremely high, in the order of 10^3 Ks^{-1} [39], which must have suppressed equilibrium solidification. The result was an as-cast structure with τ being present, following Equation 2.1, contrary to the case of phases calculated with the Scheil model in Figure 4.33.

On the other hand, Alloy 7D-V was produced by cooling in vacuum where the cooling rate was lower. A lower cooling rate allowed enough time for the quasi-peritectic reaction of Equation 2.2 to be completed. This time, the result was that the η phase formed.

5.3.3. Effect of alloy composition

The cooling rate by HPDC for Alloys 7A to 7E was all very fast, in the order of 10^3 Ks^{-1} for HPDC [39]. It would then be expected that all the alloys would have the τ phase in their structures, but it was not the case, especially for Alloys 7A and 7B which only had the η phase.

An over simplistic explanation could be found by inspecting the alloy compositions shown in Table 5.4, which also shows the Zn:Cu ratio of all the alloys. It was clear that a higher Zn:Cu ratio (Alloys 7A and 7B) stabilised the η phase, while the lower Zn:Cu ratios (Alloys 7C to 7E) stabilised the τ phase. It could be that because the hexagonal $MgZn_2$ phase has a high stoichiometric Zn content of 66.6%. More Cu would be found in the cubic $Mg_{32}(Al,Cu)_{48}$ phase, which has an isotypic structure with the $Mg_{32}(Al,Zn)_{48}$ phase. The Zn:Cu ratio of Alloy 7D was an exception, falling between the ratios of Alloys 7C and 7E. The absolute value of Cu could maybe have some effect.

Table 5.4. Bulk compositions and Zn:Cu ratio of R-HPDC alloys.

	Zn	Mg	Cu	
Alloy		at.%		Zn : Cu
7A	2.98	2.11	0.34	8.88
7B	2.68	1.76	0.29	9.13
7C	3.66	3.08	0.73	5.00
7D	2.80	2.48	0.59	4.77
7E	2.52	2.85	0.72	3.49

5.3.4. Eutectic alloys

The rationale for the eutectic Alloys E-A and E-B was to reproduce the eutectics of Alloys 7A and 7D on a macro-scale in order to assess the properties of the respective eutectics. The eutectics in Alloys E-A and E-B consisted of a dilute (Al) phase (Tables 4.5 and 4.6 in Sections 4.7.1 and 4.7.2) and, the other was a highly alloyed Al-Zn-Mg-Cu containing phase.

Alloys E-A and E-B were targeted to be the same as the eutectic compositions of Alloys 7A and 7D, respectively. The comparison of Alloy E-A to Alloy 7A shows that in both cases a hexagonal phase was present, as expected.

It was unexpected that the phases in Alloys E-B and 7D differed, the hexagonal phase and the cubic phase being present in different alloys, while FCC (Al) appeared in both structures. This was most probably due to a cooling rate effect discussed in Section 5.3.2, because the eutectic compositions of Alloys E-B and 7D were the same.

Table 5.4 shows the average EDX results of the phases found in the two eutectic alloys. It was clear that as the Cu concentration of the alloy increased, so did the Cu concentration in the Al-Zn-Mg-Cu-containing and Al-rich phases, while the Zn content of these phases decreased and the Al concentration stayed constant.

The Mg concentration in the Al-Zn-Mg-Cu phase changed slightly with the changes in alloying, while the Mg concentration increased in the Al-rich phase with increased Cu alloying and decreased Zn alloying. It can also be seen that there is a limit to the mutual solid solubility of Zn, Mg and Cu in Al at ~11 at.%.

The cooling DSC results of Alloys E-A to E-C showed that a second peak developed. This second peak was interpreted as a ternary eutectic reaction with three phases co-solidifying. The relative size of the three phases was also very similar. The third phase, Al_2Cu, sometimes seemed divorced from the other two phases and at other places was associated with (Al). The first reaction peak was Equation 2.2, while the second reaction could be a ternary eutectic reaction presented as Equation 5.1:

$$L \leftrightarrow (Al) + \eta + Al_2Cu \qquad 5.1$$

Equation 5.1 is totally speculative because EDX were performed on the as-cast samples solidified in air, while the DSC analyses were at a cooling rate of 20 °C/min. No comment can be made on the mechanism of reaction, but this could be a future topic for research.

Table 5.5 shows the adjusted EDX results of the phases found in the three eutectic alloys. It was clear that as the Cu concentration of the alloy increased, so did the Cu concentration in the Al-Zn-Mg-Cu containing and Al-rich phases, while the Zn content of these phases decreased and the Al concentration stayed constant. A third phase, Al_2Cu, was found in Alloy E-C, because the alloy was probably super-saturated with Cu.

Eutectic Alloy E-C was produced to be compared to the Al-Zn-Mg-Cu phase of the eutectic in an as-cast structure from literature Alloy H [32] for which the Al:Zn:Mg:Cu

ratio of ~1:1:1:1 was found. Table 5.6 shows that the eutectic Alloy E-C compared favourably with the findings measured with TEM EDX.

Table 5.5. Corrected EDX values of eutectic alloy lamellae.

		Al	Zn	Mg	Cu
	Alloy	at.%			
Al-Zn-Mg-Cu lamellae	E-A	22.8	38.5	25.9	12.8
	E-B	21.9	31.1	28.1	18.9
	E-C	24.0	25.9	28.7	21.5
Al lamellae	E-A	89.2	7.7	2.2	0.9
	E-B	89.0	7.6	1.4	2.0
	E-C	89.9	6.7	1.1	2.4
Al_2Cu	E-C	67.2	1.6	0.4	30.8

Table 5.6. Compositions of Al-Zn-Mg-Cu lamellae in Alloys E-C and H [32].

		Al	Zn	Mg	Cu
	Alloy	at.%			
Al-Zn-Mg-Cu lamellae	E-C	24.0	25.9	28.7	21.5
	H	25.0	24.0	27.0	23.0

The Mg-content of the Al-Zn-Mg-Cu phase was ~27 at.% in the Al-Zn-Mg-Cu lamellae, which was different from the stoichiometric composition of the σ phase ($Mg(Al,Cu,Zn)_2$) with a Mg-content at 33.3 at.%, based on the $MgZn_2$ phase detected with XRD. Thus there was a Al-Zn-Mg-Cu phase with a hexagonal crystal structure but a different composition than $MgZn_2$. The Mg-content was also not the stoichiometric content of 39.5 at.% of the T ($Mg_{32}(Al,Cu,Zn)_{48}$) phase. This finding could be important for modelling the crystal structure of the Al-Zn-Mg-Cu phase in the eutectic.

5.3.5. Al-Mg-Zn and Al-Mg-Cu system similarities

In the Al-Mg-Cu system [38], there are two phases that have isotypic crystal structures to those of Equation 2.2 in the Al-Mg-Zn system. The one phase similar to the τ phase was the cubic structure T phase with the formula $Mg_{32}(Al,Cu)_{48}$. The

other one similar to the η phase is the hexagonal structured λ_3 phase with the formula $Mg(Al,Cu)_2$.

After the success of producing the eutectic phases, (Alloy E-A with the eutectic composition of dilute Alloy 7A), it was possible to measure the composition of the Al-Zn-Mg-Cu-containing phase, Section 5.3.3. It was expected that because of the similarity of these phases that Cu could be incorporated into the Al-Mg-Zn phases. The quantitative analysis of the Al-Zn-Mg-Cu phase, in the eutectic Alloy E-A, points to the probability that there was some mixing on the Mg sub-lattice which was the cause that the Mg-content of the Al-Zn-Mg-Cu phase was lower than the Mg-content of the η phase. The atomic arrangement in the unit cell was unclear, and could be a future topic of research.

The intention with Alloy E-B was to produce the eutectic of dilute Alloy 7D. The compositions were nearly identical (Section 4.7.2), but the crystal structures were different. The eutectic of the dilute alloy, Alloy 7D, had a cubic crystal structure, while the Al-Zn-Mg-Cu-containing phase in the eutectic alloy, Alloy E-B, had a hexagonal crystal structure. It was unfortunate that eutectic Alloy E-B had not turned out to exhibit the cubic crystal structure found in Alloy 7D and so it was also not possible to measure the composition for this cubic phase.

5.4. Microstructure observations in the T6 condition

5.4.1. General observations

The eutectic phases dissolved into the primary (Al) grains in all the alloys in the T6 condition after homogenisation, indicating that ample time was given for the dissolution to occur. All that remained in the microstructures were intermetallic phases on the grain boundaries and dispersoids within grains.

The grain sizes of the alloys in the T6 condition, Table 4.14, were larger than in the as-cast condition in Table 4.13. Manganese as an alloying element restricts grain growth during homogenisation through grain pinning by dispersoids [1], as was the case for Alloys 7A (0.33 wt% Mn) and 7D (0.40 wt% Mn). The level of Mn in Alloy 7B (0.11 wt% Mn) did not seem to have the same effect on the restriction of grain growth as in the other two Mn-containing alloys, Alloys 7A and 7D.

The grain size of Alloy 7C was also unchanged. Grain growth was restricted, in this case, by undissolved intermetallic phases on the grain boundaries. Alloy 7E did

not have the same level of grain boundary intermetallic phases, and therefore showed some increase in grain size.

Porosity was visible after heat treatment, which was most probably due to some gas that was still left after degassing. The long time, 170 h, at the homogenisation temperature, 470 °C, could lead to some porosity, even with small quantities of dissolved gas.

5.4.2. T6 impurity phases

The ratios of the elements in Table 4.12 are important to identify the different intermetallic phases. These intermetallic phases are also common to other 7xxx series aluminium alloys after homogenisation [1,29,30,34,36].

Manganese was not an impurity element, but an alloying element used for grain growth restriction during homogenisation. However, it formed an intermetallic compound with a major alloying element, namely Cu. Table 4.2 shows that Mn was not found in the eutectic areas of the Mn-containing alloys. In contrast, Figures 4.56, 4.57 and 4.59 showed that the Mn-containing intermetallic phase was found inside grains. This indicated that Mn was in solid solution in the grains after casting and that the Mn-containing intermetallic phase formed during the homogenisation heat treatment.

On assessing the intermetallic compositions of the Mn-containing alloys, Alloys 7A and 7D in Table 4.10, the ratio of Mn:Cu on average was ~1.72:1. Kolobnev et al. [48] referred to $Al_{12}Mn_2Cu$ in an aluminium alloy containing 5.1 wt% Cu and 0.83 wt% Mn. The experimentally measured ratios for the Al-Cu-Mn intermetallic phases fall within the range of the τ_1 phase in the Al-Cu-Mn system [49], which has a composition range with the formula: $Mn_{6+x}Cu_{4+y}Al_{29-x-y}$ where $0 \leq x \leq 2$, $0 \leq y \leq 1$, $y \leq x$. A Mn:Cu ratio of 1.75:1 was used for subsequent calculations.

Table 4.2 shows that Fe was present in the eutectic areas of Alloys 7C and 7E. This suggested that the Fe-containing intermetallic phase was present already in the eutectic in the as-cast condition, although not visually distinguishable with the SEM. It was expected because the temperatures of formation of Fe intermetallic phases were higher than the eutectic temperature of the alloys. Surprisingly, these intermetallic phases were needle-shaped and ~2 μm (Figures 4.62a and 4.64a), suggesting a high solidification cooling rate.

Alloys 7C and 7E with Fe-containing intermetallic phases had a Fe:Cu ratio of ~1:2, and Al:Fe close to ~7:1. This is the regularly reported intermetallic phase with a composition of Al_7FeCu_2 [1,29,30,34,36].

The second intermetallic phase in Alloy 7E was the regularly reported S phase (Al_2MgCu), with an Al:Mg:Cu ratio of ~2:1:1 [1,29,30,33].

Table 4.2 shows that Si was also found in the eutectic of Alloy 7C. Alloy 7C had an intermetallic phase containing Mg-Si-O with a ratio of ~1:1:1 (which was expressed as ~2:2:2 for the calculation below). It was deduced that there were two compounds, Mg_2Si [1] and SiO_2. This can easily be demonstrated because half of the Si-content is combined with the Mg-content resulting from Mg_2Si with a Mg:Si ratio of 2:1, while the other half of the Si-content is combined with the O-content resulting from SiO_2 with a Si:O ratio of 1:2. The SiO_2 was foreign to Alloy 7C as it lodged in the softer Mg_2Si during final polishing with colloidal SiO_2.

The Mg_2Si intermetallic phase was visually indiscernible with the SEM in the as-cast eutectic structure. It was unexpected since the formation temperature of the Mg_2Si intermetallic phases was higher than the eutectic temperature of the alloy [50].

5.5. T6 mechanical properties-grain size relationships

5.5.1. Influence of grain size on T6 hardness

It is not unusual to argue that the hardness measurements for the alloys in the T6 condition were dependent on the grain size. Figure 5.2 shows a plot of the T6 hardness (Table 4.15) as a function of the grain size (Table 4.14) according to the normal Hall-Petch relationship [51] presented in Equation 5.2:

$$Mechanical\ property \propto \frac{1}{\sqrt{Grain\ size}} \qquad 5.2$$

It can be seen from Figure 5.2 that there is no relationship of the hardness with the T6 grain size. The errors in Figure 5.2 seem large, but it should be remembered that the error value is the inverse square root of the linear error. Michalak et al. [52] in 1973, found that the grain sizes for different levels of deformation for AA7075 in the T6 condition did not influence the hardness of the alloy, which stayed constant. Miura et al. [53] also found that hardness was not a function of the grain size

comparing single crystal and polycrystalline microstructures of AA7475 in the T6 condition.

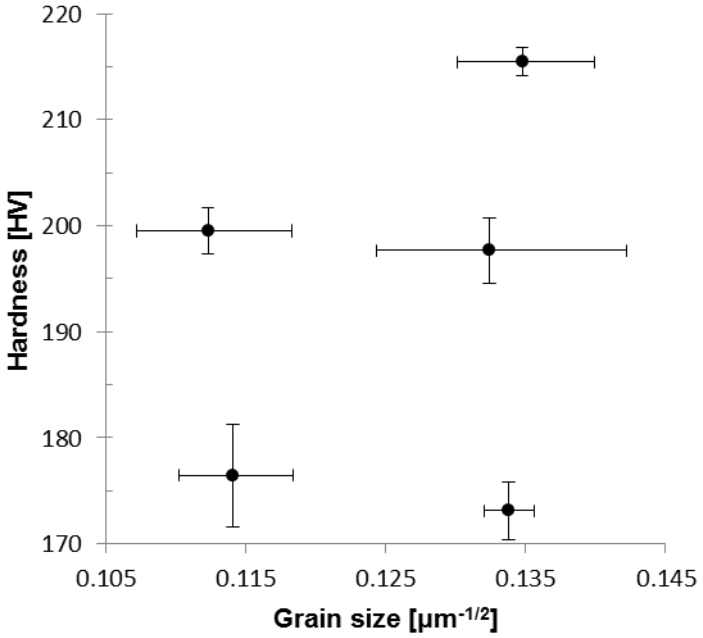


Figure 5.2. Hardness of Alloys 7A to 7E, in the T6 condition, as a function of the inverse square root of the grain size.

5.5.2. Influence of grain size on T6 yield strength

It could also be argued that the yield strength measurements for the alloys in the T6 condition were dependent on the grain size. Figure 5.3 shows a plot of the T6 yield strengths, in Table 4.18, as a function of the grain sizes, in Table 4.14, again according to the Hall-Petch relationship presented in Equation 5.1.

It can be seen from Figure 5.3 that again there is no relationship of the yield strength with the T6 grain size. The spread of yield strength data is similar to the spread of hardness data presented in Figure 5.2. Michalak et al. [52] also found that the grain sizes for different levels of deformation for AA7075 in the T6 condition did not influence the yield strength of the alloy but stayed constant. Their data took into account the influence of tensile sample geometry by using the same size tensile specimens.

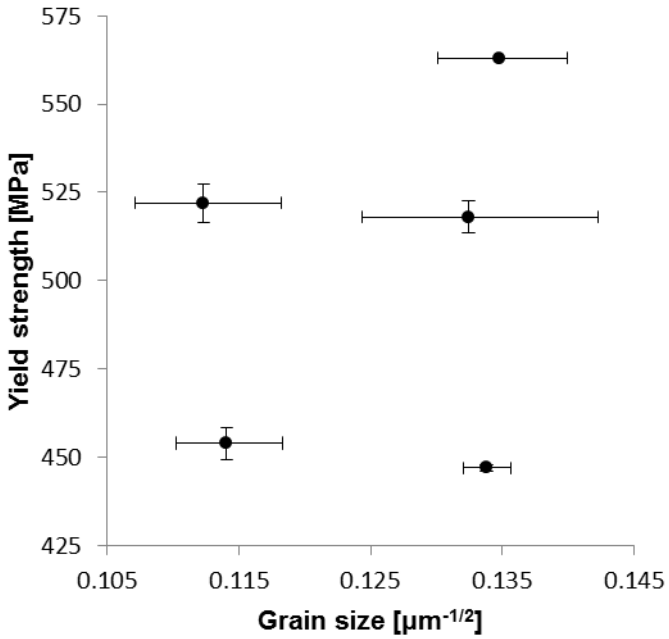


Figure 5.3. Yield strength of Alloys 7A to 7E, in the T6 condition, as a function of the inverse squar root of the grain size.

6. Mechanical properties modelling

6.1. Mechanical properties-composition model considerations

Material properties must be related to the composition of the material, and usually microstructure. Three situations are possible as the level of alloying increases: material properties could increase, or as the matrix becomes supersaturated, material properties could reach a plateau, or there could also be a decline in material properties after supersaturtion of the matrix.

In this study, it was postulated the hardness and/or yield strength could be modelled as a function of the level of alloying. Properties of the Al-Zn-Mg-Cu aluminium alloy family can be influenced by precipitation heat treatment by changing the microstructure on the nanoscale [1]. The yield strength, for instance, changes as a function of the artificial ageing time and temperature [1], Figure 2.24.

Unfortunately, precipitate composition studies for Al-Zn-Mg-Cu aluminium alloys, specifically in the T6 condition were extremely rare.

6.2. T6 mechanical properties-composition model

6.2.1. Weight fraction to atomic fraction conversion

Microsoft Excel was used to calculate the atomic fractions of the precipitate phase present. Equation 6.1 is the elementary chemistry equation that relates the amount of moles of a substance to the weight of a substance by the molecular weight of the substance found in the Periodic Table:

$$n = \frac{m}{M} \tag{6.1}$$

where *n* is the number of moles, *m* is the weight and *M* is the molecular weight.

Element quantity inputs in the calculations were done in weight percentage (wt%) (in which unit the OES results were reported). Equation 6.2, an extended form of Equation 6.1, was then used to convert the wt% to atomic percentages (at.%) for an multi-element alloy:

$$at.\%_i^0 = \frac{\frac{wt\%_i}{M_i}}{\sum_i \frac{wt\%_i}{M_i}} \times 100 \tag{6.2}$$

where $at.\%_i^0$ is the initial atomic percentage of a specific element in the alloy's composition and M_i is the molecular weight of the specific element.

6.2.2. T6 Precipitate composition

The precipitate composition determined by Sha et al. [54] was used in the T6 mechanical properties-composition model. The composition of the precipitate is given in atomic fractions in Table 6.1, Al is the balance, where purple is for Zn, blue for Mg and orange for Cu.

Table 6.1. Atomic fractions of T6 precipitate by Sha et al. [54]. The Zn fraction is purple highlighted, the Mg fraction is blue highlighted and the Cu fraction is orange highlighted.

Element	Atomic fraction	
Zn	0.454	(f_{Zn})
Mg	0.386	(f_{Mg})
Cu	0.086	(f_{Cu})

$$f_{Zn} + f_{Mg} + f_{Cu} + f_{Al} = 1$$

6.2.3. T6 precipitate volume fraction calculations

Evaluation of the initial T6 hardness-composition model was done with the measured compositions of Zn, Mg and Cu. Equations 6.3 to 6.5 and the precipitate composition fractions in Table 6.1 were used to calculate the volume fraction of the precipitate.

$$f_v^{Zn} = \frac{at.\%_{Zn}^0}{f_{Zn}} \quad 6.3$$

$$f_v^{Mg} = \frac{at.\%_{Mg}^0}{f_{Mg}} \quad 6.4$$

$$f_v^{Cu} = \frac{at.\%_{Cu}^0}{f_{Cu}} \quad 6.5$$

where f_v^i expressed in a percentage is the precipitate volume fraction associated with each major alloying element.

The atomic percentage available for precipitation of the precipitate should be governed by the element that is limiting, in other words, the calculated volume

fraction of the precipitate for the element which had the smallest value. Table 6.2 shows the calculated precipitate volume fractions according to the limiting composition element, calculated for each of the major alloying elements. Purple blocks denote Zn-limited, the blue block denotes Mg-limited, and orange blocks denote Cu-limited compositions respectively. Equations 6.3 to 6.5 were used for the calculations.

A Zn-limited alloy infers that there was an excess of Mg and Cu relative to the composition of the precipitate. In turn, a Mg-limited alloy infers that there was an excess of Zn an Cu relative to the precipitate composition. Again, a Cu-limited alloy infers that there was an excess of Zn and Mg relative to the precipitate composition.

6.2.4. T6 hardness-composition relationship

Figure 6.1 shows the relationship of the T6 hardness as a function of precipitate volume fraction for the limiting element in Table 6.2. The colours of the markers have the same significance as the blocks in Table 6.2. Figure 6.1 shows that there is a reasonable linear correlation (R^2 = 0.941) between the hardness and the precipitate volume fraction for the limiting element. The line was fitted to the points of all five R-HPDC alloys in the T6 condition.

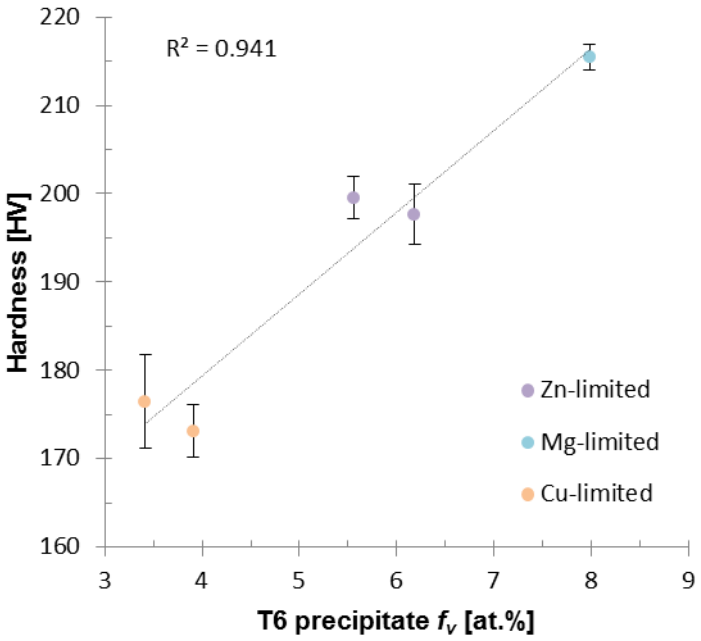


Figure 6.1. Effect of precipitate volume fraction on T6 hardness, excluding impurity reactions.

Table 6.2. Precipitate volume fraction calculations excluding impurity reactions. Purple blocks indicate Zn-limited, the blue block indicates Mg-limited and orange blocks indicate Cu-limited alloys.

Alloy	Element	f_V (at.%)
7A	Zn	6.57
	Mg	5.47
	Cu	3.91
7B	Zn	5.91
	Mg	4.55
	Cu	3.42
7C	Zn	8.07
	Mg	7.98
	Cu	8.53
7D	Zn	6.18
	Mg	6.45
	Cu	6.84
7E	Zn	5.56
	Mg	7.38
	Cu	8.39

6.2.5. T6 yield strength-composition relationship

Figure 6.2 shows the relationship for the T6 yield strengths as a function of precipitate volume fraction for the limiting element in Table 6.2. The colours of the markers have the same significance as the blocks in Table 6.2.

Figure 6.2 shows that there is again a reasonable linear correlation (R^2 = 0.9431) between the yield strength and the precipitate volume fraction for the limiting element. The line was again fitted to the points of all five R-HPDC alloys in the T6 condition.

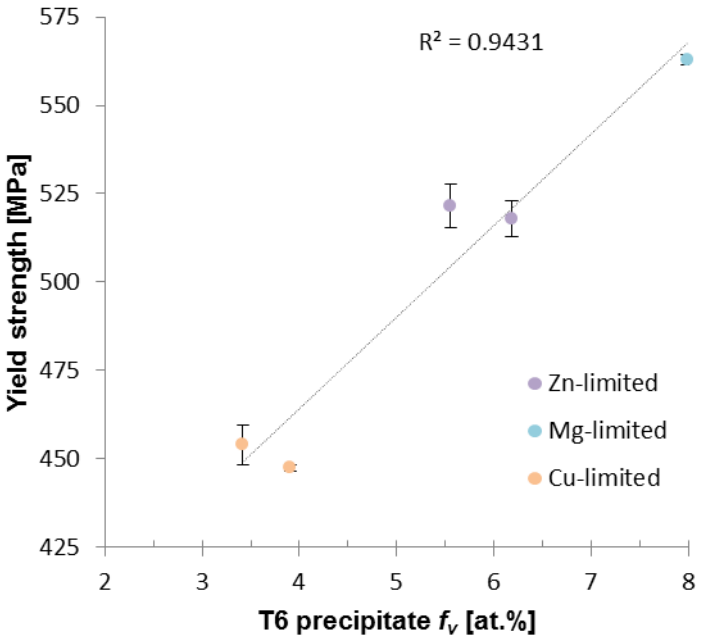


Figure 6.2. Effect of precipitate volume fraction on T6 yield strength, excluding impurity reactions.

6.3. Improved T6 mechanical properties-composition model

6.3.1. Improved model considerations

It was seen from Figures 6.1 and 6.2 that there is definitely a relationship of the mechanical properties in the T6 condition to the alloy composition with the precipitate composition as an intermediary.

The findings beg the question whether the other elements in the composition played a role. Could the basic mechanical properties-composition model be improved by taking into account the effect of the other impurity elements?

6.3.2. Improved precipitate volume fraction calculations

The reaction of impurity elements were taken into account by subtracting the necessary at.% amount from the specific major alloying element. The major alloying elements together with the reaction ratios of the phases identified in Section 5.4.2 for the T6 heat treated condition are given in Equations 6.6 to 6.8.

There were no reactions with Zn by impurity elements, thus:

$$at.\%_{Zn}^{A} = at.\%_{Zn}^{0} \quad 6.6$$

For Mg reacting with Si to form Mg_2Si:

$$at.\%_{Mg}^{A} = at.\%_{Mg}^{0} - 2 \times at.\%_{Si}^{0} \quad 6.7$$

For Cu reacting with Fe and Mn to form Al_7FeCu_2 and $Al_{12}Mn_{1.75}Cu$:

$$at.\%_{Cu}^{A} = at.\%_{Cu}^{0} - 2 \times at.\%_{Fe}^{0} - 0.571 \times at.\%_{Mn}^{0} \quad 6.8$$

where $at.\%_{i}^{A}$, in Equations 6.6 to 6.8, are the atomic fractions *available* for precipitation.

The precipitate composition was the same as in Table 6.1. The individual volume fractions for precipitation were calculated for each precipitate element using Equations 6.9 to 6.11:

$$f_v^{Zn+} = \frac{at.\%_{Zn}^{A}}{f_{Zn}} \quad 6.9$$

$$f_v^{Mg+} = \frac{at.\%_{Mg}^{A}}{f_{Mg}} \quad 6.10$$

$$f_v^{Cu+} = \frac{at.\%_{Cu}^{A}}{f_{Cu}} \quad 6.11$$

where f_v^{i+} again expressed in a percentage was the precipitate volume fraction associated with each major alloying element, ***plus*** taking into account the effect of the impurity reactions.

Again, the atomic percentage available for precipitation of the precipitate was governed by the element that is limiting, in other words, the calculated volume fraction of the precipitate for the element which had the smallest value.

In this case, Table 6.3 shows the calculated precipitate volume fractions according to the limiting composition element including impurity reactions, with the different colours for the different elements. Equations 6.9 to 6.11 were used for the calculations. Table 6.3 shows the volume fraction values results calculated for each of the major alloying elements taking into account the contribution of the impurity element reactions.

Again, a Zn-limited alloy infers that there was an excess of Mg and Cu relative to the Zn composition of the precipitate. In turn, a Mg-limited alloy infers that there was an excess of Zn an Cu relative to the Mg precipitate composition, and a Cu-limited

alloy infers that there was an excess of Zn and Mg relative to the Cu precipitate composition.

Table 6.3. Precipitate volume fractions as a function of the element found in the precipitate, controled by the limiting element. Purple indicates a Zn limit, blue a Mg limit and orange a Cu limit.

Alloy	Element	f_V (at.%)
7A	Zn	6.57
	Mg	5.47
	Cu	2.61
7B	Zn	5.91
	Mg	4.55
	Cu	2.96
7C	Zn	8.07
	Mg	7.30
	Cu	7.69
7D	Zn	6.18
	Mg	6.45
	Cu	5.25
7E	Zn	5.56
	Mg	7.38
	Cu	7.83

6.3.3. Improved T6 hardness-composition relationship

Figure 6.3 shows the effect of taking into account the impurity reactions on the volume fraction of the precipitate. The line in Figure 6.3 was nearly a perfect fit (R^2 = 0.9996) in comparison with the relationship without taking into account the effect of impurity element reactions (R^2 = 0.941), Figure 6.1.

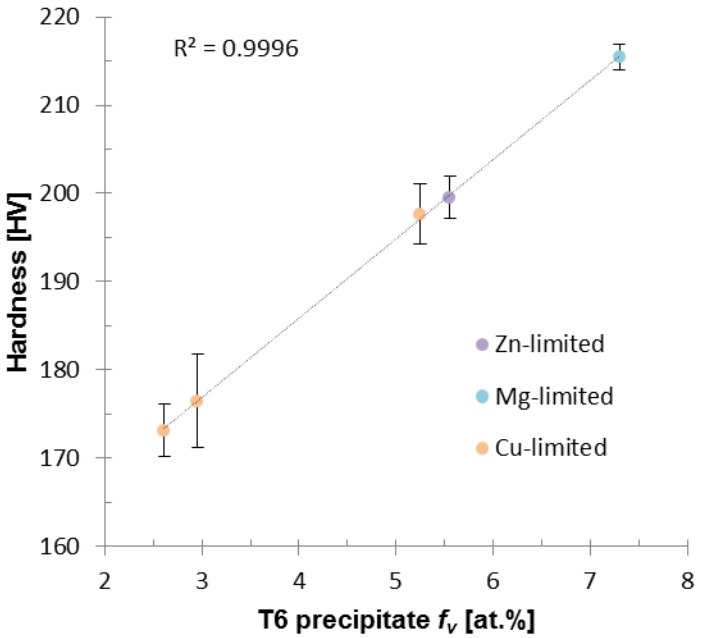


Figure 6.3. Effect of precipitate volume fraction on T6 hardness, including impurity element reactions.

6.3.4. Improved T6 yield strength-composition relationship

Figure 6.4 shows the effect taking into account the impurity reactions on the volume fraction of the precipitate and the yield strength. The line in Figure 6.4 was again nearly a perfect fit (R^2 = 0.9973) in comparison with the relationship without taking into account the effect of impurity element reactions (R^2 = 0.9431), Figure 6.2.

6.4. T6 hardness-composition model applied to wrought alloys

Applicability of the hardness-composition model to wrought alloys was also tested. Table 6.4 shows the compositions and corresponding hardness values of different Al-Zn-Mg-Cu aluminium alloys in the T6 condition, 120 °C for 50 h [55-58]. Alloy designations are also included.

Table 6.4 also indicates the precipitate volume fractions that were calculated with the improved composition model in this work. It can be seen that the precipitate volume fractions are limited by different elements, be it Zn, Mg or Cu. Only the limiting volume fraction was given in the Table 6.4 for clarity.

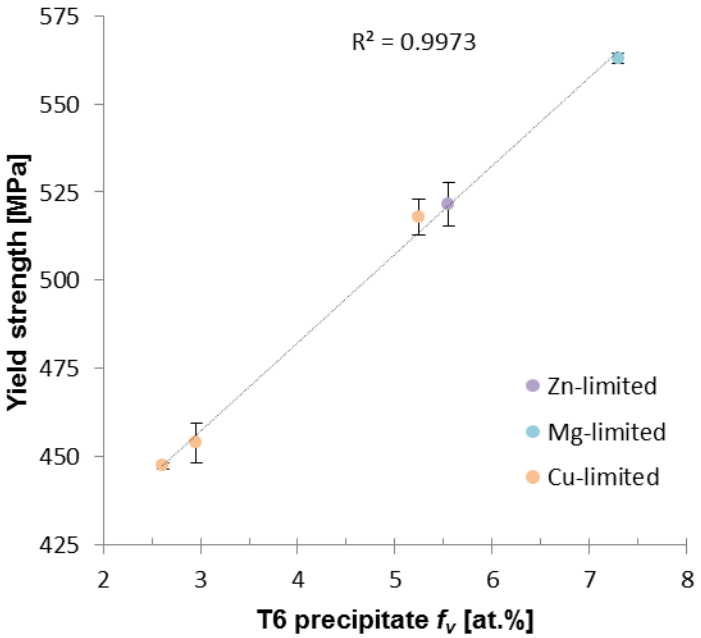


Figure 6.4. Effect of precipitate volume fraction on T6 yield strength, including impurity element reactions.

Figure 6.5 is a plot of the hardness values as a function of the precipitate volume fractions in Table 6.4. The wrought AA7040 material used in this study was heat treated the same as the R-HPDC material. It can be seen from Figure 6.5 that the T6 hardness-composition model describes the data well. Relevance of the model to wrought alloys was unexpected, because of the difference in processing.

Table 6.4. Composition and hardness data from literature [55-58] and calculated precipitate volume fractions, including impurity reactions. Purple blocks indicate Zn-limited, blue blocks indicate Mg-limited and the orange block indicates Cu-limited alloys.

	Zn	Mg	Cu	Si	Fe	Al		f_v	
Alloy designation	wt%						HV	at.%	Reference
Wrought AA7040	5.32	1.49	1.31	-	0.05	91.83	189	4.45	
not specified	8.02	1.75	1.99	-	-	88.24	197	5.34	[55]
Wrought AA7475	5.39	2.19	1.46	0.04	0.05	90.87	194	5.09	[56]
Wrought AA7475	5.74	2.58	1.65	0.06	0.07	89.90	199	5.44	[57]
SSM AA7075	6.08	2.50	1.93	0.40	0.46	88.63	190	4.57	[58]

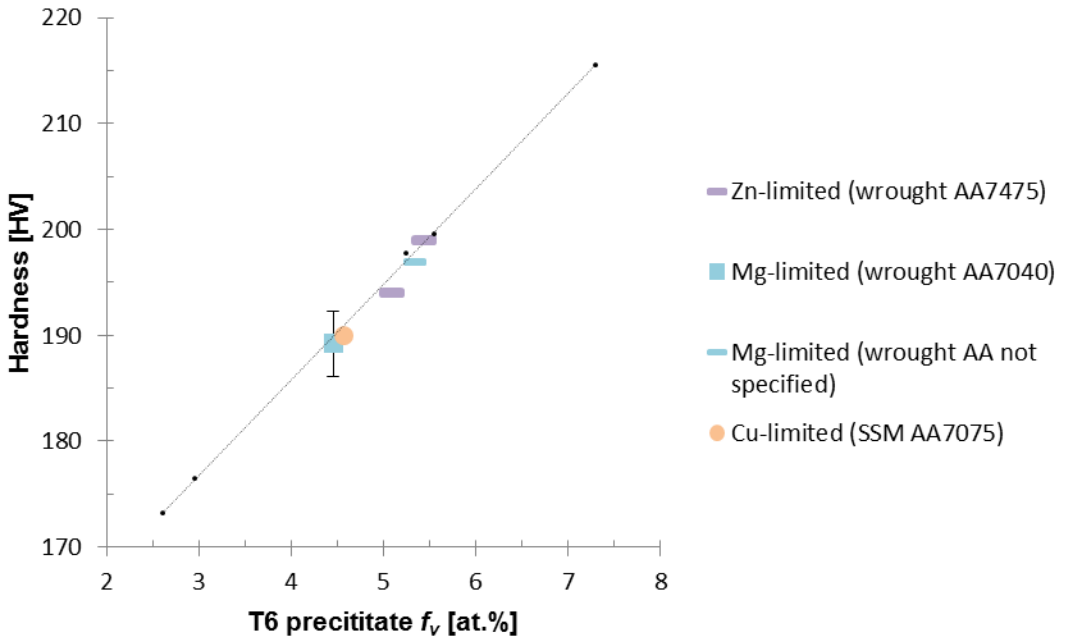


Figure 6.5. Effect of precipitate volume fraction on T6 hardness, applied to wrought alloy literature data [55-58] (including impurity reactions).

6.5. T6 yield strength-composition model applied to AA7075 T6

Aluminium alloy 7075 is the common standard for comparing properties of Al-Zn-Mg-Cu aluminium alloys due its long development history. The maximum tensile properties are achieved in the T6 condition for which the artificial ageing heat treatment is conventionally performed at 120 °C for 24 h, Figure 2.24.

Other Al-Zn-Mg-Cu aluminium alloys have different two-step combinations in the temperature range from 120 °C to 177 °C to acquire the T6 condition [4]. This makes it difficult to directly compare typical mechanical property data of other Al-Zn-Mg-Cu aluminium alloys, other than the typical mechanical properties for AA7075.

Table 6.5 shows the alloying ranges of elements for AA7075, as well as the nominal composition of major alloying and impurity elements. Lastly, Table 6.5 shows the commonly accepted typical yield strength of AA7075 [59].

Table 6.5. Composition specifications of AA7075 and the typical yield strength [59].

	Zn	Mg	Cu	Si	Fe	Mn	Al	YS
AA7075				wt%				MPa
Minimum	5.10	2.10	1.20	-	-	-	Balance	
Nominal	5.60	2.50	1.60	0.20	0.25	0.15	Balance	503
Maximum	6.10	2.90	2.00	0.40	0.50	0.30	Balance	

Table 6.6 shows the calculated precipitate volume fractions for the nominal composition of AA7075 in Table 6.5. These calculations take into account the reactions of the major alloying elements with impurity elements. This shows that the nominal composition of AA7075 in limited by the amount of Cu.

Table 6.6. Precipitate volume fractions as a function of the element found in the precipitate, controled by the limiting element for the nominal comopostion of AA7075, including impurity element reactions.

	Element	f_v (at.%)
AA7075	Zn	5.31
	Mg	6.46
	Cu	4.80

Figure 6.6 is a plot of the precipitate volume fraction from Table 6.6, and the *typical* yield strength for AA7075 in the T6 condition from Table 6.5. Again, as with the hardness data [55-58], it was unexpected that the yield strength-composition model describes the data point so well, especially considering that the R-HPDC and wrought alloys were processed so differently.

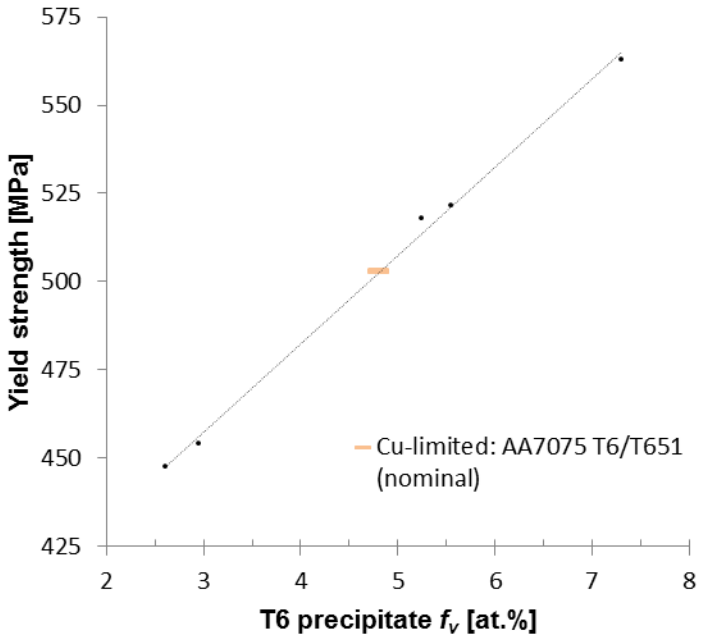


Figure 6.6. Applying the composition model to the typical yield strength of the nominal composition of AA7075 in the T6 condition, including impurity reactions.

6.6. T73 mechanical property-composition model

The T73 condition was a condition in which the alloys were fully over-aged. The hardness that resulted from this heat treatment condition could also be evaluated by the proposed composition model.

6.6.1. T73 Precipitate composition

The equilibrium precipitate composition measured by Marlaud et al. [4] was used in the T73 hardness-composition model. The composition of the precipitate is given in atomic fractions in Table 6.6.7, Al is the balance, where purple is for Zn, blue for Mg and orange for Cu as before.

Table 6.7. Atomic fractions of T73 precipitate by Marlaud et al. [4] where the Zn fraction is purple highlighted, the Mg fraction is blue highlighted and the Cu fraction is orange highlighted.

Element	Atomic fraction	
Zn	0.390	(f_{Zn})
Mg	0.330	(f_{Mg})
Cu	0.130	(f_{Cu})

$$f_{Zn} + f_{Mg} + f_{Cu} + f_{Al} = 1$$

6.6.2. T73 hardness-composition relationship

Evaluation of the T73 hardness-composition model was done in the same way as in Section 6.2.3 with Equations 6.3 to 6.5, but this time with the T73 precipitate composition given in Table 6.7. The measured appropriate compositions of Zn, Mg and Cu were again used.

In the same way as before, the atomic percentage available for precipitation of the precipitate was governed by the element that is limiting, in other words, the calculated volume fraction of the precipitate for the element which had the smallest value. The influence of impurities was not taken into account, at this point, in calculations.

Table 6.8 shows the calculated precipitate volume fractions according to the limiting composition element. All the alloys were Cu-limited compositions. Table 6.8 also shows the volume fraction values results calculated for each of the other major alloying elements. A Cu-limited alloy infers that there was an excess of Zn and Mg relative to the precipitate composition.

Table 6.8. Precipitate volume fraction calculations excluding impurity reactions. Orange blocks indicate Cu-limited alloys.

Alloy	Element	f_V (at.%)
7A	Zn	7.65
	Mg	6.40
	Cu	2.58
7B	Zn	6.88
	Mg	5.33
	Cu	2.26
7C	Zn	9.39
	Mg	9.34
	Cu	5.64
7D	Zn	7.20
	Mg	7.54
	Cu	4.52
7E	Zn	6.47
	Mg	8.63
	Cu	5.55

Figure 6.7 shows the relationship of the T73 hardness as a function of precipitate volume fraction for the limiting element. The colours of the markers have the same significance as the blocks in Table 6.8.

Figure 6.7 shows that there is a linear correlation (R^2 = 0.9867) between the hardness and the T73 precipitate volume fraction for the limiting element. The line was fitted to four points of the R-HPDC alloys, excluding Alloy 7D, in the T73 condition.

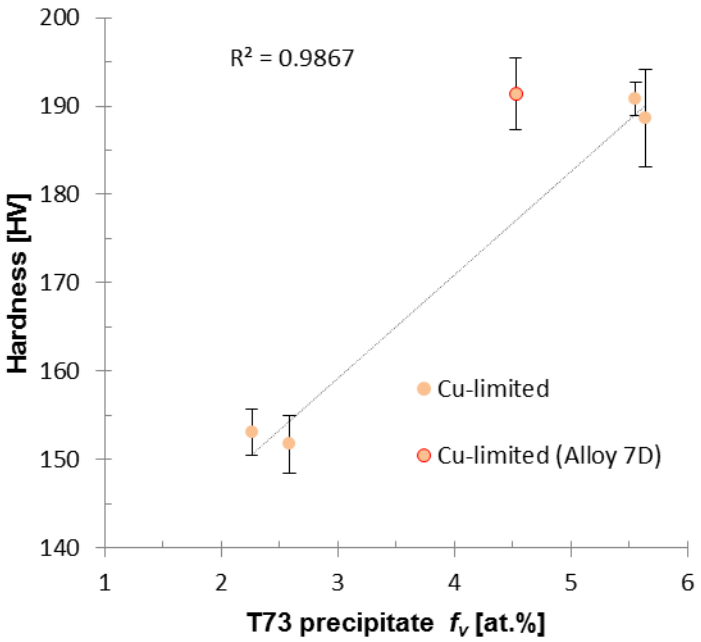


Figure 6.7. Effect of precipitate volume fraction on T73 yield strength, excluding impurity reactions.

6.6.3. Improved T73 hardness-composition relationship

The reaction of impurity elements were now taken into account in the same way as described in Section 6.3.2 by Equations 6.6 to 6.8. Table 6.9 shows the calculated precipitate volume fractions, according to the limiting composition element including impurity reactions; orange blocks denote Cu-limited compositions. Again, a Cu-limited alloy infers that there was an excess of Zn and Mg relative to the precipitate composition.

Table 6.9. Precipitate volume fractions as a function of the element found in the precipitate, including impurity reactions, where orange blocks denote a Cu limited composition.

Alloy	Element	f_v (at.%)
7A	Zn	7.65
	Mg	6.40
	Cu	1.73
7B	Zn	6.88
	Mg	5.33
	Cu	1.96
7C	Zn	9.39
	Mg	8.54
	Cu	5.09
7D	Zn	7.20
	Mg	7.54
	Cu	3.47
7E	Zn	6.47
	Mg	8.63
	Cu	5.18

Figure 6.8 shows the effect taking into account the impurity reactions on the volume fraction of the T73 precipitate and the hardness. The line in Figure 6.8 was nearly a perfect fit (R^2 = 0.999) in comparison with the relationship without taking into account the effect of impurity element reactions (R^2 = 0.9867), Figure 6.7. The line was again fitted to four points of the R-HPDC alloys, excluding Alloy, 7D condition.

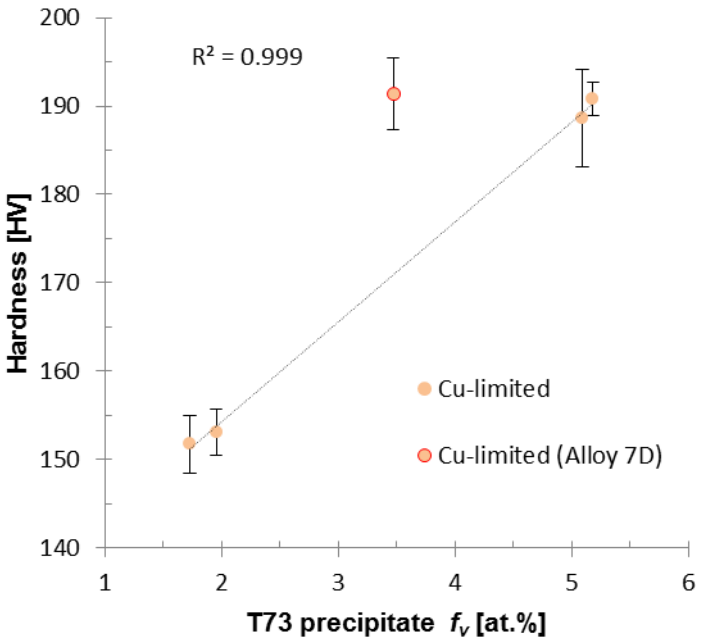


Figure 6.8. Effect of precipitate volume fraction on T6 hardness, including impurity element reactions.

6.6.4. A T73 hardness-composition model exception

In Figure 6.8 it is apparent that the point for Alloy 7D was an outlier in the T73 condition. There must have been some other contribution to the hardness of this alloy. The difference between Alloy 7D and the other alloys was that it contained a much higher concentration of Mn as an alloying element. Figure 6.9 shows the SEM-BSE image of the microstructure of Alloy 7D. It can be seen that there are many bright features in the shape of needles. These had been identified as $Al_{28}Mn_7Cu_4$ intermetallic compounds in Sections 4.12 and 5.4.2. Figures 6.10 and 6.11 show a smaller amount of $Al_{28}Mn_7Cu_4$ needles in Alloys 7A and 7B, which also contained Mn.

It could be argued that the hardness of a material is the sum of the deformation resistance of two contributors. If it was the case, then the T6 hardness would also not follow the hardness-composition relationship. It seems rather that if there are two contributors present that the contributor with the highest deformation resistance contributes the most. The intermetallics compounds and precipitates were both present implying the same amount of resistance in both the T6 and T73 conditions. The $Al_{28}Mn_7Cu_4$ intermetallics needles in the T73 could have played a more significant role than the η precipitates to resist deformation compared to the role of the η precipitates played in the T6 condition.

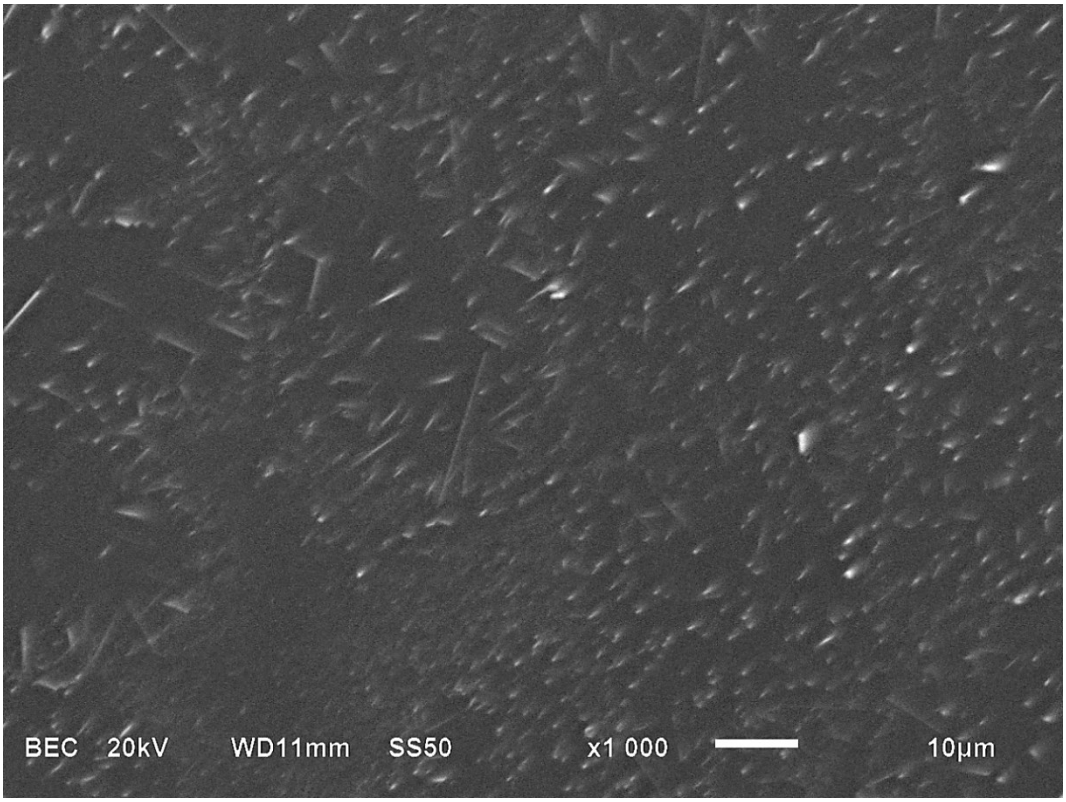


Figure 6.9 .SEM-BSE image of AlFeMn intermetallic needles in Alloy 7D in the T73 condition.

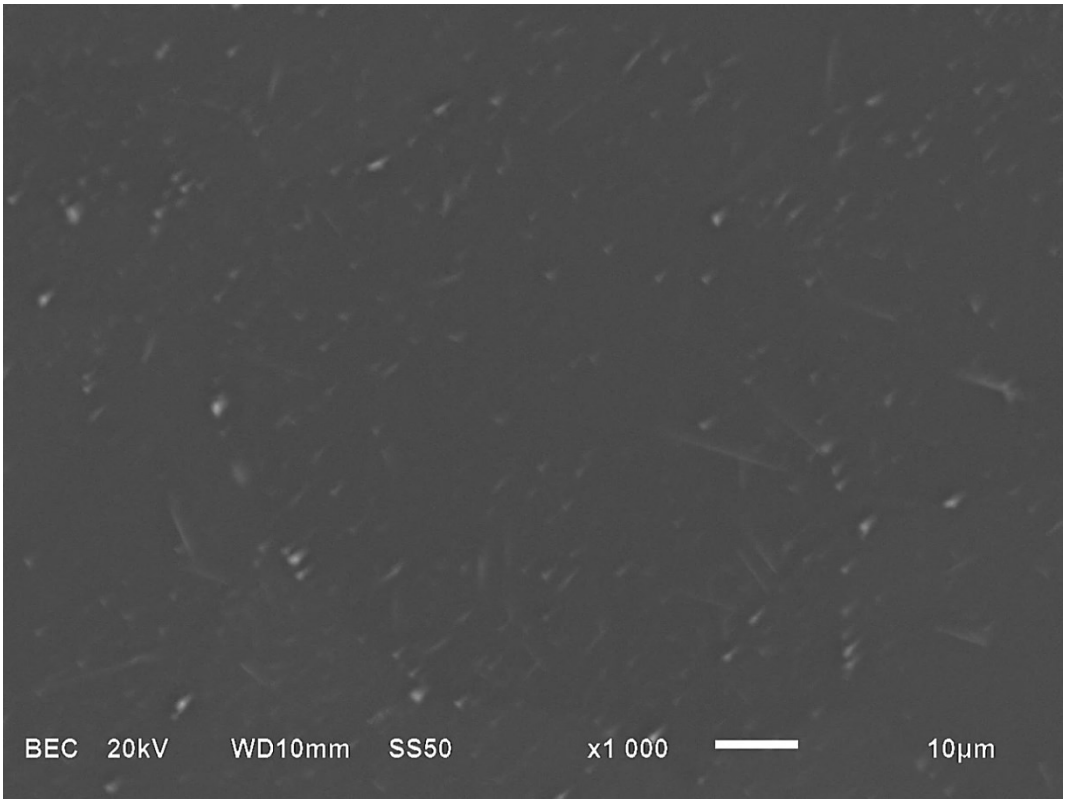


Figure 6.10. SEM-BSE image of AlFeMn intermetallic compounds in Alloy 7A in the T73 condition.

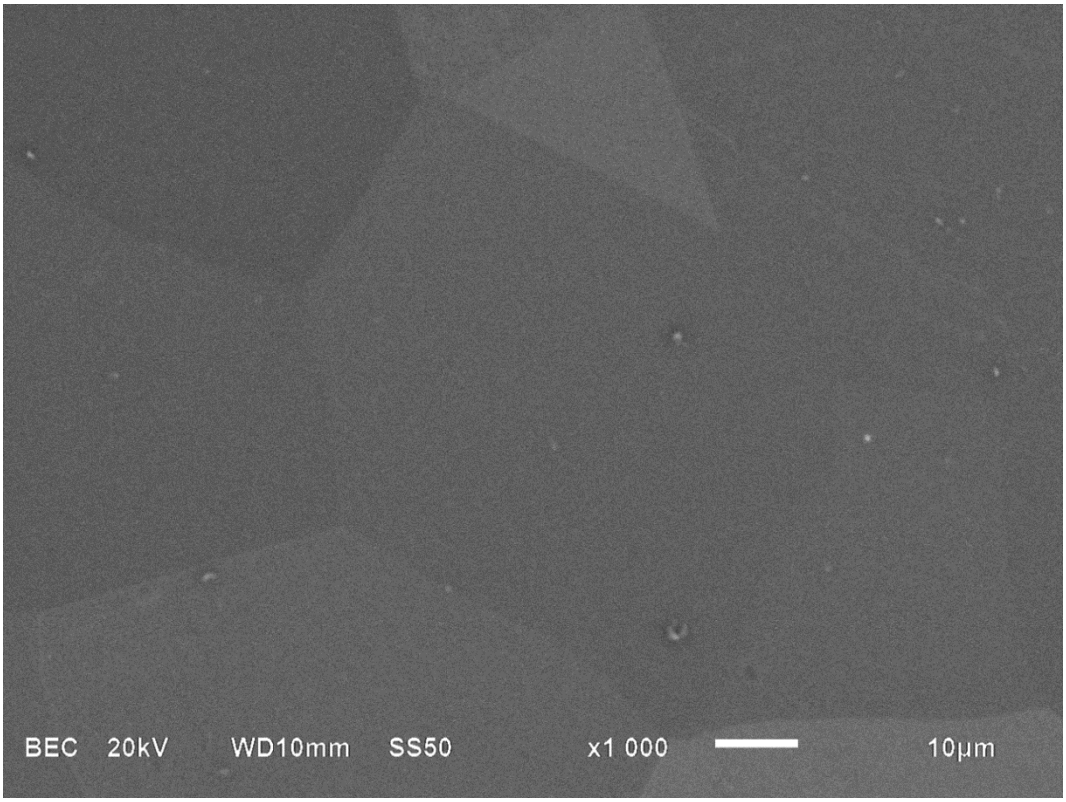


Figure 6.11. SEM-BSE image of AlFeMn intermetallic compounds in Alloy 7B in the T73 condition.

6.6.5. Improved T73 model applied to a wrought alloy

The wrought alloy AA7040 sample was also subjected to the same T73 heat treatment used on the R-HPDC alloys. The limiting element calculation was again performed with the OES measured composition of the alloy. Table 6.10 shows the volume fractions of each element and shows that Cu is the limiting element.

Table 6.10. Precipitate volume fractions as a function of the element found in the precipitate, including impurity reactions. Orange block denote a Cu limited composition.

	Element	f_v (at.%)
AA7040	Zn	5.85
	Mg	5.21
	Cu	4.08

The hardness of the wrought AA7040 in the T73 condition was plotted in Figure 6.12. The hardness felled on the line, which indicates that the hardness-composition model was also relevant for wrought alloys.

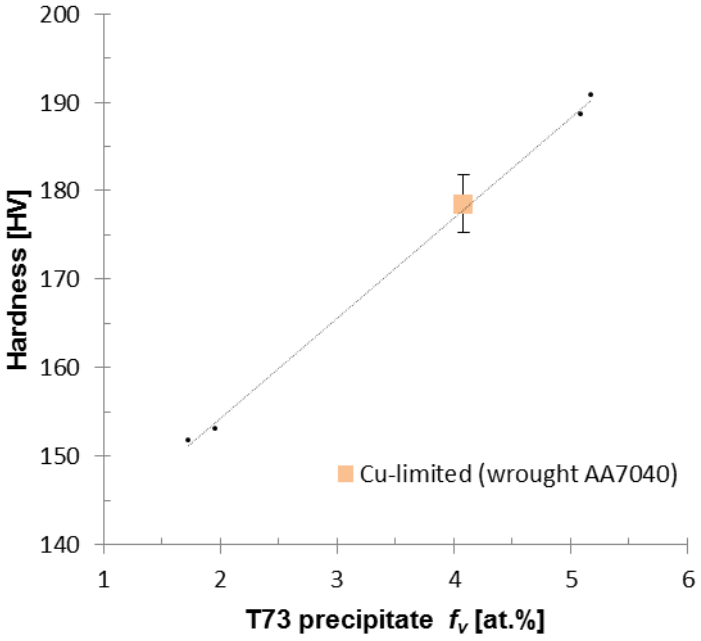


Figure 6.12. Applying the composition model to the hardness of wrought alloys 7040 in the T73 condition, including impurity reactions.

6.7. Interpretation of mechanical properties-composition model

6.7.1. General comments

The mechanical properties-composition model showed the expectation that material properties increase with increasing alloying additions is justified, in the range of alloying used in this study.

The basic mechanical properties-composition model, Sections 6.2.4 (Figure 6.1) and 6.2.5 (Figure 6.2), showed that there is a reasonable straight line relationship between the hardness of the R-HPDC alloys and their compositions, as well as a reasonable straight line relationship between the yield strengths of the R-HPDC alloys and their compositions.

On the other hand, the improved mechanical properties-composition model, Sections 6.3.3 (Figure 6.3) and 6.3.4 (Figure 6.4), showed that the mechanical

property relationships improved tremendously by including the effect of impurity element reactions with major alloying element reactions.

Another reason for the near-perfect fit of the improved material properties-composition model was the great care taken to be precise with the sampling of the composition with OES and correlating it to the hardness measurements in the same vicinity as the composition measurements.

6.7.2. T6 and T73 precipitate compositions

The T6 [54] and T73 [4] precipitate compositions (nano-scale) chosen were the intermediaries between composition and mechanical properties, hardness and yield strength (macro-scale), considered here.

As mentioned in Section 6.1 precipitate compositions were little reported in literature due to the difficulty with measuring on the atomic level. Precipitate compositions, if reported, were determined with atom probe tomography (APT). No APT results were available in open literature for Al-Zn-Mg-Cu aluminium alloys, especially 7075, in the standard T6 heat treatment (120 °C for 24 h).

Sha et al. [54] measured the composition of η-variant precipitates in an Al-Zn-Mg-Cu aluminium alloy that was subjected to equal channel angular pressing (ECAP) by which material was severely deformed. They [54] postulated that the precipitates found after one pass of ECAP were the same as those found after conventional T6 artificial ageing according to Equation 2.3 [42]. It seems that the postulate of Sha et al. [54] holds, considering that the artificial ageing heat treatment used in this study was basically the same as the conventional T6 artificial ageing heat treatment, especially for AA7075.

It is accepted that metastable precipitates evolve to equilibrium precipitates when Al-Zn-Mg-Cu aluminium alloys are heat treated to the over-aged condition, especially, the T73 condition. Marlaud et al. [4] measured the composition of large surface precipitates with SEM-EDX and the precipitates contained 39 at.% Zn, 33 at.% Mg and 13 at.% Cu and postulated that precipitate composition evolution finally ended in the composition of these near-equilibrium precipitates, as suggested by Equation 2.3.

This mechanical properties-composition model is unique, because no more information was necessary about the precipitates beside their compositions.

6.7.3. T6 hardness-composition relationship

It was clear from Section 5.5.1 that hardness was not a function of the grain size. Figure 6.7 is a re-examination of Figure 5.2, keeping in mind the results of the improved composition model. The lines in Figure 6.13 are for different levels of precipitate volume fraction. Results of the improved composition model show that alloys with a similar precipitate volume fractions had the same hardness level, irrespective of the grain size when Figure 5.2 is redrawn.

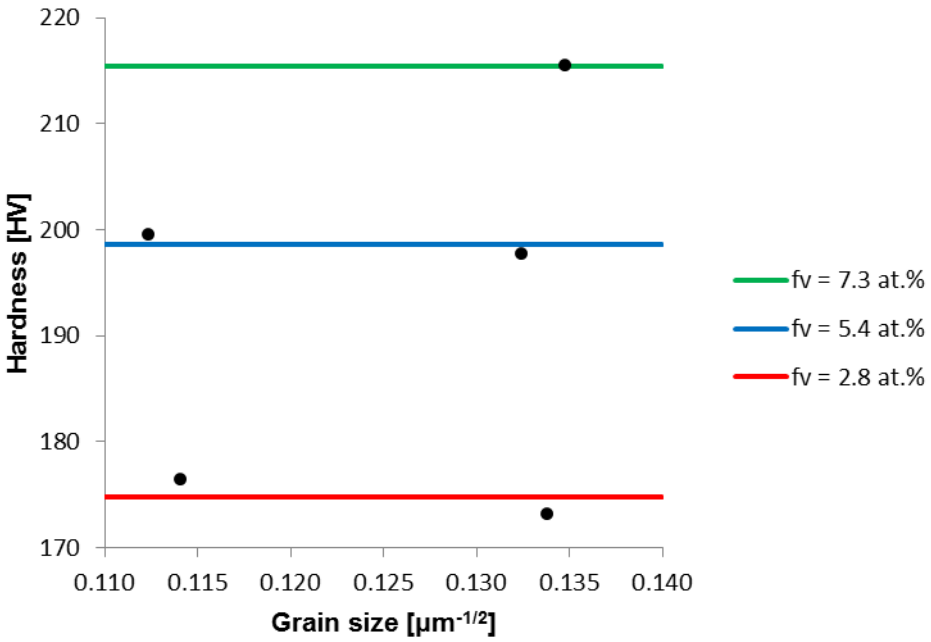


Figure 6.13. Hardess of Alloys 7A to 7E in the T6 condition, as a function of the square root of the grain size and precipitate volume fraction.

It can be concluded that Equation 2.4 can be reduced to Equation 6.13, for the hardness of Al-Zn-Mg-Cu aluminium alloys in the T6 condition:

$$Hardness \propto f(composition) \qquad 6.13$$

Further, application of the composition model to the hardness of wrought alloys validates the finding that hardness was not a function of grain size since grain sizes for the wrought alloys from literature, Table 6.4, was not specified but would surely vary.

6.7.4. T6 yield strength-composition relationship

It was clear from Section 5.5.2 that the yield strength was not a function of the grain size for these alloys. Figure 6.8 is again a re-examination of Figure 5.3 keeping in mind the results of the improved composition model. The lines in Figure 6.14 are for different levels of precipitate volume fraction. Results of the improved composition model show that alloys with a similar level of precipitate volume fraction had the same yield strength level irrespective of the grain size when Figure 5.3 is redrawn.

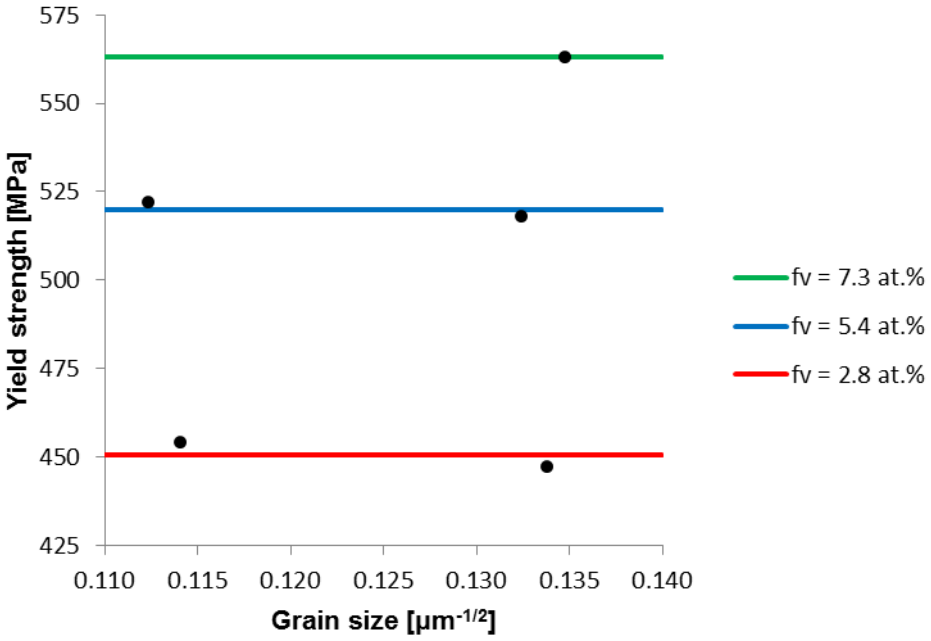


Figure 6.14. Yield strength of Alloys 7A to 7E, in the T6 condition, as a function of the grain size and precipitate volume fraction.

It can again be concluded that Equation 2.4 can be reduced to Equation 6.14, for the yield strength of Al-Zn-Mg-Cu aluminium alloys in the T6 condition:

$$Yield\ strength \propto f(composition) \qquad 6.14$$

Application of the composition model to the yield strength of the typical AA7075 wrought alloy also validated the finding that yield strength was not a function of grain size, since this wrought alloy was processed totally differently and had a different microstructure.

6.7.5. T73 hardness-composition relationship

It should not be surprising that the T73 hardness-composition relationship fitted the data well. It was important to again include the reactions of the impurity elements with the major alloying elements. The data point for the wrought alloy also followed the relationship which shows that the grain size due to difference in processing was not a factor.

All the alloys were Cu-limited, due to the fact that the Cu content of the T73 precipitate was so high. This shows that there was an excess of Zn and Mg relative to the Cu.

7. Conclusions

The objectives of this research were to investigate and explain the solidification properties of different R-HPDC processed Al-Zn-Mg-Cu aluminium alloy compositions. The following conclusions can be drawn regarding the studied Al-Zn-Mg-Cu aluminium alloys in the as-cast condition after R-HPDC and vacuum solidification:

- Al-Zn-Mg-Cu aluminium alloys produced with R-HPDC contained the cubic τ phase or the hexagonal η phase or a mixture of these two phases together with the (αAl) matrix phase in the eutectic, as determined with XRD.
- The melting reaction temperatures, determined with DSC, were 476 °C for alloys containing only $(\alpha Al) + \eta$ or a combination of $\tau + (\alpha Al) + \eta$, while 480 °C for the alloy containing only $(\alpha Al) + \tau$.
- The R-HPDC alloys follow the $L \leftrightarrow (\alpha Al) + \tau$ and $L + \tau \leftrightarrow (\alpha Al) + \eta$ equilibrium reactions of the Al-Mg-Zn system.
- Cooling rate, for the same alloy, determined the extent of the reaction. The τ phase appeared according to $L \leftrightarrow (\alpha Al) + \tau$ for a high cooling rate (R-HPDC), while the η phase appeared according to $L + \tau \leftrightarrow (\alpha Al) + \eta$ for a low cooling rate (vacuum cooling).

Al-Zn-Mg-Cu eutectic alloys were produced, based on eutectic compositions of the dilute Al-Zn-Mg-Cu aluminium alloys, to assess the chemical and melting point of the phases present in the eutectic; the following was concluded:

- The eutectic alloys had coarse regular eutectic microstructures.
- As the Cu content of the eutectic alloys increased, so did the Cu content of both phases in the eutectic, up to a point where the phases were supersaturated.
- Al_2Cu appears in the microstructure if the Cu content becomes too high.
- The Mg content of the Al-Zn-Mg-Cu phase was around 28 at.%, which was very different to the stoichiometric content of 33.3 at.% for the σ phase or 39.5 at.% for the T phase.

The primary objective of this research was to evaluate and model the T6 mechanical properties of R-HPDC processed alloys on a semi-theoretical base as a

function of the composition of the alloy and testing applicability of the model to wrought processed alloys.

The as-cast alloys were homogenised and artificially aged and the hardnesses of the five R-HPDC Al-Zn-Mg-Cu aluminium alloys were assessed and the following were concluded.

- Insoluble intermetallic phases were observed for alloy alloys in the T6 condition although not in the as-cast condition.
- The intermetallic phases were Mg_2Si, Al_7FeCu_2 and $Al_{28}Mn_7Cu_4$.
- The Mn-containing intermetallic phase seemed to have formed after homogenisation from Mn solid solution within Al grains.
- Mn, Fe and Si intermetallic phases were visually indiscernible with the SEM-BSE from the eutectic in the as-cast condition.
- Supersaturated alloys also exhibited major alloying element phases after homogenisation i.e. Al_2MgCu and an Al-Zn-Mg-Cu compound.

The T6 hardness and yield strength was evaluated as a function of the T6 grain size and the appropriate composition of the alloy and modelled through a precipitate composition found in literature for the strengthening precipitate:

- No relationship for the hardness or yield strength as a function of grain size was found.
- The hardness-composition relationship was shown to be linear, with a good fit (R^2=0.941) if the reactions with impurity elements were neglected.
- The linear fit improved to nearly perfect (R^2=0.9996), after the reactions with impurity elements were taken into account.
- T6 hardness data from literature were used to test the validity of the relationship for wrought alloys and was found to be valid.
- The T6 yield strength depended in the same way as the hardness on the atomic percentage of the limiting element of the precipitate, also with a near perfect linear fit (R^2=0.9973) when the impurity elements were taken into account.
- The improved yield strength-composition model was also tested with the nominal composition and typical yield strength of AA7075 T6 and also validated the model.

- The precipitate composition measured by APT for the ECAP process by Sha et al. [54] was found to be a very good approximation for the mechanical properties-composition model developed in this study, indicating that the thermal precipitates developed by the same sequence as for the severely strained material of their study.
- The model was based on the composition of the precipitate and therefore had a major influence on the results.
- The limiting element according to the T6 precipitate composition determines the volume fraction available for precipitation.
- Knowledge of the T6 precipitate crystal structure was not a prerequisite for the model, because the composition is sufficient.

The T73 hardness was evaluated as a function of the appropriate composition of the alloy and modelled through a precipitate composition found in literature for the over-aged strengthening precipitate:

- The hardness was shown to have a linear relationship with the composition of the alloy. The fit of the line to the data was again nearly perfect (R^2 = 0.999) if reactions with impurity elements were included.
- The wrought alloy data point fell on the T73 hardness-composition model line.
- The near-equilibrium precipitate composition measured by Marlaud et al. [4] was found to delineate the T73 hardness-composition relationship.
- All alloys were Cu-limited, which indicates that the Cu content required for the precipitate was high.
- Knowledge of the T73 precipitate crystal structure was not a prerequisite for the model.

The last objective was to propose an overall optimum Al:Zn:Mg:Cu ratio for Al-Zn-Mg-Cu aluminium alloys.

- The ratio of Al:Zn:Mg:Cu in the precipitate used in the improved mechanical properties-composition model was found to be the ultimate ratio for predicting T6 hardness and yield strength: $Al_{7.4}Zn_{45.4}Mg_{38.6}Cu_{8.6}$. The overall Zn, Mg and Cu contents in the alloy composition must also account for reactions with impurity or minor alloying elements.

- The ratio of Al:Zn:Mg:Cu in the precipitate used in the improved hardness-composition model was found to be the ultimate ratio for predicting T73 hardness: $Al_{15}Zn_{39}Mg_{33}Cu_{13}$. The overall Zn, Mg and Cu content in the alloy composition must again also account for reactions with impurity or minor alloying elements.
- Applicability of the improved mechanical properties-composition model to wrought alloy data also holds promise for designing wrought Al-Zn-Mg-Cu aluminium alloys.

References

[1] Davis JR (Ed.). ASM Specialty Handbook, Aluminum and Aluminum Alloys, fourth ed., ASM International, USA, 1998.

[2] Hughes DR (Ed.). Introduction to ALUMINIUM, Third ed., Aluminium Federation of Southern Africa, Bedfordview, Gauteng, South Africa, 2007.

[3] Li XM, Starink MJ. DSC study on phase transitions and their correlation with properties of overaged Al-Zn-Mg-Cu alloys. Journal of Materials Engineering and Performance 21 (2012) 977-984.

[4] Marlaud T, Deschamps A, Bley F, Lefebvre W, Baroux B. Influence of alloy composition and heat treatment on precipitate composition in Al-Zn-Mg-Cu alloys. Acta Materialia 58 (2010) 248-260.

[5] Bruwer R, Wilkins JD, Ivanchev LH, Rossouw P, Damm OFRA. US7368690. 2008.

[6] Curle UA, Möller H, Wilkins JD. Shape rheocasting of high purity aluminium. Scripta Materialia 64 (2011) 479-482.

[7] Curle UA, Möller H, Wilkins JD. Shape rheocasting of unmodified Al-Si binary eutectic. Materials Letters 65 (2011) 1469-1472.

[8] Möller H, Govender G, Stumpf WE, Pistorius PC. Comparison of heat treatment response of semisolid metal processed alloys A356 and F357. International Journal of Cast Metals Research 23 (2010) 37-43.

[9] Masuku EP, Govender G, Ivanchev L, Möller H. Rheocasting of Al-Cu alloy A201 with different silver contents. Diffusion and Defect Data Pt.B: Solid State Phenomena 141-143 (2008) 151-156.

[10] Curle UA. Semi-solid near-net shape rheocasting of heat treatable wrought aluminum alloys. Transactions of Nonferrous Metals Society of China (English Edition) 20 (2010) 1719-1724.

[11] Curle UA, Ivanchev L. Wear of semi-solid rheocast SiC_p/Al metal matrix composites. Transactions of Nonferrous Metals Society of China (English Edition) 20 (2010) s852-s856.

[12] Curle UA, Wilkins JD, Govender G. R-HPDC of magnesium alloys. Diffusion and Defect Data Pt.B: Solid State Phenomena 192-193 (2013) 225-230.

[13] Curle UA, Möller H, Govender G. R-HPDC in South Africa. Diffusion and Defect Data Pt.B: Solid State Phenomena 192-193 (2013) 3-15.

[14] Chou HN, Govender G, Ivanchev L. Opportunities and challenges for use of SSM forming in the aerospace industry. Diffusion and Defect Data Pt.B: Solid State Phenomena 116-117 (2006) 92-95.

[15] Atkinson HV. Alloys for semi-solid processing. Diffusion and Defect Data Pt.B: Solid State Phenomena 192-193 (2013) 16-27.

[16] Maciel Camacho A, Atkinson HV, Kapranos P, Argent BB. Thermodynamic predictions of wrought alloy compositions amenable to semi-solid processing. Acta Materialia 51 (2003) 2319-2330.

[17] Tsutsui Y, Kiuchi M, Ichikawa.K. (Eds.). 7th International Conference on Semi-Solid Processing of Alloys and Composites, (2002) 1-868.

[18] 8th International Conference on Semi-Solid Processing of Alloys and Composites, Cyprus, (2004), on CD.

[19] Kang CG, Kim SK, Lee SY (Eds.). 9th International Conference on Semi-Solid Processing of Alloys and Composites, Korea, 2006. Solid State Phenomena 116-117 (2006) 1-797.

[20] Hirt G, Rassili A, Bührig-Polaczek A (Eds.). 10th International Conference on Semi-Solid Processing of Alloys and Composites, Germany, 2008. Solid State Phenomena 141-143 (2008) 1-978.

[21] Huang WD, Kang YL, Yang XJ (Eds.). 11th International Conference on Semi-Solid Processing of Alloys and Composites, China, 2010. Transactions of Nonferrous Metals Society of China 20 (2010) 1556-1814.

[22] Möller H, Govender G (Eds.). 12th International Conference on Semi-Solid Processing of Alloys and Composites, South Africa, 2012. Solid State Phenomena 192-193 (2013) 1-574.

[23] Huang WD, Kang YL, Yang XJ (Eds.). 11th International Conference on Semi-Solid Processing of Alloys and Composites, China, 2010. Transactions of Nonferrous Metals Society of China 20 (2010) s714-s1054.

[24] Atkinson HV. Modelling the semisolid processing of metallic alloys. Progress in Materials Science 50 (2005) 341-412.

[25] Dantzig JA, Rappaz M. Solidification, first ed., EPFL Press, Italy, 2009.

[26] Xie F, Yan X, Ding L, Zhang F, Chen S, Chu MG, Chang YA. A study of microstructure and microsegregation of aluminum 7050 alloy. Materials Science and Engineering A 355 (2003) 144-153.

[27] Mondal C, Mukhopadhyay AK. On the nature of T($Al_2Mg_3Zn_3$) and S(Al_2CuMg) phases present in as-cast and annealed 7055 aluminum alloy. Materials Science and Engineering A 391 (2005) 367-376.

[28] Deng YL, Wan L, Wu LH, Zhang YY, Zhang XM. Microstructural evolution of Al-Zn-Mg-Cu alloy during homogenization. Journal of Materials Science 46 (2011) 875-881.

[29] Fan X, Jiang D, Meng Q, Zhong L. The microstructural evolution of an Al-Zn-Mg-Cu alloy during homogenization. Materials Letters 60 (2006) 1475-1479.

[30] Fan XG, Jiang DM, Meng QC, Zhang BY, Wang T. Evolution of eutectic structures in Al-Zn-Mg-Cu alloys during heat treatment. Transactions of Nonferrous Metals Society of China (English Edition) 16 (2006) 577-581.

[31] LI NK, CUI JZ. Microstructural evolution of high strength 7B04 ingot during homogenization treatment. Transactions of Nonferrous Metals Society of China (English Edition) 18 (2008) 769-773.

[32] Gao F, Zhao G, Bian W, Tian N. TEM in-situ investigation on non-equilibrium eutectics in semicontinuous casting ingot of Al-6.2Zn-2.3Mg-2.3Cu super-high strength aluminum alloy. Materials Science Forum 638-642 (2010) 384-389.

[33] Mazibuko NE, Curle UA. Effect of solution heat treatment time on a rheocast Al-Zn-Mg-Cu alloy. Materials Science Forum 690 (2011) 343-346.

[34] Lv X, Guo E, Li Z, Wang G. Research on microstructure in as-cast 7A55 aluminum alloy and its evolution during homogenization. Rare Metals 30 (2011) 664-668.

[35] Li WB, Pan QL, Xiao YP, He YB, Liu XY. Microstructural evolution of ultra-high strength Al-Zn-Cu-Mg-Zr alloy containing Sc during homogenization. Transactions of Nonferrous Metals Society of China (English Edition) 21 (2011) 2127-2133.

[36] Zou YB, Wang S, Zhao ZH, Cui JZ, Zhang HT, Tu GF. Constituents evolution of LFEC 7050 aluminum alloy during processing. Transactions of Nonferrous Metals Society of China 17 (2007) s249-s253.

[37] M. Bulanova, J. Gröbner, H. L. Lukas, D. Petrov, P. Rogl, J. Tedenac, et al. Landolt-Börnstein - Group IV Physical Chemistry, Al-Mg-Zn (Aluminium - Magnesium - Zinc), Light Metal Systems Part 3, Springer Berlin Heidelberg (2005) 191-209.

[38] G. Effenberg and A. Prince. Landolt-Börnstein - Group IV Physical Chemistry, Al-Cu-Mg (Aluminium - Copper - Magnesium), Light Metal Systems Part 3, Springer Berlin Heidelberg (2005) 47-78.

[39] Otarawanna S, Gourlay CM, Laukli HI, Dahle AK. Microstructure formation in AlSi4MgMn and AlMg5Si2Mn high-pressure die castings. Metallurgical and Materials Transactions A: Physical Metallurgy and Materials Science 40 (2009) 1645-1659.

[40] Seifert HJ. Computational phase studies in commercial aluminium and magnesium alloys. Materials Science and Technology 16 (2000) 1429-1433.

[41] Gao FH, Li NK, Tian N, Sun Q, Liu XD, Zhao G. Overheating temperature of 7B04 high strength aluminum alloy. Transactions of Nonferrous Metals Society of China (English Edition) 18 (2008) 321-326.

[42] Polmear I. Light Alloys: From Traditional Alloys to Nanocrystals, Burlington, 2006.

[43] SAE Aerospace. AMS 2770J: Heat Treatment of Wrought Aluminum Alloy Parts, Revision J., SAE International, USA, 2011.

[44] Starink MJ, Wang SC. A model for the yield strength of overaged Al-Zn-Mg-Cu alloys. Acta Materialia 51 (2003) 5131-5150.

[45] Thermo-Calc Software (TTAL8). http://www.thermocalc.com/media/5985/dbd_ttal8.pdf. Accessed 6/10/2014.

[46] Boettinger WJ, Kettner UR, Moon KW, Perepezko JH. DTA and Heat-Flux DSC Measurements of Alloy Melting and Freezing, National Insitute of Standards and Technology, Washington, 2006.

[47] Möller H, Curle UA, Masuku EP. Characterization of surface liquid segregation in SSM-HPDC aluminium alloys 7075, 2024, 6082 and A201. Transactions of Nonferrous Metals Society of China (English Edition) 20 (2010) s847-s851.

[48] Kolobnev IF, Lyut'tsau VG, Aristova NA. Effect of manganese on the hot strength of aluminum alloys. Metallovedenie i Termicheskaya Obrabotka Metallov 9 (1960) 38-41.

[49] Lukas HL. Landolt-Börnstein - Group IV Physical Chemistry, Al-Cu-Mn (Aluminium - Copper - Manganese), Light Metal Systems Part 3, Springer Berlin Heidelberg (2005) 79-96.

[50] Kumar HKC, Chakraborti N, Lukas HL, Bodak O, Rokhlin L. Landolt-Börnstein - Group IV Physical Chemistry, Al-Mg-Si

(Aluminium-Magnesium-Silicon), Light Metal Systems Part 3, Springer Berlin Heidelberg (2005) 165-177.

[51] Hansen N. Boundary strengthening in undeformed and deformed polycrystals. Materials Science and Engineering: A 409 (2005) 39-45.

[52] Michalak R, Niessen P, Plumtree A. The influence of grain size on the tensile and fatigue behaviour of 7075-T6 aluminum sheet. Canadian Metallurgical Quarterly 12 (1973) 147-153.

[53] Miura S, Mimaki T, Moriwaki S, Ono N. Hardness and stress-strain curves of Al-Zn-Mg-Cu alloy single crystals. Materials Transactions 49 (2008) 2709-2713.

[54] Sha G, Wang YB, Liao XZ, Duan ZC, Ringer SP, Langdon TG. Influence of equal-channel angular pressing on precipitation in an Al-Zn-Mg-Cu alloy. Acta Materialia 57 (2009) 3123-3132.

[55] Tang JG, Chen H, Zhang XM, Liu SD, Liu WJ, Ouyang H, Li HP. Influence of quench-induced precipitation on aging behavior of Al-Zn-Mg-Cu alloy. Transactions of Nonferrous Metals Society of China (English Edition) 22 (2012) 1255-1263.

[56] Ono N, Gouya J, Miura S. Hall-Petch relation and strengthening mechanisms in Al-Zn-Mg-Cu alloy polycrystals. Nippon Kikai Gakkai Ronbunshu, A Hen/Transactions of the Japan Society of Mechanical Engineers, Part A 68 (2002) 1136-1142.

[57] Osamura K, Ochiai S, Uehara T. Precipitation behaviour and change of yield strength during artificial aging in Al-Zn-Mg-Cu alloys. Journal of Japan Insitute of Light Metals 34 (1984) 517-524.

[58] Mahathaninwong N, Plookphol T, Wannasin J, Wisutmethangoon S. T6 heat treatment of rheocasting 7075 Al alloy. Materials Science and Engineering A 532 (2012) 91-99.

[59] Data sheet 7075-T6, T651. http://www.matweb.com/search/DataSheet.aspx?MatGUID=4f19a42be94546b686bbf43f79c51b7d. Accessed 02/10/2014.

Appendix A

The full ranges of angles for the XRD analyses are shown in Figures A.1 to A.9.

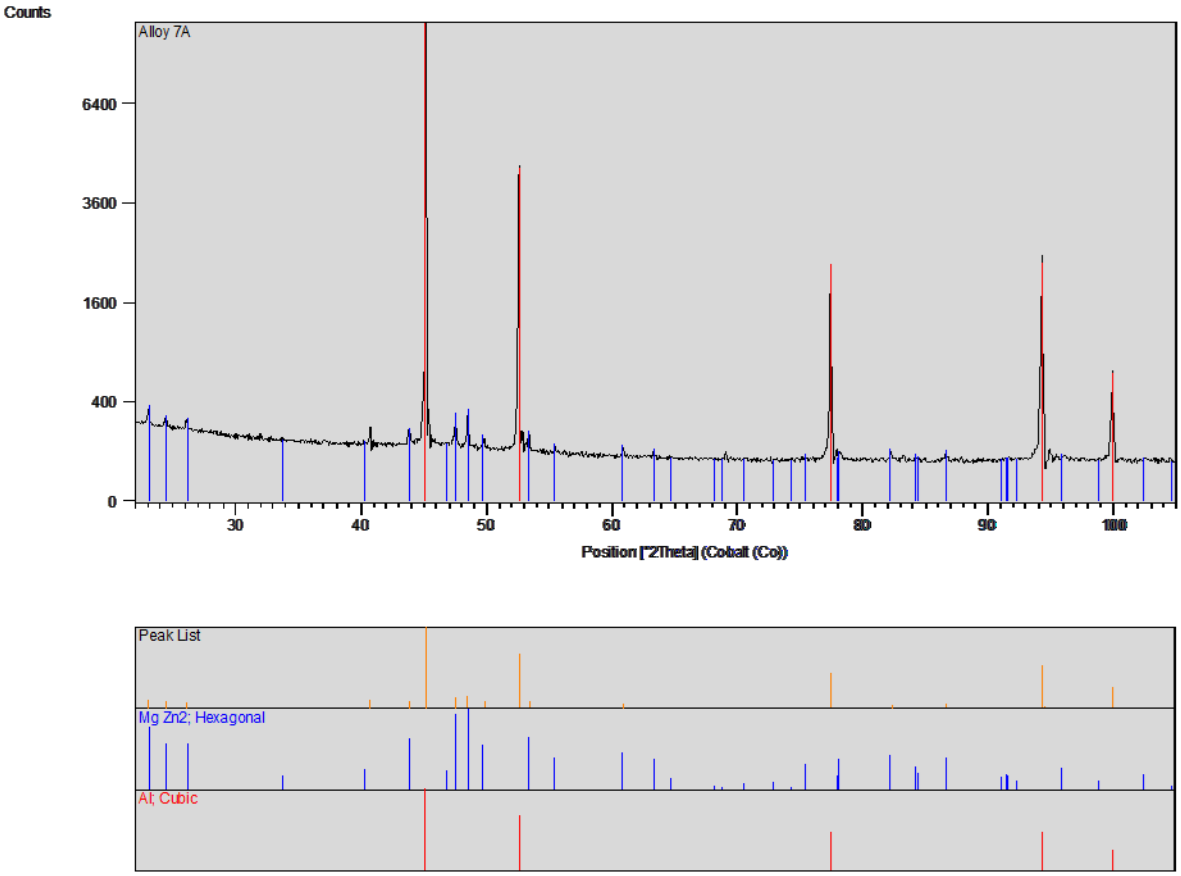


Figure A.1. Full range XRD pattern for as-cast Alloy 7A.

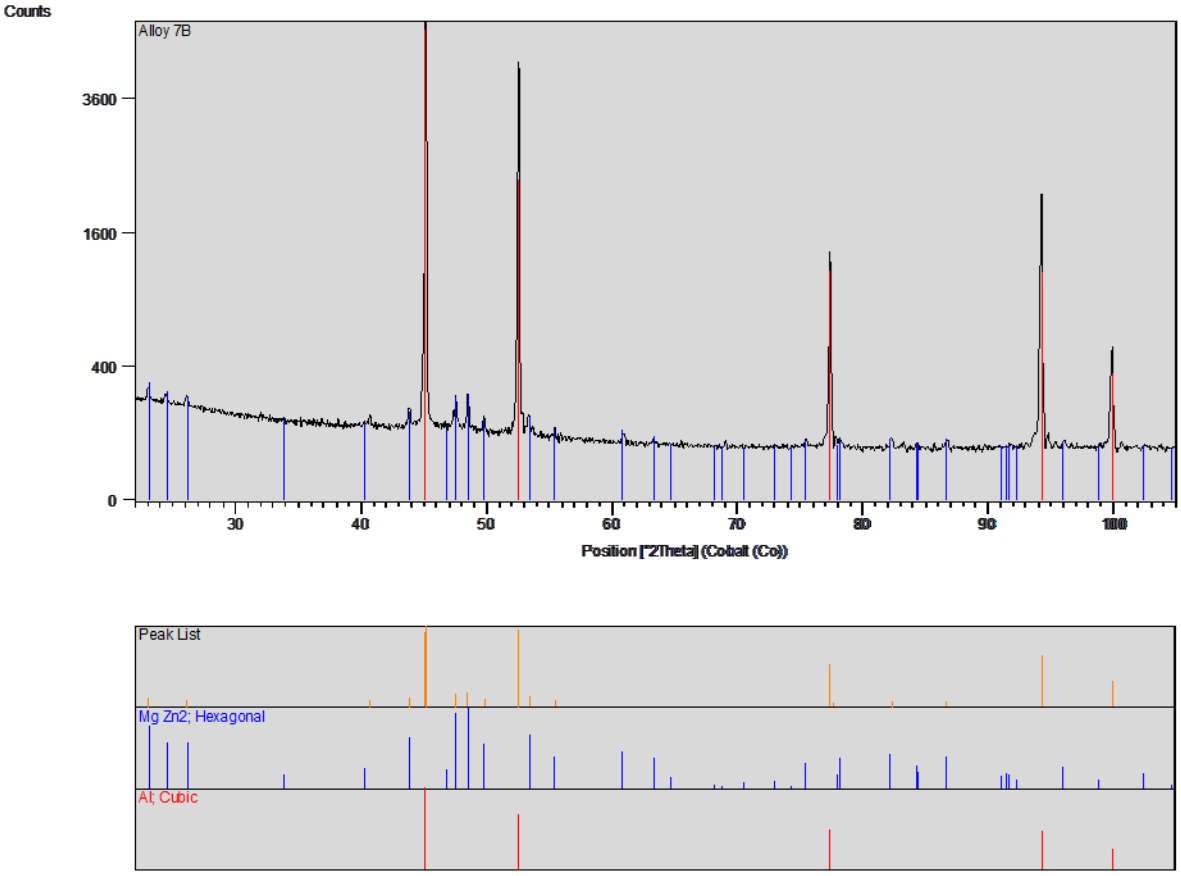


Figure A.2. Full range XRD pattern for as-cast Alloy 7B.

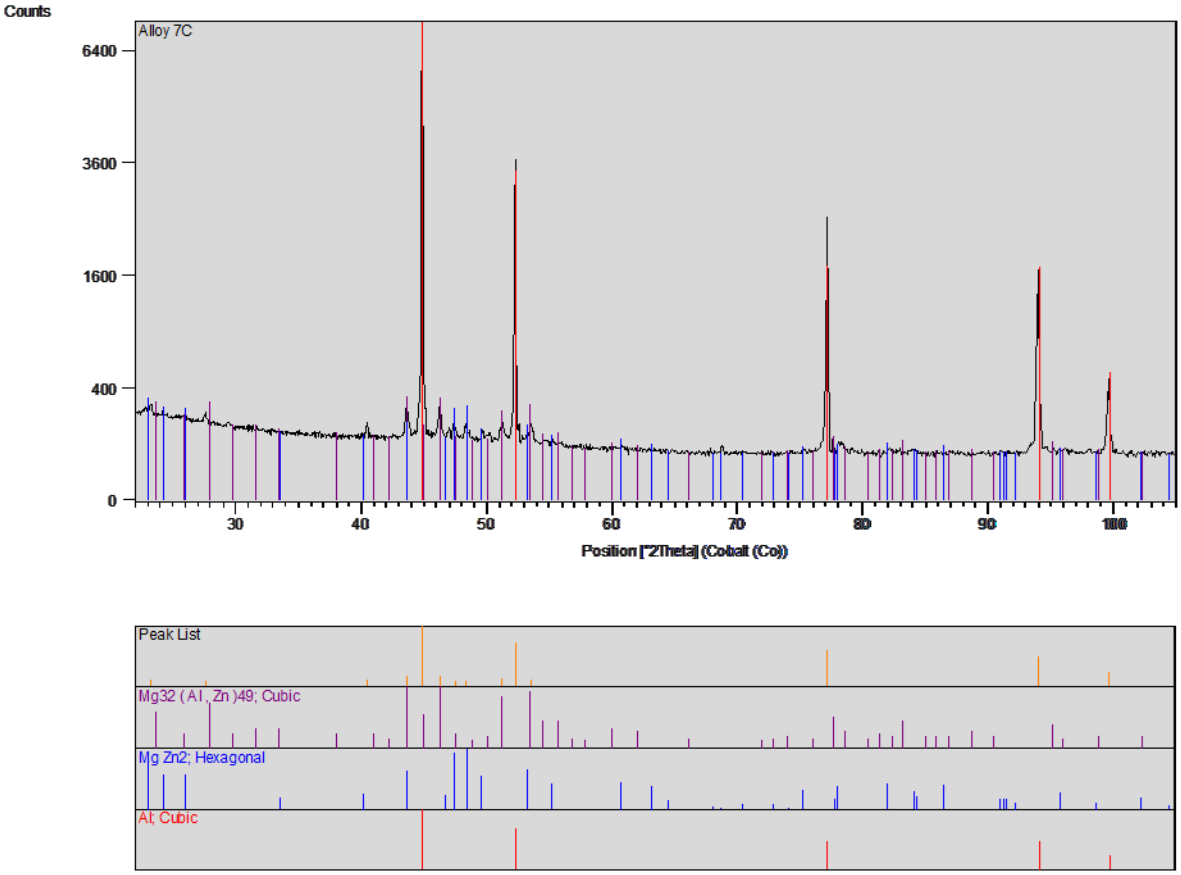


Figure A.3. Full range XRD pattern for as-cast Alloy 7C.

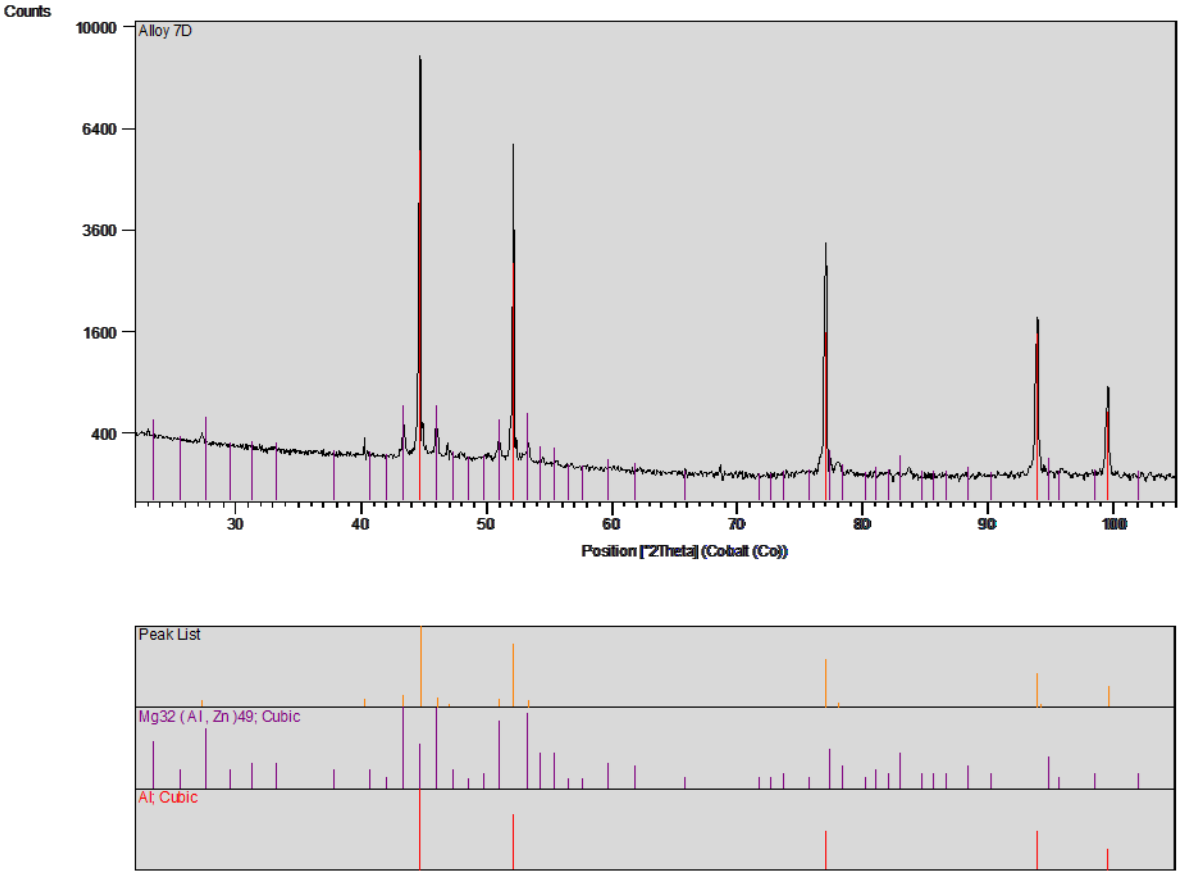


Figure A.4. Full range XRD pattern for as-cast Alloy 7D.

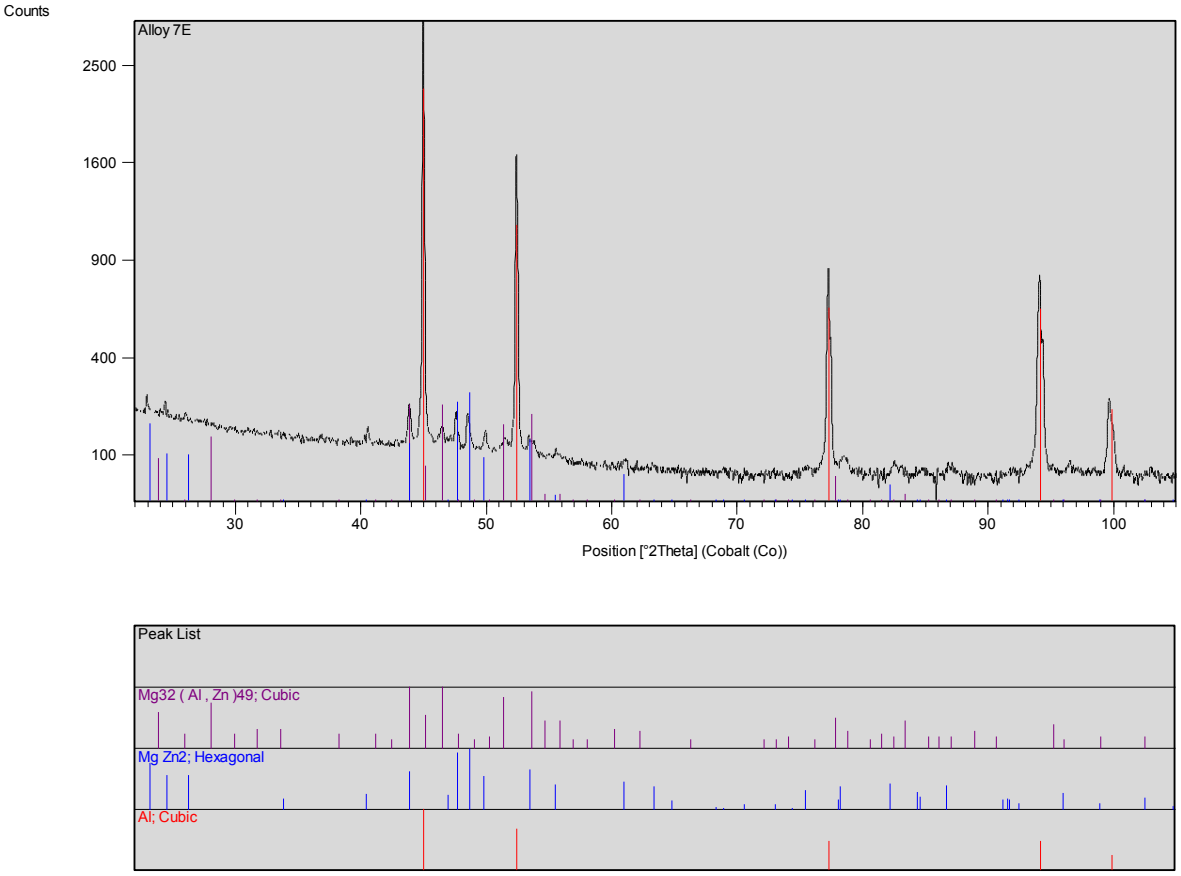


Figure A.5. Full range XRD pattern for as-cast Alloy 7E.

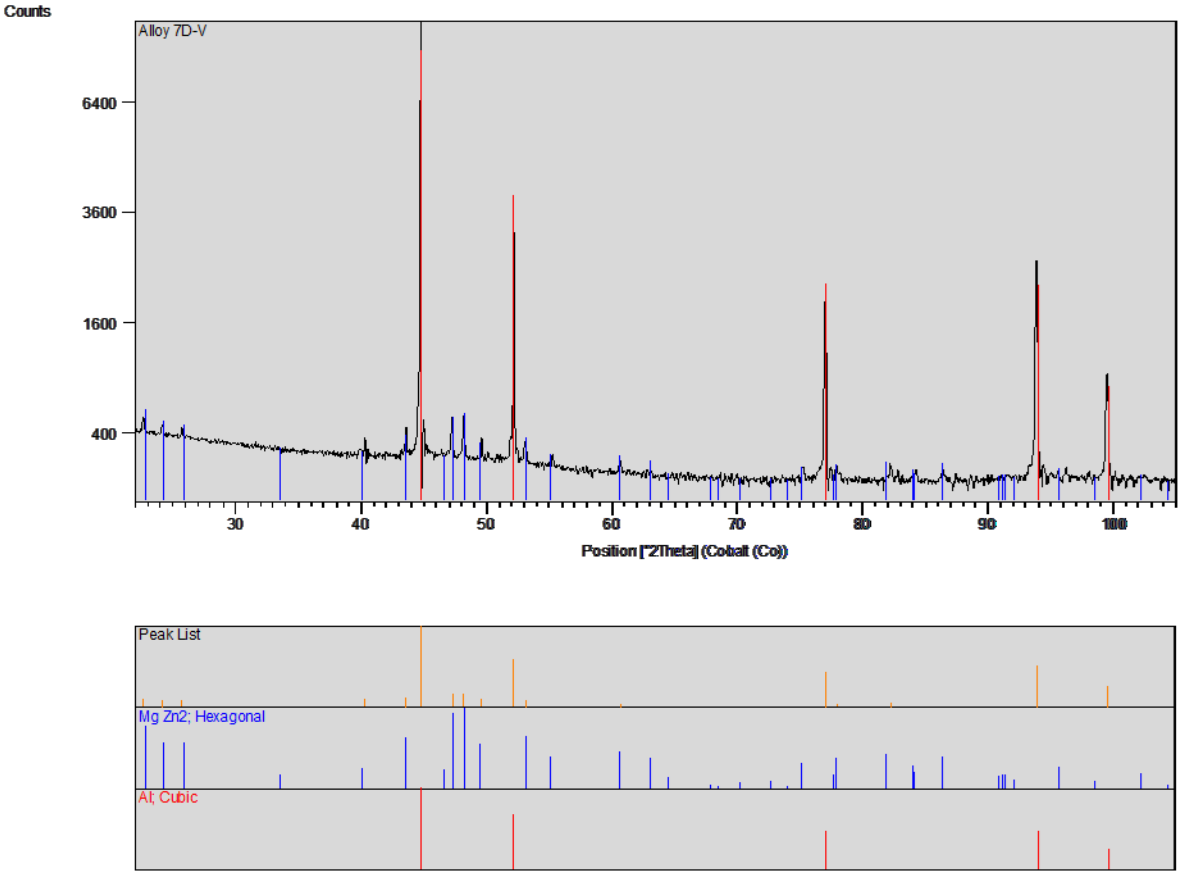


Figure A.6. Full range XRD pattern for as-cast Alloy 7D-V.

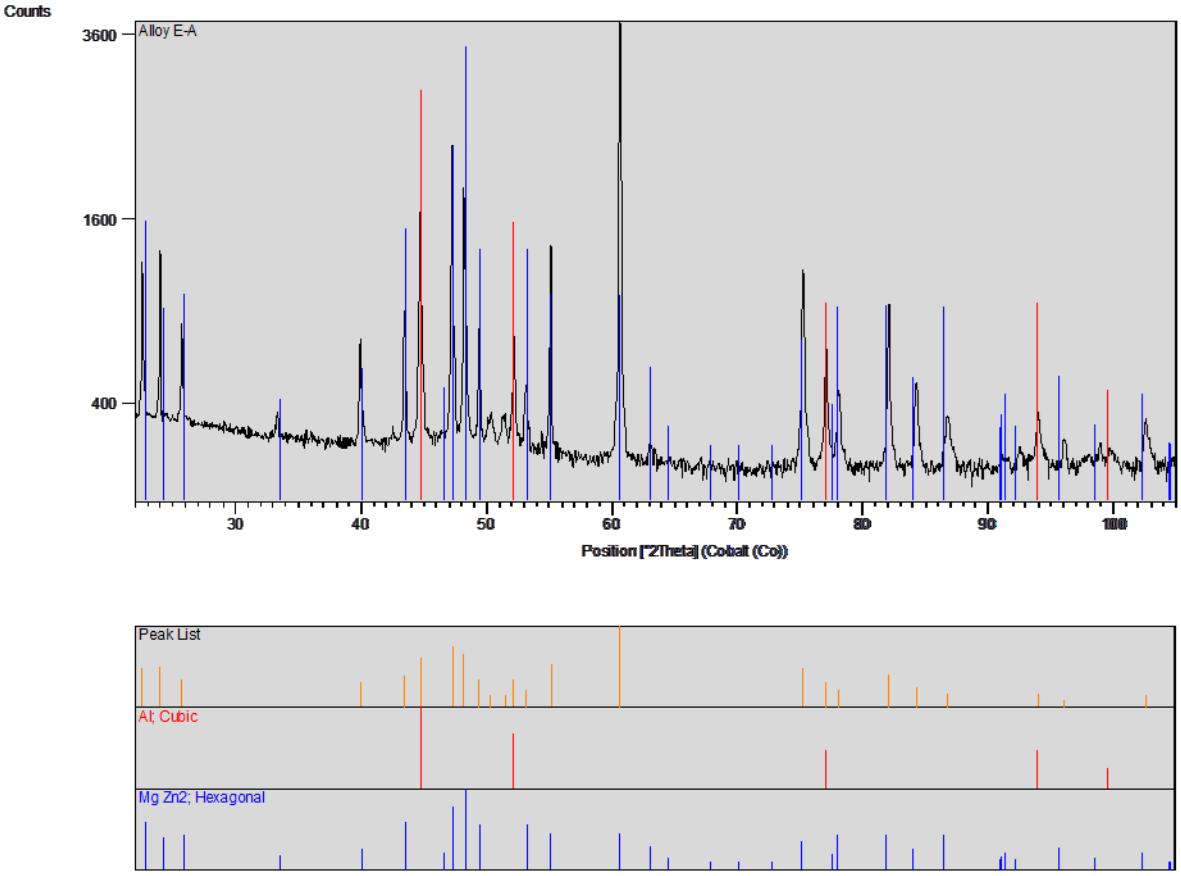


Figure A.7. Full range XRD pattern for eutectic Alloy E-A.

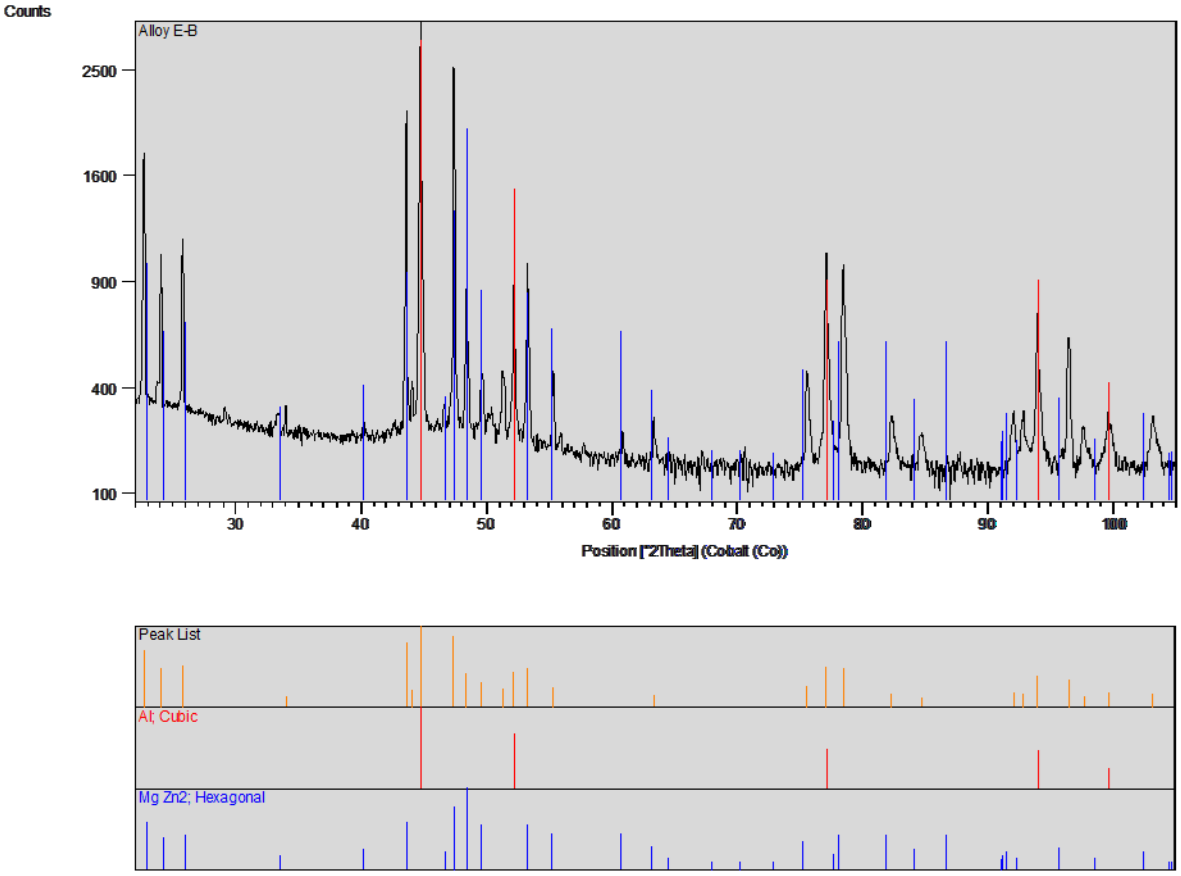


Figure A.8. Full range XRD pattern for eutectic Alloy E-B.

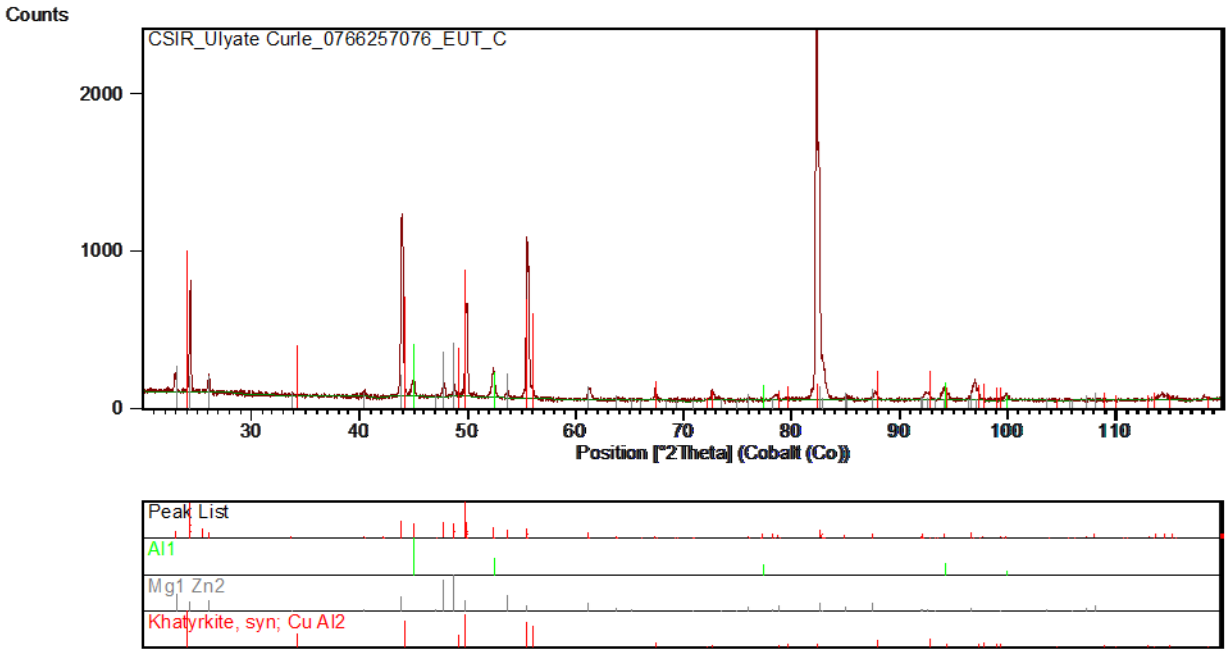


Figure A.9. Full range XRD pattern for eutectic Alloy E-C.